Geochemistry and metallogeny of magnetite-apatite deposits of the Bafq Mining District, Central Iran

Doctoral Thesis
(Dissertation)

to be awarded the degree of
Doctor rerum naturalium (Dr. rer. nat.)

submitted by
Farhad Mohammad Torab
from Tehran, Iran

approved by the Faculty of Energy and Economic Sciences
Clausthal University of Technology

Date of oral examination
19 February 2008

Chairperson of the Board of Examiners
Prof. Dr. H. Y. Schenk-Mathes

Chief Reviewer
Prof. Dr. Bernd Lehmann

Reviewer
Prof. Dr. Kurt Mengel

This dissertation was undertaken at the Institute of Mineralogy and Mineral Resources of Technical University of Clausthal.

Abstract

The Bafq mining district is in the Early Cambrian Kashmar-Kerman volcano-plutonic arc in Central Iran and hosts important “Kiruna-type” magnetite-apatite deposits. The hydrothermal magnetite-apatite mineralization occurs mostly as massive orebodies and metasomatic replacements with locally elevated rare-earth element contents and peripheral uranium mineralization. The geochemical signature, hydrothermal alteration zoning and magnetite chemistry point to IOCG (Iron Oxide-Copper-Gold) affinity. The apatite content of the deposits varies from relatively low-P magnetite ore (Choghart mine; 216 Mt @ 60 % Fe, 0.92 % P_2O_5, 0.08 % S) to magnetite-apatite ore (Chador-Malu mine; 400 Mt @ 55 % Fe, 2.15 % P_2O_5, 0.19 % S) to high-P apatite-(magnetite) ore (Esfordi mine; 17 Mt @ 14 % P_2O_5, 17 % Fe). Apatite (low-Sr fluor-apatite with small amounts of hydroxyl) has partially undergone hydrothermal overprint which involves leaching of sodium, chlorine, and rare-earth elements (REE). The REE are then remobilized into monazite (and minor allanite, parisite and xenotime) which nucleates as inclusions within apatite or as individual crystals outside of apatite. The monazites have very low ThO_2 content (usually less than 1 wt%), but they occasionally show an inner core of high-Th monazite, with low-Th overgrowth rims. Chemical Th-U-total Pb dating of the high-Th monazites by electron microprobe analysis yields an isochron age of 515 ± 21 Ma (initial PbO intercept = 68 ppm), or 529 ± 21 (forced initial PbO = 0), which is contemporaneous with the emplacement of the volcano-plutonic host rocks of the magnetite-apatite mineralization, as well as with widespread sedimentation of Late Proterozoic to Early Cambrian phosphorites and evaporitic rocks in Central Iran. The congruent ages of magnetite-apatite mineralization, uranium mineralization (507-542 Ma), and phosphorite and evaporite sedimentation suggest a genetic relationship. Nd isotope data exclude an origin of the REE inventory of the magnetite-apatite mineralization dominantly from igneous rocks and are in favor of a model of hydrothermal remobilization from the Early Cambrian sedimentary sequence. The monazite age, Nd isotope, mineralogical and geochemical data suggest that the magnetite-apatite deposits are likely related to large-scale basinal brine circulation induced by Cambrian felsic magmatism. Ar-Ar data on potassic alteration show variably disturbed age spectra which reveal younger thermal overprint at >300°C during the Mesozoic-Cenozoic evolution of Central Iran. The reinterpretation of the geotectonic and metallogenic setting of the magnetite-apatite deposits as of Andean-type, provides new exploration potential for the more than 1000-km-long Kashmar-Kerman volcano-plutonic arc for similar and other ore deposits of the general IOCG spectrum.

Acknowledgements

First and foremost, I would like to thank my supervisor, Prof. Bernd Lehmann. The most influential and constructive ideas in this thesis came from him. I am grateful to him for his enthusiastic supervision and academic advice. During writing several papers, he reviewed all of my manuscripts with an amazing efficiency and rigor which helped to much improve them. I also thank Prof. Kurt Mengel, for acceptance to be the second reviewer of this thesis and for his helpful comments.

The managers and technical staff of the Choghart, Esfordi and Chador-Malu mines are acknowledged for access to the deposits, sampling and support during field work. I would like to thank the faculty and the staff of the Institute of Mineralogy and Mineral Resources at the Technical University of Clausthal. Special thanks are due to Dr Eike Gierth for his kind assistance in ore microscopy, Klaus Herrmann for help with electron microprobe analysis, Fred Türck for computer support and Ulf Hemmerling for excellent sample preparation. I also would like to acknowledge my colleagues at the Mining Engineering Department of Yazd University in Iran for supplying some basic information and help with first stage sampling and sample preparation.

Dr Boris Belyatsky from Institute of Precambrian Geology and Geochronology of the Russian Academy of Science, and Dr Ray Burgess from Department of Earth, Atmospheric & Environmental Sciences at University of Manchester are thanked for performing Sm-Nd and Ar-Ar isotopic analyses, respectively. Dr Sergei Felitsyn from Institute of Precambrian Geology and Geochronology of the Russian Academy of Science is also thanked for providing some basic information on the sedimentary phosphorite of the Soltanieh Formation.

My good friends at the Institute of Mineralogy and Mineral Resources of TU Clausthal, Mohammad Ali Nekouvaght Tak, Daniel Hennig, Kouadio Etienne Assie, Akwinga Victor Asaah and Jens Wittenbrink are thanked for helpful academic discussions, providing nice environment during work, and reminding me that there is life outside the institute, too.

Last but not least, I would like to express my love and gratitude to my wife, my son and my family for their love and patience. This thesis is dedicated to them.

Contents

List of Figures

List of Tables

List of publications related to this thesis

Torab, F.M., and Lehmann, B., 2006, Iron oxide-apatite deposits of the Bafq district, Central Iran: an overview from geology to mining: World of Mining - Surface and Underground, v. 58, p. 355-362.

Torab, F.M., and Lehmann, B., 2007, Magnetite-apatite deposits of the Bafq district, Central Iran: apatite geochemistry and monazite geochronology: Mineralogical Magazine, v. 71, p. 347-363.

Torab, F.M., and Lehmann, B., 2007, Magnetite-apatite deposits of the Bafq district, Central Iran: monazite geochronology and ore formation: Digging Deeper, Proceedings of the Ninth Biennial SGA Meeting, Dublin, v. 1, 439-442.

Torab, F.M., Lehmann, B., Belyatsky, B., and Burgess, R., 2008, Reconnaissance study of iron oxide-P-REE±U deposits of the Bafq mining district, Central Iran: a new exploration perspective: Economic Geology, submitted.

Chapter 1: Introduction

1-1 Preface and background

The Bafq mining district in Central Iran hosts several economically important and active magnetite-apatite deposits, which are locally enriched in REE and are peripherally associated with U mineralization. In addition, there is volcano-sedimentary hosted massive sulfide Pb-Zn mineralization. It appears likely that all of these deposits formed in a common geotectonic setting and may have a common genetic affiliation. The focus of this thesis is on the geochemistry and metallogeny of the magnetite-apatite deposits, the most prominent members of this ore deposit spectrum.

The international iron ore market has recently attracted much attention due to strong demand from the steel industries. Mining capacities are extended worldwide, and the Central Iranian Bafq iron ore district is no exception. Most of the world iron ore production is from banded iron formations (BIF), magnetite-apatite deposits (“Kiruna-type”), as well as orthomagmatic titaniferous iron ores (such as iron ores in the Bushveld complex and nelsonites). Table 1-1 shows the iron ore reserve-base and production in different countries. The geological reserve of iron ore in Iran is only about 2,500 Mt but the bulk ore is relatively high grade (Table 1-1).

Table 1-1 World iron ore reserve-base and production (USGS, 2006)

Country	**Mine production (Mt)**		**Reserve base * (Mt)**	**Iron Content (Mt)**	**Average grade (%)**
	2004	**2005**			
Australia	231	280	40,000	25,000	62.5
Brazil	255	300	61,000	41,000	67.2
Canada	28	30	3,900	2,500	64.1
China	310	370	46,000	15,000	32.6
India	121	140	9,800	6,200	63.3
Iran	17	17	2,500	1,500	60.0
Kazakhstan	20	19	19,000	7,400	38.9
Mauritania	11	11	1,500	1,000	66.7
Mexico	12	12	1,500	900	60.0
Russia	97	95	56,000	31,000	55.4
South Africa	39	40	2,300	1,500	65.2
Sweden	22	23	7,800	5,000	64.1
Ukraine	66	69	68,000	20,000	29.4
United State	55	55	15,000	4,600	30.7
Venezuela	22	22	6,000	3,600	60.0
other countries	37	40	30,000	17,000	56.7
World total (rounded)	1,340	1,520	370,000	180,000	48.6

* Reserve base = measured plus indicated in-situ resources

Most of the Iranian iron ore reserves are located in the Bafq area in central Iran which were extensively explored during the 1960s and 70s in an Iranian-Russian cooperation project when 34 aeromagnetic anomalies were delineated, of which four deposits are currently mined. Individual deposits range up to several hundred million tonnes of iron ore with variable amounts of apatite. The iron ore deposits of the Bafq district are associated with volcano-sedimentary rocks and high-level intrusions, and have a sulfide-poor mineral assemblage of low-Ti magnetite (± hematite) with varying but characteristic amounts of fluorapatite and actinolite. This assemblage is similar to the iron ore deposits of the Kiruna district in northern Sweden, whence such ores are known as "Kiruna-type". The origin of "Kiruna-type" deposits is much debated and during the last decades a number of alternative processes of ore formation have been suggested for such deposits, ranging from magmatic (liquid immiscibility) (e.g. Frietsch, 1978; Nyström & Henriquez, 1994; Naslund et al., 2000), to exhalative-synsedimentary (Parak, 1975) to epigenetic-hydrothermal (e.g. Hildebrand, 1986; Bookstrom, 1977; Sillitoe & Burrows, 2002; Gleason et al., 2000). Current understanding tends to group the "Kiruna-type" deposits as end-member of the IOCG (Iron-Oxide Copper Gold) clan (see e.g. Hitzman et al., 1992, Hitzman, 2000). This is supported by similarity of geotectonic setting, abundance of early-stage magnetite, occurrence of late-stage pyrite, chalcopyrite and gold in or near some massive magnetite deposits, and commonality of certain alteration (sodic, potassic) and gangue minerals especially actinolite and apatite.

IOCG ore deposits have high economic potential and include a wide spectrum of sulphide-deficient low-Ti magnetite and/or hematite ore bodies of hydrothermal origin (breccias, veins, stockworks or massive lenses) with polymetallic enrichment (Cu, Au, Ag, P, U, REE, …) which are genetically associated (either proximal or distal) with large scale calc-alkaline or alkaline magmatism (Hitzman, 2000; Pollard, 2000; Corriveau, 2005; Williams et al., 2005). The recognition of this deposit type was triggered by the discovery of the giant Olympic Dam deposit in Australia by WMC (Western Mining Corporation) in 1975 (Roberts and Hudson, 1983) followed by discovery of similar deposits in other parts of Australia, South America, Canada, Brazil and some other countries (Fig. 1-1). Because of the diversity of IOCG deposits, there is debate whether they form a single deposit type or if they are iron oxide-rich variants of other deposit types. The group covers a compositional range of ores from Fe-apatite ores as at Kiruna without any significant Cu-Au, to Fe-REE-F at Bayan Obo, again without any Cu or Au of economic value, to the Fe-Cu-U-Au-REE mineralization of Olympic Dam, etc. (Porter, 2000). There are some exotic deposits such as Phalaborwa

(Palabora) which could be members of the family (see e.g. Vielreicher et al., 2000). Fig. 1-1 shows the main districts and important IOCG and related deposits worldwide.

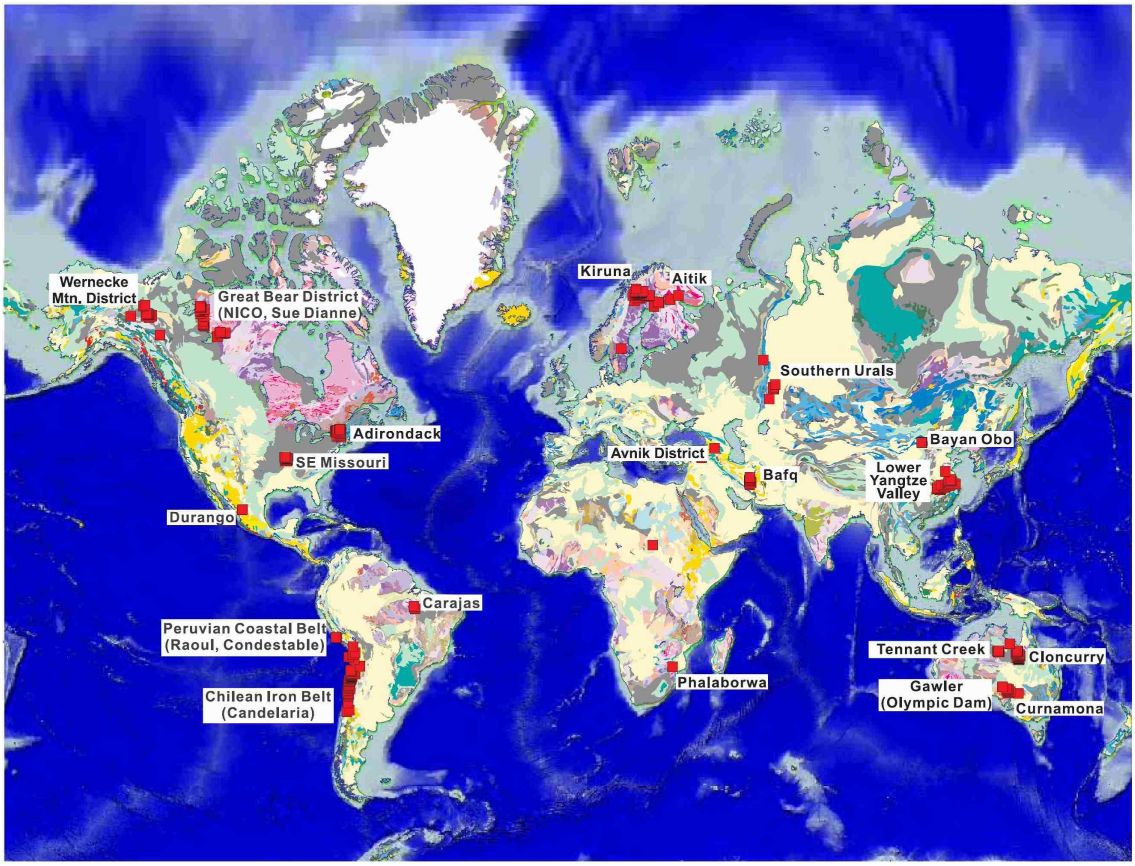

Fig. 1-1 Main districts and distribution of important IOCG and related deposits worldwide (Corriveau, 2005). **Australia:** Gawler (Olympic Dam, Acropolis, Moonta, Oak Dam, Prominent Hill and Wirrda Well deposits), Cloncurry (Ernest Henry, Eloise, Mount Elliot, Osborne and Starra deposits), Curnamona (North Portia and Cu Blow deposits) and Tennant Creek (Gecko, Peko/Juno and Warrego deposits) districts; **Brazil:** Carajas district (Cristalino, Alemao/Igarapé Bahia, Salobo, and Sossego deposits); **Canada:** Great Bear Magmatic Zone (Sue-Dianne and NICO deposits), Wernecke, West Coast skarns and Central Mineral Belt districts, and Kwyjibo deposit; **Chile:** Chilean Iron Belt (Candelaria, El Algarrobo, El Romeral, Manto Verde, and Punta del Cobre deposits); **China:** Bayan Obo deposit (Inner Mongolia), Lower Yangtze Valley district (Meishan and Daye deposits); **Iran:** Bafq district (Choghart, Chador-Malu, Se-Chahun, Esfordi deposits); **Mauritania:** Akjoujt deposit; **Mexico:** Durango district (Cerro de Mercado); **Peru:** Peruvian Coastal Belt (Raul, Condestable, Eliana, Monterrosas and Marcona deposits); **Sweden:** Kiruna district (Kiirunavaara, Loussavaara), Aitik deposit (also described as a porphyry Cu deposit); **South Africa:** Phalaborwa and Vergenoeg deposits; **Turkey:** Avnik district; **USA:** Southeast Missouri (Pea Ridge and Pilot Knob deposits), Adirondack and Mid-Atlantic Iron Belt (Reading Prong); **Zambia:** Shimyoka, Kantonga, and Kitumba prospects.

Because most of these ore bodies occur in highly deformed Proterozoic belts, the geological setting and the source of the metals and fluids are controversial. This style of mineralization shows a direct relationship with large scale faults and broad zones of sodium-calcium (albite-actinolite) or potassic (K-feldspar or biotite) alteration. Their lithological hosts and ages are non-diagnostic but their alteration zones are, with calcic-sodic regional alteration at deep levels, superimposed by potassic and sericitic alterations. The deposits form at shallow to mid crustal levels in extensional, anorogenic or orogenic, continental settings such as intracratonic and intra-arc rifts, continental magmatic arcs and back-arc basins with different host rocks (Fig. 1-2) (Hitzman et al., 1999; Hitzman, 2000; Corriveau, 2005). They are formed by hypersaline oxidized fluids and the origin of the fluids is interpreted as magmatic (e.g., Pollard, 2000; Sillitoe, 2003; Pollard, 2006), or metamorphic or basinal (evaporitic) brines heated by nearby intrusions (e.g. Barton and Johnson, 1996, 2000, 2004) (Fig. 1-3).

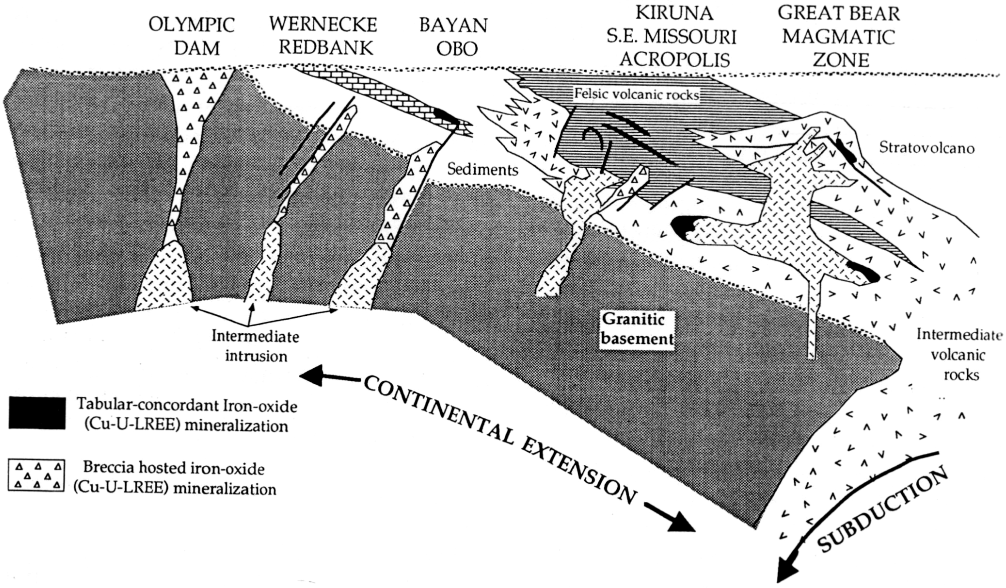

Fig. 1-2 Schematic representation of the tectonic setting and host rock sequence for some iron oxide (Cu-U-REE-Au) deposits (after Hitzman et al., 1992).

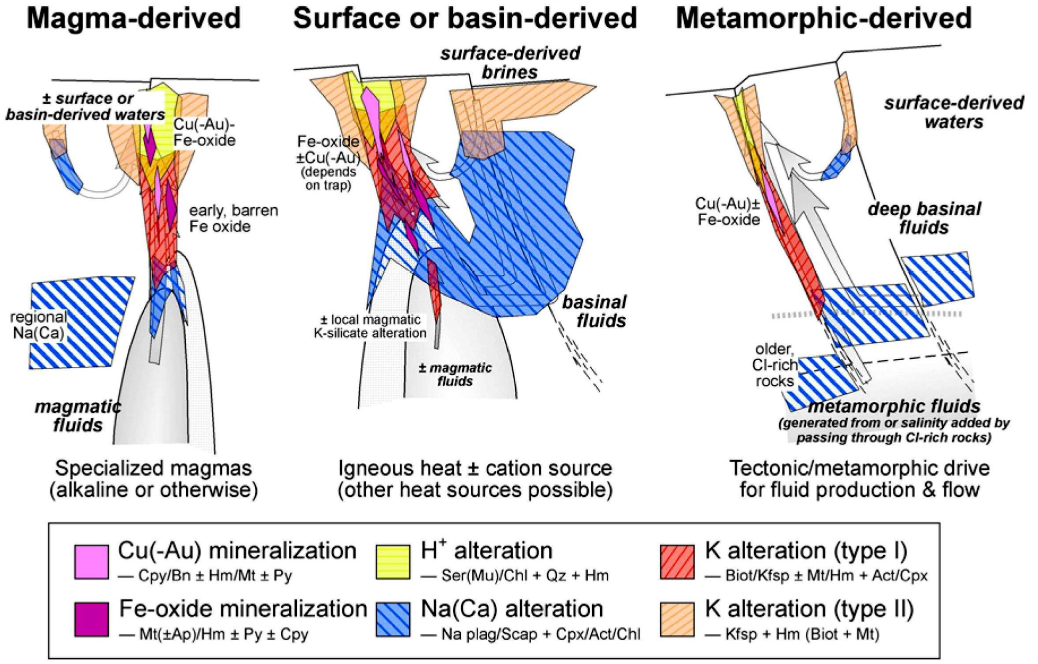

Fig. 1-3 Schematic illustration of alternative fluid sources, flow paths and hydrothermal features in different IOCG deposits (after Barton and Johnson, 2004).

IOCG deposit classification

The diversity of IOCG deposits and of different opinions on their genesis necessitates classifying them. The classification elaborated by Gandhi (cited in Corriveau, 2005) for the World Minerals Geoscience Database Project is used herein (Table 1-2).

Table 1-2 Classification of magmatic-hydrothermal iron oxide deposits and related Cu Au deposits (after Gandhi, 2003; Corriveau, 2005)

<table>
<tr><th colspan="4">Source → Proximal → Distal</th></tr>
<tr><th colspan="4"><i>Calc-alkaline magma</i></th></tr>
<tr><th>Iron Skarn-type</th><th>Kiruna-type</th><th>Olympic Dam-type</th><th>Cloncurry-type</th></tr>
<tr><td>Massive magnetite- garnet-pyroxene</td><td>Massive magnetite-apatite-actinolite</td><td>Breccia (one or more stages), magnetite-hematite matrix</td><td>Hydrothermal veins & disseminations in older 'ironstones' or FeOx mineralization</td></tr>
<tr><td>Stratabound lensoid & irregular bodies at intrusive contact</td><td>Tabular, pipe-like & irregular bodies, dykes & veins</td><td>Pipe-like & irregular bodies, vent or fault-controlled</td><td>Stratabound, breccia or fault-controlled</td></tr>
<tr><td>Monometallic Fe and related FeOx-Cu-Au deposits</td><td>Monometallic Fe & related Cu-FeOx deposits</td><td>Polymetallic: Fe, Cu, Au, Ag, REE</td><td>Polymetallic: Cu, Au, Ag, Bi, Co, W</td></tr>
<tr><td>Main alteration: Sodic</td><td>Main alteration: Sodic</td><td>Main alteration: Potassic</td><td>Main alteration: Potassic</td></tr>
<tr><td>Magnitogorsk deposit, Russia</td><td>Kiirunavaara deposit, Sweden</td><td>Olympic Dam deposit, Australia</td><td>Osborne & Starra deposits, Australia</td></tr>
<tr><th colspan="4">Source → Proximal → Distal</th></tr>
<tr><th colspan="4"><i>Alkaline-carbonatite magma</i></th></tr>
<tr><th colspan="2">Phalaborwa-type</th><th colspan="2">Bayan Obo-type</th></tr>
<tr><td colspan="2">Within or marginal to intrusion</td><td colspan="2">Hosted by country rock</td></tr>
<tr><td colspan="2">Veins, layers, disseminations and aggregates; late intrusive phase</td><td colspan="2">Veins, layers, disseminations and aggregates, stratabound lenses</td></tr>
<tr><td colspan="2">Low (to moderate) Ti magnetite, apatite, olivine, phlogopite, carbonate, fluorite, Cu sulphides, pyrite, PGE, Au, Ag, uranothorianite, baddeleyite</td><td colspan="2">Magnetite (replacive and/or pre-existing), hematite, bastnaesite, phlogopite, Fe-Ti-Cr-Nb oxides, fluorite, monazite, carbonate</td></tr>
<tr><td colspan="2">Zoning in ore; Na & K alteration</td><td colspan="2">Zoning in ore; Na & K alteration</td></tr>
<tr><td colspan="2">Phalaborwa deposit, South Africa</td><td colspan="2">Bayan Obo deposit, China</td></tr>
</table>

The Olympic Dam sub-type consists of granite-associated, breccia-hosted deposits where polymetallic ore is spatially and temporally associated with iron oxide alteration (Corriveau, 2005). In this sub-type, some 75 deposits and prospects are in the World Minerals Geoscience Database (WMD; Gandhi, 2004). The giant Olympic Dam iron oxide-Cu-U-Au-Ag-REE deposit is located in the Stuart Shelf geological province of South Australia, on the eastern margin of the Gawler Craton. The deposit is hosted by a 7 by 5 km (in plan), funnel-shaped, hematite-rich hydrothermal breccia (Olympic Dam Breccia Complex), wholly contained within the Roxby Downs Granite of middle Proterozoic age (1590 Ma) (Creaser & Cooper, 1993, Johnson & Cross, 1995; Reynolds, 2000).

The total resource of the Olympic Dam deposit (including measured, indicated and inferred) has been reported as 2,320 Mt in 1999 by WMC (Western Mining Corporation) (Reynolds, 2000). However, recent data by WMC (2004) give a global resource of 3,810 Mt with 1 wt% Cu, making it one of the world's largest Cu deposits. The deposit also contains 0.5 g/t Au and 400 g/t U_3O_8 (Williams et al., 2005), and elevated Ag, F, Ba and REE (~5000 ppm ∑REE), and its average Fe content is 26 wt% predominantly in the form of hematite (Oreskes & Einaudi, 1990; Rynolds, 2000). Although the grade of U in this deposit is low compared to other uranium-only deposits (e.g., unconformity U deposits), this deposit is currently the world's largest producer of uranium due to its huge tonnage (Hitzman & Valenta, 2005). The breccia complex comprises a hematite-quartz breccia core, a peripheral hematite-granite breccia and a halo of weakly altered and brecciated granite. Potassic alteration with hematite, sericite, chlorite, carbonate ± Fe-Cu sulphides ± uraninite, pitchblende and REE minerals prevail, and are locally superimposed on magnetite-biotite alteration (Reynolds, 2000; Skirrow et al., 2002). Like many other IOCG deposits and prospects, Olympic Dam is a blind deposit discovered by its coincident positive magnetic and gravity anomalies (Reynolds, 2000).

The Cloncurry sub-type, with 55 examples in the WMD, is named after the Cloncurry district in the Mount Isa inlier of Northwest Queensland, Australia. It comprises deposits where hydrothermal Cu ± Au mineralization overprints pre-existing 'ironstones' or iron formations (Starra, Salobo) or distinctly earlier hydrothermal iron oxide concentrations (Ernest Henry) (Requia and Fontboté, 2000; Gandhi, 2003; Requia et al., 2003, Williams et al., 2005). Though host lithologies play an important local role, mineralization is mainly fault or shear controlled. In the ca. 1.50 Ga Ernest Henry deposit, mineralization postdates peak metamorphism of the ca. 1.74 Ga volcanic host and is synchronous with granite intrusions and regional alteration (Mark et al., 2000). Early magnetite-apatite mineralization and associated Na-Ca alteration were followed by brecciation and then overprinted by Cu-Au mineralization. Host lithologies may be significantly deformed and metamorphosed prior to mineralization and granite emplacement (up to upper amphibolite facies), or as at Osborne, mineralization may be metamorphogenic. The Osborne deposit, formerly considered to be of the same age as the other IOCG deposits of the Cloncurry district at ca. 1.5 Ga, is in fact older (1595-1600 Ma) and syn-peak metamorphism (Gauthier et al., 2001). Local remobilization of iron oxides in the host rocks and/or addition of iron oxides from external sources may occur (Partington and Williams, 2000). Potassic and calcic-sodic (Na-Ca) alterations are common and, in many cases, widespread and intense.

The Kiruna sub-type, with more than 355 deposits and prospects, comprises monometallic, low Ti and V magnetite-apatite deposits with little or no Cu and Au (Hitzman et al., 1992; Hitzman, 2000). It is named after the classic Kiruna district in northern Sweden and includes the world class Kiirunavaara massive magnetite deposit, as well as the Luossavaara, Rektorn, Haukivaara, Nukutusvaara, Lappmalmen and Mertainen deposits in Sweden (Frietsch et al., 1979), the Bafq district in Iran (Förster & Jafarzadeh, 1994; Daliran, 2002; Torab & Lehmann, 2006, 2007), Avnik district in Turkey (Helvaci, 1984), as well as several deposits in the Andes (Bookstrom, 1977; Naslund et al., 2002; Sillitoe, 2003). These deposits are generally coeval with, and genetically related to their host volcanic and plutonic rocks. Their massive veins, tabular, pipe-like, or irregular bodies and associated sodic and calcic-sodic alteration represent a precursor to some significant Cu-Au mineralizations both in intracratonic and in continental arc settings (Hitzman, 2000; Mark and Foster, 2000; Mark et al., 2000; Ray and Dick, 2002; Skirrow et al., 2002; Sillitoe, 2003). Large-scale sodic metasomatism results in the formation of very diagnostic albitites.

The Phalaborwa (Palabora) sub-type consists of magnetite-rich deposits formed coevally with and proximal to alkaline-carbonatite intrusions (Groves and Vielreicher, 2001; Goff et al., 2004). Primary characteristics are the presence of apatite and strong fenitization, the strong enrichment in REE, F and P, and the extremely high LREE to HREE ratios. The REE are contained in apatite and in a variety of REE-bearing phases. Zirconium can be high and resides in baddeleyite. Titanium content of magnetite in the host intrusions is variable (< 1 to 4 wt % TiO2) and is higher than in magnetite of most IOCG deposits. The lowest Ti contents of magnetite are in the ore zones related to the intrusions.

Among the alkaline-carbonatite intrusions, the 2.06 Ga Phalaborwa Complex in South Africa is exceptional in having an economic grade of copper. It consists of a magnetite-rich pipe-like ore body hosted in a carbonatite phase of an alkaline pyroxenite intrusion. The ore body is zoned, with copper sulphides concentrated in the core, and magnetite toward the margin (Harmer, 2000). Copper sulfides (chalcopyrite or bornite and minor chalcocite) postdate the iron-oxide mineralization. No structural control has been documented for the Phalaborwa Complex, but its setting at the margin of an Archean craton is viewed by Vielreicher et al. (2000) as a key element in the development of the ore deposit.

The Bayan Obo sub-type consists of magnetite-rich, Cu-Au deficient, REE (-Nb) deposits distal to an alkaline-carbonatite plutonic source that display the diagnostic mineral assemblages and metals of the source magmas (Smith and Chengyu, 2000). The Bayan Obo deposit is in a graben on the margin of the Archean North China craton. The ore occurs as massive, banded and disseminated in marble. The ore mineralogy, with some 70 minerals, is dominated by magnetite, bastnaesite, fluorite, alkali amphiboles and pyroxenes. The alteration assemblage consists of apatite, aegirine, aegerine-augite, fluorite, alkali amphibole, phlogopite and barite (Smith et al., 2000). This mineral suite is diagnostic of an alkaline-carbonatite magmatic source for the mineralizing fluids. However, the only exposed link with such magmatism is the presence of some carbonatite dykes. The age of mineralization is quoted either as between 555-420 Ma (Chao et al., 1997; Smith et al., 2000) or at 1.3-1.2 Ga (Yang et al., 2003). The fact that marble is a host complicates the recognition of carbonatite in the field, as the two lithologies may look very similar. The lack of significant coeval magmatism but the presence of deep-seated faults active since the Proterozoic time in the area illustrate that significant iron oxide ore may form even if coeval magmatism is volumetrically insignificant as long as channel ways for fluids are available.

The iron-skarn sub-type shares some features with the Kiruna sub-type, and includes major deposits in the southern Urals region and in the Peruvian Coastal Belt (Ray and Lefebure, 2000; Herrington et al., 2002; Injoque, 2002; Sillitoe, 2003).

Associated mineral deposit types: On a district scale, IOCG deposits are known to occur in the vicinity of alkaline and calc-alkaline porphyry Cu-Mo or Cu-Au deposits, Cu-Ag manto deposits, volcanic-hosted uranium ore bodies, hematite-rich massive ironstones, sediment-hosted Au-PGE, polymetallic Ag-Pb-Zn±Au veins and SEDEX deposits, and rarely near volcanic-hosted massive sulfide deposits (Pollard, 2000; Boric et al., 2002; Grainger et al., 2002; Sillitoe, 2003).

1-2 Objectives and methodology

The genesis of the magnetite-apatite deposits of the Bafq district is controversial, similar to their world counterparts. Several different tentative genetical models, from carbonatitic, to iron ore magma (intrusion or volcanic) to metasomatic replacement were proposed (see e.g., Samani, 1988; Daliran, 1990; Förster & Jafarzadeh, 1994; Mücke & Younessi, 1994; Daliran, 2002). These different interpretations may firstly derive from the complexity of the ore deposit system, but also can come from lack of precise dating of the ore, and insufficient geochemical investigations. For instance, it is not exactly clear in which geotectonic regime these deposits formed, and which the relationship of geotectonic setting and ore formation could be? What is the relationship of the ore and the host rocks, and what is the role of igneous rocks in the ore forming process? Why some of these deposits contain high apatite content while the others are relatively pure iron ores? Are Fe and P originated from a common source or are they derived from different sources? What is the relationship between the ore and REE mineralization and why some of these deposits are enriched in REE? Can these deposits be considered as a subset of the IOCG family? What are the new exploration suggestions to discover similar deposits and/or perhaps another sub-type of the IOCG family in this potentially rich district?

Although there is still a long way to go, this thesis aims to unravel some of these mysteries in the genesis and geochemistry of these deposits and to develop exploration strategies. To achieve this, first some important magnetite-apatite deposits of the Bafq district (Chador-Malu, Choghart and Esfordi) were investigated and a total of more than 150 samples from ore (outcrops or drill-cores), host rocks and alteration zones was taken during two phases of field work. The samples were transferred to the Technical University of Clausthal for further studies. Some of the sample preparation work, including crushing and pulverizing was carried out at Esfordi mine as well as in the mineral processing laboratory of the Mining Engineering Department at Yazd University, Iran, and the remainder was done in Clausthal. About 90 samples from the ore and host rocks were selected and analyzed for major elements and some trace elements by X-ray fluorescence spectrometry (XRF) at the Geological Survey of Germany in Hannover, and other trace and rare earth elements were analyzed by INAA and ICP methods at Actlabs in Canada. Details of analytical techniques and data are compiled in Appendix 1. More than 40 thin, polished and polished-thin sections were prepared in Clausthal for microscopic examinations and electron microprobe analysis (EMPA) which were performed at the Institute of Mineralogy and Mineral Resources of Technical University of Clausthal. Details of analytical conditions and data are given in Appendix 2. Eight bulk samples from the ore and host rocks of the deposits were selected and analyzed for Sm-Nd isotopes at the Institute of Precambrian Geology and Geochronology of the Russian Academy of Sciences, and three samples with potassic alteration (high K content) from the Chador-Malu and Esfordi deposits were analyzed by the ^{40}Ar/^{39}Ar thermal release method in the Department of Earth, Atmospheric & Environmental Sciences, University of Manchester. The analytical techniques are compiled in Appendix 3.

This thesis consists of 7 chapters. The following chapter (chapter 2) explains the geographical situation, tectonic setting and regional geology of the Bafq district. Chapter 3 describes some of the most important and active magnetite-apatite deposits in this district. The local geology of each deposit, as well as some economic aspects will be discussed briefly. Chapter 4 deals with the mineralogy and alteration at these deposits. Bulk rock as well as ore geochemistry are discussed in chapter 5. In chapter 6 we deal with dating the ore on the basis of monazite geochronology. Sm-Nd and Ar-Ar isotopic studies are also described in this chapter. Finally, the last chapter (chapter 7) is allocated to the genetical model and conclusions.

Chapter 2: Geographical situation, tectonic setting and regional geology

2-1 Geographical situation

The town of Bafq is situated in Central Iran, in Yazd province, at a distance of 115 km E of Yazd and is accessible by asphalt road and railway.

The studied area (Bafq mining district) is between 31°, 30´ to 32°, 45´ north latitude and 55°, 20´ to 55°, 50´ east longitude. The region of Bafq (Bafq town altitude 1010 m) is very dry and desert-like (Fig 2-1). The average annual precipitation rate is about 40-50 mm. The evaporation rate is much higher and prevents the existence of permanent rivers. The morphology is dominated by desert land forms.

Fig. 2-1 A general view of the Bafq desert environment

The dry desert climate, like in most other parts of Central Iran, which is caused by the climatic barriers of the two mountain ranges of Alborz in the north and Zagros in the south-southwest, is intensified by the local geography. The temperature may exceed 50°C during July and August, particularly after several years of weak precipitation. Occasional sandstorms paralyze normal life. In winter, the weather, although cold and dry, is agreeable for field work. However, spring and autumn are the best seasons for this. Because of the water shortage, this region is also weakly populated. The largest town is Bafq, which has some 30,000 inhabitants.

In addition there are a few small villages, such as Saghand, Robate-Poshte-Badam, Zarigan, … each with a few hundred people. The natural vegetation has been reduced to low bushes and cultivation is limited to small fields of corn, wheat and palm trees.

2-2 Tectonic setting

The Bafq district, extending from Bafq to Saghand, is part of the Central Iranian micro-plate which is now embedded within the Alpine-Himalayan orogenic system (Fig. 2-2).
The Central Iranian Terrane is an assemblage of several Precambrian fragments of Gondwanaland which cover an approximately 230,000 km^2 region of moderate relief surrounded by Mesozoic-Cenozoic fold-and-thrust belts of the Alpine-Himalayan system.
The Alborz and Kopeh-Dagh ranges to the north, Zagros and Makran ranges to the west and south, and the East Iran Ranges to the east border this terrane. This terrane is an area of continuous continental deformation in response to the ongoing convergence between the Arabia and Turan (Eurasian) plates (Fig. 2-2).

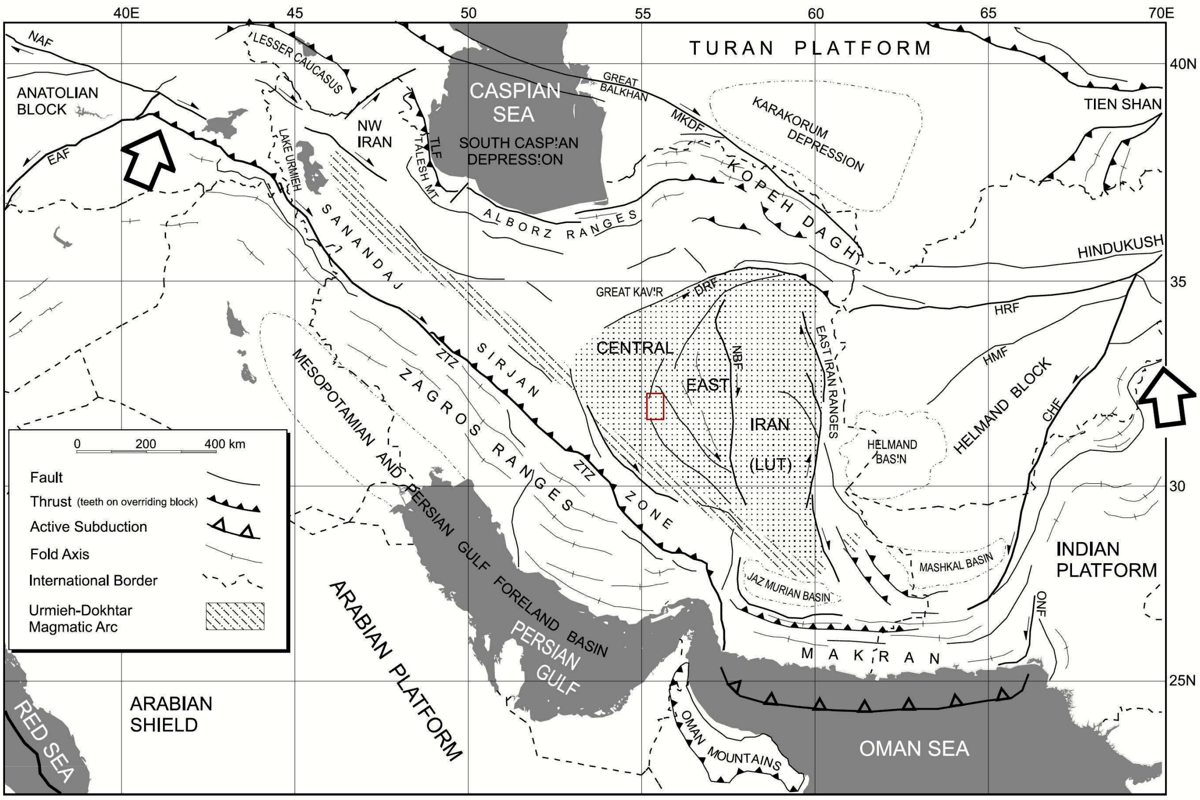

Fig. 2-2 Simplified structural map of Iran and adjacent regions (Ramezani & Tucker, 2003: Fig. 1). The Bafq mining district is located with reddish rectangular shape.

The Central Iranian Terrane consists, from east to west, of three major crustal domains: the Lut Block, Tabas Block and the Yazd Block. These blocks are separated by a series of intersecting regional-scale faults (Fig. 2-3). The Tabas and Yazd blocks are separated by a more than 1000-km-long, and up to 80-km-wide, arcuate and structurally complex belt composed of variably deformed supracrustal rocks, i.e. the Kashmar-Kerman Tectonic Zone (Ramezani & Tucker, 2003) which hosts the Bafq mining district. The Kashmar-Kerman Tectonic Zone provides remarkable exposures of the deeper sections of the Central Iranian platform strata, among which the Late Neoproterozoic and Early Paleozoic rocks are abundant.

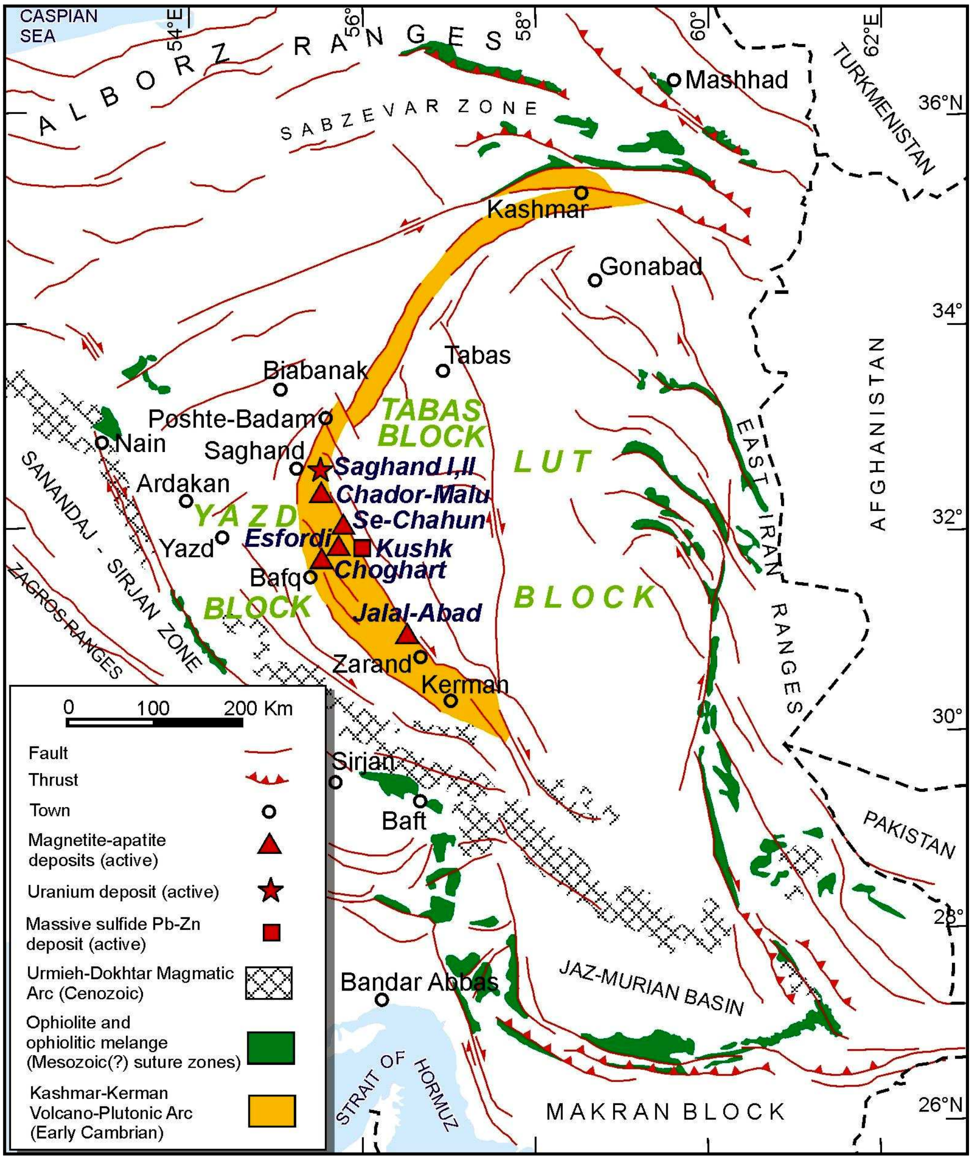

Fig. 2-3 Structural map of eastern Central Iran and surrounding Mesozoic-Cenozoic foldbelts (Modified from Ramezani & Tucker, 2003). The Bafq mining district covers the area between Bafq and Saghand as a part of the Kashmar-Kerman Tectonic Zone which encompasses the most important magnetite-apatite deposits.

A previously proposed model for the Early Cambrian (formerly Infracambrian) tectonics and magmatism in the Bafq district has been crustal extension associated with intracontinental rifting. It has been proposed that this rifting event is associated with alkaline magmatism, including alkaline volcanic rocks, alkaline granites and carbonatites (see for example, Samani, 1988; Daliran, 1990, 2002). However, there is no firm evidence for carbonatite magmatism and it seems that in some places the mildly alkaline character of the volcanic and plutonic rocks is not of igneous nature but is due to widespread hydrothermal Na-K alteration. Berberian & Berberian (1981) attribute the magmatism to the Late Precambrian. They pointed out that the elongated belt of the Late Precambrian calc-alkaline intrusives in east Central Iran seems to be generated in an island arc environment above an ocean-ocean subduction zone. Recent work by Ramezani and Tucker (2003) showed that the Kashmar-Kerman Tectonic Zone represents an active continental-margin environment and does not show primary alkaline affinities attributable to intra-plate magmatism. The chemical composition of the volcano-plutonic rock association and zircon U-Pb age data provide evidence for subduction under the Central Iranian microplate and closure of a Proto-Tethys ocean in the Early Cambrian (Fig 2-4).

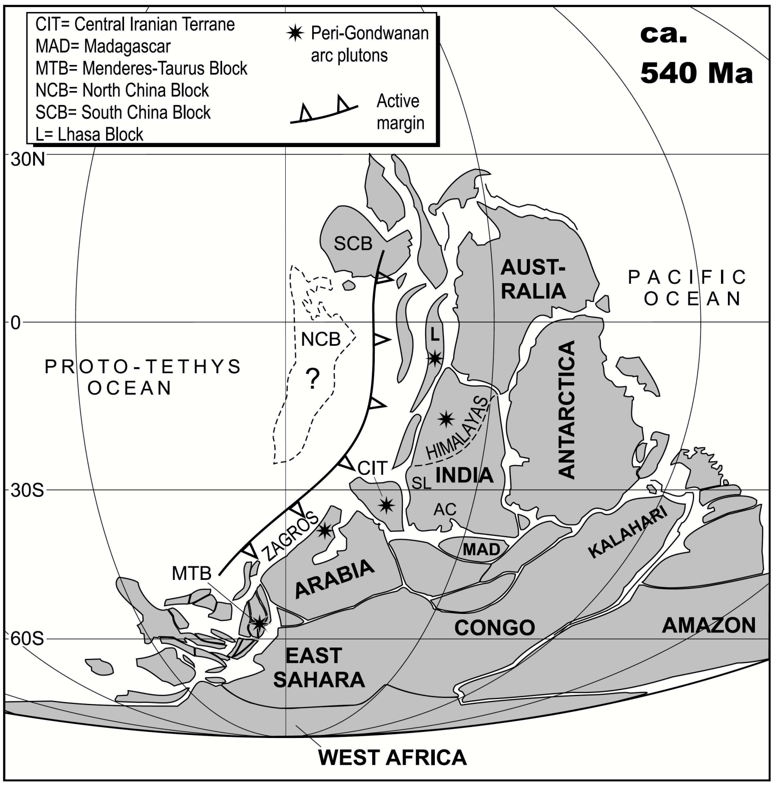

Fig. 2-4 Gondwanaland reconstruction in the Early Cambrian based on projection of tectonic plates at 540 Ma (after Ramezani & Tucker, 2003). Note the position of the Central Iranian Terrane (CIT) at the margin of the Proto-Tethys ocean.

2-3 Regional geology

The structural evolution, paleogeography and metallogeny of the Precambrian-Cambrian in Iran have long been disputed subjects among geologists. The consolidation of the Central Iranian basement is attributed to a Late Precambrian orogenesis, termed Assyntic or Baikalian by several authors (e.g. Huckriede et al., 1962; Stöcklin, 1968). However, because of the geodynamic and structural linkage between Central Iran and the African-Arabian plate, Davoudzadeh et al. (1986) proposed the term Katangan/Pan-African for this orogeny.

2-3-1 Precambrian basement

The Precambrian basement rocks of Iran seem to be a continuation of the Arabian shield and they appear to have both formed a united Arabian-Iranian platform, as a part of Gondwanaland. Precambrian complexes in the form of granite-gneisses and migmatite have been reported from the Bafq to Robate-Poshte-Badam region in Central Iran (Haghipour, 1977). Their composition varies from granite-gneiss to biotite gneiss with disthene and garnet. These include the Chapedony and Boneh-shurow Complexes. The mentioned basement complexes are overlain by metamorphic rocks, up to amphibolite facies, which include biotite schists, amphibolites, quartzitic schists and marbles, often containing garnet and andalusite. These complexes were mapped as the Sarkuh Complex and Tashk Formation in Central Iran (Haghipour, 1974). The upper part of the Precambrian consists of greenschist or slightly higher grade metamorphic rocks. This unit is composed mainly of various shales and schists with intercalations of effusive rocks of acid to intermediate composition, marbleized dolomites and limestones. This unit of great thickness and uniform lithology is widespread in Iran (Samani, 1988). The degree of metamorphism decreases upwards and unmetamorphosed facieses make up most of the unit. This formation has been identified by several litho-stratigraphic names in different places in Iran such as the Kahar Formation and the Morad Series (Stöcklin, 1968) (Fig. 2-5).

2-3-2 Early Cambrian ("Infracambrian")

In the stratigraphic division of Iran, the "Infracambrian" is applied to the time interval between the Late Precambrian and the Cambrian (Stöcklin, 1968). Succeeding the Precambrian complexes unconformably are non-metamorphosed (or slightly metamorphosed) rocks, consisting in some places of dolomites, dolomitic limestones and evaporites associated with rhyolitic tuffs and lavas, and in others of andesites and basaltic andesites associated with shales, sandstones, and detrital material (Haghipour et al., 1977). The angular disconformity with the underlying metamorphosed Precambrian basement, a lack of regional thermo-dynamo metamorphism in the Infracambrian formations, and the different lithology, define the stratigraphical position of the Infracambrian, relative to the Precambrian in Central Iran (Daliran, 1990). However, in some areas the separation of the Precambrian and Infracambrian is difficult and their contacts are generally obscured by deformation, granite intrusion and/or hydrothermal alteration.

According to Samani (1988) the Infracambrian consists of different facies in Iran. In Central Iran it consists of a complex set of volcano-sedimentary rocks which is very extensive from Poshte-Badam to Zarand and hosts the most important iron oxide-apatite, Pb-Zn and U ore deposits in Iran (Fig. 2-3). The volcanogenic rocks vary from acid to basic in composition, and include rhyolite, agglomeratic tuff, splitic lava and diabase, and most are subjected to widespread alkaline metasomatism. The sedimentary rocks consist of dolomites, dolomitic limestones and evaporites. These sequential series have been introduced as Rizu and Desu series by Huckriede et al. (1962) in Central Iran. Borumandi (1973) proposed the term “Esfordi Formation” for these series in the Bafq region. Ramezani and Tucker (2003) assigned an Early Cambrian age (529-554 Ma) for the volcanic suites of this volcano-sedimentary unit and named this sequential unit as CVSU (Cambrian Volcano Sedimentary Unit). The dolomitic rocks in Central Iran are stratigraphically equivalent to dolomites of the Early Cambrian Soltanieh Formation in the Alborz region (Fig. 2-5) which contains prominent sedimentary phosphate horizons in the Zanjan, Alborz and Azarbaijan regions (Samani, 1988). The Infracambrian evaporitic horizons are stratigraphically equivalent to the Hormoz (Hormuz) salt formation (Fig. 2-5) which builds up the conspicuous salt domes and plugs in the Zagros Range and Persian Gulf. The Hormoz Formation mainly consists of evaporite, evaporitic carbonate, sandstone, shale, rhyolite, diabase flows and mudstones. Xenoliths of large blocks of basement gneiss-granite, greenschists and phyllites have been found locally. Apatite, iron-oxide and U mineralization have been discovered in the exposed Infracambrian salt pluges in the south of Iran (Samani, 1988). The distribution of these sedimentary facies (dolomites, evaporites) suggests that during Late Precambrian-Early Cambrian the Central Iran and Zagros regions together with the Salt Range of Pakistan as well as Oman were part of the same landmass and were partly covered by shallow sea (Fig. 2-6). The evaporites are accumulated in domes and ridges under the large anticlinal structures and appear now as salt plugs and disturbed anticlinal cores with residual dolomites and recrystallized volcanic-tuffaceous blocks (Davoudzadeh et al. 1986).

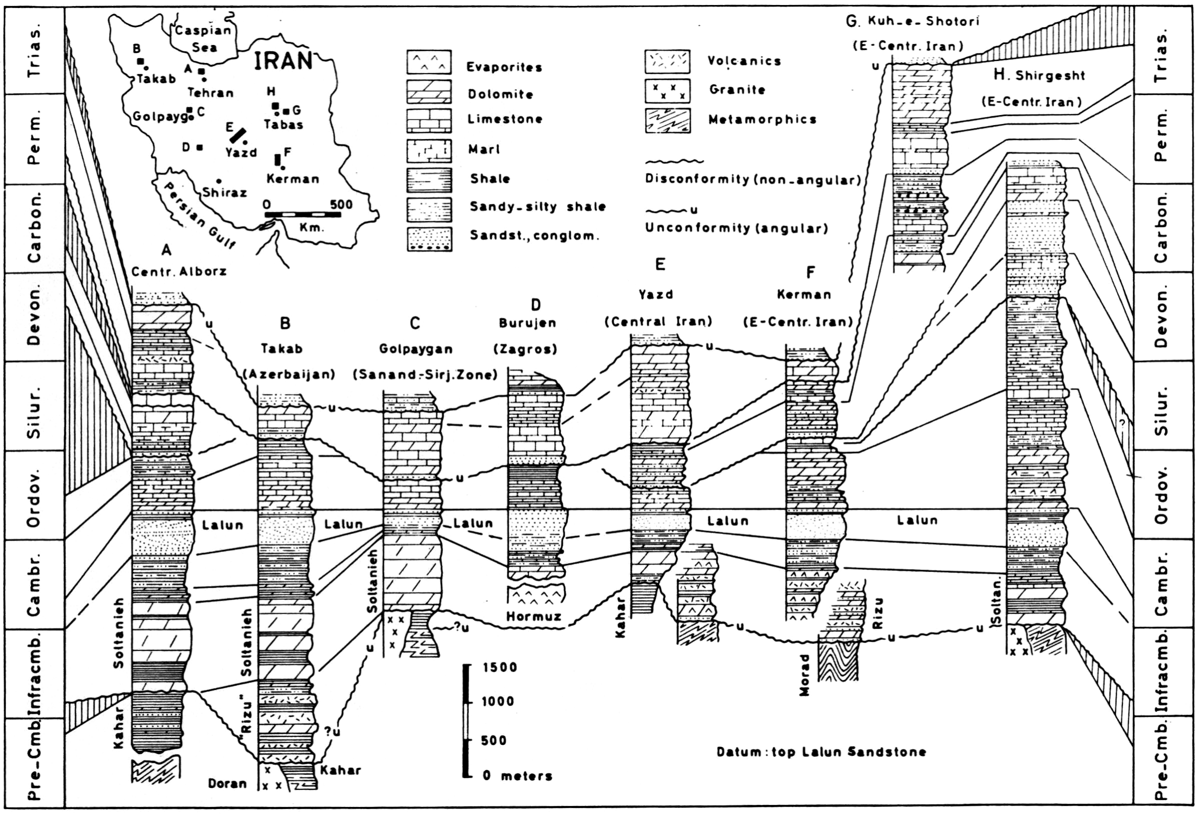

Fig. 2-5 Correlated stratigraphic sections of Late Precambrian-Paleozoic sequences in Iran (after Stöcklin, 1968)

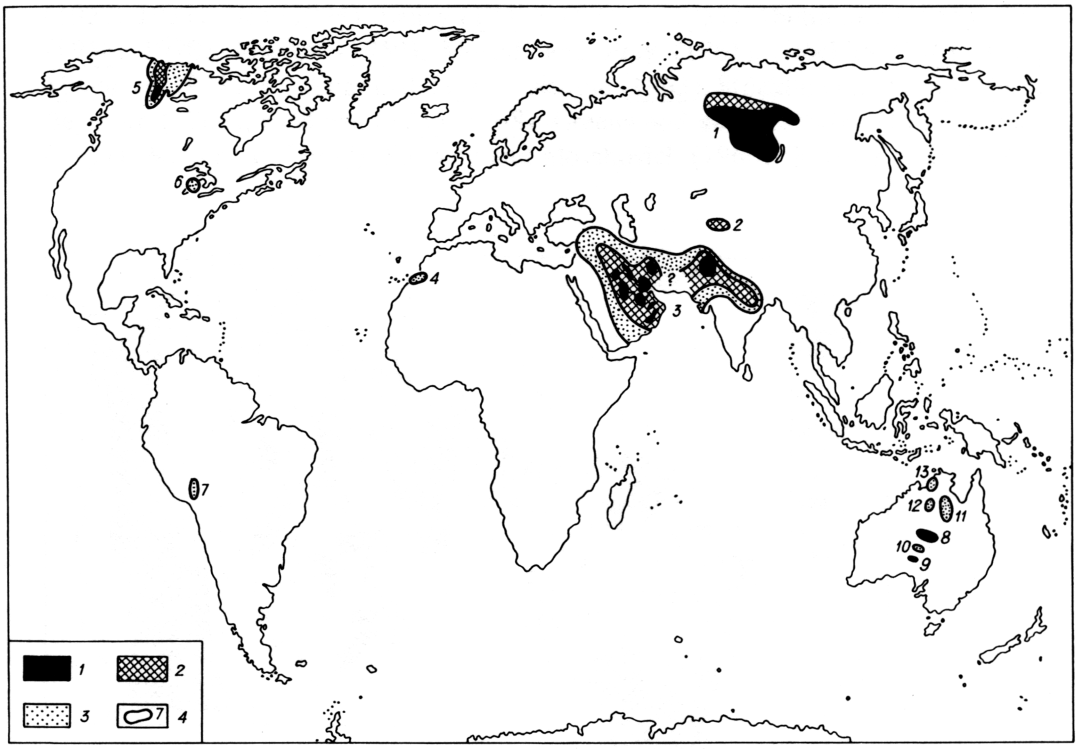

Fig. 2-6 Distribution of Late Neoproterozoic-Early Cambrian evaporites in the world (after Zharkov, 1984) Legend description: 1-Known areas of salt deposits 2-Inferred areas of salt deposits 3-Areas and basins of sulfate sedimentation 4-Boundaries and evaporite basins number shown in the figure:
(1-East Siberian, 2-Tarim, 3-Iran-Pakistan, 4-Anti-Atlas, 5-Mackenzie, 6-Michigan, 7-Cis-Andean, 8-Amadeus, 9-Arckaringa, 10-Officer, 11-Georgina, 12-Wiso, 13-Daly River).

2-3-3 Magmatism

Igneous rocks, mainly granites, are quite common in Central Iran. They comprise intrusives and volcanics of Late Precambrian, Infracambrian (recently Cambrian), Mesozoic and Tertiary age (Haghipour et al., 1977). Volcanics are acid to basic (mostly rhyolite or quartz porphyry as well as dacite, andesite and basalt) and are of different facies, such as lavas, tuffs, ignimbrites and volcanic detrital rocks. They have mostly been albitized and transformed to keratophyre and spilite (Haghipour et al., 1977). These volcanic rocks can be attributed to submarine volcanism as they show a sequential facies with dolomitic rocks. Plutonic bodies range in composition from granite to gabbro and are usually intruded into the Upper Precambrian metamorphic rocks as well as into the Early Cambrian ("Infracambrian") volcano-sedimentary unit (CVSU). The characteristics of some of the more important plutonic rocks in the Bafq mining district are described here.

Zarigan granite: The Zarigan intrusion is the largest intrusive body exposed in the study area, and is in the mountains west of Zarigan village (in the middle of Fig. 2-7). The Zarigan intrusion is emplaced into the Precambrian and the CVSU. This intrusion is a shallow-level, leucocratic body that ranges in texture from a typical medium-crystalline granite to a sub-volcanic granite porphyry (Ramezani & Tucker, 2003). The rock is characterized by a conspicuously low content of mafic minerals. The granite consists mostly of alkali feldspar (40-50%), quartz (25%) and plagioclase (An_{15}, 15-25%). Accessories and secondary minerals are green biotite (altered to chlorite), rutile, apatite, calcite, muscovite and sericite. The intrusion is cut by swarms of mafic dykes (dolerites) of general east-west strike (Haghipour et al., 1977; Haghipour, 1974). Berberian & Berberian (1981) described the Zarigan intrusion as Late Precambrian-Cambrian alkali granite. However, Ramezani and Tucker (2003) defined an age of 525±7 Ma (U-Pb on zircon) for this granite and described it as trondhjemite.

Narigan granite: The Narigan granite is a pale-pink, medium-grained biotite granite intruded into the CVSU sequence, near the Narigan deposit about 20 km east of the Choghart mine (Fig. 2-7). The granite has a granite-porphyry to quartz-porphyry marginal facies and has produced thermal contact effects on the sedimentary rocks of the CVSU. It consists of quartz (39%), orthoclase (29%), plagioclase (31%), biotite and chlorite (~ 1%) (Berberian & Berberian, 1981).

Chador-Malu granite: This is an aplitic granite conspicuously lacking in mafic minerals except for accessory opaque minerals. The granite forms an intrusive body in metamorphic rocks of the Chador-Malu area (at the west of Chador-Malu mine in Fig. 2-7). It consists of orthoclase (51%), quartz (32%), plagioclase (14.3%) and sphene (0.6%) (Berberian & Berberian, 1981). The age of this granitic intrusion has been determined as 529±16 Ma (Ramezani & Tucker, 2003).

Although Berberian and Berberian (1981) described these three granitic intrusions originally as alkali-granite (due to relatively high sodium content), it seems that these rocks are affected by widespread sodic alteration (albitization), especially near the surface and adjacent to the ore deposits. Therefore they can be considered as equivalents of other calc-alkaline intrusions in the Kashmar-Kerman Tectonic Zone (see chapter 4 and 5 for more explanation). In Table 2-1 the whole-rock analyses of some of these granitic intrusions are compiled. The bulk rock geochemistry of the igneous rocks of the Bafq district and their probable tectonic regime are described in detail in chapter 5.

Diorite (locally gabbro-diorite): The dioritic rocks are widely distributed and form bodies varying in size. They have grano-lepidomorphic, hypidiomorphic or xenomorphic texture and contain plagioclase (40-60%, An_{35-50}), amphibole (10-35%), biotite (5-15%) and some have a very small quantity of alkali feldspar. Accessory and secondary minerals are scapolite, epidote, chlorite, sphene, opaque minerals, zircon, apatite, calcite, and albite (Haghipour et al., 1977). Gabbro is rare and usually found in the Precambrian rocks or around and within diorite bodies (gabbro-diorite). It consists essentially of plagioclase (An_{50-60}), augite, locally olivine, hypersthene, amphibole, and biotite. Most of these rocks have been affected by post-Precambrian metamorphism. The pyroxenes are in part transformed to amphiboles and on to biotite. In the latter transformation, some quartz, and more especially magnetite is formed. These rocks have also been widely affected by sodic metasomatism. During that process the plagioclase was partly transformed to scapolite and albite, and the pyroxenes and amphiboles to sodic amphiboles and magnetite. Epidote, clinozoisite, and chlorite are secondary minerals, formed perhaps during Mesozoic and younger alterations (Haghipour et al., 1977). Although the exact ages of these basic intrusive bodies have not been identified so far, Haghipour et al. (1977) assigned a Late Precambrian age to them due to their stratigraphic occurrences. For a representative example the whole-rock analysis of Chador-Malu diorite is shown in Table 2-1.

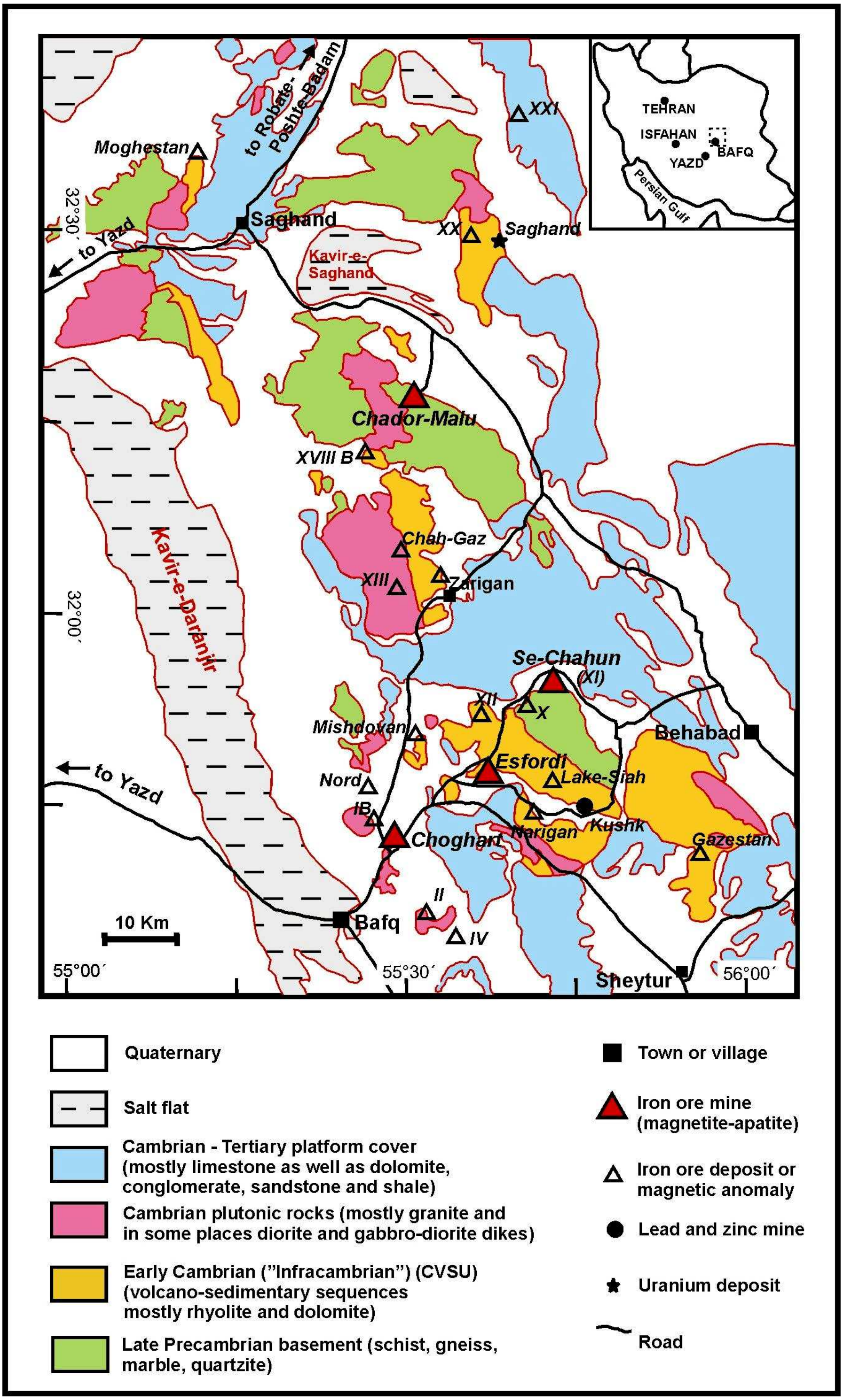

Fig. 2-7 Simplified geological map of the Bafq mining district and location of ore deposits and igneous rocks (Modified from Haghipour, 1977; Förster and Jafarzadeh, 1994).

Table 2-1 Whole-rock analyses of some representative samples of igneous rocks of the Bafq district (in wt.%)

	Chador-Malu Granite[1]	Zarigan Granite[1]	Chador-Malu Diorite	Choghart Rhyolite	Esfordi Rhyolite
SiO_2	74.67	74.58	49.66	70.81	72.22
TiO_2	0.39	0.31	2.77	0.20	0.35
Al_2O_3	14.99	14.77	13.13	11.91	15.02
Fe_2O_3	0.72	0.78	14.63	1.74	1.08
MnO	0.01	0.01	0.20	0.03	0.01
MgO	0.10	0.12	3.70	1.10	1.31
CaO	0.37	0.84	4.55	1.92	0.23
Na_2O	8.47	7.16	6.70	5.75	0.22
K_2O	0.23	1.09	0.21	1.04	4.91
P_2O_5	0.03	0.04	0.97	0.16	0.07
LOI	0.41	0.57	2.86	4.95	4.21
Total	100.39	100.27	99.38	99.62	99.62

[1] Data from Ramezani and Tucker (2003)

2-3-4 Younger sedimentary cover

Although some iron ore deposits, as well as the Early Cambrian volcano-sedimentary host rocks locally have prominent outcrops, the greatest area of the Bafq district is covered by younger sedimentary rocks, especially of Quaternary terraces, gravel fans, recent alluvium, sand dunes and salt and mud flats. In some places, especially between Choghart and Narigan and at the west of Zarigan granite, Cretaceous limestones have outstanding outcrops. The Neogene rocks consist of conglomerate, sandstone and gypsiferous red beds, and also cover a vast area to the east of Zarigan. Other sedimentary rocks which occur very locally, especially in the north of study area, consist of Cambrian Lalun and Mila Formations (sandstone and shale), Permian and Triassic limestone and dolomites, and Jurassic sandstone and shales.

Chapter 3: Bafq magnetite-apatite deposits and their economic aspects

Old mine workings in the Bafq area indicate mining activity since many years ago. Systematic exploration work during the 1960s and 1970s outlined 34 zones of aeromagnetic anomalies in between Bafq in the south to Saghand in the north with a total reserve of more than 1500 Mt iron ore. Among these deposits, Choghart, Chador-Malu, Se-Chahun and Esfordi are currently mined (Fig. 2-7). The ore reserves of the individual deposits vary from low tonnage (10-20 Mt) to large bodies of several hundred million tonnes (up to 400 Mt). Most of these deposits are high-grade (Fe >55%). Some deposits, such as Esfordi and Gazestan, have high-grade apatite mineralization and represent important phosphorus resources. In the following, we describe the currently active iron ore/apatite mines in this district.

3-1 Choghart iron ore deposit

The Choghart iron ore deposit is located 12 km northeast of Bafq and 125 km southeast of Yazd (Fig. 2-7). Choghart was initially a prominent black hill of iron ore measuring 800 x 300 m, standing 150 m above the surrounding plain at about 1150 m above sea level (Fig. 3-1). The current mining depth is at 1050 m above sea level. Systematic exploration activities started in 1961 and the first iron ore was mined and shipped to the Isfahan steel mill in 1971.

The main orebody at Choghart is in the form of a roughly vertical, discordant, pipe-shaped body plunging 73°N-NW. The orebody is explored to a depth of 600 m, where it appears to interfinger with metasomatized and brecciated wall-rock which consists of volcanic and dolomite units of the Early Cambrian Esfordi Formation (CVSU). Figures 3-2 and 3-3 show the schematic geological map and cross section of the deposit, respectively. The Esfordi Formation was recently dated at 528.2 ± 0.8 Ma in the Saghand area (U-Pb on zircon, Ramezani and Tucker, 2003) and unconformably overlies the high-grade metamorphic Precambrian basement of the Boneh-Shurow Complex. The main host to the orebody is a highly metasomatized magmatic rock with altered dolomite fragments of the Esfordi Formation of varying size and shape. The igneous rock is locally described as "syenite" which is strongly albitized (Moore & Modabberi, 2003). All rocks in the mine area display extensive mineralogical, textural and compositional diversity, with varying degree of hydrothermal alteration. The orebody and country rocks are cut by several mafic dikes (Moore & Modabberi, 2003).

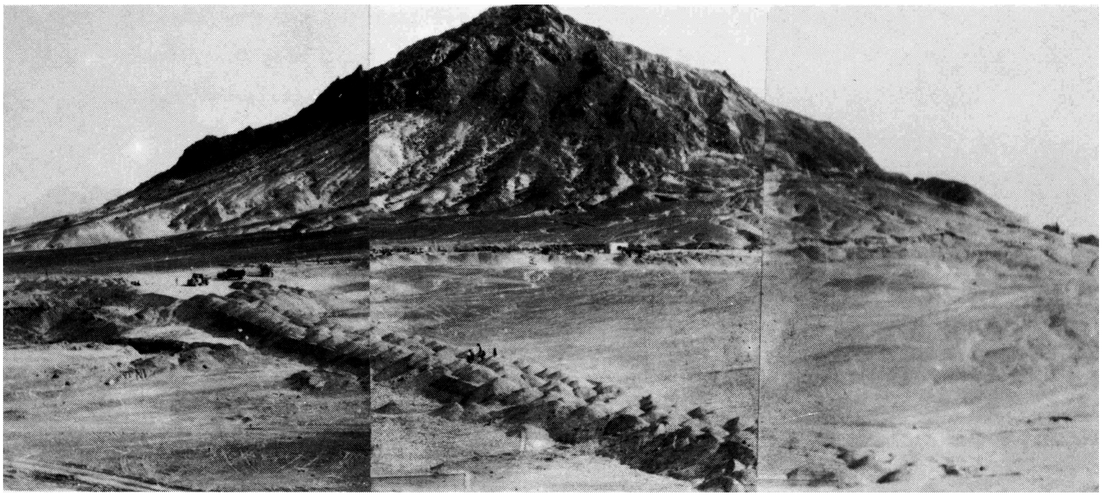

Fig. 3-1 Choghart iron ore deposit (Black hill of rich iron ore) and surrounding plain before mining started (view to northeast) (photo from Cyrus Behain in 1968).

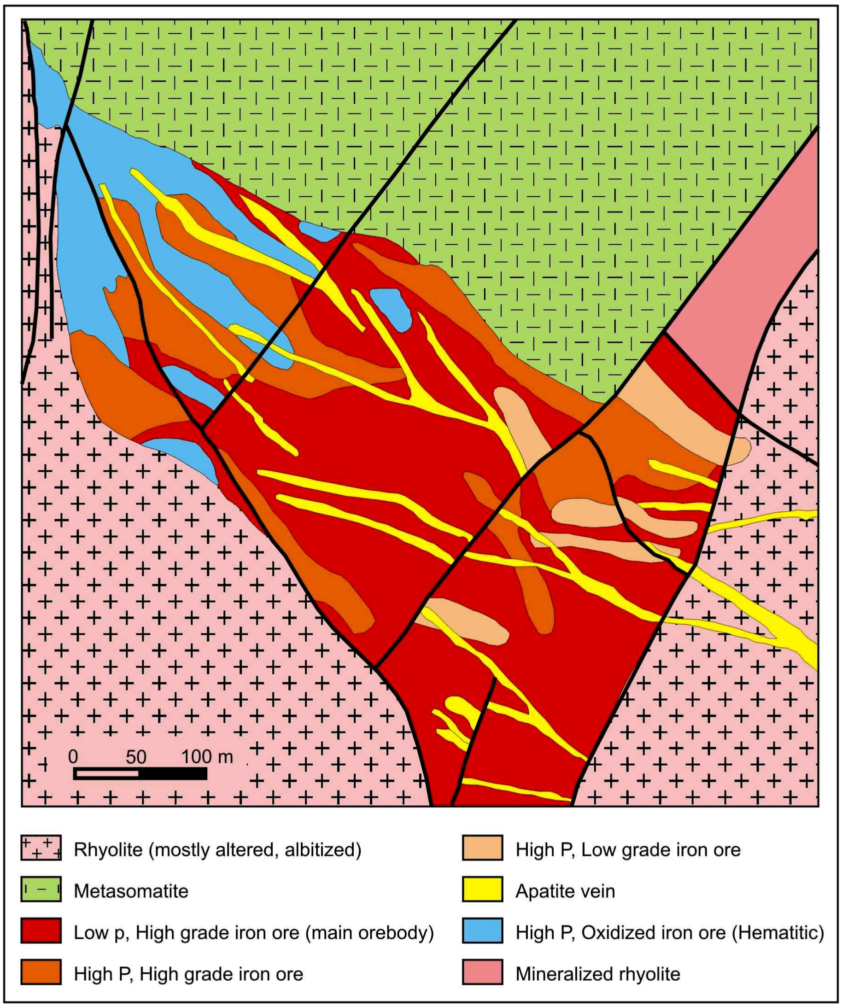

Fig. 3-2 Simplified geological map of the Choghart deposit (Modified from Moore & Modabberi, 2003).

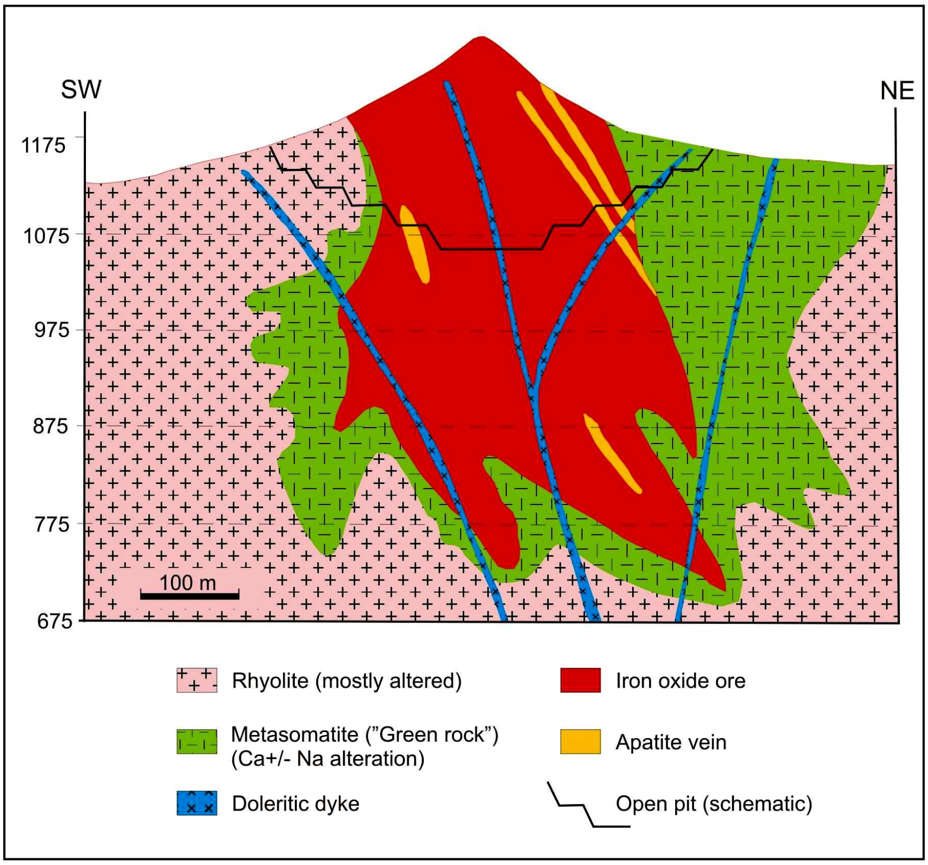

Fig. 3-3 Simplified geological cross section of the Choghart deposit (Modified from Förster & Jafarzadeh, 1994).

The lower part of the Choghart orebody consists largely of massive magnetite. Accessory minerals include apatite, pyrite, amphiboles (mainly actinolite and tremolite), calcite, talc, quartz, monazite, davidite and allanite. The oxidation zone reaches down to 150 m depth and varies from incipient martitization to complete replacement of magnetite by martite near the surface. Hematite is the second ubiquitous mineral after magnetite. Although some primary hematite is found in the drill cores, most of the hematite is secondary in origin. Some goethite and hydrous iron oxides occur near the surface, but disappear rapidly with depth. Apatite is the most abundant gangue mineral at Choghart. Fine- and coarse-grained apatite occurs in varying proportions with magnetite. At least two generations of apatite are discernible. The first, which is contemporaneous with the main phase of magnetite formation, displays euhedral crystals ranging in size from a few millimeters to a few centimeters in diameter, intimately intergrown with magnetite. The second generation occurs as subhedral to anhedral crystals in lenses, veins, and veinlets of varying size and thickness, which cut the magnetite-apatite ore (Moore & Modabberi, 2003).

According to composition and degree of oxidation, the iron ore of Choghart has been classified into different groups (Table 3-1). The estimated pre-mining reserve for Choghart was 215.7 Mt on the basis of a 20%-cut-off-grade for total iron (Table 3-1). The iron ore is of low-sulfur type, and about 90% of the Choghart orebody is non-oxidized (magnetite ore). More than 65% of the reserve is of low-phosphorus type (<0.18 wt% P) (Torab & Lehmann, 2006). The Choghart iron ore mine is an open pit operation, which includes the five stages of drilling, blasting, loading, hauling and crushing. Loading and transporting is done by a truck-shovel system (Fig. 3-4)

Table 3-1 Choghart pre-mining estimated reserve and ore classification

Iron ore type	**Oxidation situation**	**Fe (total) %**	**Fe_2O_3 %**	**FeO %**	**P_2O_5 %**	**SiO_2 %**	**SO_3 %**	**Fe/FeO**	**Reserve (Mt)**
Rich iron ore (Low phosphorus)	Oxidized	63.81	81.15	9.07	0.16	3.07	0.10	7.03	**4.7**
	Unoxidized	62.43	69.88	17.44	0.11	4.92	0.15	3.58	**137.3**
Rich iron ore (High phosphorus)	Oxidized	54.16	70.83	5.94	3.39	4.97	0.25	9.12	**17.1**
	Unoxidized	57.49	63.37	16.94	2.24	6.60	0.20	3.39	**45.6**
Poor iron ore		38.95	40.67	13.52	1.97	15.86	0.52	2.88	**11.0**
Overall (whole orebody)		59.56	67.33	16.04	0.92	5.79	0.19	3.71	**215.7**

The ROM ore (Run-of-Mine ore) is sent to the plant and crushed in three stages by a jaw crusher, a coarse cone crusher, and two fine cone crushers. Next, it is screened into two fractions: agglomerate (1-10 mm) and blast furnace feed (10-25 mm), and stored in two separate stockpiles ready for railway transportation. The main consumer of this ore is the Isfahan steel mill, minor amounts are exported to Pakistan. The poor (low-grade) and high-phosphorus ores are stored in different stockpiles for future beneficiation. At present an agglomeration plant is under construction, and ballast production from mine wastes has started. The Choghart Expansion Project will allow production of concentrate from high-phosphorus, low-grade Choghart ore as well as concentrate production from low-grade ore in the 35 km away Se-Chahun deposit. On the basis of the Choghart Expansion Project report, the remaining reserve of the deposit is about 167 Mt (at a cut-off-grade of 20% Fe) of which 140 Mt is mineable. Table 3-2 gives the parameters of the final-stage pit design.

Fig. 3-4 Choghart open-pit (view to the south)

Table 3-2 Choghart open-pit parameters at final stage

Shape and Size of pit	Ellipse (840 m x 640 m)
Overall stripping ratio (W/O)	0.66/1
Ground level (above sea level)	1140 m
Open-pit final depth	327.5 m
Overall slope angle	55°
Bench height	10 m (from 1140 to 1100 level)
	12.5 m (from 1100 to 812.5 level)
Shovel capacity	Present: 5 m^3
	Expansion project: 7.6 m^3
Truck capacity	Present: 32 t
	Expansion project: 85 t

The objectives of the Choghart Expansion Project are: (1) secure the supply of 3 Mt/y of DSO (Direct Shipping Ore) from the Choghart open pit as feed for blast furnace; and (2) produce 3.2 Mt/y of iron ore concentrate as feed to the agglomeration plant from the Se-Chahun open pit and low-grade high-phosphorus ore of Choghart. Due to differences between the ores from the Choghart and Se-Chahun mines, two separate processing lines are planned: The Choghart process line with the feed capacity of 2.3 Mt/y will produce 1.6 Mt/y of fine concentrate, and the Se-Chahun process line with the feed capacity of 3.4 Mt/y will produce 1.6 Mt/y of fine concentrate. The ore beneficiation method employed in both production lines is mainly wet magnetic separation.

3-2 Se-Chahun iron ore deposit

The Se-Chahun deposit consists of two separate ore zones (anomaly X and XI) of which anomaly XI is the most important one (Fig. 2-7). Anomaly X crops out as some small black hills containing only 11 Mt iron ore reserve (mainly rich magnetite ore). The main orebody of Se-Chahun (anomaly XI) is blind, covered by conglomerate, young terraces, and gravel fans (Fig. 3-5). This deposit has been explored by geophysical methods and extensive drilling. The deposit is divided into two parts (north and south orebodies) with a total reserve of about 140 Mt low-grade iron ore with an average grade of 36% Fe. Mining is by two open pits. The south pit applies selective mining, and due to thick overburden, the north pit has a relatively high stripping ratio. The mineable reserve of the Se-Chahun deposit (both pits) is about 106 Mt with a stripping ratio (W/O = 2.48/1). A primary crusher has been installed at Se-Chahun and the ore will be transported to Choghart after primary crushing, once the beneficiation plant at Choghart is finished.

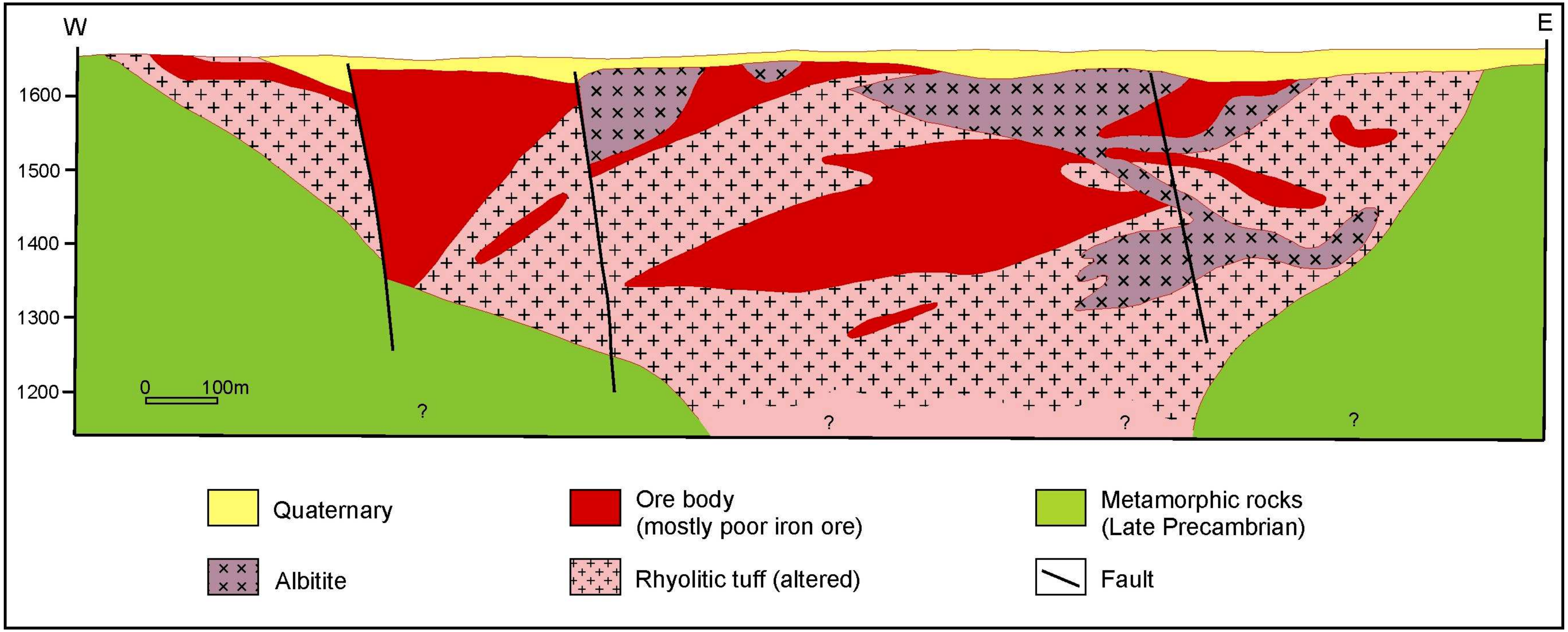

Fig. 3-5 Simplified cross section of the Se-Chahun deposit (anomaly XI) (Modified from Förster & Jafarzadeh, 1994)

3-3 Chador-Malu iron ore deposit

The Chador-Malu iron ore deposit is the largest known iron ore deposit in Iran with a pre-mining reserve of 400 Mt @ 55% Fe, 2.15% P_2O_5; cut-off 25% Fe. About 40 Mt of this reserve has been mined so far. The deposit is located about 80 km north of Bafq (Fig. 2-7), and was discovered by the German geologist Kümel in 1941 in a group of black hills standing out 250 m above the Quaternary flat. The deposit consists of two parts (northern and southern orebodies) and some separate magnetic anomalies. Detailed exploration from 1975 to 1978 included adits, cross-cuts, followed by dense core drilling (124 boreholes with a total of 35,350 m drill core). Complementary studies and operations for exploitation and plant construction were carried out from 1981 to 1996, and the plant was formally inaugurated in the summer of 1997. The open pit is currently at a depth of 100 m below the surface and the mine is equipped to extract nominally 12 Mt/y. However, the actual production is about 7.8 Mt/y.

The northern orebody has the shape of an upright cylinder with several horizontal extensions, interpreted as a magnetite-filled vent, more than 600 m deep. The southern orebody is a flat-lying lens, interpreted as magnetite lava flow or sill emitted from the vent in the ring graben toward south-southwest (Förster & Jafarzadeh, 1994). Country rocks of the orebodies are Precambrian metamorphic rocks, and Early Cambrian subvolcanic intrusive “syenite”, gabbro-diorite, volcanic rocks (predominantly rhyolite) with intercalations of siliceous dolomite, and pyroclastic breccia. Fig. 3-6 shows the geological map of the deposit. Due to contact metamorphism by the resurgent Sorkh granite (Chador-Malu granite), portions of the country rocks have been converted to hornfels. The deposit is dissected by many dikes (quartz porphyry, dolerite, lamprophyre). Portions of the rhyolites are affected by intensive hydrothermal alteration (formation of alunite, pyrophyllite, sericite, and kaolinite). Rhyolite is strongly albitized for several meters at the contact to massive magnetite ore. The porphyritic texture is preserved, but the feldspars are transformed to albite. Fluorapatite is the main gangue. The P_2O_5 content of the ore mainly ranges between 1.4 and 5.0 wt%, rarely to more than 10 wt%. Dolomite, quartz, calcite, talc, chlorite, actinolite, albite, and phologopite occur within the coarse-grained magnetite-apatite ore. Cracks in large apatite crystals are filled with talc. The oxidation zone reaches down to 150 m depth, and ranges from incipient martitization to complete replacement of magnetite by martite and secondary formation of hematite. The magnetite contains 0.4 wt% V_2O_5 and 0.65 wt% TiO_2 . Exsolution textures in magnetite are rare (Förester & Jafarzadeh, 1994).

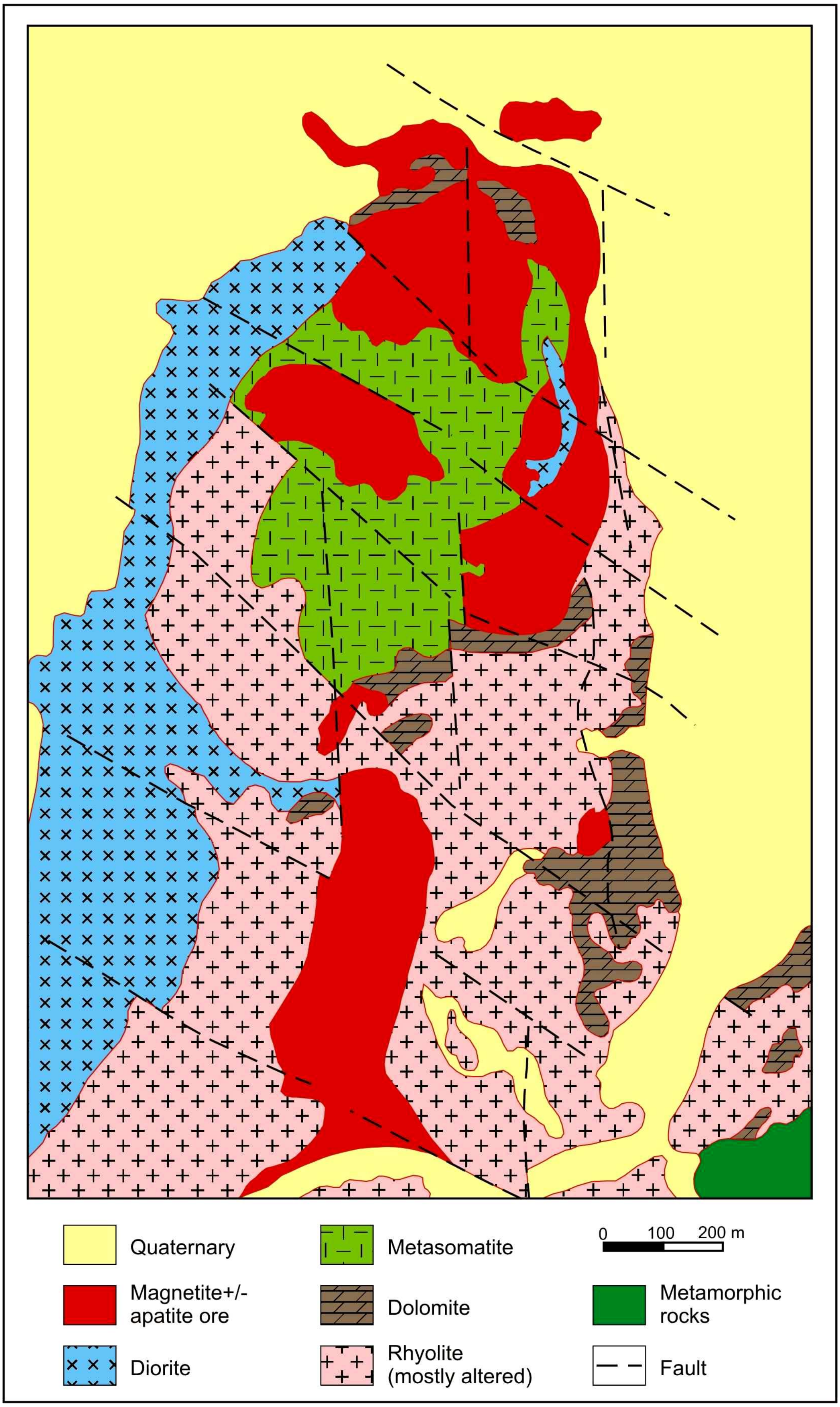

Fig. 3-6 Simplified geological map of the Chador-Malu deposit (Modified from Jafarzadeh, 1981)

According to composition (iron, phosphorus and sulfur content) and degree of oxidation, the iron ore of the Chador-Malu deposit has been classified into 9 different groups (Table 3-3). The boundary between high-P and low-P ore is at 0.2 wt% P, and for high-S and low-S ore at 0.3 wt% S. The table reveals that only a small portion of the orebody is low-phosphorus iron ore (less than 10 % of the whole reserve) and more than 90 % of the ore needs to be beneficiated. Almost 25 % of the ore is oxidized; the remainder is magnetite ore (Torab & Lehmann, 2006).

Table 3-3 Chador-Malu estimated reserve and ore classification

Iron ore type	**Reserve (Mt)**
1-Unoxidized, low P, low S, rich iron ore[1]	27.9
2-Oxidized, low P, low S, rich iron ore	6.3
3-Unoxidized, high P, low S, rich iron ore	179.2
4-Oxidized, high P, low S, rich iron ore	80.1
5-Unoxidized, low P, high S, rich iron ore	3.8
6-Unoxidized, high P, high S, rich iron ore	52.1
7-Oxidized, high P, high S, rich iron ore	2.1
8-Unoxidized, poor iron ore[2]	37.4
9-Oxidized, poor iron ore	10.0
Total	**398.9**

[1] Rich iron ore = Fe > 45%
[2] Poor iron ore = Fe < 45%

Fig. 3-7 shows the Chador-Malu open pit. The ROM (Run-of-Mine) ore is first crushed by a gyratory crusher, and then is sent to two parallel 55,000 tonne stockpiles for blending. Next, the ore is milled via an autogenous mill and subjected to several stages of low and high intensity magnetic separation and then flotation to give two different concentrates, i.e. iron ore and apatite. The high-grade iron ore concentrate contains about 68 wt% Fe and less than 0.06 wt% P, while the apatite concentrate contains about 33 wt% P_2O_5 and a maximum of 3.1 wt% Fe. The Chador-Malu complex has three parallel production lines with a nominal capacity of 7.8 Mt/y as feed and can produce 4.5 Mt/y iron concentrate and 144,000 t/y apatite concentrate. The iron ore concentrate is used for steel production by direct reduction, and the apatite concentrate is used for production of phosphoric acid and fertilizers. Table 3-4 gives some information on the open-pit design and Tables 3-5 and 3-6 show the types and quality of the iron and apatite concentrates, respectively.

Fig. 3-7 Chador-Malu open-pit (view to the southwest)

Table 3-4 Chador-Malu open-pit parameters at final stage

Shape and size of pit	Ellipse (1000 m x 800 m)
Overall stripping ratio (W/O)	0.95/1
Ground level (above sea level)	1525 m
Open-pit final depth	225 m
Overall slope angle	55°
Bench height	15 m
Shovel capacity	11-13 m^3
Truck capacity	136 t

Table 3-5 Types and quality of iron concentrates at the Chador-Malu mine

Products	**Fe $_{total}$ (%)**	**FeO (%)**	**SiO_2 (%)**	**Al_2O_3 (%)**	**P (%)**	**S (%)**
Pellet feed	67.5	10.5	2	0.35	0.06	< 0.03
Lump ore	60.0	12-14	4-5	0.3	0.18	< 0.12
Sinter feed (fine ore)	59.0	11-13	4-5	0.6	0.19	< 0.12

Table 3-6 Quality of apatite concentrate

P_2O_5 (%)	33.0
MgO (%)	2.7
Fe (%)	3.1
F (%)	2.1

3-4 Esfordi apatite-magnetite deposit

The Esfordi apatite-magnetite deposit is located 35 km northeast of Bafq (Fig. 2-7). Esfordi was initially investigated in the early 1970s for its iron ore potential but due to the presence of high-grade apatite mineralization, it has been studied for its phosphate potential by the Geological Survey of Iran since 1981. After detailed exploration (drilling of more than 70 exploration boreholes) during 10 years (1982-1992), plant construction started in 1993 and mining activity began in 1999 with production of a phosphate concentrate for use in the fertilizer industries and for phosphoric acid.

The Esfordi deposit lies within the intensively folded and faulted Early Cambrian Esfordi Formation which consists of a volcano-sedimentary sequence of rhyolite plus minor siliceous dolomite (CVSU), cut by dolerite dikes and gabbro-diorite stocks. Figures 3-8 and 3-9 show geological map and cross section of the Esfordi deposit, respectively. The lenticular apatite-magnetite orebody (450 x 80 m) consists of dominantly magnetite and apatite in variable proportions. Magnetite has largely undergone martitization not only at the surface but also at depth. Although some primary hematite is found in the drill cores, most hematite is secondary in origin. The apatite occurs as coarse euhedral to subhedral, and very fine-grained anhedral crystals. The large apatite crystals are set in a fine-grained matrix which mostly consists of calcite, quartz, talc, tremolite-actinolite and fine-grained apatite and hematite.

Apatite also occurs in stockworks and vein networks crosscutting the magnetite-apatite orebody. Large prismatic crystals are up to 8 cm long. The apatite consists of fluorapatite, and is associated with accessory REE bearing minerals such as monazite, allanite, parasite and xenotime. Total REE concentrations reach up to 2 wt%. Sulfide minerals are relatively rare. Very minor pyrite and fine-grained chalcopyrite occur in some boreholes, associated with secondary apatite or gangue minerals as late stage mineralization. Pervasive alteration is associated with the mineralization. Hydrothermal alteration includes silicification, potassium metasomatism and sericitization of volcanic rocks, and alteration of siliceous dolomite to actinolite (locally known as "Green rock"). Chlorite-calcite alteration of mafic volcanic rocks (basaltic tuff) is laterally widespread.

The total reserve of the deposit is about 17 Mt @ 13.9% P_2O_5 and 17.2% Fe. Esfordi is mined by the open pit method (Fig. 3-10) and, on the basis of the final pit design, the mineable reserve is about 10 Mt. Table 3-7 gives some open-pit parameters at the final stage. The mine is designed to feed 360,000 t/y of iron oxide-apatite ore to the plant. The current annual production is 103,000 apatite concentrate (38% P_2O_5) and 130,000 t iron concentrate (64% Fe). The ROM ore is first crushed by an open-circuit jaw crusher and a closed circuit cone crusher, and then is sent to the grinding section which comprises an open-circuit rod mill and a closed-circuit ball mill. After grinding and size distribution by hydrocyclones, the pulp is conducted to flotation cells for apatite concentration. The iron concentrate is produced by use of high- and low-intensity magnetic separators.

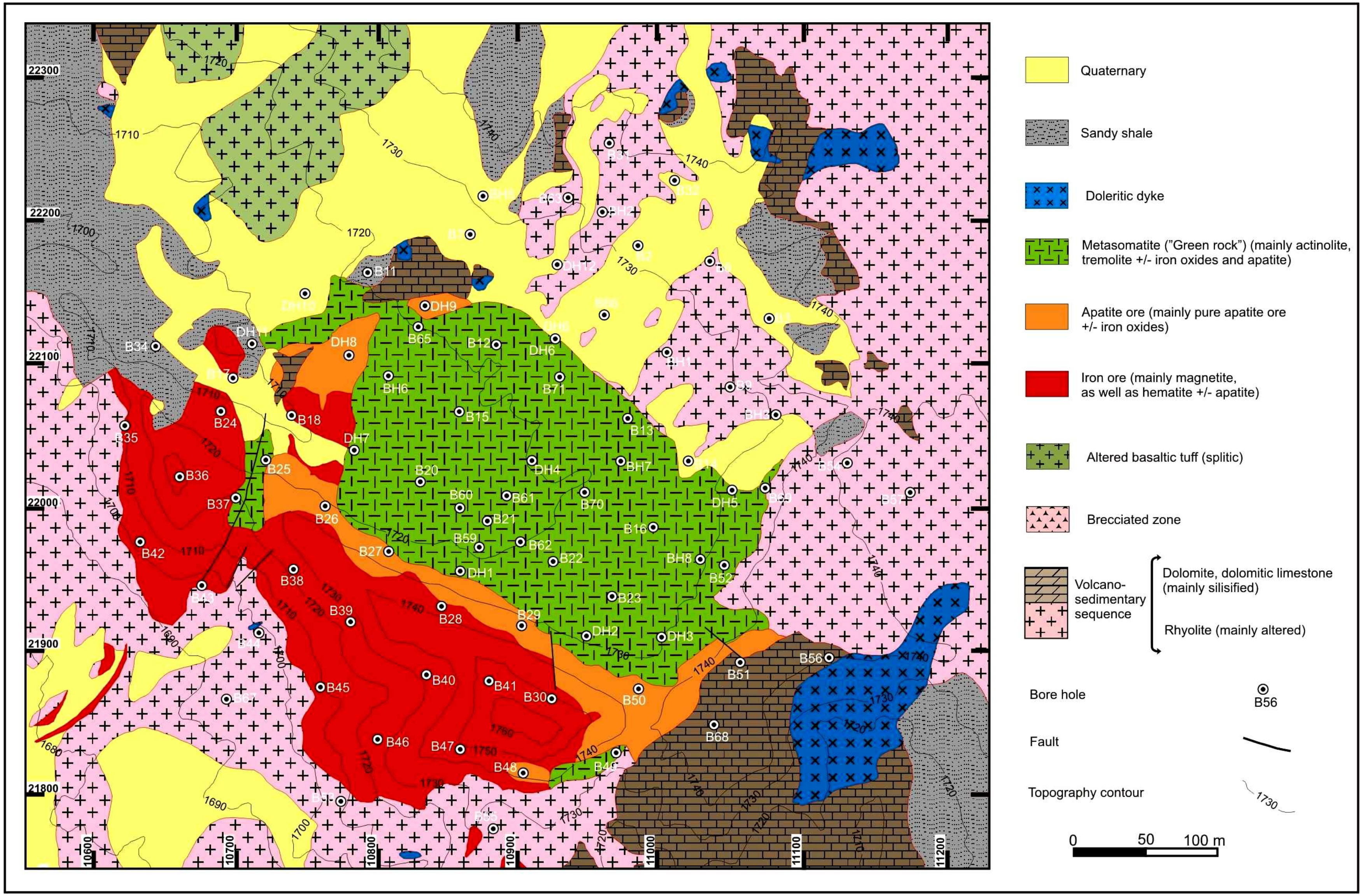

Fig. 3-8 Geological map of the Esfordi apatite-magnetite deposit (Modified from Phosphate Mines Development Co.)

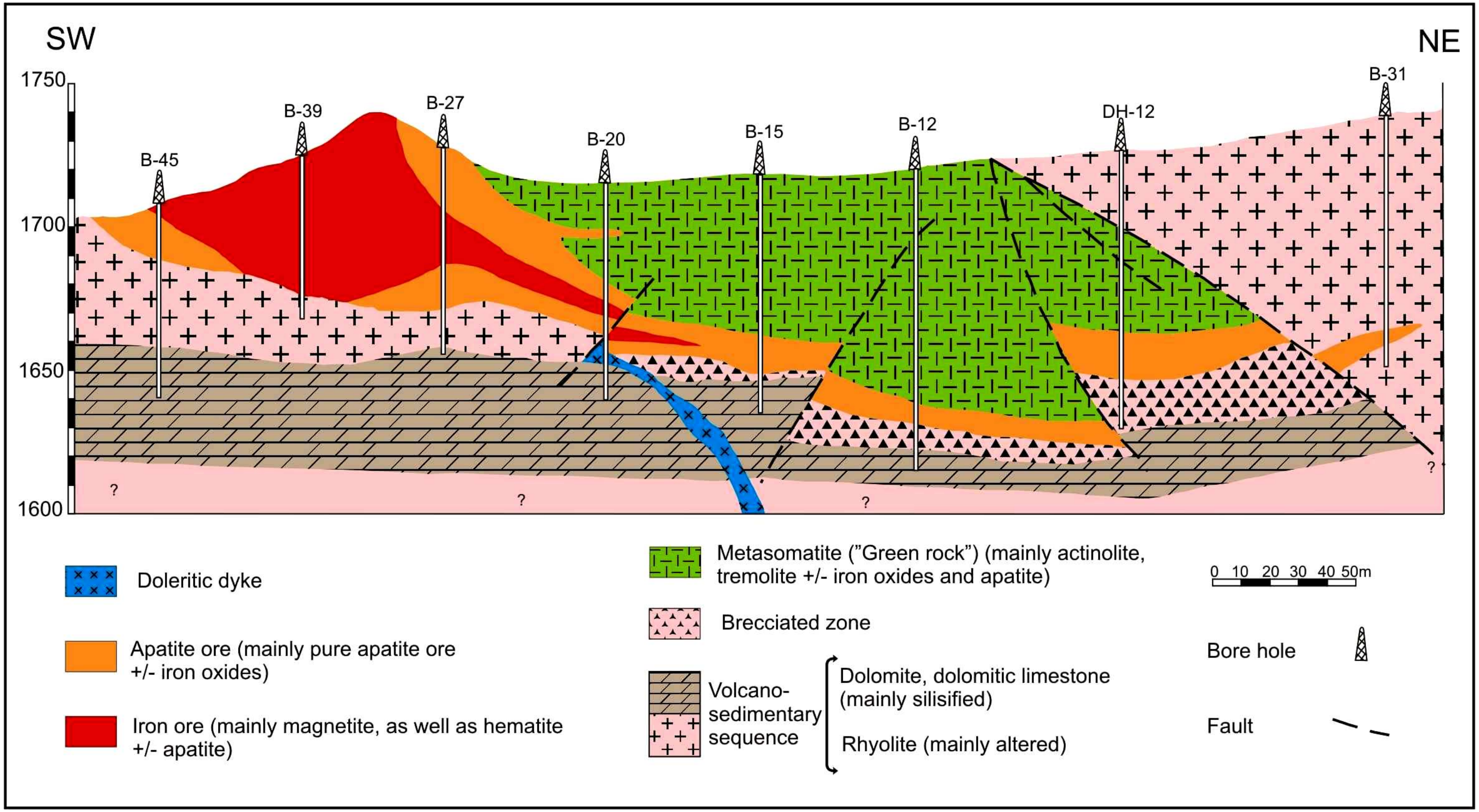

Fig. 3-9 Geological cross section of the Esfordi deposit (Modified from Phosphate Mines Development Co.)

Fig. 3-10 The Esfordi hill with tectonic contact (thrust fault) between Cretaceous (?) dolomitic limestone (right) and Early Cambrian volcano-sedimentary sequence of the Esfordi Formation (left), and the open-pit operation in front (view to the north)

Table 3-7 Esfordi open-pit parameters at final stage

Shape and size of pit	Circle (450 m diameter)
Overall stripping ratio (W/O)	1.1/1
Ground level (above sea level)	1755 m
Open-pit final depth	120 m
Overall slope angle	50°
Bench height	10 m (with 5 m sub-levels)
Loading and transporting system	Truck-loader

Chapter 4: Mineralization style, mineralogy and alteration

4-1 Mineralization style and mineralogy

The Bafq iron ore deposits show a spectrum of mineralization styles such as massive orebodies, metasomatic replacements, veins and stockworks, of which their distribution varies considerably within the individual deposits. The ore is characterized by abundant low-Ti magnetite and hematite and may contain significant P, carbonate and partially REE enrichment. The ore deposits are hosted in volcanic and volcano-sedimentary rocks with extensive alteration. Fig. 4-1 shows the paragenetic relationships and sequence of ore minerals and alteration assemblages on the basis of microscopic and EMP studies which are described in detail in this chapter. However, the exact age relationships between these various alteration-mineralization assemblages are unknown. The dominant hydrothermal minerals are magnetite, apatite, and actinolite in different proportion. Although the main iron mineral is magnetite, all gradations towards hematite (martitization) can be recognized. Some primary hematite is also found in the drill cores. However, most hematite is secondary in origin.

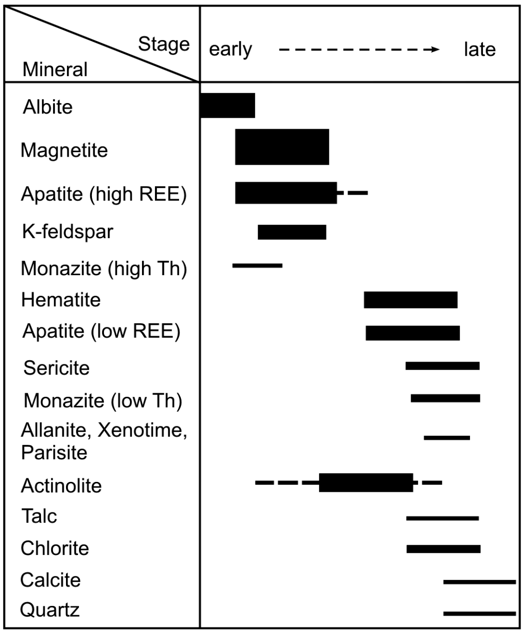

Fig. 4-1 Paragenesis of ore minerals and associated alteration assemblage

Most of the iron ore bodies have dome-shaped discordant to concordant structure and mostly consist of lenses or irregular masses of massive magnetite surrounded by ore breccia and disseminated magnetite in the host rocks. In some places irregular bodies of massive magnetite are enclosed by a stockwork of magnetite ± actinolite ± apatite veins. An important feature of these deposits is that they typically display gradational contacts with their host rocks. Sharp contacts are largely restricted to structurally controlled zones.

Fig. 4-2 Massive iron ore bodies. Left: Massive high grade magnetite ore. Right: Massive low grade iron ore which is mostly martitized.

Fig. 4-3 Apatite vein cutting massive magnetite ore.

Fig. 4-4 Iron ore breccia zone. Left: Iron ore veins which cut the dolomitic host rocks (the host rock is mostly converted to actinolite). Right: A block of metasomatite rock ("Green Rock") which mostly consists of actinolite and apatite with hematite stockworks.

Fig. 4-5 Iron ore breccia in the form of veins and veinlets which cut the volcano-sedimentary sequence.

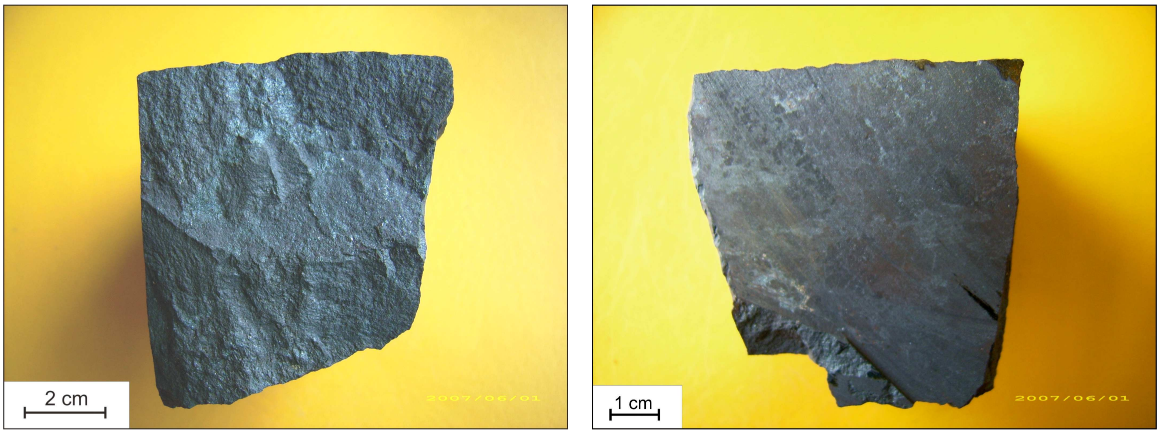

Fig. 4-6 Hand specimens of rich magnetite ore.

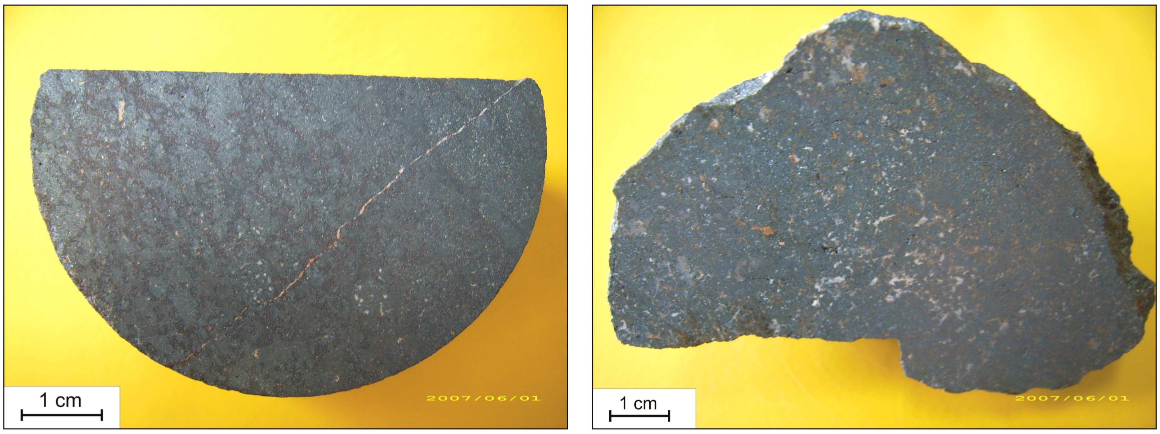

Fig. 4-7 Hand specimens of oxidized (left) and low-grade (right) iron ore.

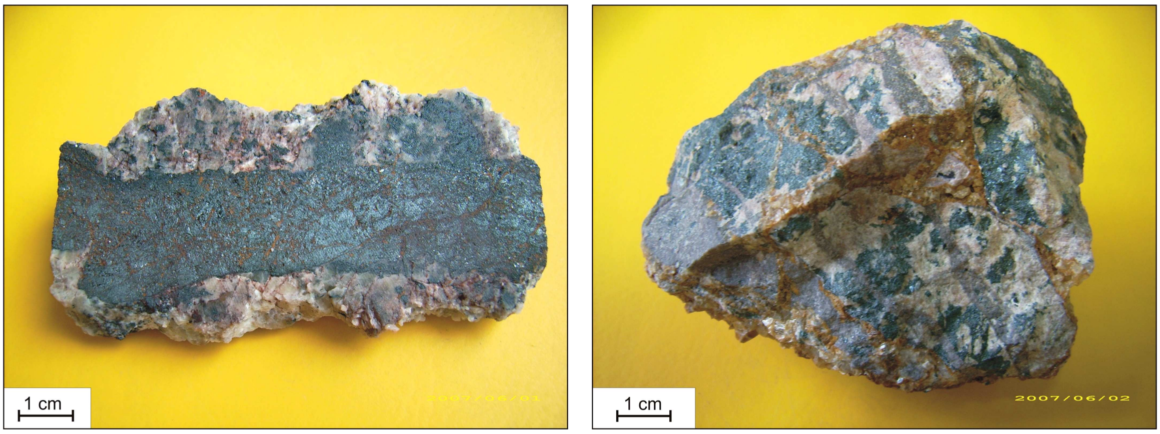

Fig. 4-8 Veinlets (left) and iron ore breccia (right) in hand samples. Note calcite veinlets as fracture and open-space filling in the right picture.

The iron ore bodies usually show mineralogical and textural zonation from core to margins. The massive cores are magnetite-rich with sparse apatite intergrowth whereas the marginal zones are mostly brecciated with higher hematite and apatite content and martitization. Under the microscope, the massive ores display a granular, partly brecciated texture and consist of subhedral to anhedral magnetite grains of variable size which show different martitization stages (Fig. 4-9). Martitization is observed not only near the surface of the ore bodies but also at depth, usually along grain margins and fractures in magnetite, suggesting the role of hydrothermal overprint and metasomatic fluid-ore interaction besides weathering (see next section for detailed description of alteration process of magnetite).

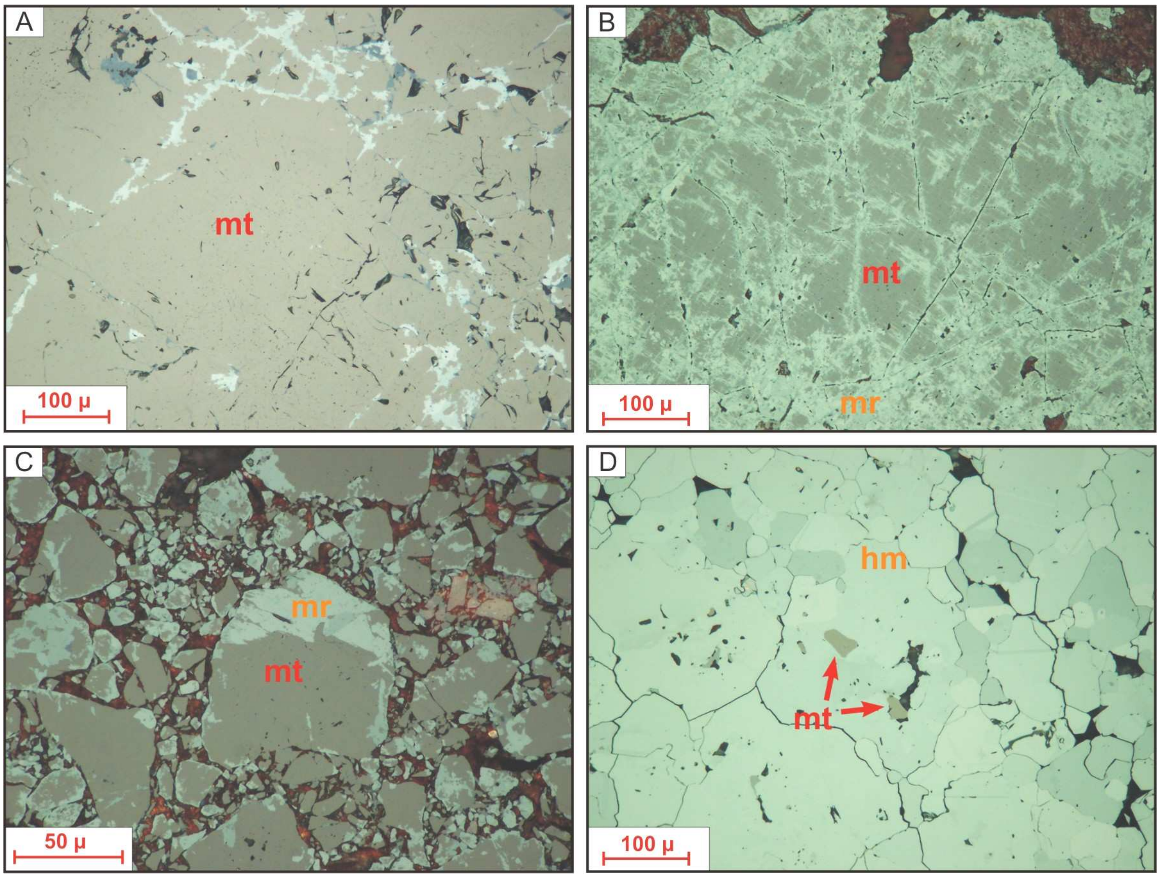

Fig. 4-9 Photomicrographs of massive iron ores (Reflected plane light, oil immersion).
A- Massive rich magnetite ore with incipient martitization around crystal boundaries (Chador-Malu deposit). B- Pervasive martitization of massive iron ore (Choghart deposit) C- Granular magnetite (mt) which is intensively brecciated and shows incipient martitization (mr) (Esfordi deposit). D- Complete replacement of magnetite (mt) by martite or secondary hematite (hm). Note the two small magnetite relics and the preserved crystal form of magnetite in secondary hematite (Esfordi deposit).

In addition to secondary hematite (martite), blades of primary hematite are also present in the ore bodies as individual crystals or aggregates which are usually associated with apatite or gangue minerals as late stage mineralization between the magnetite (Fig. 4-10). These hematites have variable size and are typically euhedral to subhedral.

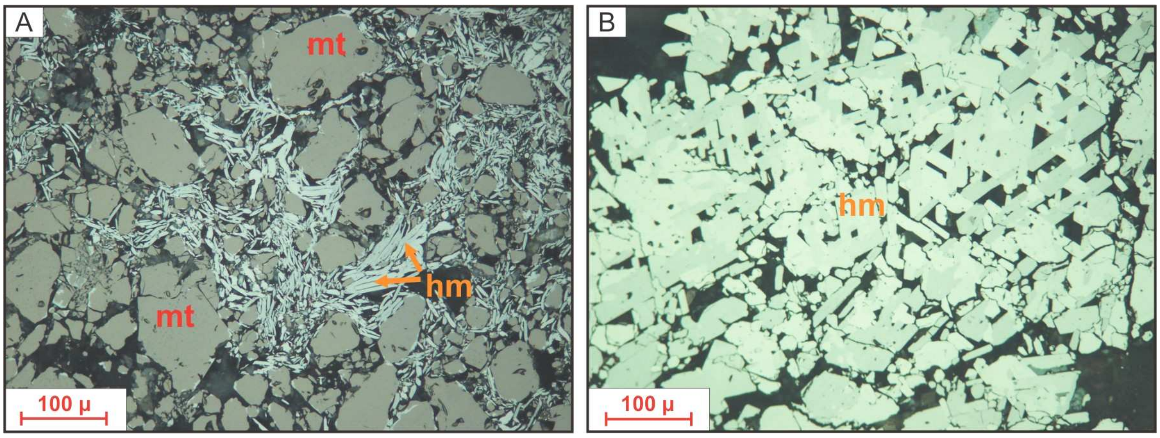

Fig. 4-10 Photomicrographs of hematite mineralization in Esfordi deposit (Reflected plane light, oil immersion). A- Blades of primary hematite (hm) as late-stage iron mineralization between magnetite (mt) crystals. B- Blades of primary hematite (hm) associated with completely martitized ore.

The iron-oxide-rich breccias usually occur at the tops of the massive ores, as veinlets or veins ranging up to a few meters wide, which cut the volcano-sedimentary sequence. The ore breccias may grade upwards into a zone of low-grade iron ore with magnetite and/or hematite ± apatite ± actinolite ± quartz ± calcite. Stockwork iron ore locally occurs as irregular cross-cutting veinlet networks of magnetite and apatite, which commonly cut the massive orebodies as well as the associated volcanic rocks. The veinlets vary in thickness, from a few millimeters to a few centimeters.

Replacement features on all scales are widespread. Locally, the magnetite bodies contain feldspar and quartz phenocrysts which decrease in abundance toward the center of the ore bodies. Some iron ores display a metasomatic replacement texture within dolomitic host rocks where the carbonate matrix is selectively converted to actinolite. Although disseminated magnetite is widespread around the deposits in the volcanic rocks, most magnetite is commonly concentrated adjacent to massive and ore breccia zones. Some volcanic rocks are dusted or cut by very fine-grained hematite which gives a pinkish or brick-red color to these rocks (Figs. 4-11, 4-12). Most volcano-sedimentary host rocks have been altered and the original chemistry of these rocks is strongly modified by sodic, potassic and calcic overprint (see next section).

Fig. 4-11 Veinlets and stockworks of iron ore. Note replacement of the volcanic host rock.

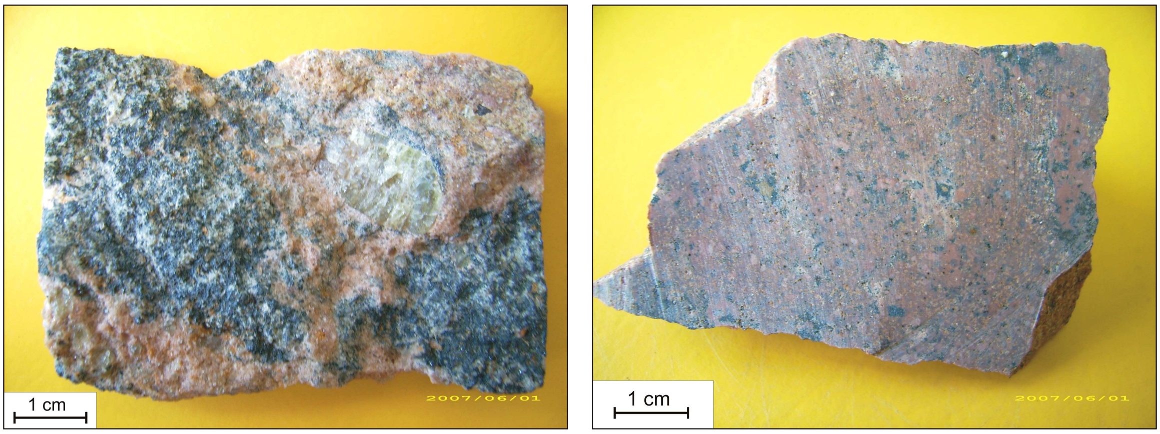

Fig. 4-12 Replacement feature in volcanic rocks. Left: A rhyolitic rock (brick-red) which is metasomatically replaced by iron ore (black) and a relatively big crystal of apatite (light-green). Right: A rhyolitic rock which is dusted by very fine-grained hematite.

Apatite, either in massive or in breccia ores, is characterized by fluorapatite containing small amounts of hydroxyl but no chlorine (see next chapter for details). Fine- and coarse-grained apatite occurs in varying proportion with magnetite, ranging from sporadic grains to bodies of relatively pure apatite veins. Two generations of apatite are recognized. The first, which is contemporaneous with the main phase of magnetite formation, is characterized by euhedral crystals ranging in size from a few millimeters to a few centimeters, intimately intergrown with magnetite. The second generation occurs as subhedral to anhedral crystals of varying size, in veins and veinlets, which cut the magnetite-apatite ore. In some ore deposits (e.g. Esfordi, Gazestan), there is an apatite-rich zone in the form of massive to vein-type apatite ores which are usually accompanied by minor actinolite and hematite. These high-grade apatite zones usually have between 12-15 wt% P_2O_5, but locally consist of relatively pure apatite ores (apatitite) which may have up to 35 wt% P_2O_5.

Most large apatite crystals have been broken into angular fragments due to post-ore brecciation. Late carbonate alteration overprints the massive apatite ore as matrix and fracture filling of calcite. Locally, very fine-grained or dusty interstitial hematite produces a very distinctive pinkish to brick-red color in some of the apatitites. Apatite, commonly in the stockwork zones or as open space filling, occurs in the form of prismatic crystals and occasionally forms big idiomorphic crystals as much as 8 cm long and may contain small inclusions of magnetite. Locally some relatively big euhedral crystals of magnetite are visible in the massive magnetite bodies or in ore breccia zones.

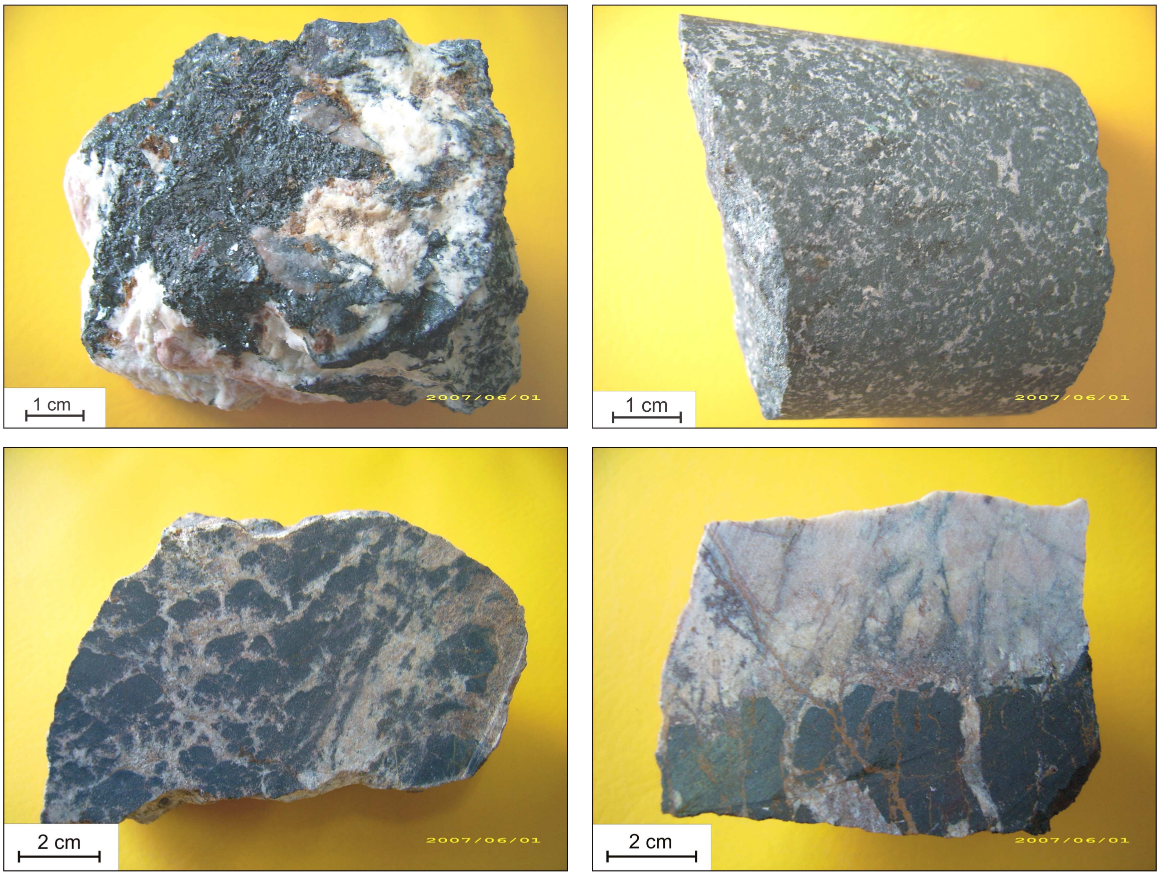

Fig. 4-13 Different features of magnetite (black) - apatite (white) intergrowth.

Fig. 4-14 Apatite-rich zone in the Esfordi deposit. The pinkish color in part of these apatite ores is due to interstitial dusty hematite.

Fig. 4-15 Blocks of pure apatite ore (apatitite) after blasting in Esfordi Mine.

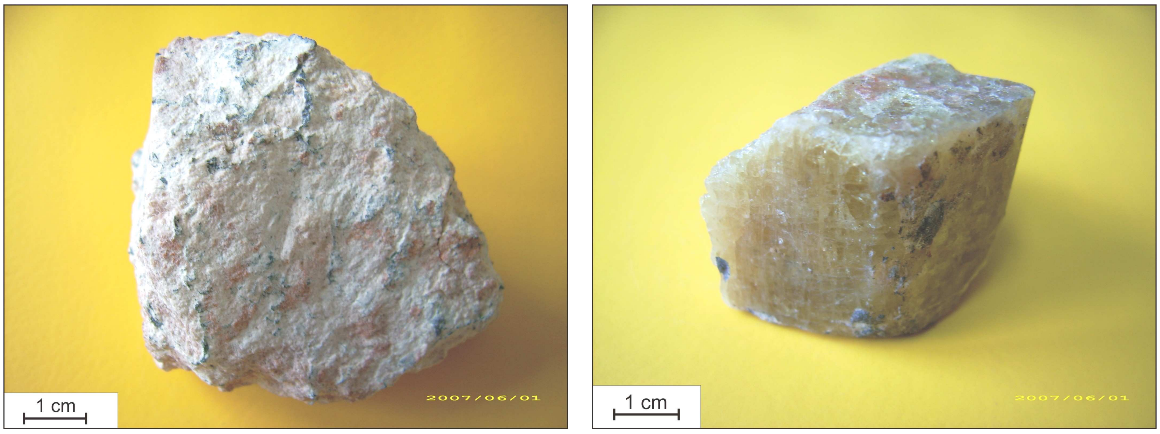

Fig. 4-16 Hand specimens of pure apatite from Esfordi deposit. Left: Fine-grained relatively pure apatite ore (apatitite). Right: A relatively big idiomorphic crystal of apatite.

It is obvious in some places that the main host rocks of the deposits are calcareous. The carbonates are selectively replaced by apatite-rich ores due to hydrothermal metasomatism. The solubility of apatite in hydrothermal solutions is essentially controlled by pH (e.g., Ayers and Watson, 1991). The experiments of Ayers and Watson (1991) have shown that the solubility of apatite decreases with increasing pH. From these experiments, it follows that apatite precipitates when acid fluids are neutralized for example by interaction with carbonate rocks. The experimental results thus provide an explanation for the presence of apatite in many skarns and carbonate-hosted apatite deposits. This mechanism can be typically shown by the following reaction (Giere, 1996):

$$\underset{\text{calcite}}{5CaCO_3} + 3H_3PO_{4\,(aq)} + HF_{(aq)} \leftrightarrow \underset{\text{fluorapatite}}{Ca_5(PO_4)_3F} + 5CO_{2(aq)} + 5H_2O$$

Actinolite is the most important silicate mineral present in the iron deposits (Fig. 4-17). It occurs as anhedral to subhedral grains and displays a continuous series with tremolite, indicating variable degree of iron metasomatism of the host rocks. In some deposits (e.g. Esfordi), it occurs in massive bodies ("Green rock") due to metasomatism of dolomitic rocks adjacent to or interfingering with magnetite-apatite ore, which manifests a skarn setting. Other hydrothermal minerals are quartz, calcite, albite, K-feldspar, sericite, chlorite, talc, sphene, and epidote. Monazite, and relatively rare parisite, allanite and xenotime occur particularly in those deposits with high apatite content.

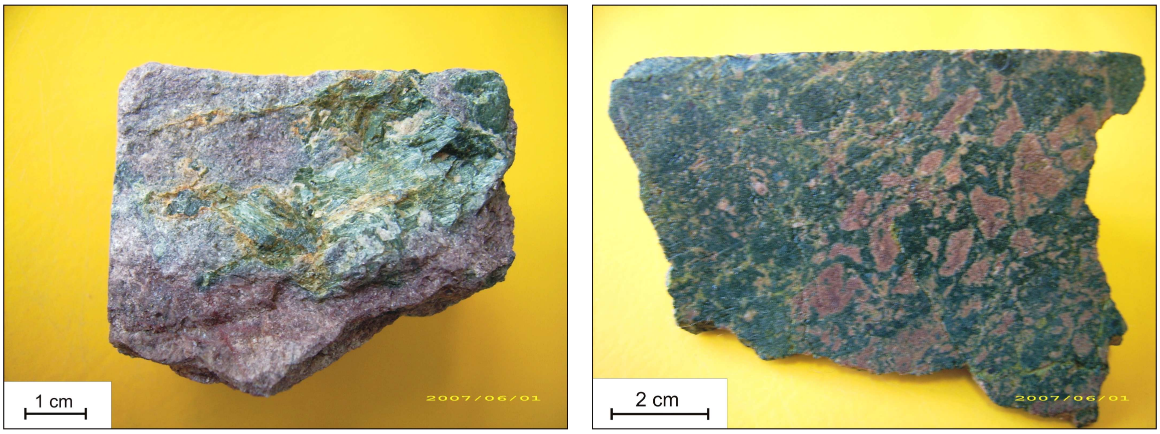

Fig. 4-17 Hand specimens showing actinolite (green) and apatite + dusty hematite (purple) intergrowth

Sulfides are rare. Only some pyrite and few fine-grained chalcopyrite crystals were found sporadically in some drill cores. They are associated with late-stage gangue minerals (Fig. 4-18). Goethite and other hydrous iron oxide minerals occur near the surface, but disappear rapidly towards deeper levels (Fig. 4-18).

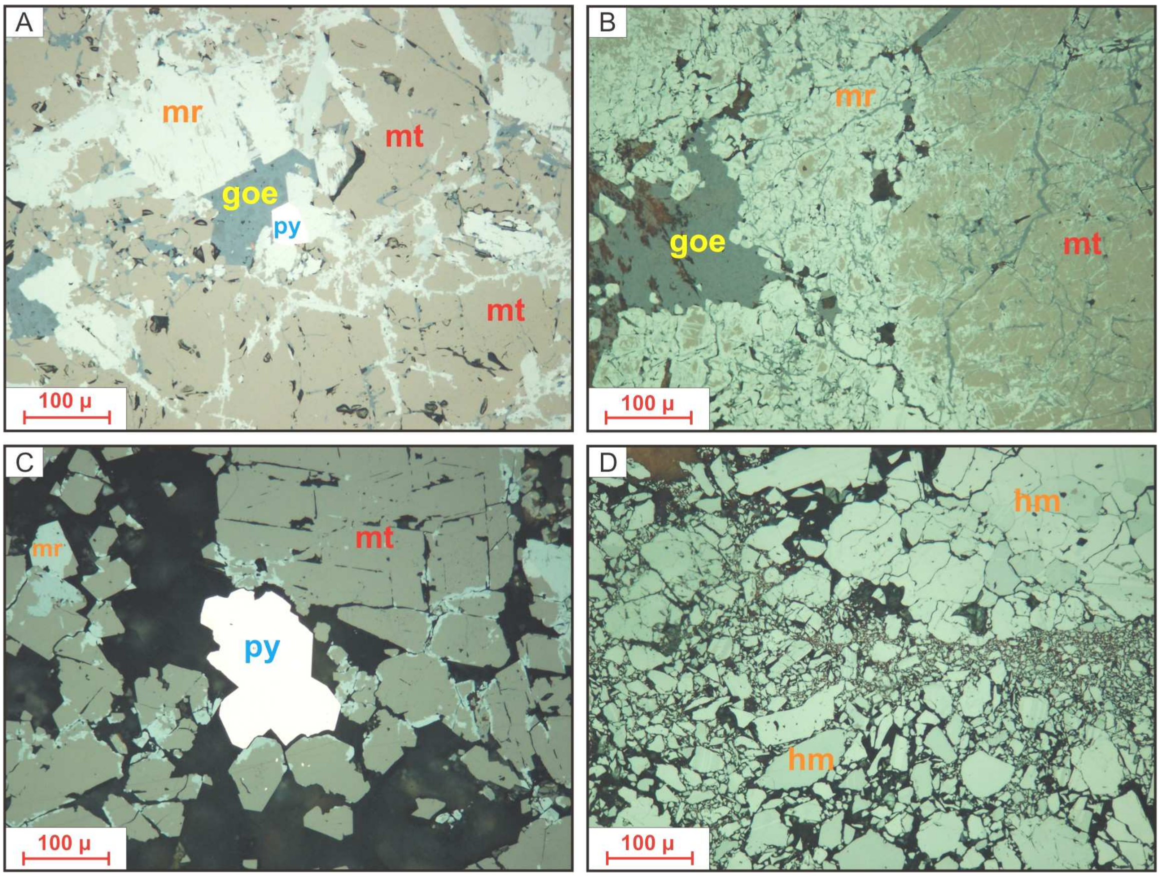

Fig. 4-18 Photomicrographs of the Bafq iron ores in polished sections, reflected plane light (oil immersion). A- Martitization (mr) of magnetite (mt) and relict pyrite (py) and formation of martite (mr) and goethite (goe) (Chador-Malu deposit). B- Martitization and formation of goethite (goe) in surface sample (Choghart deposit). C- Presence of rare sulfide mineralization usually as pyrite (py) as late stage mineralization associated with gangue minerals (black) (Esfordi deposit). D- Post ore brecciation of martitized powdery rich iron ore (Esfordi deposit).

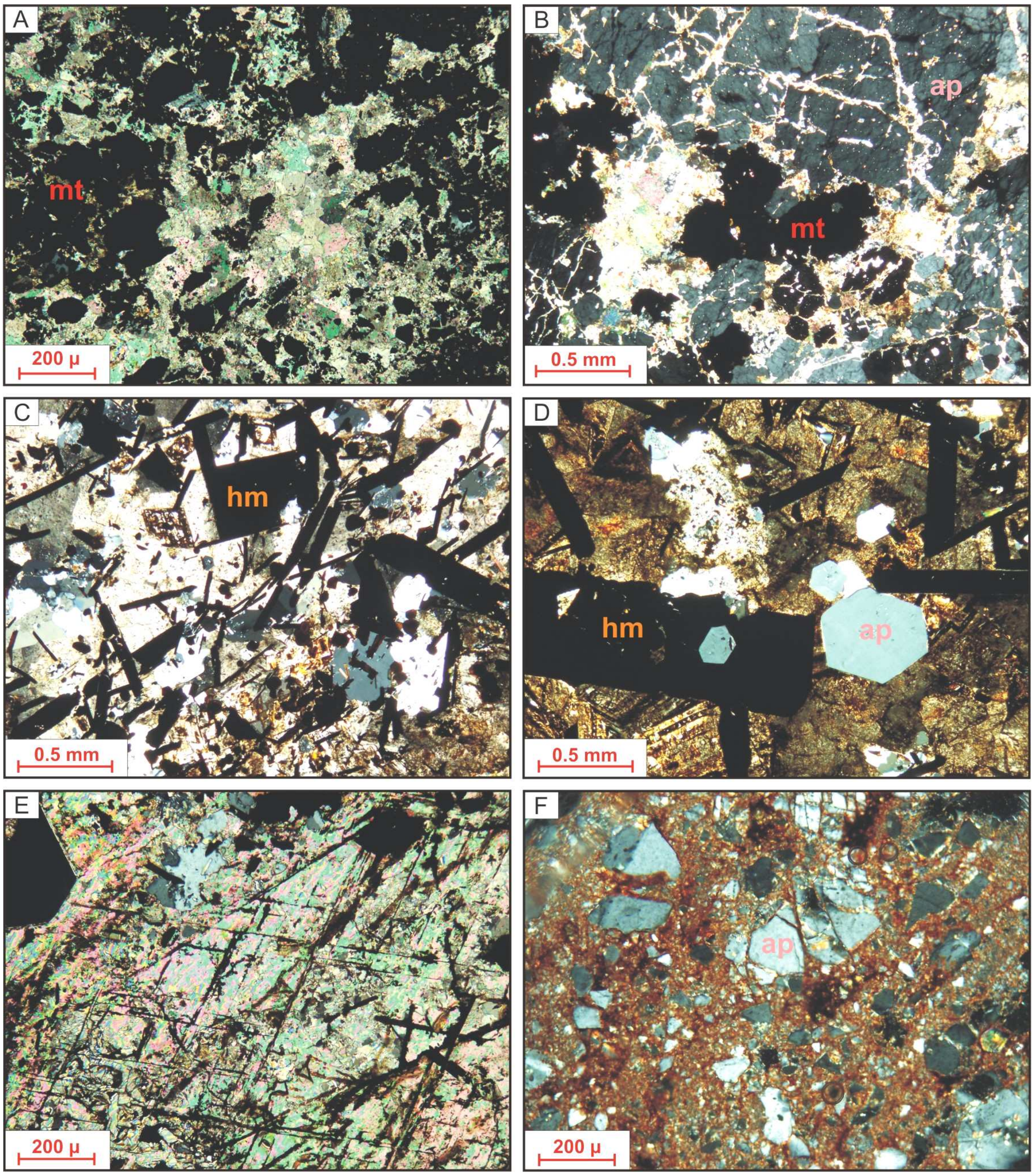

Fig. 4-19 Photomicrographs of iron oxide-apatite ores in thin section (XPL).
A-Magnetite (mt) ore in carbonate matrix (Chador-Malu deposit). B- Magnetite (mt) - apatite (ap) ore in carbonate matrix. Note the post-ore brecciation of apatites which are cut by carbonate veinlets (Choghart deposit). C- Precipitation of hematite (hm) blades in carbonate host (Esfordi deposit). D- Euhedral crystals of hematite (hm) and apatite (ap) in carbonate matrix. Note the inclusion of an idiomorphic crystal of apatite within hematite (Esfordi deposit). E- Emplacement of iron oxide in cleavages (rhombohedric) and fractures in dolomite (Esfordi deposit). F- Fully brecciated apatite (ap) ore with interstitial dusty hematite (red).

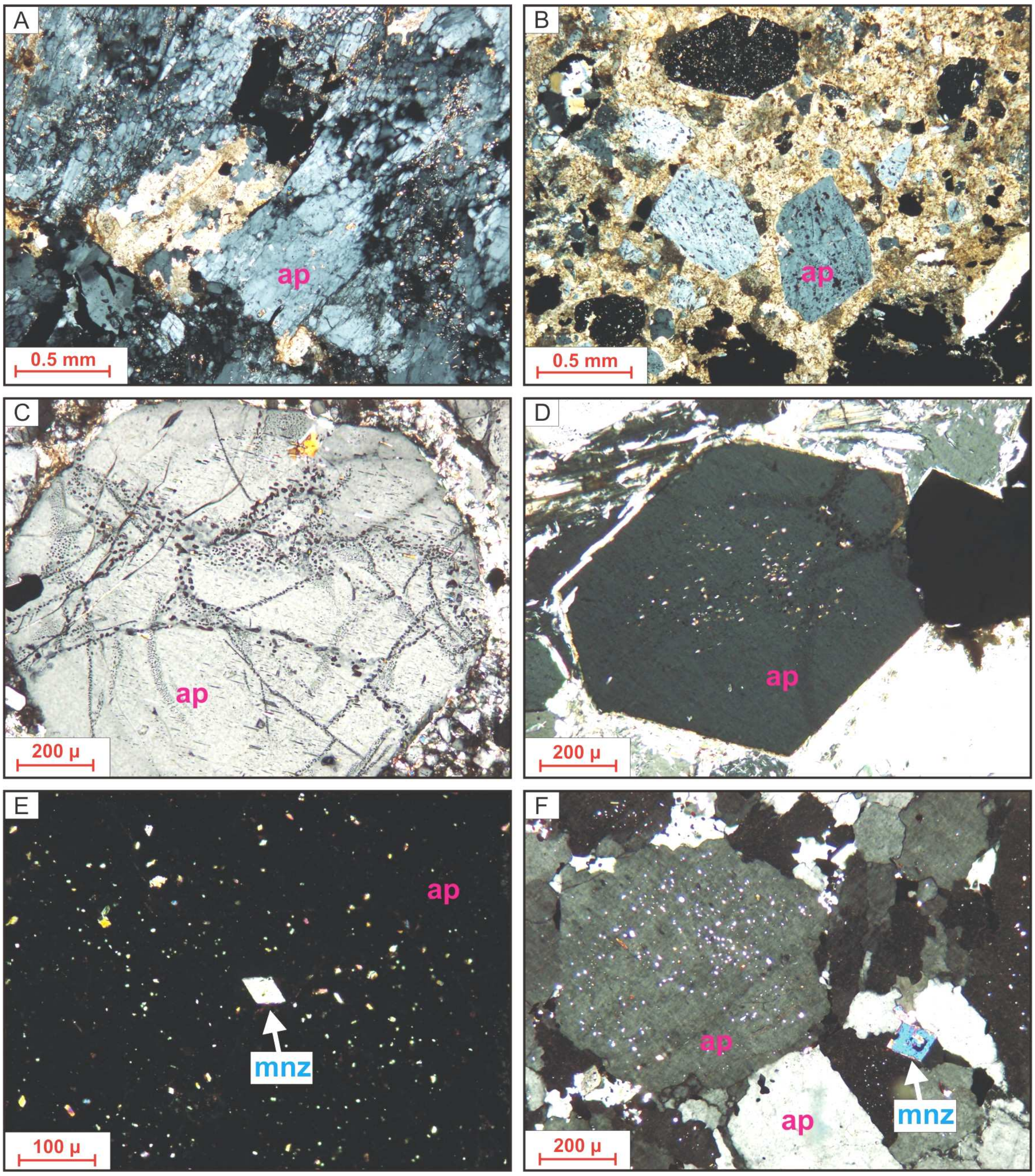

Fig. 4-20 Photomicrographs of pure apatite ores in thin section (XPL) from the Esfordi deposit.
A- Apatite (ap) aggregates in the rich apatite ore zone (apatitite). The orientation of brecciated apatites confirms that the ore has been affected tectonically by strong post-mineralization stress. B- Emplacement of apatite in carbonate matrix. C- Euhedral crystal of apatite with oriented fluid inclusions. D- Euhedral crystal of apatite with fine colorful monazite inclusions. E- An euhedral monazite (mnz) inclusion inside host apatite (black). Note the other numerous fine-grained monazites inside the apatite. F- Monazite inclusions inside apatite and a relatively big individual crystal of monazite (mnz) which crystallized outside.

4-2 Hydrothermal alteration

The Bafq deposits typically display extensive wall-rock alteration. The type and intensity of this alteration, and the associated mineral paragenesis (Table 4-1), varies considerably both within and between districts, but appears to depend on the original wall-rock composition and the depth of formation of the deposit. The alteration assemblages associated with the iron ore deposits are evidence of an important metasomatic component in the ore-forming process, in which the alteration mineralogy is controlled by bulk-rock chemistry, composition of the mineralizing fluids, and P-T conditions of formation. However, the alteration shows a general transition from sodic alteration (albite-rich) at deeper levels especially in the plutonic rocks or their adjacent volcanics, to potassic alteration (potassium feldspar + sericite) at intermediate levels (in the volcanics), to sericitic and silicic alteration (sericite + quartz) in the uppermost portion of the system. Actinolite also occurs widely in the district, locally associated with albite as Na-Ca alteration at deeper levels, or as patches or massive bodies in carbonate rocks (especially dolomite) due to hydrothermal metasomatism. Usually, alteration of the volcanic and volcano-sedimentary host rocks is chemically, mineralogically and texturally complex and due to the high intensity of the alteration, especially in the vicinity of mineralization zones, the primary situation is obscured and recognition of the precursor rock composition is commonly impossible.

Sodic alteration especially has been observed in the some subvolcanic granites in the Bafq district. A large part of these granitic rocks, especially their roof, and their adjacent volcanics has been subjected to this kind of metasomatism. These granites are fine-grained at the margin and usually void of mafic minerals. Their characteristic feature is the presence of chequer-albite in the groundmass, and as xenomorphic porphyritic crystals (Daliran, 1990).
The chequer fabric does not always invade an entire albite crystal, and can only be developed at either the marginal rim of a grain or as a patchy distribution. Such fabrics are strong evidence of hydrothermal replacement, and of secondary albite (Daliran, 1990; and references therein). These granites can have up to 8 wt% Na_2O and have been classified as trondhjemite (due to high Na content) rather than granite by Ramezani and Tucker (2003). In the footwall volcanics, especially in the vicinity of granites, the dominant alteration assemblage is also sodic (sodic ± calcic) alteration. Plagioclase in the footwall volcanics throughout the district has largely been converted to albite. Locally, especially in rocks of originally felsic to intermediate composition (rhyolite - rhyodacite), complete conversion to albite (albitite) occurs.

Alteration of rocks toward albite-rich compositions (albitization) may occur as a consequence of hydrothermal fluid circulation around sea-floor hydrothermal cells (e.g., Rose et al., 1992). Albite-rich rocks in continental rifts have also been interpreted as the products of syngenetic, diagenetic, or metamorphic recycling of evaporite components (Cook and Ashley, 1992; Oliver et al., 1994), and have been considered as a result of regional-scale metasomatism in the Bafq district (Haghipour, 1974; Haghipour et al., 1977). Barton and Johnson (1996) proposed that circulation of saline, evaporite-derived brines is instrumental in stripping iron and base metals from wall rocks which show intensive sodic-calcic alteration. Alternative models describe this type of alteration as a product of highly saline fluids derived from crystallizing intermediate to felsic magma (e.g., Pollard, 2001; Sillitoe, 2003). Oliver et al. (2004) have shown that sodic alteration has an important role in the genesis of IOCG deposits in the Eastern Mount Isa Block, Australia. The albitization process added Na to the rocks and released Fe, K, Ba, Rb and base metals to the fluid. According to these authors, this mechanism (albitization) can be considered via forward progress of the followings (unbalanced) reactions:

(1) biotite + plagioclase ± K-feldspar ± magnetite ± ilmenite + NaCl ± $CaCl_2$ ± CO_2 → albite + titanite ± scapolite ± cacite + KCl (in intrusive rocks)

(2) biotite + calcite + quartz + NaCl → actinolite + albite + titanite + KCl + CO_2 ± microcline (in impure marbles)

(3) muscovite + biotite + plagioclase (or calcite) + NaCl → tremolite/actinolite + albite + titanite + KCl (in weakly calcareous metapelites)

Due to these reactions iron will be released from the host rocks and will be carried by the hydrothermal fluid as $FeCl_2$ or other chloride complexes and consequently precipitates as magnetite or hematite in suitable pH and Eh conditions. The KCl in the hydrothermal system is then responsible for subsequent potassic alteration in the upflow zone of the alteration system.

In the Bafq district the sodic zone is overlain by or enclosed in a potassic and/or sericitic alteration assemblage. The majority of hangingwall volcanic rocks are subjected to potassic alteration with a pinkish color which is mainly due to occurrence of K-feldspar with fine-grained hematite inclusions. Whereas least altered rhyolitic rocks usually have a grey to cream color. In some districts the potassic zone is overlain by a zone of sericitic or hydrolytic alteration. In this situation the K-feldspar is partially or in some cases completely replaced by sericite. In uppermost levels there is also evidence of a late period of silicification.

Magnetite, in massive bodies or irregular stockworks, is confined to the sodic and potassic alteration zones. Hematite predominates in higher level sericitic alteration zones, and in late cross-cutting breccia bodies. Rare earth element mineralization is found in all stages of alteration, although the highest concentration of REE minerals especially in the form of monazite (which is due to apatite metasomatism) is generally contemporaneous with potassic and sericitic alteration. Other REE minerals (allanite, parisite, …) usually are associated with late quartz-calcite breccia veinlets.

The distribution of sodic versus potassic alteration, their zoning and relation to mineral deposits have been documented in numerous other localities with similar mineralization (Hitzman et al., 1992). Na-metasomatism (albitization) is a common process in zones of descending or heating hydrothermal fluids at deep levels associated with metal leaching where hydrothermal fluids may be intracting with heat sources (e.g., granitic intrusions), whereas K-metasomatism (potassic alteration) should be dominant in upflow zones where hydrothermal fluids are cooling by interaction with country rock or meteoric water. This system usually proceeds with lower temperature sericitic and silicic alteration at higher levels near or at the paleosurface (Fig. 4-21) (Hitzman et al., 1992).

The actinolite–rich alteration shows variable intensity and mineralogy in different parts of the alteration system and varies in distribution between the Bafq magnetite-apatite deposits. Significant controlling factors in its distribution seem to be precursor chemical composition, porosity, and proximity to the mineralization. This alteration occurs either as massive altered bodies (“Green Rock”) or as actinolite-rich veins and veinlets cutting through altered rhyolitic rocks. Large veins are generally developed along faults, brecciated zones and lithological discontinuities. The peripheral volcanics may also exhibit minor actinolite alteration in the form of disseminations and veinlets. The actinolite-rich alteration strongly overprinted precursor rocks and usually masks original textures and structures. However, there are localized occurrences of the actinolite-calcite-apatite-hematite assemblage that reflect more carbonate-rich components in the original package and seem to be the products of hydrothermal metasomatism of dolomitic host rocks.

Actinolite occurs as anhedral to subhedral and mainly as elongate crystals with strong single-set parallel cleavages (Fig. 4-23). Late-stage chlorite±epidote±talc-carbonate alteration overprinted the actinolite-rich zone locally. The distribution of this assemblage is not uniform and spatially decreases away from actinolite-rich altered rocks in the vicinity of ore towards the pervasive peripheral K-feldspar alteration. The massive magnetite and/or apatite ores generally have very low actinolite content, but the ore breccias show actinolite aggregates within apatite-iron oxide-carbonate matrix.

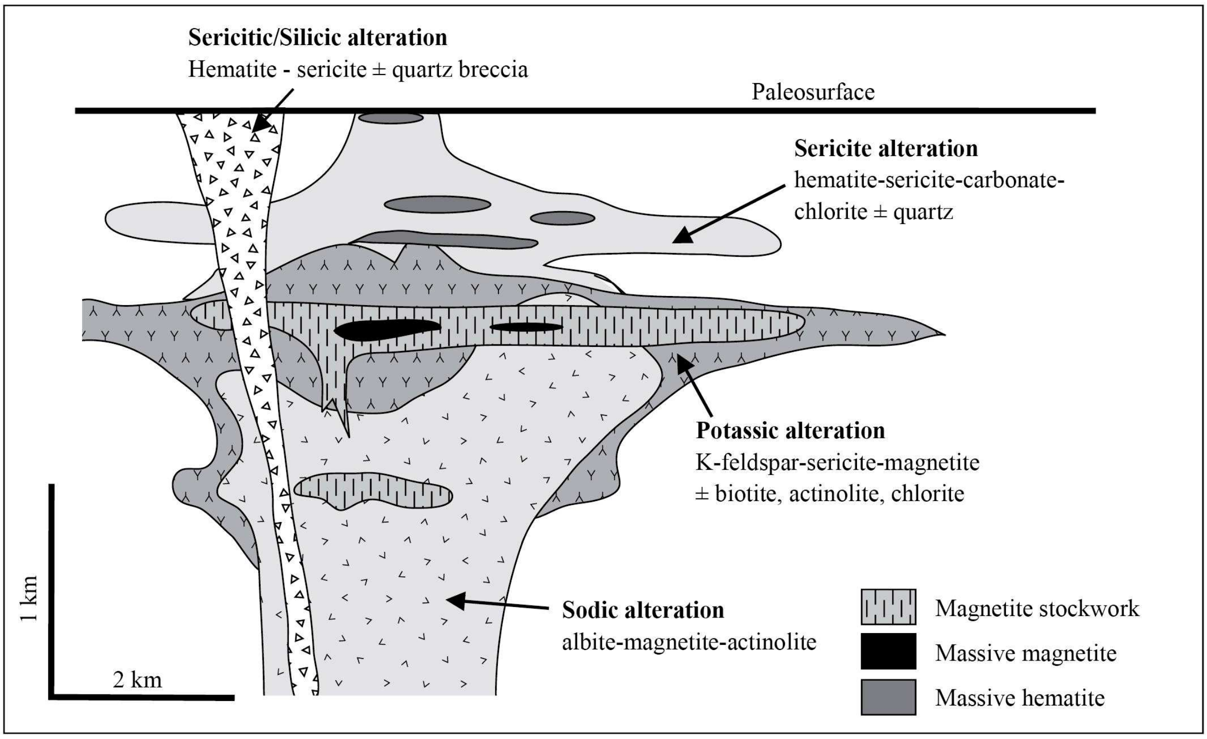

Fig. 4-21 Schematic vertical cross section of alteration zoning in IOCG and Kiruna-type iron ore deposits (after Hitzman et al., 1992)

In some localities, e.g. Chador-Malu, the sulfur content in the hydrothermal system, however low, is relatively higher than in other deposits due to the presence of disseminated post-ore pyrite. Hydrothermal fluids with reduced sulfur content can generate abundant hydrogen ion, usually at the surface, through the following reaction:

$$H_2S + 2O_2 \rightarrow HSO_4^- + H^+$$

This reaction is reflected in extensive acid attack of wall-rocks, which are commonly converted to kaolinite as well as pyrophyllite and alunite. Post-ore alteration is also recognized at some places. The orebody and the host rock are cut by breccias containing hydrothermal potassium feldspar which is mostly sericitized (Fig. 4-24). These are cut in turn by late breccia accompanied by silicification and sericitization of the host rhyolites (Fig. 4-24), transformation of magnetite to hematite, presence of primary hematite and deposition of quartz, calcite and late-stage REE minerals. Table 4-1 gives some typical alteration suites as exposed in the open pits of the Bafq deposits. Variation in the alteration assemblage between individual deposits is likely due to compositional differences in the host rocks, depth of formation and erosion.

Table 4-1 Type of the ore and alteration suite exposed in the open-pits of the Bafq deposits

Deposit	Type of ore	Main alteration suite exposed at open-pit
Esfordi	Apatite rich-iron ore	Mainly actinolitization as well as sericitization, chloritization and silicification
Chador-Malu	Iron-apatite ore	Mainly K-alteration (K-feldspar and sericitization) as well as chloritization, kaolinization, (albitization in intrusive bodies)
Choghart	Mostly rich iron ore	Mainly Na-alteration (albitization) as well as K-feldspar and actinolitization
Se-Chahun	Mostly poor iron ore	Mainly albitization and actinolitization

As it has been described in the previous section, much of the hematite (martite) is an alteration product of magnetite. This alteration process can be observed not only at the surface of the ore deposits but also at depth, indicating the role of hydrothermal fluids besides natural weathering. Although the transformation of magnetite to hematite has generally been described by the following oxidation reaction, i.e.:

$$2\ Fe_3O_4\ (mt) + \frac{1}{2}\ O_2\ (g) \rightarrow 3\ Fe_2O_3\ (hm) \qquad (1)$$

an alternative mechanism which is a non-oxidation reaction, i.e.:

$$Fe_3O_4\ (mt) + 2H^+ \rightarrow Fe_2O_3\ (hm) + Fe^{2+} + H_2O \qquad (2)$$

may have been the principal mechanism for this transformation, typical of hydrothermal environments (Ohmoto, 2003). This mechanism shows that the oxidation-reduction condition is not a prerequisite in martitization and formation of secondary hematite. Reaction (2), is an acid-base reaction and shows that the acidity of hydrothermal fluids attacking the magnetite orebodies has a significant role. This is why the presence of secondary hematite is temporally and spatially accompanied by acidic attack with pervasive alteration of the host rocks. Excess Fe^{2+} in reaction (2), which is due to leaching of Fe^{2+} from magnetite, may be consumed in the formation of other minerals such as actinolite or late-stage pyrite, or in the formation of a new generation of magnetite at lower temperature, as veins or veinlets. The molar volumes of magnetite and hematite are 44.524 cm^3 and 30.274 cm^3, respectively (Ohmoto, 2003).

Therefore, the transformation of magnetite to hematite through oxidation reaction (1) will result in a volume increase of only 0.89 cm^3 per one mole of magnetite, i.e., only a 2% volume increase. In contrast, the non-oxidation reaction (2) produces a volume decrease of 14.25 cm^3 per one mole of magnetite corresponding to a 32 % volume decrease. This appreciable decrease in volume significantly increases the permeability between magnetite crystals and facilitates enhanced fluid-rock interaction and complete conversion of magnetite to hematite, plus formation of other minerals between the brecciated magnetite. This is why most of the hematitized iron ores are brecciated and powdery. The high porosity and the coexistence of rare disseminated pyrite and hematitized ore support the suggestion that the transformation of magnetite to hematite in these deposits essentially occurred by the leaching of Fe^{2+} through reaction (2). If the transformation of magnetite to hematite had occurred by the oxidation reaction (1), then pyrite should have been completely oxidized to hematite, because the oxidation rate of pyrite is much faster than that of magnetite.

In some places, spilitic basalts have been observed, e.g. in the Mishdovan deposit (Daliran, 1990) and in the Esfordi deposit (this study). The spilites are volcanic rocks with light green color and porphyritic texture which resemble andesite-porphyries (andesitic tuffs) in hand samples, but show basaltic normative composition. However, they differ from normal basalts in their modal minerals, namely, the presence of plagioclase of albitic composition and secondary minerals due to extensive alteration. The microscopic study of the spilites indicates a holocrystalline, fine-grained to cryptocrystalline texture formed by densely packed albite crystals in a groundmass of chlorite, iron oxides, titanite, calcite and minor amounts of quartz. Amygdaloidal or vesicular textures are common. The vesicles are usually filled by chlorite, carbonate, chalcedony and minor epidote (Fig. 4-24). These vesicles are usually surrounded by dark-colored fine-grained iron oxides. In comparison to other volcanic rocks in the Bafq district, the iron content of the spilitic basalts is relatively high. Spilitization has usually been considered as characteristic of sub-seafloor hydrothermal alteration.

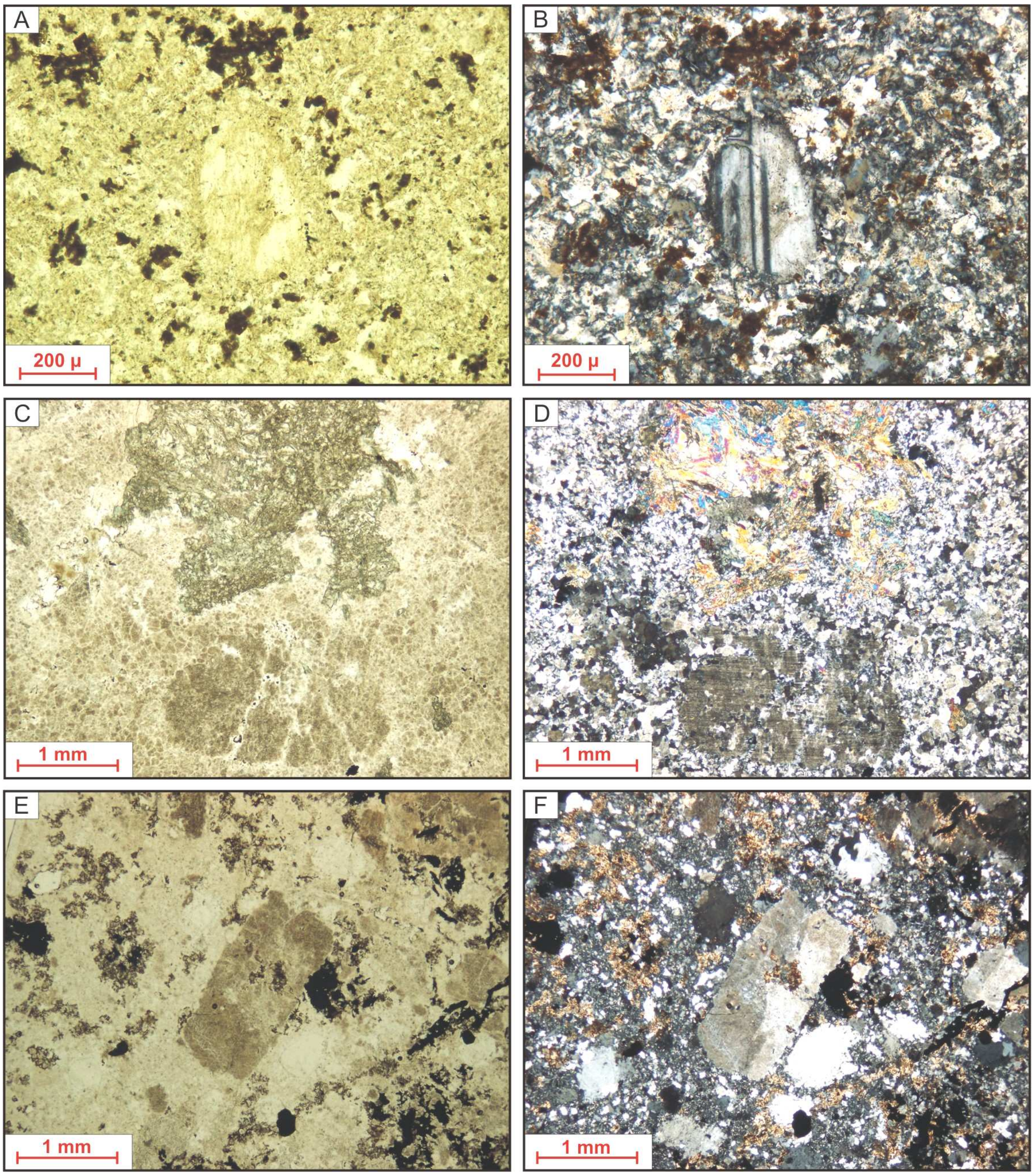

Fig. 4-22 Photomicrographs of alteration mineral assemblages.
A & B (PPL & XPL): Albitization in the rhyolitic host rocks (Choghart deposit).
C & D (PPL & XPL): Sodic-calcic alteration in volcanic rocks in the form of chequer albite (lower part) and actinolite (upper part) (Choghart deposit).
E & F (PPL & XPL): Potassic alteration in the form of K-feldspar in volcanic host rocks (Chador-Malu deposit).

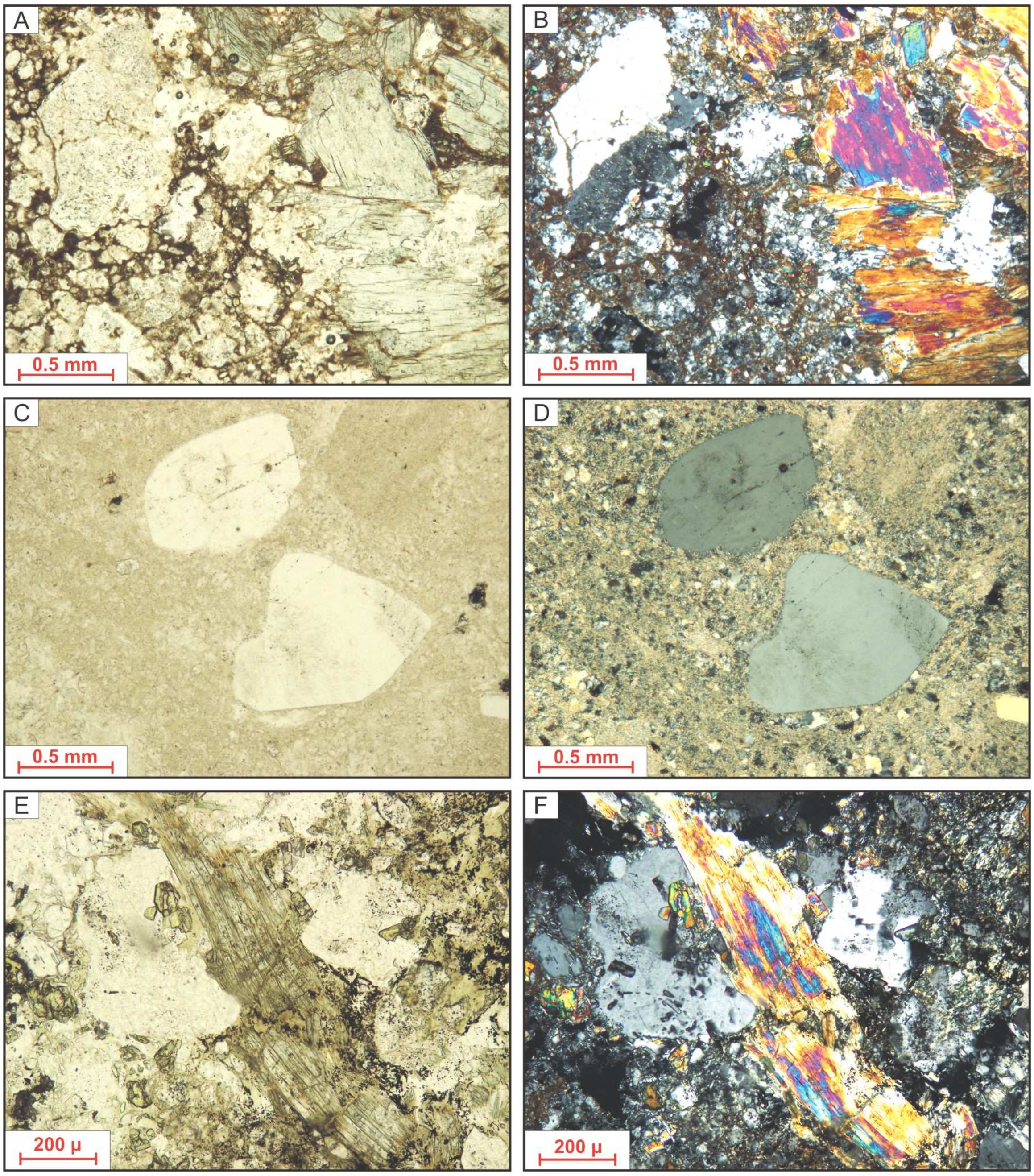

Fig. 4-23 Photomicrographs of alteration mineral assemblages in the Esfordi deposit.
A & B (PPL & XPL): Potassic alteration (left) and actinolite alteration (right).
C & D (PPL & XPL): Rhyolite with quartz phenocrysts affected by intensive sericitization.
E & F (PPL & XPL): Apatite-actinolite intergrowth in actinolite rich alteration zone ("Green Rock").

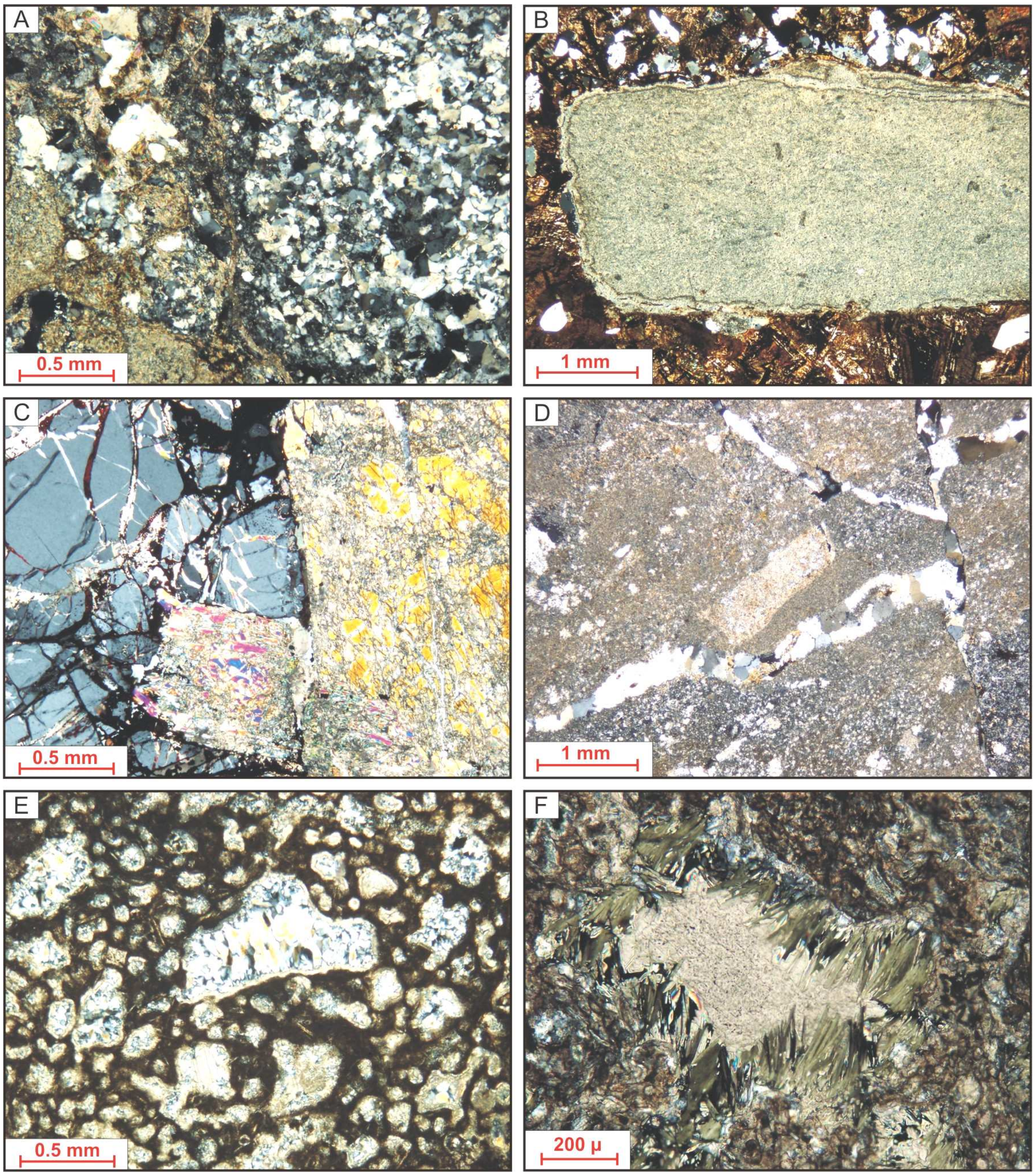

Fig. 4-24 Photomicrographs of alteration mineral assemblages in the Esfordi deposit (all pictures in XPL).
A- Sericitization (left) and silicification (right) in rhyolite. B- Completely sericitized feldspar phenocryst. C- Apatite (left) and actinolite (right). D- Rhyolitic tuff with a K-feldspar phenocryst in the middle. Note that the rock is extensively cut by quartz veins. E- Spilitic rock with amygdaloidal texture. The vesicles are mostly filled by chalcedony, calcite and chlorite and are surrounded by fine-grained hematite (black). F- Close-up of a vesicle in the spilitic rock which is filled by chlorite (green) and carbonate (in the center) as main alteration products.

Chapter 5: Geochemistry

5-1 Bulk rock geochemistry

The igneous rocks of the Bafq district can be generally classified into two main groups, plutonic to hypabyssal rocks, and their equivalents volcanics. The plutonic rocks are mainly of granitic composition. However, locally diorites and gabbro diorites are also observed. Most of the igneous rocks, especially volcanics, have suffered from extensive alteration and their primary composition has been obscured by widespread sodic-potassic and calcic alteration. Therefore, dealing with the chemical composition of these highly metasomatized rocks for their classification, especially nearby ore deposits, requires special care. To distinguish between alkaline and subalkaline suites, the samples have been plotted in a diagram of total alkalis (Na_2O+K_2O) versus silica (SiO_2) (Fig. 5-1). In this diagram, the high-SiO_2 rocks, either plutonic or volcanic, mostly plot in the subalkaline field. However, some of these felsic rocks are relatively rich in total alkalis. The basic rocks mostly fall in the alkaline field. However, as deduced from microscopic examination, this is due to extensive sodic alteration and precludes the real alkaline affinity of igneous origin.

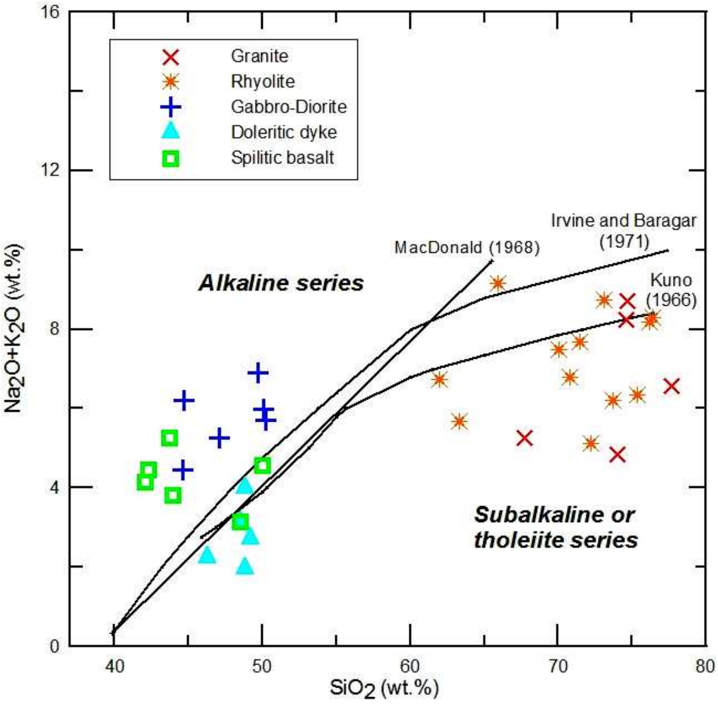

Fig. 5-1 Discriminant diagram between alkaline-subalkaline series of igneous rocks of the Bafq district. Analytical data from Daliran (1990), Ramezani & Tucker (2003) and this study.

The K_2O versus Na_2O diagram (Fig. 5-2) illustrates that most, if not all, felsic volcanics plot in the high-K fraction, while most plutonic or hypabyssal rocks plot in the high-Na fraction. This observation advocates the fact that in the magnetite-apatite deposits of the Bafq district, similar to most IOCG systems, the sodic alteration usually occurs at deeper levels where the hypersaline fluids are in interaction with the heat source intrusions, while the felsic volcanics at higher levels are commonly affected by potassic alteration.

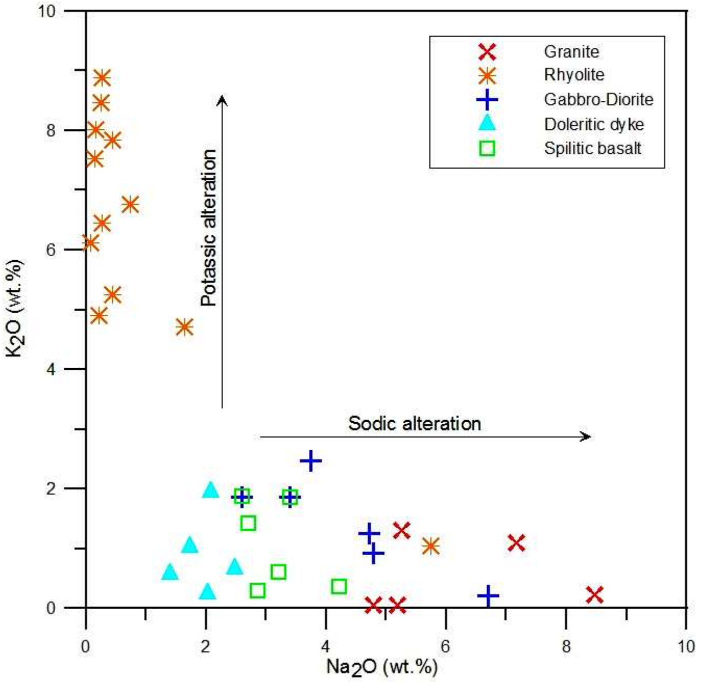

Fig. 5-2 Composition of igneous rocks of the Bafq district in the K_2O versus Na_2O diagram (Data source as described in Fig. 5-1).

For the chemical classification of volcanic rocks, the TAS (total alkalis versus silica) diagram is commonly used (Fig. 5-3). The volcanic rocks of the Bafq district show compositional bimodality. Most acidic volcanics plot in the "Rhyolite" field while the basic rocks plot in the "Basalt" or "Tephrite" field. Because most of these samples have been affected by extensive alteration, alternatively, the samples have been plotted in the discrimination diagram of Winchester & Floyd (1977) which is widely used to discriminate between altered volcanic rocks (Fig. 5-4). In this diagram the more felsic volcanics plot in the "Rhyodacite-Dacite" compositional field while the more basic suites plot in the "Andesite" to "Andesite-Basalt" field. The bimodality in the composition of the Bafq volcanic rocks has been addressed by Daliran (1990) as an evidence of rift-related (within-plate) volcanism. However, the geochemical data of the felsic rocks (both volcanic and plutonic) are against an intracontinental rift-related setting and suggest calc-alkaline volcanic-arc magmatism (Figs. 5-4 and 5-5). The definition of the tectonic regime of the basaltic rocks is complicated and hampered by the limited number of samples and their extensive alteration, such that different diagrams show different tectonic regime and do not allow any discrimination.

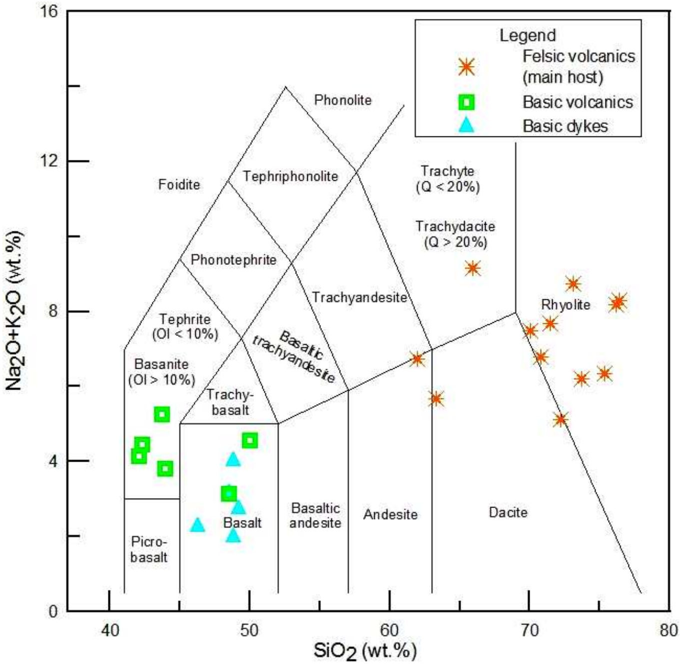

Fig. 5-3 Discrimination of volcanic rocks of the Bafq district in the TAS (Total alkalis versus Silica) diagram (Data source as Fig. 5-1).

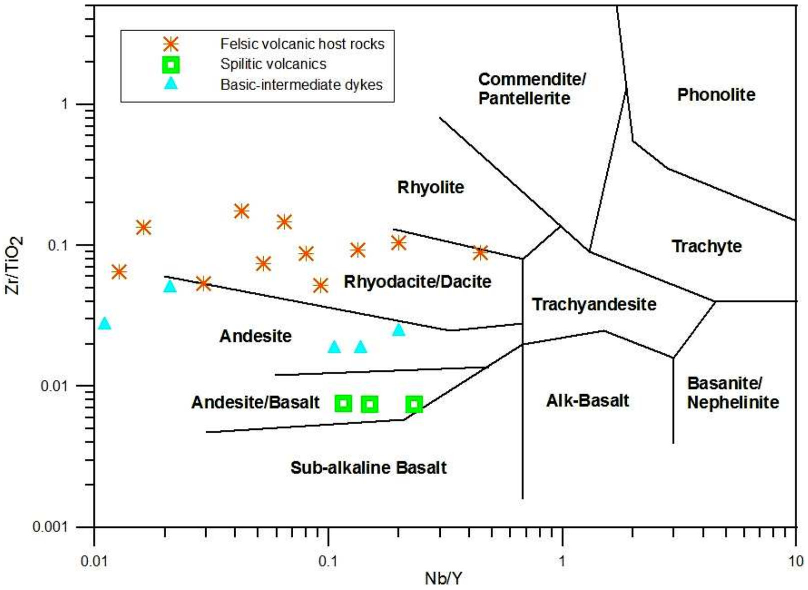

Fig. 5-4 Compositions of volcanic rocks of the Bafq district in the discriminant diagram of Zr/TiO_2 versus Nb/Y of Winchester & Floyd (1977). Data source from Ramezani & Tucker (2003) and this study.

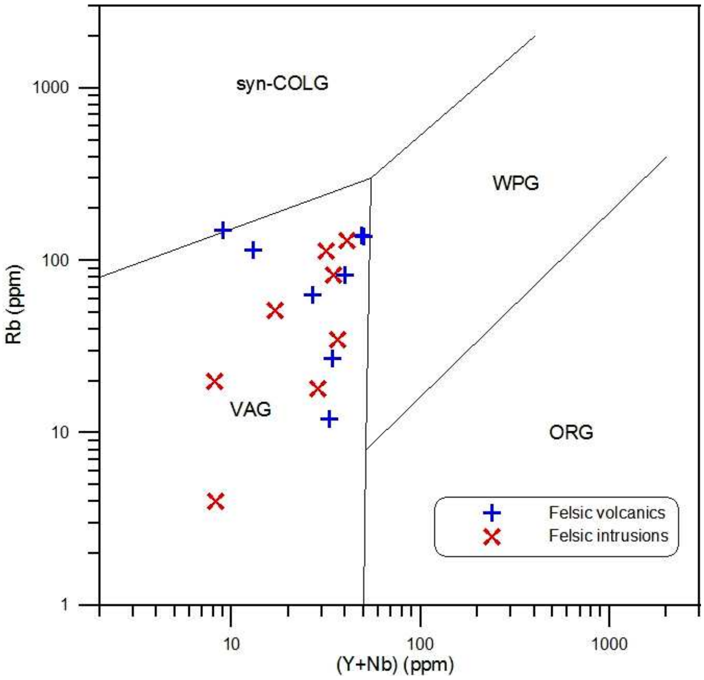

Fig. 5-5 Tectonic regime of felsic rocks of the Bafq district in the Rb versus Y+Nb discriminant diagram (Pearce et al., 1984). Data source from Ramezani & Tucker (2003) and this study.
VGA=Volcanic-arc granite magmatism; WPG=Within plate granite magmatism; ORG=Ocean-ridge granite magmatism; Syn-COLG=Syn-collisional granite magmatism. Note that postorogenic granite magmatism is around the triple point VAG-Syn-COLG-WPG.

Generally speaking, the magmatic rocks of the Bafq district are calc-alkaline in composition and due to extensive sodic and potassic alteration, they locally and partially (especially the basic suites) show more or less alkaline affinity. Our geochemical investigation and tectonic evidence show that all igneous rocks are emplaced in an arc-related extensional regime. The presence of regional-scale faults in this district suggests that the magmatism is controlled by these arcuate faults attributable to a back-arc extensional setting (see also Ramezani & Tucker, 2003).

In Fig. 5-6, REE patterns of some of the igneous rocks are presented. The igneous rocks which are not or only slightly affected by hydrothermal alteration show a common trend of evolved felsic igneous rocks with negative slope and relatively high LREE/HREE fractionation. The negative Eu anomaly is also obvious and characteristic. The volcanic rocks which are host of the magnetite-apatite mineralization show the same pattern but with slightly higher REE content reflecting the effect of mineralizing fluids. The two main granitic intrusions in the Bafq district i.e., Zarigan granite and Chador-Malu granite, which are both extensively albitized, show much lower REE content and a strong positive Eu anomaly. This feature is complementary to the high REE content and strong negative Eu anomaly in the magnetite-apatite ore system (see section 5-3). It can be assumed that these large granitic intrusions played a major role as heat source for convection causing widespread hydrothermal circulation. During sodic alteration by high-salinity brines (probably of evaporitic source), Eu is selectively fixed in the plagioclase structure during albitization, while other rare earth elements are leached from these igneous rocks and remobilized into the hydrothermal system.

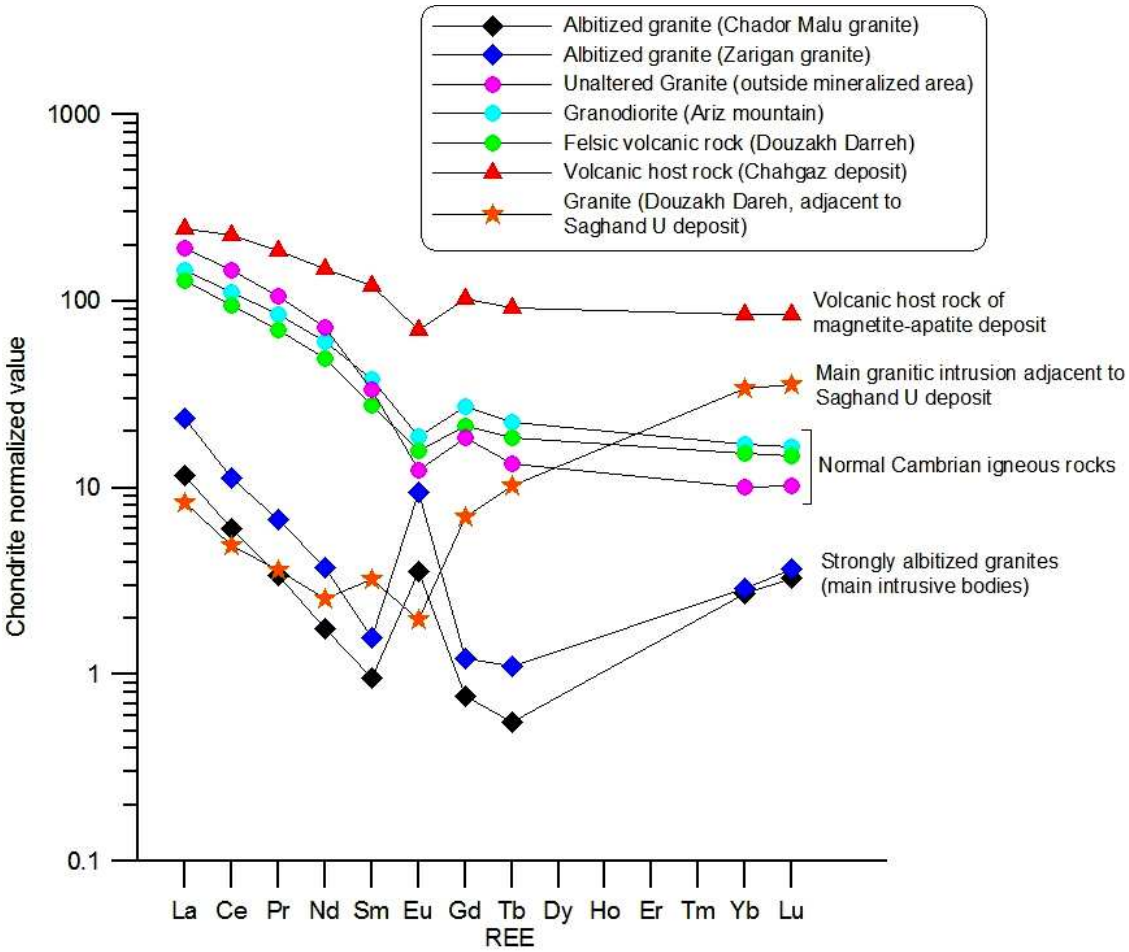

Fig. 5-6 Spider diagram representing REE patterns of different igneous rocks of the Bafq-Saghand district (analytical data from Ramezani & Tucker, 2003; chondrite value from Anders & Grevesse, 1989)

Another granitic intrusion in the district (Douzakh Darreh granite), which is near the Saghand uranium deposit, is enriched in U (4.58 ppm) and especially in Th (26.90 ppm) and shows a positive slope in its REE pattern reflecting a high HREE/LREE ratio. At first, it seems that this small granitic intrusion could be the source of radioactive elements, but alternatively and more probably this pattern may be from hydrothermal alteration and U-Th mineralizing fluids.

To find out inter-elemental relationships of the ore and the volcanic host rocks and classifying them, correlation coefficient analysis on bulk-rock data was used. Table 5-1 shows the correlation matrix of 58 analytical data from the magnetite-apatite ore and the host volcanic rocks. On the basis of these calculated correlation coefficients, elements can be classified into three different groups:

Group 1 consists of: P, Ca, F, Cl, REE, Th, Y, Sr and As, which all show a strong positive correlation and are the main or trace constituents of apatite.

Group 2 consists of: Fe, V, Ti and Ni, which all show a positive correlation and are associated with magnetite.

Group 3 consists of: Si, Al, Mg, K, Na, Zr with a strong positive correlation which are the main or trace constituents of the volcanic rocks.

The table also shows that there is a negative correlation between Group 1 and Group 2 which may apparently reflect a different origin for the iron ore and apatite ore components. However, more likely this is a forced negative correlation because the ore samples consist essentially of magnetite and apatite in variable proportions. Both of these groups show a relatively high negative correlation with Group 3, suggesting the absence of a genetical relationship between magnetite-apatite mineralization and the volcanic host rocks. The strong positive correlation between P and REE ($r = +0.98$) reflects the fact that the most important REE bearing phases are phosphates (mainly as apatite and minor later monazite). REE can substitute for Ca in the apatite structure by the following two coupled substitution reactions:

$Na^{+} + REE^{3+} = 2\ Ca^{2+}$

$Si^{4+} + REE^{3+} = P^{5+} + Ca^{2+}$

The necessary charge balance during the REE^{3+} substitution for Ca^{2+} in the apatite structure involves Si^{4+} and Na^{+} (Harlov et al., 2002; Roeder et al., 1987).

Table 5-1 Correlation matrix demonstrating positive/negative inter-elemental relationships of magnetite-apatite ores and the volcanic host rocks (on the basis of 58 analytical data)

	Si	Ti	Al	Fe	Mg	Ca	Na	K	P	Cl	F	As	Au	Cu	Ni	Sn	Sr	Th	U	V	Y	Zn	Zr
REE	🟩 -0.54	-0.28	🟩 -0.51	-0.27	-0.43	🟧 0.96	-0.32	-0.42	🟧 0.98	🟧 0.90	🟧 0.97	🟩 0.70	🟩 0.59	0.09	-0.17	-0.26	🟩 0.75	🟧 0.88	0.11	-0.21	🟧 0.96	-0.18	-0.47
Zr	🟧 0.87	-0.40	🟧 0.92	🟩 -0.56	🟩 0.60	-0.45	0.47	🟧 0.86	🟩 -0.51	-0.43	🟩 -0.51	-0.31	-0.28	-0.24	-0.35	-0.31	-0.26	-0.35	-0.25	🟩 -0.58	🟩 -0.53	0.42	
Zn	0.33	0.04	0.41	-0.28	0.42	-0.14	0.27	0.31	-0.21	-0.14	-0.22	-0.11	-0.21	0.02	0.08	-0.19	0.06	-0.17	-0.19	-0.32	-0.22		
Y	🟩 -0.56	-0.27	🟩 -0.57	-0.22	-0.44	🟧 0.93	-0.35	-0.48	🟧 0.97	🟧 0.85	🟧 0.95	🟩 0.71	🟩 0.58	0.10	-0.13	-0.19	🟩 0.71	🟧 0.85	0.13	-0.15			
V	🟩 -0.62	🟩 0.62	🟩 -0.56	0.93	🟩 -0.50	-0.29	-0.39	-0.47	-0.17	-0.16	-0.14	-0.16	-0.20	0.15	🟩 0.58	🟩 0.69	-0.43	-0.30	0.43				
U	-0.48	0.37	-0.35	0.43	-0.36	0.07	-0.38	-0.32	0.14	0.12	0.15	0.05	0.11	0.07	0.27	0.37	-0.05	0.05					
Th	-0.39	-0.36	-0.41	-0.33	-0.32	🟧 0.85	-0.22	-0.36	🟧 0.87	🟩 0.70	🟧 0.84	🟩 0.63	🟩 0.67	0.07	-0.30	-0.34	🟩 0.69						
Sr	-0.23	-0.14	-0.06	-0.48	-0.18	🟩 0.76	0.14	-0.20	🟩 0.75	🟩 0.67	🟩 0.73	🟩 0.54	0.49	0.07	-0.21	-0.43							
Sn	-0.37	0.46	-0.37	🟩 0.74	-0.41	-0.34	-0.32	-0.31	-0.22	-0.25	-0.21	-0.29	-0.20	-0.02	0.33								
Ni	-0.40	0.47	-0.29	🟩 0.59	-0.16	-0.21	-0.20	-0.30	-0.14	-0.15	-0.10	0.03	-0.21	0.32									
Cu	-0.24	-0.02	-0.25	0.19	-0.15	0.10	-0.12	-0.21	0.10	0.11	0.08	0.13	0.15										
Au	-0.32	-0.20	-0.30	-0.19	-0.37	🟩 0.60	-0.23	-0.28	🟩 0.62	0.46	🟩 0.59	0.27											
As	-0.40	-0.28	-0.35	-0.23	-0.20	🟩 0.71	-0.28	-0.27	🟩 0.73	🟩 0.61	🟩 0.72												
F	🟩 -0.59	-0.21	🟩 -0.53	-0.22	-0.48	🟧 0.95	-0.34	-0.45	🟧 0.99	🟧 0.89													
Cl	🟩 -0.51	-0.20	-0.46	-0.26	-0.38	🟧 0.89	-0.26	-0.37	🟧 0.88														
P	🟩 -0.58	-0.24	🟩 -0.53	-0.24	-0.47	🟧 0.96	-0.34	-0.45															
K	🟩 0.75	-0.27	🟧 0.83	-0.47	0.44	-0.42	0.23																
Na	🟩 0.57	-0.01	🟩 0.62	-0.40	0.47	-0.27																	
Ca	🟩 -0.50	-0.28	-0.48	-0.36	-0.34																		
Mg	🟩 0.77	-0.19	🟩 -0.56	🟩 -0.53																			
Fe	🟩 -0.61	🟩 0.58	🟩 -0.54																				
Al	🟧 0.84	-0.18																					
Ti	-0.35																						

REE = La+Ce+Pr+Nd+Sm+Eu+Tb+Yb+Lu

🟧 High correlation

🟩 Medium correlation

⬜ Low or no correlation

Group 1: Apatite ore (P, Ca, F, Cl, REE, Th, Y, Sr, As)

Group 2: Magnetite ore (Fe, V, Ti, Ni)

Group 3: Volcanic rocks (Si, Al, Mg, K, Na, Zr)

5-2 Magnetite geochemistry

Magnetite and/or hematite display a range of composition in terms of trace element content that can be related to the mineral deposit type from which they formed (see e.g., Loberg and Horndahl, 1983; Beaudoin et al., 2007). Discriminant diagrams such as V versus Ti or (Ni+Ca)/(Cr+Mn) versus Ti/V are useful tools to distinguish iron oxides formed in IOCG deposits from those in Kiruna-type, BIF, and orthomagmatic or titaniferous iron ore deposits (Beaudoin et al., 2007).

Selected magnetite samples from three active magnetite-apatite ore deposits (Chador-Malu, Choghart, Esfordi) were analyzed for some trace elements by electron microprobe, using the CAMECA SX100 at the Institute of Mineralogy and Mineral Resources, Technical University of Clausthal. The magnetite crystals, whether fresh or martitized, are free of exsolution phases. They have low Ti (<120 ppm up to 3500 ppm), low to moderate V (270-5000 ppm) and very low Cr (<50 ppm up to 220 ppm), Ni (<120 ppm up to 360 ppm) and Mn content (<80 ppm up to 900 ppm). The discrimination diagrams exclude a relationship to magmatic titanomagnetite and BIF deposits (Fig. 5-7).

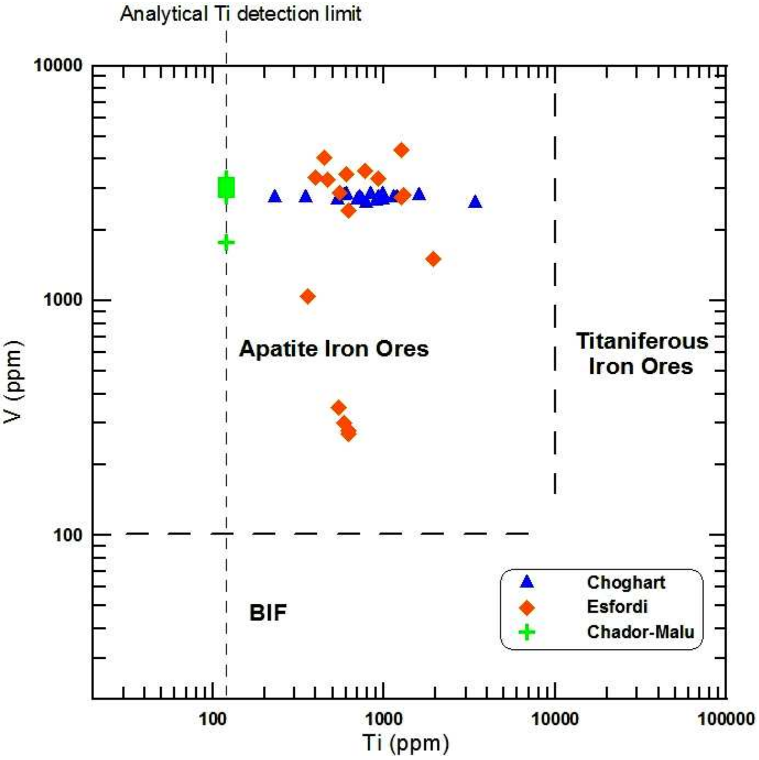

Fig. 5-7 Magnetite composition in the Ti versus V discriminant diagram. Reference fields according to Loberg & Horndahl (1983). Note that the Chador-Malu samples consist of 24 analytical data (overlapped data) with Ti content below the detection limit of 120 ppm Ti.

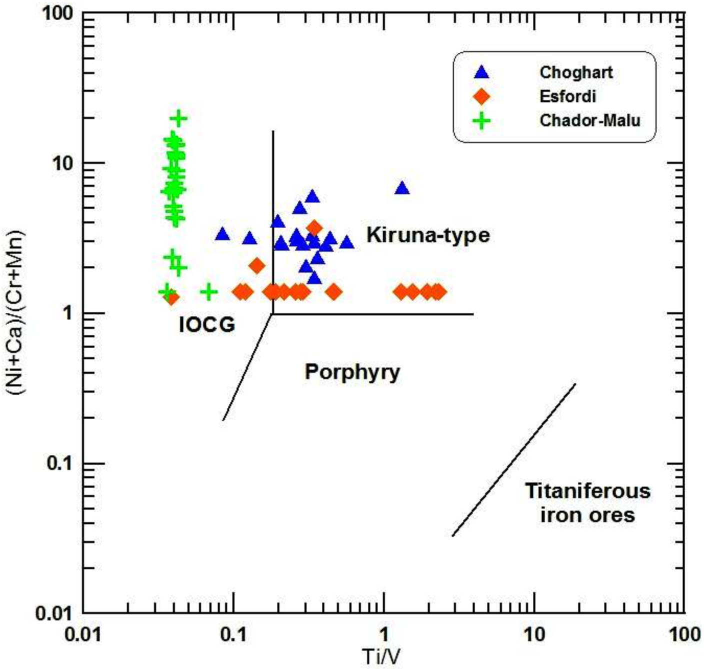

Fig. 5-8 Magnetite composition in the Ti/V versus (Ni+Ca)/(Cr+Mn) discriminant diagram. Reference fields according to Beaudoin et al. (2007). The samples from Chador-Malu are vertically aligned due to the fact that most samples have Ti<120 ppm, but are plotted as equal to this analytical detection limit of the electron microprobe.

The (Ni+Ca)/(Cr+Ni) versus Ti/V diagram is used to distinguish IOCG and Kiruna sub-type deposits (Fig. 5-8). Most of the magnetite samples plot in the "Kiruna-type" field, especially the samples from the Choghart and Esfordi deposits. However, all samples from Chador-Malu fall in the "IOCG" field and show that the iron ore deposits of the Bafq district display both characteristics, and that a distinction between IOCG and Kiruna-type is not warranted.

5-3 Apatite geochemistry

Fig. 5-9 shows the probability plot of P_2O_5 distribution in different rock suites on the basis of 890 analytical samples from more than 70 exploration boreholes of the Esfordi deposit. The graph shows that the phosphorus content of these rocks varies widely from less than 0.65 wt% P_2O_5 in the volcanic rocks to more than 25 wt% P_2O_5 (up to 35 wt%) in the apatite veins. There are at least three different geochemical populations of phosphorus. The populations are separated at inflection points and plotted individually in the second diagram. The median (m) and variation of P_2O_5 at ±1s around this geometric mean are illustrated for each population separately.

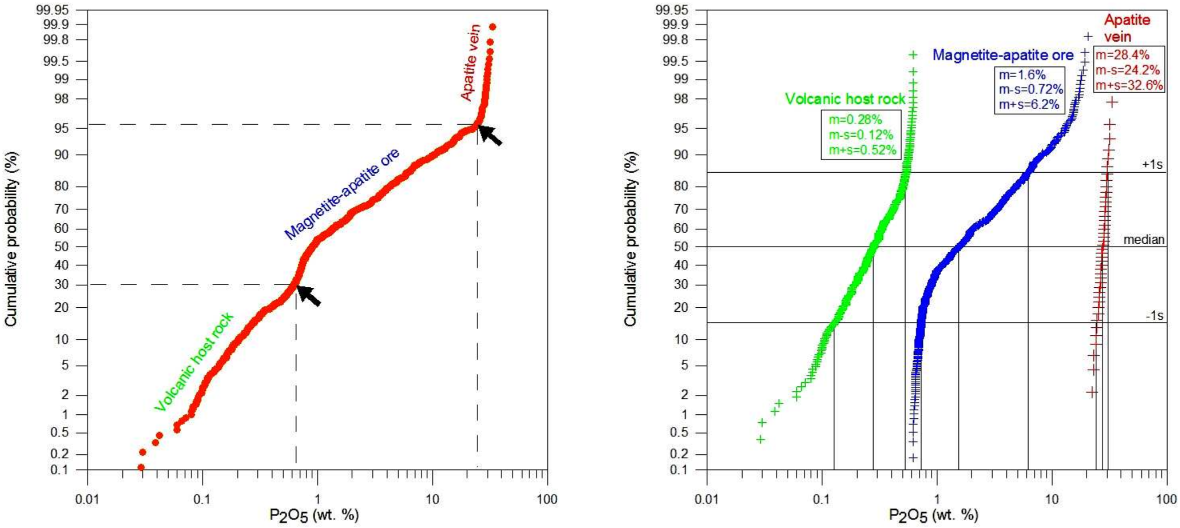

Fig. 5-9 Probability plot of P_2O_5 distribution in different rock suites of the Esfordi deposit (890 analytical data)

Table 5-2 shows 20 representative analyses of apatite from the Esfordi deposit. The apatite is enriched in LREE, Y, as well as Na and Si. Fig. 5-10 shows a ternary diagram of the Esfordi apatite composition in terms of F-OH-Cl content. The diagram reveals that the apatite at Esfordi is mostly hydroxyl-fluorapatite with a F/OH ratio of >2; the chlorine content is low. The same pattern applies to the other magnetite-apatite deposits of the Bafq district (not shown here, see, e.g., the analysis of apatite from Choghart in Moore and Modabberi, 2003).

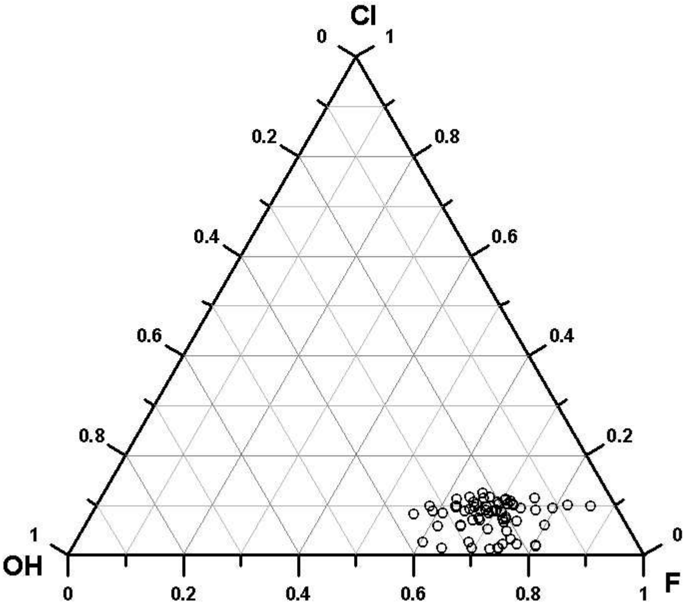

Fig. 5-10 Ternary plot of the apatite composition from the Esfordi mine in terms of F-OH-Cl atomic proportions (n=60).

Table 5-2 Representative electron-microprobe analyses of apatite from the Esfordi deposit (analytical data in wt%)

	#1	#2	#3	#4	#5	#6	#7	#8	#9	#10	#11	#12	#13	#14	#15	#16	#17	#18	#19	#20
P_2O_5	41.49	41.23	41.57	41.65	40.24	40.92	41.00	40.80	40.80	41.04	41.05	41.45	41.15	40.77	40.97	42.09	41.52	42.17	42.20	40.54
SiO_2	0.13	0.24	0.17	0.16	0.29	0.24	0.24	0.23	0.26	0.23	0.27	0.21	0.26	0.24	0.21	0.12	0.11	0.05	0.13	0.19
Y_2O_3	0.14	0.22	0.20	0.13	0.25	0.24	0.17	0.22	0.15	0.16	0.16	0.18	0.15	0.18	0.25	0.20	0.16	0.06	0.11	0.23
Nb_2O_3	0.02	0.00	0.02	0.00	0.03	0.00	0.02	0.00	0.00	0.04	0.00	0.00	0.02	0.05	0.01	0.02	0.06	0.04	0.00	0.02
La_2O_3	0.25	0.40	0.24	0.31	0.45	0.38	0.31	0.37	0.35	0.31	0.38	0.39	0.47	0.43	0.36	0.16	0.09	0.07	0.14	0.31
Ce_2O_3	0.58	0.95	0.55	0.70	1.01	0.89	0.77	0.96	0.83	0.75	0.92	0.93	1.03	1.01	0.90	0.40	0.24	0.14	0.31	0.77
MgO	0.04	0.01	0.02	0.08	0.03	0.06	0.04	0.07	0.09	0.13	0.10	0.06	0.08	0.05	0.07	0.02	0.03	0.02	0.03	0.03
CaO	55.22	53.97	55.07	54.65	54.26	54.82	54.76	54.64	54.71	54.76	54.29	54.50	54.22	54.59	54.51	55.38	55.90	56.30	56.18	54.87
MnO	0.01	0.02	0.02	0.01	0.00	0.01	0.02	0.01	0.01	0.01	0.02	0.01	0.01	0.02	0.01	0.01	0.01	0.01	0.01	0.01
SrO	0.05	0.04	0.04	0.03	0.03	0.03	0.03	0.02	0.01	0.03	0.01	0.02	0.03	0.03	0.03	0.05	0.05	0.02	0.03	0.06
Na_2O	0.24	0.39	0.28	0.27	0.41	0.31	0.40	0.33	0.30	0.25	0.30	0.30	0.41	0.37	0.33	0.16	0.09	0.08	0.12	0.30
F	2.51	2.68	2.70	2.57	2.66	2.25	2.51	2.68	2.61	3.21	2.59	2.58	2.18	2.06	3.04	2.26	2.79	2.79	2.58	2.72
Cl	0.62	0.53	0.46	0.60	0.50	0.60	0.52	0.70	0.78	0.68	0.62	0.63	0.62	0.58	0.70	0.19	0.16	0.11	0.19	0.33
Sum	101.30	100.66	101.32	101.16	100.14	100.75	100.78	101.03	100.89	101.59	100.72	101.25	100.62	100.37	101.39	101.05	101.20	101.87	102.02	100.38
- O = F+Cl	1.20	1.25	1.24	1.21	1.23	1.08	1.17	1.29	1.27	1.50	1.23	1.23	1.06	1.00	1.44	0.99	1.21	1.20	1.13	1.22
Total	100.10	99.41	100.08	99.95	98.91	99.67	99.61	99.74	99.62	100.09	99.49	100.03	99.56	99.37	99.95	100.06	99.99	100.66	100.89	99.16
APFU (Atom Per Formula Unit) *																				
P	2.991	2.994	2.992	3.003	2.953	2.979	2.977	2.963	2.964	2.955	2.982	2.993	2.996	2.983	2.961	3.026	2.986	3.004	3.006	2.960
Si	0.011	0.020	0.015	0.014	0.025	0.021	0.021	0.020	0.023	0.019	0.024	0.018	0.022	0.020	0.018	0.011	0.009	0.004	0.011	0.016
Y	0.006	0.010	0.009	0.006	0.011	0.011	0.008	0.010	0.007	0.007	0.007	0.008	0.007	0.008	0.011	0.009	0.007	0.003	0.005	0.011
Nb	0.001	0.000	0.001	0.000	0.001	0.000	0.001	0.000	0.000	0.002	0.000	0.000	0.001	0.002	0.000	0.001	0.003	0.002	0.000	0.001
La	0.008	0.013	0.008	0.010	0.014	0.012	0.010	0.012	0.011	0.010	0.012	0.012	0.015	0.014	0.011	0.005	0.003	0.002	0.004	0.010
Ce	0.018	0.030	0.017	0.022	0.032	0.028	0.024	0.030	0.026	0.023	0.029	0.029	0.032	0.032	0.028	0.012	0.007	0.004	0.010	0.024
Mg	0.005	0.001	0.002	0.011	0.003	0.007	0.005	0.008	0.011	0.017	0.013	0.007	0.010	0.006	0.009	0.003	0.004	0.003	0.004	0.004
Ca	5.039	4.959	5.016	4.986	5.039	5.051	5.033	5.022	5.031	4.991	4.990	4.980	4.996	5.055	4.986	5.038	5.088	5.075	5.064	5.071
Mn	0.001	0.001	0.001	0.001	0.000	0.001	0.001	0.001	0.000	0.001	0.001	0.001	0.001	0.001	0.001	0.001	0.001	0.001	0.000	0.000
Sr	0.002	0.002	0.002	0.002	0.001	0.002	0.002	0.001	0.000	0.002	0.001	0.001	0.001	0.001	0.002	0.002	0.002	0.001	0.001	0.003
Na	0.040	0.064	0.045	0.044	0.069	0.052	0.066	0.055	0.049	0.041	0.050	0.050	0.069	0.061	0.054	0.026	0.015	0.013	0.019	0.051
F	0.677	0.726	0.727	0.691	0.729	0.612	0.680	0.728	0.708	0.862	0.703	0.695	0.592	0.563	0.821	0.606	0.748	0.743	0.688	0.743
Cl	0.090	0.077	0.067	0.086	0.074	0.087	0.075	0.102	0.114	0.099	0.090	0.091	0.090	0.084	0.101	0.028	0.023	0.015	0.027	0.049
OH **	0.234	0.197	0.207	0.223	0.197	0.301	0.245	0.170	0.179	0.039	0.207	0.215	0.318	0.352	0.078	0.366	0.229	0.242	0.286	0.208

* calculation on the basis of 13 anions

** OH was calculated assuming the (F,Cl,OH) site is filled

As pointed out by Zhu and Sverjensky (1991), the formation of F-rich apatite (e.g., with a composition of $X_F > 0.9$) requires only low fluoride activity in the fluid phase ($a_{HF}/a_{H2O} < 10^{-4}$), whereas fluids with the same activity for Cl ($a_{HCl}/a_{H2O} < 10^{-4}$) are in equilibrium with apatite with $X_{Cl} < 0.1$ (where X_F and X_{Cl} are the mole fraction of fluorapatite and chlorapatite, respectively). This explains why most apatite in hydrothermal environments is F-rich, even though the activity of Cl in the fluid strongly exceeds that of F. The composition of some apatites which are associated with carbonatites similarly falls along the F-OH join (Piccoli & Candela, 2002). But most, if not all, carbonatitic apatite is dominated by the F-rich end-member (i.e. pure fluor-apatite). In some carbonatitic apatites F appears to overfill the site, especially when significant CO_3^{2-} is present (Piccoli & Candela, 2002). Apatite mineralization, especially in the form of phoscorite (magnetite + apatite + pyroxene), e.g., Phalaborwa, South Africa, is characteristic of carbonatites (see e.g. Hogarth, 1989). However, carbonatitic apatite has very high Sr content (commonly more than 2500 ppm) and relatively low Y (commonly less than 400 ppm) (Belousova et al., 2002). The apatite data from the Bafq district (Table 5-2) show their similarity to other Kiruna-type apatite occurrences and would seem to exclude a carbonatitic affinity (Fig. 5-11).

Also, the chondrite-normalized REE pattern of apatite associated with iron ores in the Bafq district shows a significant negative Eu anomaly (Fig. 5-13), whereas carbonatites generally have no or a weakly positive Eu anomaly. The composition of the apatite from Esfordi falls mostly in the field of mafic rocks and Kiruna-type iron ores. It appears likely, therefore, that the gabbro-diorite intrusions in the Bafq district have an important role in the genesis of the magnetite-apatite deposits. On the other hand, on the basis of the Mn-Sr composition, these apatites display a good affinity with sedimentary phosphorites and are far from apatites of igneous rocks (Fig. 5-12). These two different diagrams show that the Bafq apatites have possibly a bimodal origin, with an intermediate affinity between sedimentary phosphorites and igneous rocks, and may originated from remobilization of Early Cambrian phosphorites due to hydrothermal circulation powered by igneous rocks.

In Fig. 5-13, the REE patterns of the magnetite-apatite ores from the Bafq district as well as a pattern of Early Cambrian phosphorite (Soltanieh Formation) have been illustrated for comparison. The diagram shows that the magnetite-apatite ores are strongly enriched in REE with high LREE/HREE fractionation and pronounced negative Eu anomaly. The pure apatite ore (apatite vein) has much elevated REE content and inversely pure magnetite ore is depleted in REE. The similarity in the LREE portion of the magnetite-apatite and the phosphorite patterns and their similar negative Eu anomaly is obvious but their genetical relationship needs to be proved by further studies such as isotopic investigation (see next chapter).

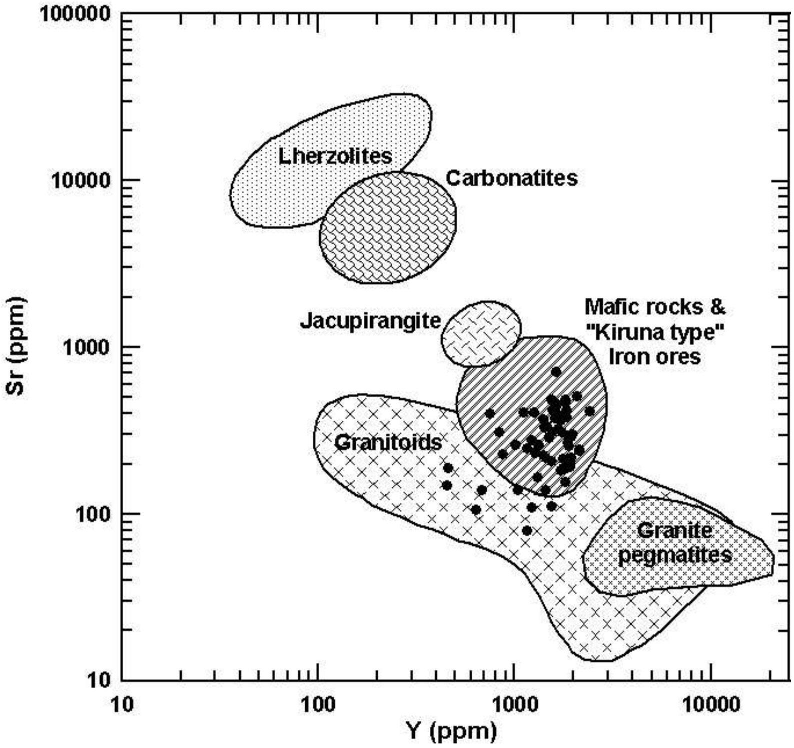

Fig. 5-11 Y-Sr composition of apatite from the Esfordi deposit (solid dots), compared to reference fields according to Belousova et al. (2002).

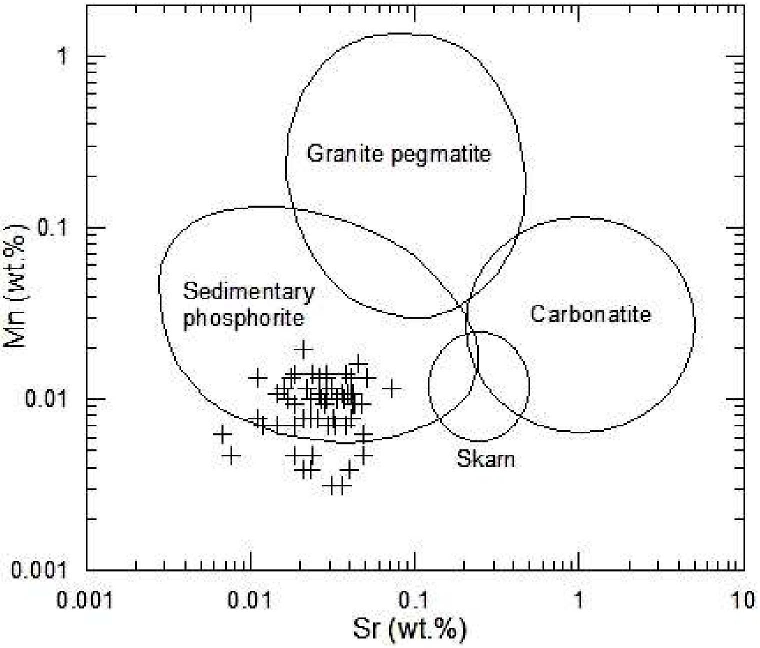

Fig. 5-12 Sr-Mn composition of apatite from the Esfordi deposit, compared to reference fields according to Hoghart (1989).

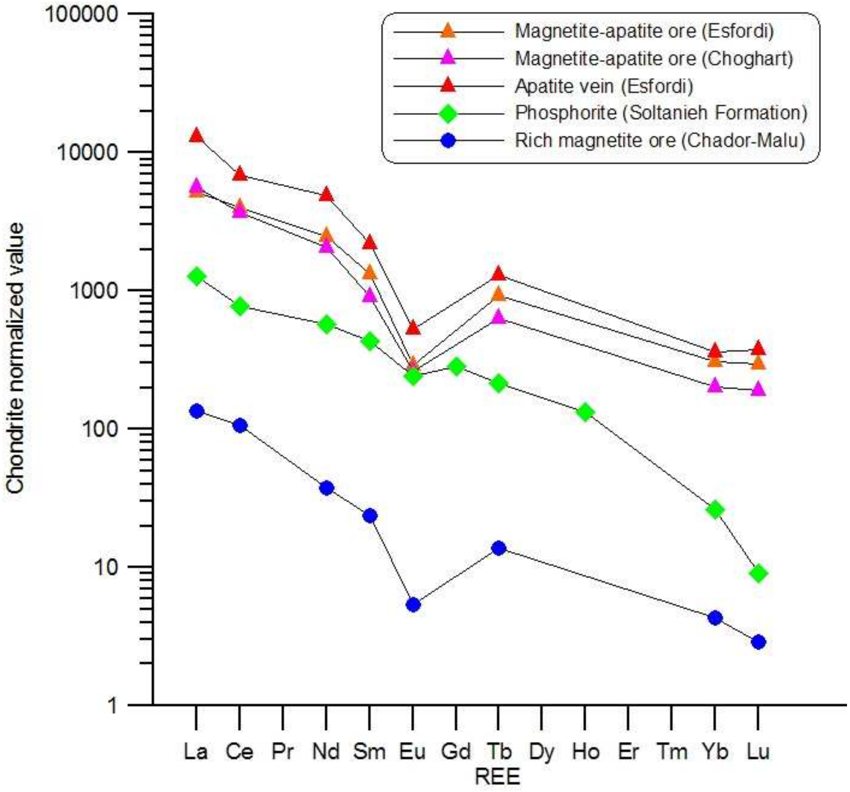

Fig. 5-13 Spider diagram representing REE patterns of magnetite-apatite ores compared to Early Cambrian phosphorite from the Soltanieh Formation (Alborz Mountains). Chondrite value from Anders & Grevesse, 1989. Data of Soltanieh phosphorite from Sergei Felitsyn by personal communication.

5-4 Apatite-monazite relationship

Under high-contrast BSE imaging, some apatite crystals show a heterogeneous pattern with two different domains (dark and bright phases) (Fig. 5-14). The difference between both phases is mainly due to different concentration of REE and some trace elements, such as Si, Na, Cl, and F (Table 5-3, Fig. 5-15). REE have high atomic weight and produce more back-scattered electrons, so that apatite with elevated REE concentration shows a brighter image, while dark domains are depleted in REE. The dark (REE-poor) domains host abundant monazite inclusions suggesting a process of REE redistribution with depletion in the host apatite and concomitant nucleation of monazite crystals (Fig. 5-14). The same overprint process also leads to nucleation of other rare REE minerals, such as allanite, xenotime, and parisite, and crystallization of major alteration components such as actinolite, talc, and chlorite along the apatite grain boundaries (Fig. 5-14).

Similar dark, REE-depleted domains within apatite and accompanied by monazite inclusions, have been observed by Harlov et al. (2002) in the Kirunavaara deposit, northern Sweden. A number of workers have also reported the presence of small grains of monazite and/or xenotime in metamorphic rocks both as inclusions in apatite as well as along apatite grain boundaries (e.g. Pan et al., 1993; Förster & Harlov, 1999; Ziemann et al., 2005). Harlov et al. (2002) have pointed out that nucleation of monazite in apatite involves the following general reaction which has been modified from Pan et al. (1993):

apatite$_{(1)}$ (bright phase) + (Ca^{2+} and P^{5+}) in fluid phase =

apatite$_{(2)}$ (dark phase) + monazite + (Si^{4+} and Na^{+}) in fluid phase

Where apatite$_{(1)}$ is primary apatite enriched in REE, Na, Si, and apatite$_{(2)}$ is the recrystallized phase depleted in REE, Na, and Si. The formation of monazite by metasomatic alteration of fluor-apatite was demonstrated experimentally in the presence of KCl brines and with variable CO_2/H_2O mixtures over a wide range of temperatures and pressures (300-900°C and 0.5-1 Gpa) (Harlov & Förster, 2003). Fluid chemistry and REE budget of the host fluorapatite are the principal parameters controlling the formation of monazite during hydrothermal fluorapatite overprint (Ziemann et al., 2005). The Bafq district shows evidence for widespread potassium metasomatism (presence of hydrothermal K-feldspar and sericitic alteration), which points to the role of K-rich solutions in hydrothermal alteration and, specifically, REE leaching from apatite and concomitant monazite nucleation.

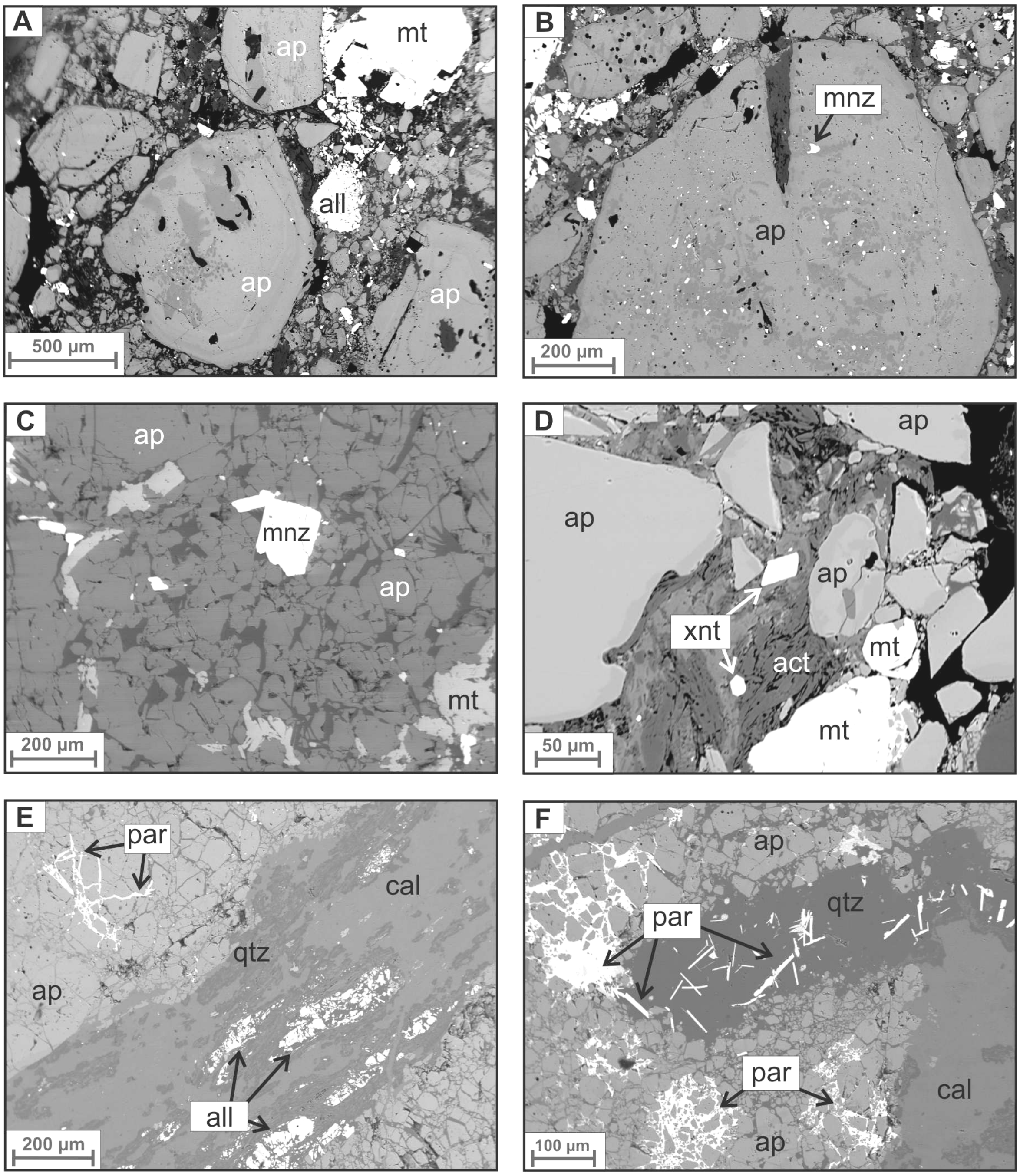

Fig. 5-14 Backscattered electron (BSE) images of apatite ore from Esfordi.

A- Apatite (ap) crystals with two different domains (dark and bright phases), associated with magnetite (mt) and a fine-grained aggregate of allanite (all) in fine-grained apatite, calcite and quartz matrix.
The voids (black) inside apatite mark the path of infiltrating fluids during apatite-fluid interaction (apatite metasomatism).

B- Euhedral crystal of apatite (ap) with monazite (mnz) inclusions in the dark apatite phase. Note numerous small monazite (white) inclusions inside apatite.

C- Individual relatively big crystal of monazite (mnz) in apatite aggregate.

D- Brecciated apatite (ap) and magnetite (mt) in a fine-grained matrix of actinolite (act), calcite, and quartz. Two small individual crystals of xenotime (xnt) are visible in the center.

E- Veinlet of calcite (cal) and quartz (qtz) with interstitial allanite (all) in fragmented apatite (ap) phenocrysts. Thin spider-like parisite (par) is visible as fracture filling in apatite.

F- Parisite (par) as fracture filling in brecciated apatite (ap) and as needles in quartz (qtz) veinlets.

Table 5-3 Analytical results of two different apatite phases by EPMA

Element	Apatite Crystal				Detection Limit
	Bright BSE phase (n=27)		Dark BSE phase (n=17)		
	Mean (wt%)	Std. Dev. (wt%)	Mean (wt%)	Std. Dev. (wt%)	(wt%)
Ca	38.86	0.49	40.42	0.34	0.06
K	bdl	-	bdl	-	0.04
Cl	0.71	0.06	0.33	0.18	0.04
P	18.02	0.17	18.49	0.20	0.08
F	2.51	0.19	2.73	0.23	0.14
Na	0.30	0.08	0.05	0.03	0.02
Mg	0.04	0.01	bdl	-	0.03
Si	0.12	0.01	0.06	0.04	0.06
Sr	0.03	0.01	0.02	0.01	0.02
Nb	bdl	-	0.03	0.02	0.02
Y	0.17	0.03	0.11	0.06	0.06
La	0.39	0.10	0.03	0.03	0.03
Mn	0.01	0.00	bdl	-	0.01
Ce	0.89	0.16	0.12	0.09	0.05
O*	38.12	0.30	38.95	0.24	-
Total	100.18	0.55	101.35	0.60	-

* by calculation   bdl = below detection limit

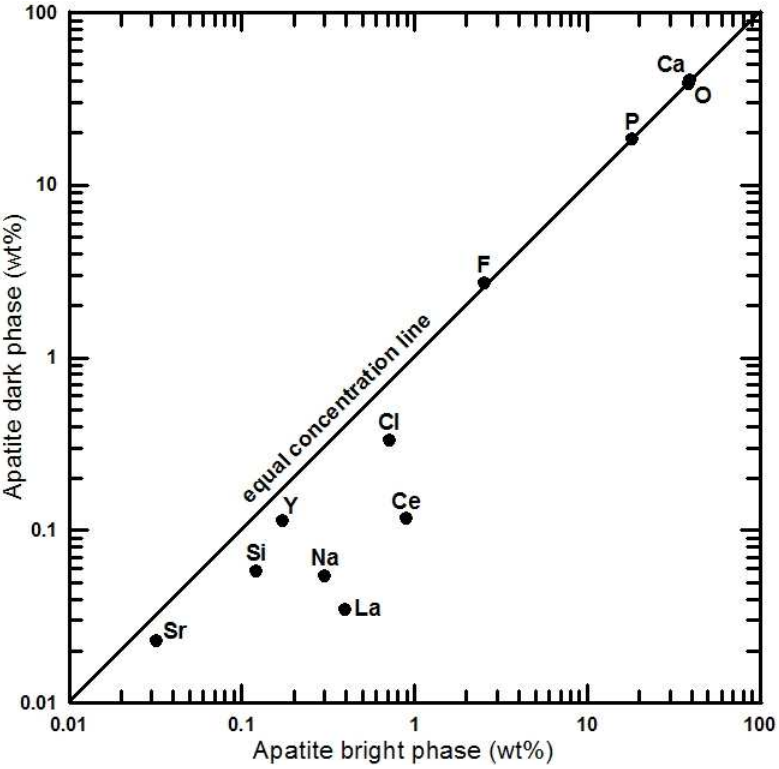

Fig. 5-15 Comparison between element concentration in bright and dark BSE domains of apatite crystals. The REE-depleted dark apatite phase is interpreted as resulting from hydrothermal overprint ("apatite metasomatism").

Monazite also occurs as relatively large (up to 200 µm), isolated grains along apatite grain boundaries, intergrown with magnetite and silicate minerals (Fig. 5-14). Most of these monazite crystals are homogeneous and do not show significant zoning. Table 5-4 reports some representative electron-microprobe analyses of monazite as inclusions in apatite and as individual monazite crystals, all of which have very low Th and no detectable U and Pb.

Hydrothermal and igneous monazite can be distinguished by their ThO_2 content, which is generally <1wt% for hydrothermal monazite and 3->5 wt% for igneous monazite (Schandl and Gorton, 2004). Also, monazites formed at high-grade metamorphic conditions show a wide range of ThO_2 concentrations and are strongly zoned with respect to Th. The generally low Th-content in the Bafq monazite (Table 5-4) is consistent with its hydrothermal origin. These low-Th monazites are relatively homogenous and do not show strong zoning as typical of metamorphic monazites. However, in some grains and under high–contrast BSE imaging, a clear zoning is distinguishable which can be considered as reflecting different stages in low-Th monazite crystallization. Some samples from the Choghart deposit have some individual (usually euhedral) monazite crystals with an irregularly shaped inner core with relatively high Th content. This inner core consists of a distinct monazite crystal with high Th and relatively high Si content (Fig. 5-16). We believe that this inner core is a high-temperature micro-crystal of monazite, which has undergone low-temperature hydrothermal overgrowth as illustrated in Fig. 5-16. In other rare cases, these inner cores possess elevated Th (>40 wt%) and Si (>4 wt%) as well as P and REE. These micro-crystals are a solid solution between monazite and huttonite and can be considered as huttonitic monazite. Huttonite ($ThSiO_4$) is a monoclinic mineral (isostructural with monazite) dimorphous with thorite. The replacement of huttonite by monazite and vice versa, can be understood by the following coupled substitution equation (Poitrasson et al., 2000):

$$Th^{4+} + Si^{4+} \leftrightarrow REE^{3+} + P^{5+}$$

Table 5-4 Micro-analytical results of hydrothermal monazites from the Esfordi deposit (in wt%)

	Monazite inclusions within apatite									Individual monazite crystals						
	#1	#2	#3	#4	#5	#6	#7	#8	#9	#1	#2	#3	#4	#5	#6	#7
P_2O_5	27.66	28.78	28.84	28.88	28.69	28.87	26.68	28.72	27.03	28.39	28.31	27.18	27.84	27.83	28.64	29.20
SiO_2	0.77	0.32	0.30	0.30	0.34	0.45	0.60	0.37	1.07	0.41	0.38	0.47	0.42	0.42	0.36	0.44
ThO_2	0.11	0.43	< 0.03	< 0.03	< 0.03	0.36	< 0.03	0.07	0.07	0.42	0.44	0.29	0.40	0.18	0.53	0.37
UO_2	< 0.02	< 0.02	< 0.02	< 0.02	< 0.02	< 0.02	< 0.02	< 0.02	< 0.02	< 0.02	< 0.02	< 0.02	< 0.02	< 0.02	< 0.02	< 0.02
Y_2O_3	0.66	0.80	0.66	0.71	0.72	0.59	0.37	0.65	0.69	0.56	0.25	0.55	0.48	0.34	0.26	0.42
La_2O_3	16.67	11.69	14.37	14.31	14.46	17.11	18.47	16.70	17.16	16.62	18.35	17.68	16.33	17.98	17.48	19.00
Ce_2O_3	32.90	28.71	33.23	33.74	34.20	33.60	34.14	33.73	34.43	35.06	35.54	34.68	34.94	35.52	35.31	36.01
Pr_2O_3	8.26	7.31	7.90	7.95	7.92	8.15	8.17	8.52	8.18	7.85	8.09	7.15	7.42	7.66	8.22	8.17
Nd_2O_3	7.73	14.20	9.18	9.48	9.47	7.93	6.00	8.84	7.81	8.21	6.99	6.47	8.54	6.67	7.65	6.46
Sm_2O_3	1.24	2.89	1.39	1.43	1.43	1.34	0.89	1.42	1.31	1.10	0.91	0.97	1.24	0.91	1.02	0.84
Gd_2O_3	0.54	1.53	0.65	0.62	0.64	0.59	0.35	0.69	0.65	0.52	0.30	0.40	0.54	0.37	0.37	0.34
CaO	1.57	0.55	1.01	0.89	0.91	1.09	1.75	1.19	1.99	0.23	0.16	1.67	0.18	1.20	0.17	0.25
PbO	< 0.025	< 0.025	< 0.025	< 0.025	< 0.025	< 0.025	< 0.025	< 0.025	< 0.025	< 0.025	< 0.025	< 0.025	< 0.025	< 0.025	< 0.025	< 0.025
Sum	98.11	97.21	97.53	98.31	98.78	100.08	97.42	100.90	100.39	99.37	99.72	97.51	98.33	99.08	100.01	101.50

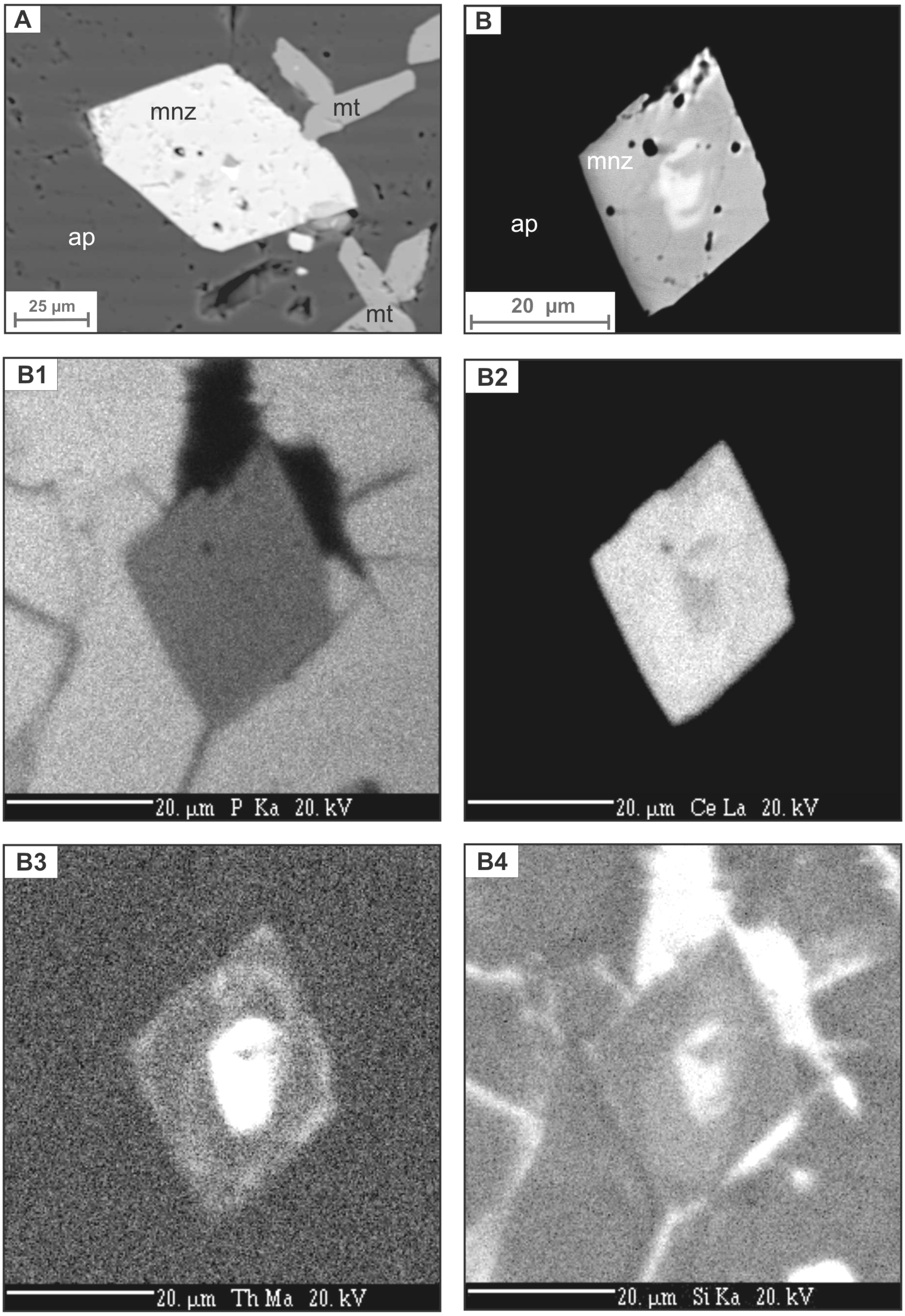

Fig. 5-16 BSE images and X-ray elemental maps of monazite crystals from the Choghart deposit.

A- BSE image of euhedral monazite (mnz) crystal (on apatite surface) overgrown on a high-Th monazite microcrystal in the center (unlabeled small bright spot in the core).

B- BSE image of euhedral monazite (mnz) crystal overgrown on a huttonitic monazite inner core. The outside black phase is apatite (ap) associated with silicates.

B1 to B4- X-ray elemental maps of the grain shown in B (B1: $P_{K\alpha}$, B2: $Ce_{L\alpha}$, B3: $Th_{M\alpha}$, B4: $Si_{K\alpha}$).

Chapter 6: Monazite geochronology and isotopic studies

6-1 Monazite geochronology

Chemical dating of monazite using the electron microprobe is a non-isotopic dating method which has become increasingly popular over the past decade. The recognition by Parrish (1990) that monazite generally contains significant amounts of Th and U and typically little initial Pb, encouraged chemical in-situ dating of monazite. By assuming that all of the Pb is radiogenic, a geologic date can be calculated from the total abundances of Th, U, and Pb (e.g., Suzuki & Adachi, 1991; Montel el al., 1996; Cocherie & Albarède, 2001). The main limitation of the method is its rather poor precision due to low Pb content and correspondingly unfavorable counting statistics (Cocherie & Albarède, 2001). However, much work has been done recently to increase the accuracy and precision of this method, e.g., Williams et al. (2006), Jercinovic & Williams (2005), Pyle et al. (2005).

We first attempted to date monazite inclusions within apatite as well as individual big monazite crystals. However, their low Th content and undetectable Pb and U (Table 5-4) did not allow dating. In the second step, we tried to analyze the inner core of monazites with higher Th content from the Choghart deposit. Although these cores are rare, and their analysis is hampered by very small size (1-5 µm), we found some relatively big inner core monazites (see, e.g., Fig. 5-13), with high Th and detectable U and Pb, suitable for electron microprobe analysis. Table 6-1 shows the results of 27 analytical points on monazite cores. Sample points with very high Th and Si (huttonite end member) are not reported in the table, because thorite (and similarly huttonite) tends to have radiogenic Pb loss (Cocherie & Legendre, 2007). The results presented in Table 6-1 show that most of the radiogenic Pb in the monazites analyzed is thorogenic and that the Pb contribution from U is insignificant ($ThO_2/UO_2 > 46$). Therefore, we used the approach of Suzuki & Adachi (1991), i.e. $ThO_2^* = f(PbO)$, instead of the $Th/Pb = f(U/Pb)$ method (Cocherie & Albarède, 2001) for age calculation. The former method permits initial Pb correction and gives reliable age information especially for high Th/U in monazite or high U/Th in the case of zircon or xenotime chronology. We calculated the age of each analytical point according to Suzuki & Adachi (1991) by using a PC supported iteration method (Table 6-1). After the calculation of the age for each individual point, the UO_2 content, however low, was converted into the equivalent ThO_2, and added to the measured ThO_2 to give the amount of apparent ThO_2, i.e., ThO_2^*. The calculated data (PbO versus ThO_2^*) were plotted on a diagram using the Isoplot/Ex (v. 2.49) program of Ludwig (2001). The best regression line (isochron) ($PbO = m .ThO_2^* + b$), shows a slope of $m = 0.0219$ and an intercept of $b = 0.0068$ (Fig. 6-1). The slope of the regression line and the calculated precision from the isochron diagram at the 95% confidence level, define an age of 515 ± 21 Ma.

Table 6-1 Electron microprobe data of high-Th monazite cores and calculated ages (samples from Choghart deposit)

No.	ThO_2 (wt%)	UO_2 (wt%)	PbO (wt%)	ThO_2/UO_2	t (Ma)	ThO_2^* (wt%)	PbO (wt%) - initial	t (Ma) (corrected)
1	5.619	0.073	0.122	77.4	489	5.859	0.115	462
2	3.839	0.052	0.102	73.6	599	4.013	0.095	559
3	3.398	0.049	0.103	69.7	680	3.561	0.097	636
4	19.031	0.153	0.470	124.3	565	19.540	0.463	556
5	9.699	0.093	0.235	104.0	551	10.009	0.228	535
6	2.017	0.037	0.061	53.9	672	2.143	0.055	598
7	3.047	0.052	0.082	58.4	597	3.221	0.075	547
8	3.336	0.035	0.072	94.9	492	3.452	0.065	446
9	2.949	0.037	0.059	78.8	454	3.073	0.052	402
10	2.079	0.029	0.061	70.5	661	2.178	0.055	588
11	7.412	0.094	0.144	78.7	441	7.722	0.138	419
12	2.258	0.035	0.064	64.2	628	2.375	0.057	561
13	1.748	0.037	0.050	46.7	621	1.873	0.043	536
14	3.860	0.054	0.096	70.9	558	4.041	0.089	518
15	1.681	0.020	0.043	82.3	579	1.749	0.036	488
16	2.190	0.027	0.061	80.5	632	2.281	0.055	562
17	22.017	0.337	0.502	65.3	511	23.132	0.495	503
18	6.806	0.057	0.146	120.0	493	6.993	0.140	470
19	5.700	0.068	0.140	83.7	556	5.926	0.133	528
20	10.926	0.137	0.248	79.6	513	11.380	0.241	498
21	4.816	0.100	0.118	48.2	541	5.147	0.112	510
22	6.212	0.085	0.154	73.0	557	6.494	0.147	533
23	19.608	0.134	0.433	146.5	508	20.051	0.426	500
24	6.071	0.103	0.165	58.8	603	6.415	0.158	578
25	4.917	0.066	0.113	74.7	518	5.135	0.106	487
26	6.627	0.047	0.153	142.5	530	6.781	0.146	507
27	1.065	0.022	0.027	49.4	556	1.137	0.020	418
Arithmetic Mean of Age (Ma) [1]					559 ± 25			516 ± 22

[1] absolute error of age was calculated at a 95% confidence level

According to Suzuki & Adachi (1991), the intercept of the correlation line is assumed to represent the concentration of the initial PbO which here is equal to 0.0068 wt% PbO. The age calculated by the isochron method is lower than the arithmetic mean of the individual ages (559 ± 25 Ma, Table 6-1). This difference is likely due to the initial Pb content. Although this initial amount is very low and negligible compared to the detection limit of Pb, it can be used to correct the individual ages. If it is assumed that the initial PbO in each monazite crystal is constant, the age can be recalculated by subtracting the initial PbO from the total PbO. The age of each individual point is corrected as shown in Table 6-1, and the arithmetic mean of individual ages becomes nearly identical to the estimated age from the isochron method. Alternatively, if it is assumed that the monazites have no initial Pb (Parrish, 1990), the isochron line can be forced to pass through the origin. Then the slope of the line slightly increases (m = 0.0225) and the age becomes 529 ± 21 Ma. Therefore, according to these two different ways of estimation, the age of the high-Th monazites is in between 515 ± 21 and 529 ± 21 Ma.

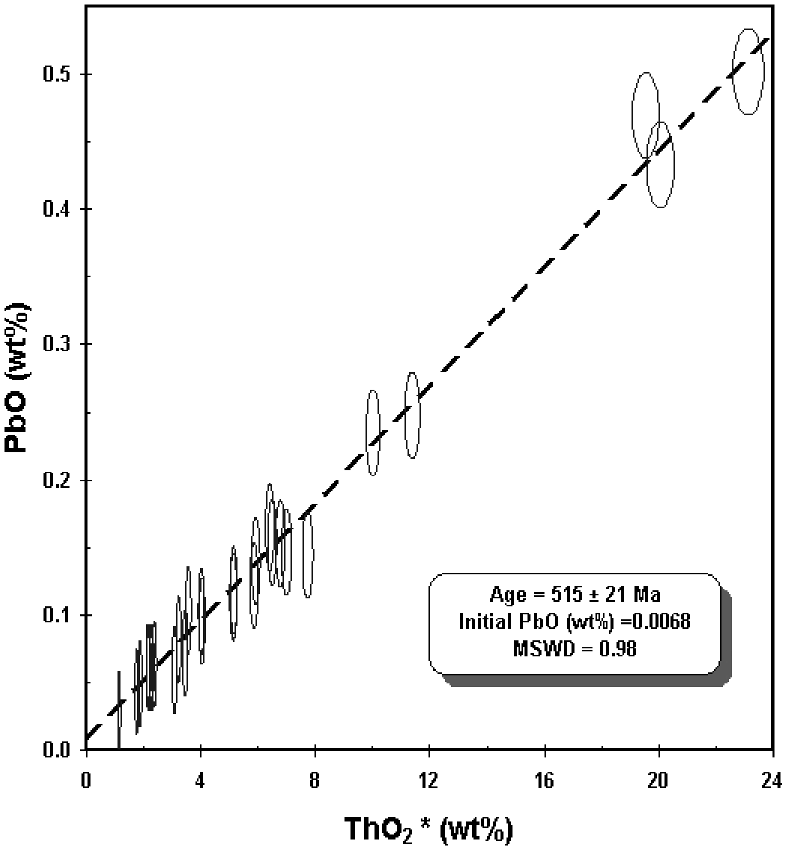

Fig. 6-1 Plot of PbO vs. ThO_2* for 27 analytical points of high-Th monazite cores.

These chemical ages are confirmed by recent U-Pb isotope/dating of apatite from the Bafq district, not yet fully published. Stosch et al. (2007) report $^{206}Pb/^{238}U$ ages on nine apatite samples which range between 527 and 539 Ma.

6-2 Sm-Nd isotope study

REE patterns are often used for petrogenetic interpretations of magnetite-apatite deposits (e.g., Avnik district, Helvaci, 1984; Kiruna district, Frietsch & Perdahl, 1995; Bafq district, Daliran, 2002), although the distinct REE enrichment is direct evidence for the hydrothermal REE mobility in such systems. Given the pervasive and large-scale hydrothermal alteration, REE patterns of magnetite-apatite mineralization and the volcanic host rocks will tend to be congruent. The presence of several monazite generations and other REE minerals overprinted on apatite (Torab and Lehmann, 2007), confirms the high mobility of REE in the hydrothermal magnetite-apatite ore systems of the Bafq district.

The source of the hydrothermal REE inventory can be traced via the Nd isotope composition of the REE-rich magnetite-apatite ores, and their country rocks. Eight bulk samples from the ore and host rocks were selected and analyzed for Sm-Nd isotopes at the Institute of Precambrian Geology and Geochronology of the Russian Academy of Sciences (analyst: Boris Belyatsky). Sample descriptions and analytical data are presented in Table 6-2. The scatter in the ^{143}Nd/^{144}Nd versus ^{147}Sm/^{144}Nd diagram (Fig. 6-2) shows that the samples are not cogenetic in terms of their Nd isotopic composition. Assuming that the samples are of similar age, the scatter must be due to variable initial Nd isotopic ratios, i.e. a heterogeneous fluid-rock system. The ε_{Nd} (525 Ma) values are plotted versus P_2O_5 content of the samples in Fig. 6-3. The magnetite-apatite ore samples have negative ε_{Nd} values while the igneous rocks have mainly positive ε_{Nd} composition, reflecting a juvenile mantle-derived lower crustal source. This evidence is against a direct genetic affinity between the magnetite-apatite ores and igneous host rocks. The magnetite-apatite ore samples have a less radiogenic Nd isotope composition with ε_{Nd} around -2, while the pure apatite ore has a distinctly crustal composition with ε_{Nd} around -5. The marine-sedimentary phosphorite of the Early Cambrian Soltanieh Formation has ε_{Nd} around -7, and therefore, a major part of the REE and P inventory of the hydrothermal apatite could derive from the Early Cambrian sedimentary strata. The ε_{Nd} value of -7 for the Soltanieh phosphorite represents the composition of biogenic apatite which was shown to preserve the geochemical signature of the Early Cambrian sea water from which it precipitated via biological mediation (Felitsyn et al. 1998). We assumed that other chemical sediments, such as the Hormuz and equivalent salt deposits, have a similar composition, although there are no data available. However, global Nd isotope signatures for Early Cambrian sediments at 530 Ma are around -4 (Brasier and Lindsay, 2001).

The overall distribution pattern of the reconnaissance data in Fig. 6-3 is in favor of two-component mixing in the ore systems of the Bafq district, with the magnetite-apatite ore in between the mantle-influenced igneous host rocks and the Early Cambrian marine sedimentary sequence. The apatite enrichment appears to be related to recycling of Early Cambrian sedimentary phosphorite, and an igneous source is unlikely. The iron component (magnetite-apatite ore) has more affinity to the igneous rocks, and both apatite and magnetite enrichment can be seen as a result of differential leaching (P from P-rich sedimentary precursors, Fe from Fe-rich igneous rocks) by basinal brines.

Table 6-2 Sm-Nd isotopic data of the magnetite-apatite ore samples and igneous rocks

Sample No.	Deposit	Rock Type	Sm (ppm)	Nd (ppm)	$^{147}Sm/^{144}Nd$	$^{143}Nd/^{144}Nd$	±2 sigma	εNd(t)
MA 2	Chador-Malu	Diorite	13.53	50.39	0.16223	0.512724	5	4.00
CH4	Choghart	Rhyolite	6.986	40.64	0.10391	0.512380	3	1.18
ES 7	Esfordi	Rhyolite	3.642	22.93	0.09600	0.512352	3	1.18
B56-S1	Esfordi	Micro-diorite	13.91	73.33	0.11465	0.512387	4	0.61
B66-S2	Esfordi	Doleritic dyke	59.62	331.8	0.10859	0.512299	4	-0.70
ES-12	Esfordi	Magnetite-apatite	115.0	496.7	0.13994	0.512362	4	-1.58
CH3	Choghart	Magnetite-apatite	174.4	892.2	0.11814	0.512258	3	-2.14
B65-S2	Esfordi	Apatite vein	381.2	1380	0.16689	0.512266	6	-5.26
SP-1	Soltanieh Fm.	Phosphorite[1]	71.06	352.7	0.12187	0.512024	11	-6.9

[1] Phosphorite data from Felitsyn & Gubanov (2002)

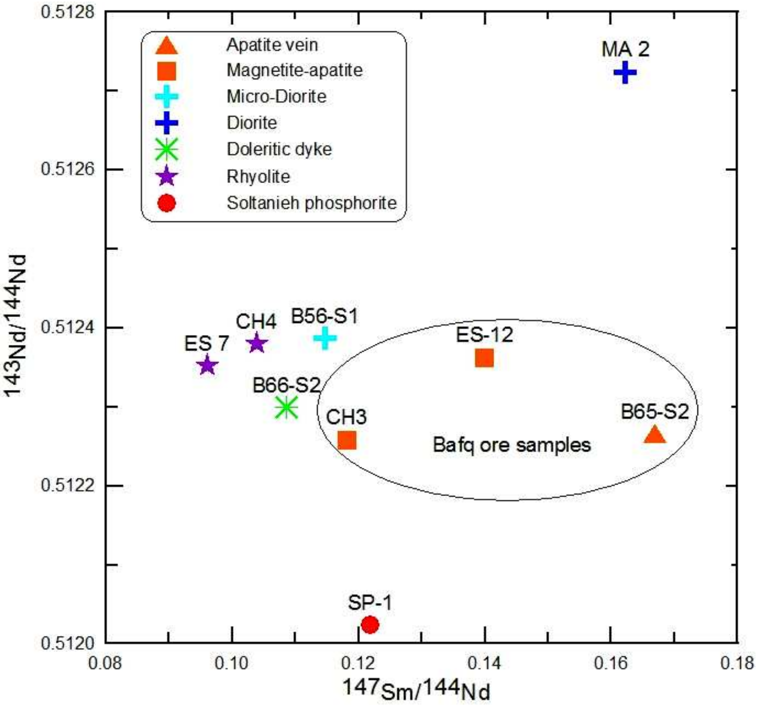

Fig. 6-2 $^{143}Nd/^{144}Nd$ versus $^{147}Sm/^{144}Nd$ diagram for samples from the Bafq district. Data for Soltanieh phosphorite from Felitsyn & Gubanov (2002).

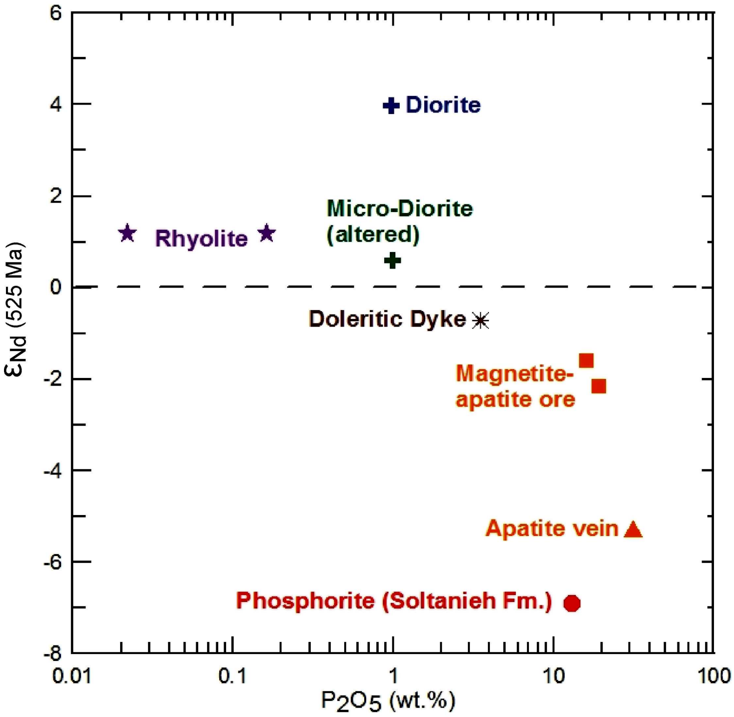

Fig. 6-3 ε_{Nd} (525 Ma) versus P_2O_5 content of the ore samples and igneous rocks. Soltanieh phosphorite data from Felitsyn & Gubanov (2002).

6-3 Ar-Ar isotope study

For successful mineral exploration, absolute time frameworks with precise ages of mineralizing events are needed. The K-Ar and $^{40}Ar/^{39}Ar$ methods have long been used to date igneous rocks associated with, and bracketing, episodes of mineralization. As well, K-bearing gangue and wall rock alteration minerals are commonly formed during epigenetic mineralization and can be dated. Therefore, the $^{40}Ar/^{39}Ar$ method was used to date the potassic alteration in rhyolitic rocks associated with the Bafq magnetite-apatite mineralization.

6-3-1 A summary of the Ar-Ar isotope technique

The conventional K-Ar isotope dating method is based upon the accumulation of radiogenic argon (^{40}Ar) produced from the decay of the naturally occurring radioactive isotope of potassium (^{40}K). The $^{40}Ar/^{39}Ar$ dating technique is a variant of the conventional K-Ar method. The method is described in detail by McDougall and Harrison (1988). To obtain an age by this technique, the sample of unknown age and a standard of known age are irradiated together in a nuclear reactor to produce ^{39}Ar from ^{39}K by fast neutron bombardment. After irradiation, the $^{40}Ar/^{39}Ar$ ratios of sample and standard are measured. The age of a sample can be calculated from its $^{40}Ar/^{39}Ar$ ratio when compared to the $^{40}Ar/^{39}Ar$ ratio of the standard. Most importantly, only the isotopic composition of argon need be measured and this is done by gas-source mass spectrometry, a very precise analytical technique. In contrast, for a conventional K-Ar date, both ^{40}K and ^{40}Ar must be measured quantitatively. To do this, argon in one aliquot of the sample is measured by isotope-dilution, gas-source mass spectrometry. Potassium in a different aliquot of sample is determined by some other analytical method such as flame photometry, X-ray fluorescence, or isotope-dilution solid source mass spectrometry. Thus, one inherent problem of the conventional K-Ar technique is the necessity of measuring isotopic abundances for separate aliquots of the same sample. This poses the danger that, because of sample inhomogeneity, different potassium and/or argon contents may exist in each aliquot. Two major advantages of the ^{40}Ar/^{39}Ar dating method are: only isotopic ratios of argon need be determined, and all measurements are made on the same sample aliquot, thus avoiding the question of homogeneity. In addition, by the ^{40}Ar/^{39}Ar thermal release method, it is possible to obtain a series of dates on a single sample when the argon is extracted by step heating. The combination of these advantages increases the precision of the ^{40}Ar/^{39}Ar method over the conventional K-Ar technique. However the ^{40}Ar/^{39}Ar technique will suffer if proper corrections are not made for interfering radiation-induced isotopes (Snee et al., 1988).

The ^{40}Ar/^{39}Ar method was first used in total fusion experiments in which an irradiated sample was completely melted and all isotopes of argon measured in a single analysis to calculate an age for the sample. This total fusion age is roughly analogous to a conventional K-Ar age of the sample except that no isotopic concentration measurements are required. Very soon after the first uses of the ^{40}Ar/^{39}Ar method, it was realized that a sample could be progressively degassed in temperature increments (Turner, 1968). An age could be calculated for each increment of gas released and the ages of all temperature increments of a sample were plotted against percent of released argon to form an age spectrum. The character of the spectrum can be calculated within a theoretical framework to interpret the apparent distribution of potassium and argon within the sample. Many studies have shown that meaningful ages of samples could be determined by the age spectrum technique even though some loss of ^{40}Ar had occurred during the geologic history of the sample. It should be noted here that loss or gain of ^{40}Ar by a sample will result in an erroneous conventional K-Ar age. Furthermore, since loss or gain of ^{40}Ar in a sample is generally thermally controlled, samples from thermally complex regions (such as ore deposits) should be analyzed by the ^{40}Ar/^{39}Ar age spectrum technique (Snee et al., 1988). In reality, the determination of an age by the ^{40}Ar/^{39}Ar technique is not a simple matter of measuring ^{40}Ar and ^{39}Ar. Some interference corrections (Roddick, 1983), and a correction for the presence of atmospheric ^{40}Ar by using

^{36}Ar and the recommended atmospheric ^{40}Ar/^{36}Ar ratio of 295.5 (Steiger and Jäger, 1977) must be made.

The age calculated for a mineral, from its accumulated radioactive decay products, is the time when the chemical system of that mineral became closed to diffusion of that particular radioactive decay product. Closure to diffusion is controlled chiefly by temperature but also to a small extent by cooling rate (Dodson, 1973) and possibly chemical composition and strain history. Each mineral has its characteristic closure temperature and its age measures the time when the mineral cooled through its closure temperature (Snee et al., 1988).

6-3-2 Ar-Ar analysis of the Bafq samples

In order to constrain timing of the potassic alteration and determine its relationship with the magnetite-apatite mineralization in the Bafq mining district, three samples with distinct potassic alteration (high K content) from the Chador-Malu and Esfordi deposits were selected and dated by the ^{40}Ar/^{39}Ar thermal release method in the Department of Earth, Atmospheric & Environmental Sciences, University of Manchester (analyst: Ray Burgess). The studied samples are altered calc-alkalic rhyolitic to rhyodacitic rocks for which their Early Cambrian age is well constrained from stratigraphically equivalent, but unaltered rocks in the Saghand area, which were dated by Ramezani and Tucker (2003) using U-Pb dating on zircon. The selected samples are listed in Table 6-3. Microscopic study confirms that the main alteration minerals are K-feldspar and sericite alteration (Table 6-3). The samples ES-7, ES-9 and MA-1 were analyzed using the ^{40}Ar/^{39}Ar age spectrum technique which was performed on the bulk-rock due to the presence fine-grained K-feldspar and sericite which did not allow to separate them from altered and very fine-grained matrix. The analytical data are listed in Table 6-4. Age spectrum diagrams for the samples are shown in Fig. 6-4. All three samples show apparent argon loss with a stair-step disturbed spectrum (Fig. 6-4) and none shows a clear plateau age. Due to the high degree of disturbance and resetting of the system no useful isochron plot (^{40}Ar/^{36}Ar against ^{39}Ar/^{36}Ar) and alternatively, inverse isochron diagrams (^{36}Ar/^{40}Ar against ^{39}Ar/^{36}Ar) were obtained. The data were scattered in the diagrams and did not show any concordant or meaningful total isochron age. These plots illustrate that the interpretation of ^{40}Ar/^{39}Ar dates from the highly altered, potassium metasomatized volcanic rocks in the Bafq district is complex.

Table 6-3 Selected samples for Ar-Ar isotopic analysis

Sample No.	Deposit	K_2O (wt%) whole rock	Sample description
ES-7	Esfordi	8.46	Rhyolite (K-feldspar alteration, silicification, partially sericitized)
ES-9	Esfordi	4.91	Rhyolite (Mainly sericitized)
MA-1	Chador-Malu	8.89	Rhyolite (Mainly K-feldspar alteration)

The sample ES-7 which is affected by silicification, fine-grained K-feldspar alteration and partially sericitization shows an age around 125 Ma in the first heating steps which increases to an age of 135.4 Ma with a pseudo-plateau pattern for the last about 60% Ar release. The total age is 130.4±1.2 Ma. These young ages obviously indicate thermal overprint by a younger event, although this event is not observed mineralogically. The Cl/K ratio in this sample is relatively high which reflects the matrix effect. However, the obtained ages are not well correlated with this ratio in each step which suggests that this effect can be neglected. The high Cl content might be due to mineralizing brine fluids trapped in the alteration minerals, especially quartz crystals, which are dispersed in the matrix. High Cl can produce some interference in the Ar isotopic system (Roddick, 1983) and increases the ^{40}Ar released which causes some disturbance in the pattern and increases the apparent age. This effect can easily be removed using the ages of high-temperature steps corresponding to lower Cl/K content. The Ca/K ratio is very low which shows there is no contaminating plagioclase phase responsible for this argon diffusion.

The ^{40}Ar/^{39}Ar date of rhyolitic sample MA-1 with only K-feldspar alteration increases monotonously with increasing gas-release temperature and fails to form a stable plateau age (Fig. 6-4). This sample shows a total age of 158.6±1.3 Ma. The Ca/K ratio in this sample is much higher than in ES-7, especially at lower temperature fractions which can be related to argon release from the higher plagioclase portions. This effect decreases in higher temperature fractions.

The sample ES-9 also does not show a plateau age pattern. However, in according with complete sericitization, it gives a much higher total age (303.4±2.4 Ma), which is probably due to the higher closure temperature and Ar-retentivity of sericite in comparison to K-feldspar. The age of this sample increases dramatically in the high temperature fractions which might be related to the effect of ^{39}Ar recoil from fine-grained sericite (<1 μm) in the matrix with higher Ca/K and Cl/K which increases the ^{40}Ar/^{39}Ar ratio and causes higher ages.

Harrison (1981) and McDougall and Harrison (1988) demonstrated that the closure temperature of minerals is a function of their grain size, so that with decreasing grain size, the closure temperature decreases dramatically. Hanes (1991) and Foland et al. (1993) recognized that fine-grained volcanic rocks, especially those containing glass, are prone to Ar loss and that their age dates are frequently much younger than crystalization ages. Parsons et al. (1988) described the reasons of argon-loss in alkali feldspars. They suggested that feldspars commonly leak argon because of the presence of numerous, possibly interconnected, sub-micrometer-scale holes in the structure which give the feldspar its characteristic turbid appearance. Perthite (Parsons et al., 1988 and references cited within) and also microcline (Faure, 1986) can loose easily radiogenic argon, consistent with their very low retentivity.

Faure (1986) showed that increase in temperature due to metamorphism (either regional or contact) will cause argon loss from most minerals without producing any other physical or chemical changes in the rocks.

The Ar-Ar data document a thermal event which has extinguished the older age information from the potassic hydrothermal alteration. The young and disturbed ages define the time elapsed since cooling through the blocking temperature of K-feldspar (230 °C) and sericite (350 °C), respectively. Similar patterns with different apparent ages from nearly 150 Ma up to 295 Ma have been observed by Verdel et al. (2007) in the Saghand area. These ages must be related to the Mesozoic collisional history of Central Iran.

Table 6-4 Step-heating Ar-Ar isotopic results

Temp. °C	^{36}Ar (× 10^{15} moles)	Cl^1 (× 10^9 moles)	Ca^2 (× 10^9 moles)	^{3}K (× 10^9 moles)	^{40}Ar (× 10^{15} moles)	^{40}Ar^{*4} (%)	Cum. ^{39}Ar (%)	^{40}Ar*/^{39}Ar	Age^5 (Ma)
ES-7	mass = 0.00908 g								
300	0.45 ± 0.06	0.1 ± 0.09	65.3 ± 22.7	1.7 ± 1.6	126 ± 0	0.0	0.01	nd	nd
400	0.19 ± 0.07	0.21 ± 0.28	19.3 ± 44.7	0.7 ± 1.3	59 ± 0	4.3	0.01	39.5 ±346.3	464 ± 3584
500	2.30 ± 0.15	22.92 ± 0.34	27.8 ± 19.6	49.1 ± 0.6	723 ± 2	6.0	0.3	9.7 ± 9.6	125 ± 120
600	1.71 ± 0.13	109.45 ± 1.59	44.3 ± 25.9	775.7 ± 5.5	1163 ± 2	56.6	4.1	9.4 ± 0.6	121 ± 7
700	0.89 ± 0.11	140.35 ± 2.03	76.2 ± 15.1	3917.4 ± 27.9	3649 ± 4	92.8	23.3	9.5 ± 0.1	123 ± 1
750	0.28 ± 0.09	10.35 ± 0.17	52.0 ± 24.2	2666.1 ± 19.0	2416 ± 6	96.6	36.4	9.6 ± 0.1	125 ± 1
800	0.14 ± 0.10	9.44 ± 0.16	38.2 ± 28.0	1773.3 ± 12.6	1635 ± 2	97.4	45.1	9.9 ± 0.2	128 ± 2
875	0.06 ± 0.14	28.64 ± 0.42	27.7 ± 14.6	2654.8 ± 19.1	2579 ± 4	99.3	58.1	10.6 ± 0.2	137 ± 2
950	0.17 ± 0.15	21.51 ± 0.32	40.4 ± 22.9	2777.8 ± 19.8	2771 ± 4	98.2	71.7	10.8 ± 0.2	139 ± 2
1025	0.12 ± 0.09	27.61 ± 0.41	22.8 ± 21.1	2312.1 ± 16.6	2224 ± 6	98.5	83.1	10.4 ± 0.1	135 ± 2
1100	0.32 ± 0.14	30.98 ± 0.45	40.8 ± 22.2	1964.5 ± 14.2	1882 ± 4	94.9	92.7	10.0 ± 0.2	129 ± 3
1200	0.32 ± 0.09	31.26 ± 0.46	27.7 ± 27.7	1419.5 ± 10.0	1449 ± 2	93.5	99.7	10.5 ± 0.2	136 ± 3
1600	2.28 ± 0.12	9.68 ± 0.18	75.3 ± 22.0	62.8 ± 1.4	792 ± 1	14.8	100.0	20.6 ± 6.1	256 ± 70
Total	*9.24* ± 0.41	*442.5* ± *2.79*	*513.7* ± *42.4*	*20375.5* ± *51.7*	*21468* ± *12*			*10.1* ± *0.1*	*131* ± *1*
ES-9	mass = 0.00447 g								
500	0.59 ± 0.11	0.3 ± 0.07	48.8 ± 24.5	37.9 ± 0.4	203 ± 0	13.8	0.5	8.2 ± 9.3	106.0 ± 117.7
600	0.23 ± 0.11	1.0 ± 0.07	55.7 ± 18.9	174.5 ± 1.4	262 ± 0	74.3	2.9	12.3 ± 2.1	157.3 ± 26.2
700	0.33 ± 0.12	2.6 ± 0.10	50.8 ± 36.2	959.4 ± 6.9	1616 ± 2	93.9	15.8	17.4 ± 0.4	219.4 ± 5.0
800	0.37 ± 0.10	2.8 ± 0.10	70.3 ± 23.4	2767.5 ± 19.5	5363 ± 6	98.0	53.0	20.9 ± 0.1	260.3 ± 1.4
900	0.52 ± 0.11	6.5 ± 0.12	61.5 ± 16.2	2591.1 ± 18.3	5636 ± 11	97.3	87.9	23.3 ± 0.1	287.8 ± 1.7
1000	0.80 ± 0.12	21.3 ± 0.32	74.7 ± 23.2	758.8 ± 5.6	2860 ± 3	91.8	98.1	38.1 ± 0.5	449.1 ± 5.6
1200	1.02 ± 0.09	9.0 ± 0.14	78.0 ± 27.7	82.4 ± 0.9	1089 ± 2	72.4	99.2	105.4 ± 3.7	1041.8 ± 28.0
1600	2.55 ± 0.08	8.6 ± 0.16	73.9 ± 25.2	60.2 ± 1.4	1514 ± 2	50.2	100.0	139.1 ± 5.3	1279.2 ± 35.1
Total	*6.40* ± 0.31	*52.0* ± *0.44*	*513.7* ± *70.8*	*7431.8* ± *28.3*	*18542* ± *14*			*24.7* ± *0.1*	*303* ± 2
MA-1	mass = 0.00804 g								
500	0.78 ± 0.11	1.6 ± 0.07	39.1 ± 14.0	35.2 ± 0.7	147 ± 1	8.7	0.2	6.9 ± 10.0	89.9 ± 127.8
600	1.10 ± 0.12	11.78 ± 0.20	126.2 ± 17.0	849.2 ± 6.2	1194 ± 3	71.3	4.4	10.4 ± 0.5	134.6 ± 5.7
700	0.85 ± 0.11	9.38 ± 0.16	2036.6 ± 28.2	2276.7 ± 16.3	6103 ± 16	89.9	15.7	10.8 ± 0.2	138.8 ± 2.1
775	0.43 ± 0.10	2.16 ± 0.10	1324.8 ± 27.7	2094.5 ± 14.9	14788 ± 26	94.2	26.1	10.8 ± 0.2	139.6 ± 1.9
850	0.39 ± 0.11	12.36 ± 0.18	85.7 ± 26.1	2143.0 ± 15.2	14213 ± 30	95.2	36.7	11.7 ± 0.2	149.9 ± 2.0
925	0.54 ± 0.11	16.09 ± 0.24	64.6 ± 25.6	2121.8 ± 15.1	23054 ± 58	93.6	47.2	12.1 ± 0.2	155.1 ± 2.2
1000	1.43 ± 0.13	27.88 ± 0.42	37.9 ± 27.6	3419.9 ± 24.5	29938 ± 73	90.0	64.2	12.3 ± 0.1	157.2 ± 1.5
1100	2.30 ± 0.16	41.18 ± 0.64	96.6 ± 25.7	3654.0 ± 26.5	33688 ± 65	87.1	82.3	13.8 ± 0.1	176.1 ± 1.7
1200	1.00 ± 0.12	15.65 ± 0.23	16.3 ± 20.7	1400.2 ± 10.1	34043 ± 97	85.0	89.2	13.1 ± 0.3	167.9 ± 3.3
1400	2.65 ± 0.12	26.62 ± 0.40	34.2 ± 14.7	2044.2 ± 14.6	34459 ± 70	77.8	99.4	14.8 ± 0.2	187.7 ± 2.3
1600	2.95 ± 0.12	2.84 ± 0.07	45.0 ± 28.5	125.0 ± 1.4	21779 ± 41	18.0	100.0	16.9 ± 3.1	212.5 ± 36.5
Total	*14.42* ± *0.40*	*167.5* ± *0.99*	*3907.0* ± *79.2*	*20163.5* ± *51.0*	*282703* ± *206*			*12.4* ± *0.1*	*159.0* ± *0.8*

[1] Determined from ^{37}Cl (n, γ, β) ^{38}Ar, [2] Determined from ^{40}Ca (n, α) ^{37}Ar, [3] Determined from ^{39}K (n,p) ^{39}Ar, [4] ^{40}Ar* = 40Ar$_{total}$ - 295.5×^{36}Ar, [5] Total age includes uncertainties on the J value

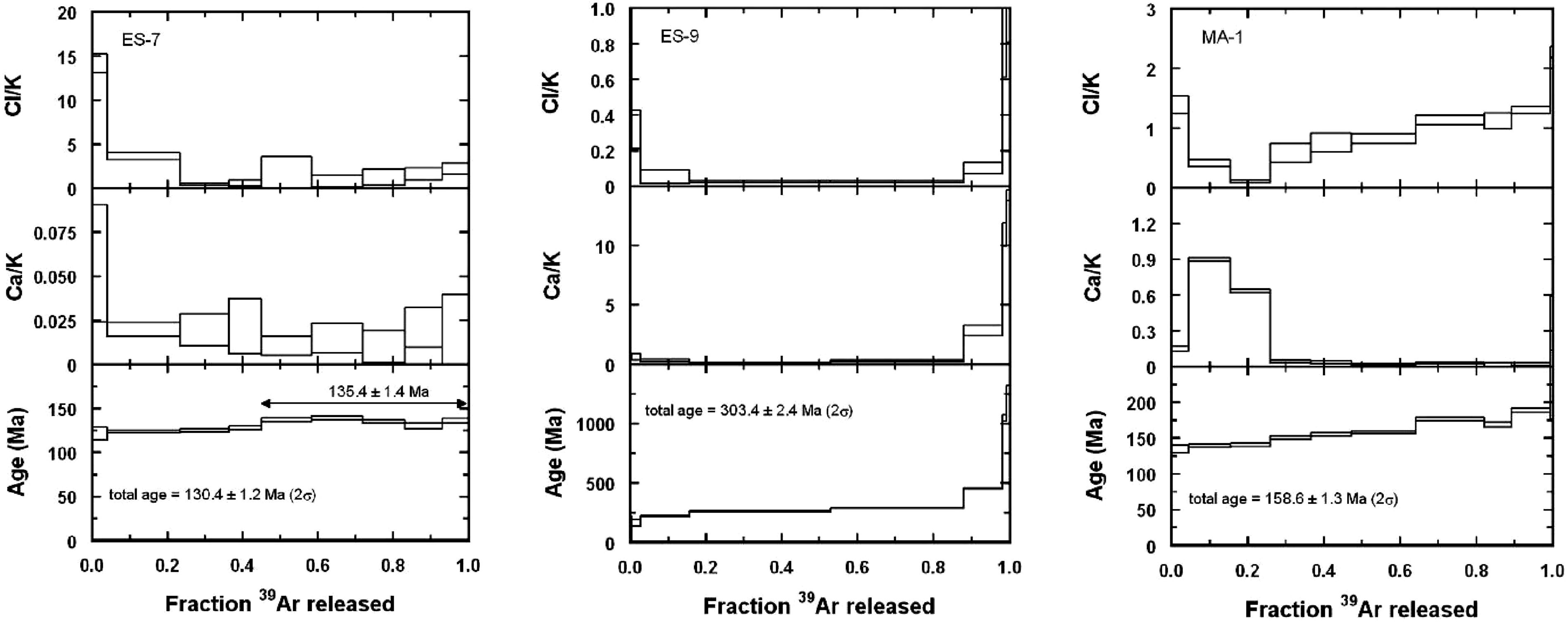

Fig. 6-4 Ar-Ar step-heating age spectra.

Chapter 7: Ore formation model and conclusions

7-1 Discussion

The origin of the magnetite-apatite deposits of the Bafq mining district, similar to their counterparts of the Kiruna-type systems, is controversial. The Bafq deposits had been considered as result of liquid immiscibility, and injection or extrusion of ore magmas originated from alkaline/carbonatitic magmas, for many years (Samani, 1988; Förster & Jafarzadeh, 1994), although there is no evidence for the presence of carbonatites. Samani (1988) reported field observations of carbonatite (?) dykes in a few locations at the Bafq and Saghand area. However, their carbonatitic origin is strongly questionable. Carbonatite dykes and carbonate lenses or veins, especially when metamorphosed, or hydrothermally altered, can not be distinguished by field observations only (Le Bas et al., 2002; Yang & Le Bas, 2004), and at least geochemical analysis as well as isotopic data are required. One of the key areas in the Bafq district is the Esfordi deposit for which some geologists (e.g., Darvishzadeh, 1982) advocated a carbonatitic origin. However, our geochemical data show that the host rocks are mainly silicified dolomitic rocks with very low Sr content (42-113 ppm, see Appendix 1), which does not correspond to the elevated Sr of carbonatites (Le Bas et al. 2002; Yang & Le Bas, 2004) and excludes a carbonatitic affinity. Although the presence of such carbonatite rocks at deep levels is not impossible, they usually are associated with alkaline rocks such as alkaline syenites which are not present in the Bafq district. Although the intrusive and volcanic rocks of the Bafq district are locally enriched in Na and/or K, it is obvious that these elements are products of widespread metasomatic alteration and there is no evidence of igneous precursor alkaline affinity. Alternatively, our geochemical data from apatites of the Bafq district also exclude their carbonatitic origin.

Daliran (1990) investigated the Mishdovan deposit and postulated its magmatic origin as an iron ore magma. But more recently, she described this deposit and similarly other deposits of the Bafq district as a result of high-temperature hydrothermal fluids probably derived from volatile-rich magmas (Daliran, 2002). However, she did not identify the source of these fluids and of the metals.

Our field observations exclude the magmatic origin of the deposits, simply because many massive iron ores are surrounded by magnetite, apatite veins and veinlets which cut the volcano-sedimentary host rocks. The presence of extensive hydrothermal alteration as evidence of high-volume fluid-rock interaction and metasomatic replacement features of the ore, are another reasons to invoke the role of hydrothermal fluids for the genesis of these deposits.

Daliran (2002) used the REE pattern of apatite of the Bafq district to decipher its origin. She demonstrated that the Bafq apatites are distinct due to their elevated REE content, strong LREE/HREE fractionation, pronounced negative Eu and slightly positive Ce anomalies. She used the positive Ce anomaly observed as evidence to exclude a derivation from marine phosphorites and sedimentary rocks. However, Moore and Modaberi (2003) demonstrated that the Choghart apatites have a slightly negative Ce anomaly, in line with the REE data presented here. These differences are likely due to the analytical techniques and normalization values used. An important matter is that the REE pattern of the Bafq apatites should be compared to sedimentary phosphorites with the same age, but not to recent phosphorites which represent the recent ocean oxidation state. Morad and Felitsyn (2001) showed that the Ce anomaly in Neoproterozoic-Cambrian phosphorites may completely differ from recent phosphorites. They pointed out that old phosphorites may have a slightly positive Ce anomaly reflecting anoxic condition of the Neoproterozoic-Cambrian oceans. Another feature is that the REE in the Bafq deposits, and similarly in other Kiruna-type deposits, are completely mobile and their patterns can not be used in a conclusive manner to find out the origin of these deposits. The presence of young monazite phases as inclusions inside or nucleated phases outside apatite (Torab & Lehmann, 2007) shows that the original REE pattern of these apatites has been obscured by a later hydrothermal overprint, and it is likely that the volcanic host rocks are also affected by the same fluids responsible for this overprinting. Therefore the similar REE pattern of ore and host volcanics is to be expected, but can not be interpreted as a cogenetic feature as supposed by some researchers (see e.g., Frietsch & Perdahl, 1995).

If all apatite originated from an igneous source as a separate melt, then the large compositional spectrum from a relatively pure magnetite ore (Choghart deposit with 60 % Fe, 0.95 % P_2O_5) to the Gazestan and Esfordi deposits with an average grade of 12-13 % P_2O_5, up to 35 % P_2O_5 within pure apatite veins, becomes difficult to explain.

Although the questionable weak Ce anomaly of these apatites is not diagnostic, their strong negative Eu anomaly is. The interesting feature is that opposite to the host volcanics which show the same REE pattern of the ore (due to similar fluid interaction), the two main granitic intrusions (Zarigan granite and Chador-Malu granite) have a pronounced positive Eu anomaly. These granites are strongly albitized, and probably played a role as main heat sources for the hydrothermal systems. Due to hydrothermal circulation, these granites suffered strong sodic alteration by high-salinity brines of evaporitic source. These brines are also perfect agents for metal leaching and transport. During albitization, Eu is selectively fixed in the plagioclase (now albite) structure, substituted for Ca which is leached, while other rare earth elements are mobilized out of the granitic rocks into the hydrothermal system and subsequently fixed into the apatite structure of the magnetite-apatite ores. This is in part, why there is strong negative Eu anomaly in the hydrothermal apatites in the Bafq district. However, a negative Eu anomaly is also observed in the source phosphorites, but not as pronounced as in the hydrothermal ore.

7-2 Metallogenic model and conclusions

The "Kiruna-type" magnetite-apatite ore deposits of the Bafq metal province have elevated REE contents and occur together with peripheral uranium mineralization. Geochemical signature, hydrothermal alteration and magnetite chemistry point to IOCG affinity. The geotectonic situation places the ore deposits in a geological framework similar to the Cretaceous Chilean iron belt in the Coastal Cordillera of the South American Andes.

The Bafq deposits show characteristic alteration zoning similar to other typical IOCG deposits. Extensive circulation of sodium-rich saline fluids is reflected in the volcanic and intrusive host rocks of the mineralization which have undergone widespread sodic alteration (albitization). This alteration is earlier than the magnetite-apatite mineralization and occurs at deeper levels. Potassic alteration occurs in upflow zones. In this situation, due to cooling and changes in pH and Eh (reaction with dolomitic country rocks), magnetite and apatite precipitate. This process is succeeded by actinolitization (especially in dolomitic host rocks) and lower temperature hydrolytic and sericitic alteration of volcanic rocks.

The calculated monazite age (515 ± 21 to 529 ± 21 Ma) of the ore overlaps with the Cambrian age of the volcano-plutonic rocks (U-Pb, 525 ± 7 to 533 ± 1 Ma, Ramezani & Tucker, 2003). The congruent ages of magnetite-apatite mineralization, uranium mineralization (507-542 Ma), and Early Cambrian phosphorite and evaporite sedimentation suggest a genetic relationship. Late Proterozoic to Cambrian evaporites are widespread in Central Iran and are equivalent to the Hormoz salt formation in the Zagros Mountains and Persian Golf with extensive salt domes. There is probably a genetic relationship, by large-scale circulation of basinal brines from an evaporitic source, induced by magmatic heat, as described by Barton and Johnson (1996). The evaporites, both coeval with mineralization, i.e. Cambrian (Zharkov, 1984; Stöcklin, 1968), and earlier, i.e., Late Neoproterozoic-Early Cambrian (Husseini & Husseini, 1990; Stöcklin, 1968), are likely to have played an important role as ligand sources for metal leaching and transport. Nd isotope data exclude an origin of the REE inventory of the magnetite-apatite mineralization dominantly from the igneous rocks and are in favor of a model of hydrothermal remobilization from the Early Cambrian sedimentary sequence (especially phosphorites) powered by Cambrian intrusive bodies. These phosphorites have relatively elevated REE content. However, the REE budget of the magnetite-apatite ore is also supplied from leaching of igneous rocks. This is why the magnetite-apatite deposits show an intermediate ε_{Nd} composition between marine phosphorites and igneous host rocks. Figure 7-1 shows a tentative model for the genesis of these deposits.

Many of the magnetite apatite deposits of the Bafq district have a discordant to concordant mushroom shape, similar to many salt domes and plugs. This similar feature may suggest that these deposits were preferentially emplaced into older leached evaporites and salt dome structures. This new speculative idea can easily explain why such a huge high grade and massive magnetite-apatite deposits can be formed. However, the metasomatic replacement in the volcano-sedimentary sequences is well documented and is clearly responsible for forming low-grade and disseminated ores, around the massive ore bodies. A combination of replacement, dissolution and mechanical disaggregation is likely, as well known from Mississippi-Valley-type (MVT) lead-zinc deposits, where platformal limestones are affected by basinal brines in a process of hydrothermal karst formation (Leach et al., 2005). The textural features are very similar in both MVT and Kiruna-type deposits.

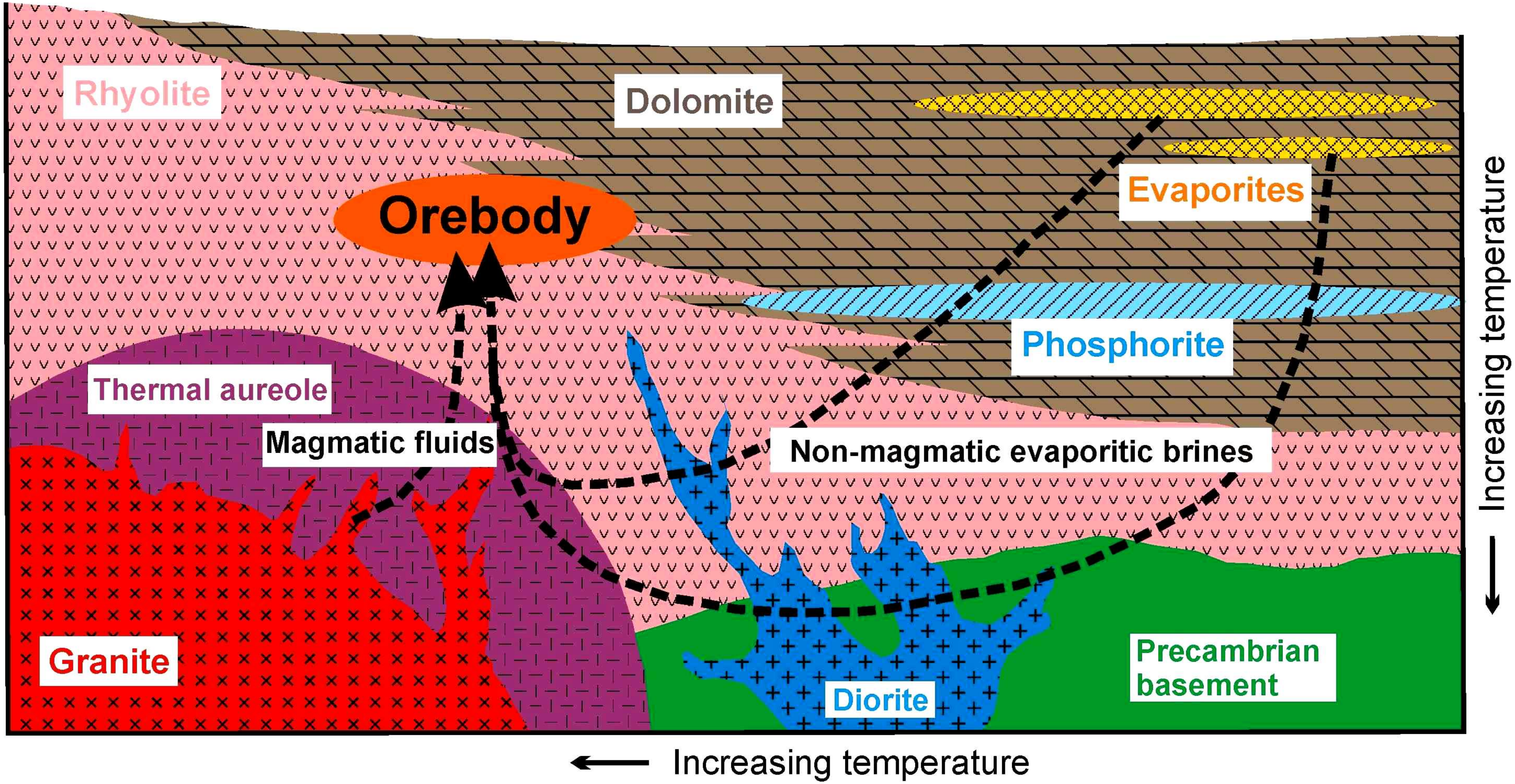

Fig. 7-1 Schematic metallogenetic model for magnetite-apatite deposits of the Bafq district (vertical section, not to scale). Modified from Mathur et al. (2002).

Another exploration key is that most, if not all, of these deposits are associated with widespread potassic (either as K-feldspar or sericite) alteration, usually at the hangingwall. These high-K areas can readily be distinguished by modern remote sensing spectral techniques and potassium aero-radioactivity surveys. These airborne surveys can also be used for the definition of areas of high radioactivity for further uranium exploration.

The Jalal-Abad iron ore deposit, 150 km SE of Bafq, located in the southern part of the Kashmar-Kerman Tectonic Zone, has a reserve figure of 200 Mt @ 45% Fe, 0.08% P, 1.18% S, and has similarities in geological situation, mineralogy and alteration style to the Bafq iron ore deposits, but is little studied so far. The Kashmar-Kerman Tectonic Zone extends for more than 1000 km, and only a small part (mostly between Bafq and Saghand) is explored so far, with focus on Kiruna-type iron ore deposits during the 1970s. The recognition of the IOCG perspective provides new exploration potential, and incentive to integrate the individual deposit styles (including the little understood Kushk massive sulfide mineralization and/or Saghand uranium deposit) into a larger metallogenic picture. Our bulk-rock chemical data from the magnetite-apatite system display very low abundances of copper and gold. However, given suitable depositional conditions (e.g., sulfide traps), other members of the IOCG deposit spectrum may be present.

References

Anders, E., and Grevesse, N., 1989, Abundances of the elements: Meteoritic and solar: Geochimica et Cosmochimica Acta, v. 53, p. 197-214.

Ayers, J.C., and Watson, E.B., 1991, Solubility of apatite, monazite, zircon, and rutile in supercritical aqueous fluids with implications for subduction zone geochemistry: Phil. Trans. R. Soc. Lond. A, v. 335, p. 365-375.

Barton, M.D., and Johnson, D.A., 1996, Evaporitic-source model for igneous-related Fe oxide-(REE-Cu-Au-U) mineralization: Geology, v. 24, p. 259-262.

Barton, M.D., and Johnson, D.A., 2000, Alternative brine sources for Fe-oxide (-Cu-Au) systems: Implications for hydrothermal alteration and metals, in Porter, T.M. ed., Hydrothermal iron oxide copper-gold & related deposits: A global perspective: PGC Publishing, Adelaide, v. 1, p. 43-60.

Barton, M.D., and Johnson, D.A., 2004, Footprints of Fe oxide (-Cu-Au) systems: University of Western Australia Special Publication 33, p. 112-116.

Beaudoin, G., Dupuis, C., Gosselin, P., and Jebrak, M., 2007, Mineral chemistry of iron oxides: application to mineral exploration, in Andrew, C.J. ed., Digging Deeper: Proceedings of the Ninth Biennial SGA Meeting, Dublin, v. 1, p. 497-500.

Belousova, E.A., Griffin, W.L., O'Reilly, S.Y., and Fisher, N.I., 2002, Apatite as an indicator mineral for mineral exploration: trace-element compositions and their relationship to host rock type: Journal of Geochemical Exploration, v. 76, p. 45-69.

Berberian, F., and Berberian, M., 1981, Tectono-plutonic episodes in Iran, in Gupta, H.K., and Delany, F.M., editors, Zagros-Hindu Kush-Himalaya geodynamic evolution: American Geophysical Union Geodynamic Series, v. 3, p. 5-32.

Bookstrom, A.A., 1977, The magnetite deposits of El Romeral, Chile: Economic Geology, v. 72, p. 1101-1130.

Boric, R., Holmgren, C., Nicholas S.F., and Zentilli, M., 2002, The geology of the El Soldado manto type Cu-(Ag) deposit, central Chile, in Porter, T.M., ed., Hydrothermal iron oxide copper-gold and related deposits: A global perspective: PGC Publishing, Adelaide, v. 2, p. 163-184.

Borumandi, H., 1973, Petrographische und lagerstättenkunliche untersuchung der Esfordi-Formation zwischen Mishdovan und Kushk bei Bafq (Zentraliran), Diss. RWTH Aachen, 174 p.

Brasier, M.D., and Lindsay, J.F., 2001, Did supercontinental amalgamation trigger the "Cambrian Explosion"?, in Zhuravlev, A.Yu., and Riding, R., eds., The ecology of Cambrian radiation, Columbia University Press, New York, p. 69-89.

Chao, E.C.T., Back, J.M., Minkin, J.A., Tatsumoto, M., Wang Junwen, Conrad, J.E., McKee, E.H., Hou Zonglin, Meng Qingrun, and Huang Shengguang, 1997, The sedimentary carbonate-hosted giant Bayan Obo REE-Fe-Nb ore deposit of Inner Mongolia, China: A cornerstone example for giant polymetallic ore deposits of hydrothermal origin: U.S. Geological Survey Bulletin 2143.

Cocherie, A., and Albarède, F., 2001, An improved U-Th-Pb age calculation for electron microprobe dating of monazite: Geochimica et Cosmochimica Acta, v. 65, p. 4509-4522.

Cocherie, A., and Legendre, O., 2007, Potential minerals for determining U-Th-Pb chemical age using electron microprobe: Lithos, v. 93, p. 288-309.

Cocherie, A., Mezeme, E.B., Legendre, O., Fanning, C.M., Faure, M., and Rossi, P., 2005, Electron-microprobe dating as a tool for determining the closure of Th-U-Pb systems in migmatitic monazites: American Mineralogist, v. 90, p. 607-618.

Cook, N.D.J., and Ashley, P.M., 1992, Meta-evaporite sequence, exhalative chemical sediments and associated rocks in the Proterozoic Willyama Supergroup, South Australia: Implications for metallogenesis: Precambrian Research, v. 56, p. 211-226.

Corriveau, L., 2005, Iron Oxide copper-gold (+/-Ag,+/-Nb,+/-REE,+/-U) deposits: A Canadian Perspective: Geological Survey of Canada, Open File, 1-23.

Creaser, R.A., and Cooper, J.A., 1993, U-Pb geochronology of Middle Proterozoic felsic magmatism, surrounding the Olympic Dam Cu-U-Au-Ag and Moonta Cu-Au-Ag deposits, South Australia: Economic Geology, v. 88, p. 186-197.

Daliran, F., 1990, The magnetite-apatite deposit of Mishdovan, East Central Iran. An alkali rhyolite hosted, "Kiruna type" occurrence in the Infracambrian Bafq metallotect (mineralogic, petrographic and geochemical study of the ores and the host rocks): Ph.D. thesis, Heidelberg, Heidelberger Geowissenschaftliche Abhandlungen 37, 248 p.

Daliran, F., 2002, Kiruna-type iron oxide-apatite ores and "apatitites" of the Bafq district, Iran, with an emphasis on the REE geochemistry of their apatites, in Porter, T.M. ed., Hydrothermal iron oxide copper-gold & related deposits: A global perspective: PGC Publishing, Adelaide, v. 2, p. 303-320.

Darvishzadeh, A., 1982, Investigation of the phosphate in Bafq (Esfordi): Bull. Fac. Sci., University of Tehran, v. 13 (1,2), p. 2-28 (in Farsi).

Davoudzadeh, M., Lensch, G., and Weber-Diefenbach, K., 1986, Contribution to the paleogeography, stratigraphy and tectonics of the Infracambrian and lower Paleozoic of Iran: Neues Jahrbuch für Geologie und Paläontologie, Abhandlungen, v. 172, p. 245-269.

Dodson, M.H., 1973, Closure temperature in cooling geochronological and petrological systems: Contribution to Mineralogy and Petrology, v. 40, p. 259-274.

Faure, G., 1986, Principles of isotope geology (second edition), John Wiley & Sons Inc., 589p.

Felitsyn, S., Sturesson, U., Popov, L., and Holmer, L., 1998, Nd isotope composition and rare earth element distribution in early Paleozoic biogenic apatite from Baltoscandia; a signature of Iapetus ocean water: Geology, v. 26, p. 1083-1086.

Felitsyn, S., and Gubanov, A.P., 2002, Nd isotope composition of early Cambrian discrete basins: Geological Magazine, v. 139, p. 159-169.

Foland, K.A., Fleming, T.H., Heimann, A., and Elliot, D.H., 1993, Potassium-argon dating of fine-grained basalts with massive Ar loss: Application of the ^{40}Ar/^{39}Ar technique to plagioclase and glass from the Kirkpatrick Basalt, Antarctica: Chemical geology, v. 107, p. 173-190.

Förster, H., and Jafarzadeh, A., 1994, The Bafq mining district in Central Iran - a highly mineralized Infracambrian volcanic field: Economic Geology, v. 89, p. 1697-1721.

Förster, H.J., and Harlov, D.E., 1999, Monazite-(Ce)-huttonite solid solutions in granulite-facies metabasites from the Ivrea-Verbano Zone, Italy: Mineralogical Magazine, v. 63, p. 587-594.

Frietsch, R., 1978, On the magmatic origin of iron ores of the Kiruna type: Economic Geology, v. 73, p. 478-485.

Frietsch, R., and Perdahl, J.A., 1995, Rare earth elements in apatite and magnetite in Kiruna-type iron ores and some other iron ore types: Ore Geology Reviews, v. 9, p. 489-510.

Frietsch, R., Rapunen, H., and Vokes, F.M., 1979, The ore deposits in Finland, Norway and Sweden - a review: Economic Geology, v. 74, p. 975-1001.

Gandhi, S.S., 2003, An overview of the Fe oxide-Cu-Au deposits and related deposit types: CIM Montreal 2003 Mining Industry Conference and Exhibition, Canadian Institute of Mining, Technical Paper, CD-ROM.

Gandhi, S.S., 2004, Magmatic-hydrothermal Fe oxide±Cu±Au deposits: classification for a digital database and an overview of selected districts: IAVCEI General Assembly 2004, Pucón, Chile, CD-ROM.

Gauthier, L., Hall, G., Stein, H., and Schaltegger, U., 2001, The Osborne deposit, Cloncurry district: A 1595 Ma Cu-Au skarn deposit, in Williams, P.J., ed., A hydrothermal odyssey: Extended Conference Abstracts, EGRU Contribution 59.

Giere, R., 1996, Formation of rare earth minerals in hydrothermal systems, in Jones, A.P., Wall, F., and Williams, C.T., eds., Rare earth minerals, chemistry, origin and ore deposits, The Mineralogical Society Series, Chapman & Hall, London, p. 105-150.

Gleason, J.D., Marikos, M.A., Barton, M.D., and Johnson, D.A., 2000, Neodymium isotopic study of rare earth element sources and mobility in hydrothermal Fe oxide (Fe-P-REE) systems: Geochimica et Cosmochimica Acta, v. 64, p. 1059-1068.

Goff, B.H., Weinberg, R., Groves, D.I., Vielreicher, N.M., and Fourie, P.J., 2004, The giant Vergenoeg fluorite deposit in a magnetite-fluorite-fayalite-REE pipe: a hydrothermally-altered carbonatite-related pegmatoid?: Mineralogy and Petrology, v. 80, p. 173-199.

Grainger C.J., Groves D.I., and Costa C.H.C., 2002, The epigenetic sediment-hosted Serra Pelada Au-PGE deposit and its potential genetic association with Fe-oxide Cu-Au mineralization within the Carajas mineral province, Amazon Craton, Brazil, in Goldfarb, R.J., and Nielsen, R.L., eds., Integrated methods for discovery: Global exploration in the 21st century: Society of Economic Geologists, Special Publication 9, p. 47-64.

Groves, D.I., and Vielreicher, N.M., 2001, The Phalabowra (Palabora) carbonatite-hosted magnetite-copper sulfide deposit, South Africa: An end-member of the iron-oxide copper-gold-rare earth element deposit group?: Mineralium Deposita, v. 36, p 189-194.

Haghipour, A., 1974, Etude géologique de la région de Biabanak-Bafq (Iran Central). Petrologie et tectonique du socle precambrien et de sa couverture. Thése Doct., Univ. Grenoble, 403 p.

Haghipour, A., 1977, Geological map of the Biabanak-Bafq area (scale 1:500,000): Geological Survey of Iran.

Haghipour, A., Valeh, N., Pelissier, G., and Davoudzadeh, M., 1977, Explanatory text of the Ardekan quadrangle map, 1:250,000, Geological Survey of Iran, H8, 114 p.

Hanes, J.A., 1991, K-Ar and ^{40}Ar/^{39}Ar geochronology: methods and applications, in Heaman, L., and Ludden, J.N., eds., Application of radiogenic isotope systems to problems in geology, Short Course Handbook, Mineralogical Association of Canada, v. 19, p. 27-57.

Harlov, D.E., and Förster, H.J., 2003, Fluid-induced nucleation of (Y+REE)-phosphate minerals within apatite: Nature and experiment. Part II. Fluorapatite: American Mineralogist, v. 88, p. 1209-1229.

Harlov, D.E., Andersson, U.B., Förster, H.J., Nyström, J.O., Dulski, P., and Broman, C., 2002, Apatite-monazite relations in the Kiirunavaara magnetite-apatite ore, northern Sweden: Chemical Geology, v. 191, p. 47-72.

Harmer, R.E., 2000, Mineralisation of the Phalaborwa complex and the carbonatite connection, in Porter, T.M., ed., Hydrothermal iron oxide copper-gold and related deposits: A global perspective: PGC Publishing, Adelaide, v. 1, p. 331-340.

Harrison, T.M., 1981, Diffusion of ^{40}Ar in hornblende: Contribution to Mineralogy and Petrology, v. 78, p. 324-331.

Helvaci, C., 1984, Apatite-rich iron deposits of the Avnik (Bingöl) region, southeasthern Turkey: Economic Geology, v. 79, p. 354–371.

Herrington, R., Smith, M., Maslennikov, V., Belogub, E., and Armstrong, R., 2002, A short review of Palaeozoic hydrothermal magnetite iron-oxide deposits of the south and central Urals and their geological setting, in Porter, T.M., ed., Hydrothermal iron oxide copper-gold and related deposits: A global perspective: PGC Publishing, Adelaide, v. 2, p. 343-353.

Hildebrand, R.S., 1986, Kiruna-type deposits: their origin and relationship to intermediate subvolcanic plutons in the Great Bear Magmatic Zone, northwest Canada: Economic Geology, v. 81, p. 640-659.

Hitzman, M.W., 2000, Iron oxide-Cu-Au deposits: what, where, when, and why, in Porter, T.M. ed., Hydrothermal iron oxide copper-gold & related deposits: A global perspective: PGC Publishing, Adelaide, v. 1, p. 9-25.

Hitzman, M.W., Oreskes, N., and Einaudi, M.T., 1992, Geological characteristics and tectonic setting of Proterozoic iron oxide (Cu-U-Au-REE) deposits: Precambrian Research, v. 58, p. 241-287.

Hitzman, M.W., Valenta, R.K., 2005, Uranium in iron oxide-copper-gold (IOCG) systems: Economic Geology, v. 100, p. 1657-1661.

Hogarth, D.D., 1989, Pyrochlore, apatite and amphibole: distinctive minerals in carbonatite, in Bell, K. ed., Carbonatites: genesis and evolution: Unwin Hyman, London, p. 105-148.

Huckriede, R., Kürsten, M., and Venzlaff, H., 1962, Zur geologie des gebietes zwischen Kerman und Sagand (Iran): Beihefte zum Geologischen Jahrbuch, v. 51, p. 197.

Husseini, M.I., and Husseini, S. I., 1990, Origin of the Infracambrian salt basins of the Middle East, in Brooks, J. ed., Classic petroleum provinces, Geological Society Special Publication 50, p. 279-292.

Injoque, J.E., 2002, Fe oxide-Cu-Au deposits in Peru, an integrated view, in Porter, T.M., ed., Hydrothermal iron oxide copper-gold and related deposits: A global perspective: PGC Publishing, Adelaide, v. 2, p. 97-113.

Irvine, T.N., and Baragar, W.R.A., 1971, A guide to the chemical classification of the common volcanic rocks: Canadian Journal of Earth Sciences, v. 8, p. 523-548.

Jafarzadeh, A., 1981, Die Magnetiterzlagerstätte Chador-Malu in Zentraliran und ihre exploration, Diss. RWTH Aachen, 152 p.

Jercinovic, M.J., and Williams, M.L., 2005, Analytical perils (and progress) in electron microprobe trace element analysis applied to geochronology: Background acquisition, interferences, and beam irradiation effects: American Mineralogist, v. 90, p. 526-546.

Johnson, J.P., and Cross, K.C., 1995, U-Pb geochronological constraints on the genesis of the Olympic Dam Cu-U-Au-Ag deposit, South Australia: Economic Geology, v. 90, p. 1046-1063.

Jourdan, F., Renne, P.R., 2007, Age calibration of the Fish Canyon sanidine ^{40}Ar/^{39}Ar dating standard using primary K–Ar standards: Geochimica et Cosmochimica Acta, v. 71, p. 387-402.

Kuno, J., 1966, Lateral variation of basalt magma types across continental margins and island arcs: Bulletin of Volcanology, v.29, p.195-222.

Le Bas, M.J., Subbarao, K.V., Walsh, J.N., 2002, Metacarbonatite or marble? – the case of the carbonate, pyroxenite, calcite-apatite rock complex at Borra, Eastern Ghats, India: Journal of Asian Earth Sciences, v. 20, p. 127-140.

Leach, D.L., Sangster, D.F., Kelley, K.D., Large, R.R., Garven, G., Allen, C.R., Gutzmer, J., and Walters, S., 2005, Sediment-hosted lead-zinc deposits: A global perspective: Economic Geology, 100th Anniversary Volume, p. 561-607.

Loberg, B.E.H., and Horndahl, A.K., 1983, Ferride geochemistry of Swedish Precambrian iron ores: Mineralium Deposita, v. 18, p. 487-504.

Ludwig, K.R., 2001, Users manual for ISOPLOT/EX, rev. 2.49 – A geochronological toolkit for Microsoft Excel. Berkeley Geochronology Center, Special Publication, No. 1a.

MacDonald, G.A., 1968, Composition and origin of Hawaiian lavas, in Coats, R.R., Hay, R.L., and Anderson, C.A., eds., Studies in volcanology: a memoir in honour of Howel Williams, Geological Society of America Memorials, v. 116, p. 477-522.

Mark, G., and Foster, D.R.W., 2000, Magmatic-hydrothermal albite-actinolite-apatite-rich rocks from the Cloncurry district, NW Queensland, Australia: Lithos, v. 51, p. 223-245.

Mark, G., Oliver, N.H.S., Williams, P.J., Valenta, R.K., and Crookes, R.A., 2000, The evolution of the Ernest Henry Fe-oxide-(Cu-Au) hydrothermal system, in Porter, T.M., ed., Hydrothermal iron oxide copper-gold and related deposits: A global perspective: PGC Publishing, Adelaide, v. 1, 123-136.

Mathur, R., Marschik, R., Ruiz, J., Munizaga, F., Leveille, R.A., and Martin, W., 2002, Age of Mineralization of the Candelaria Fe Oxide Cu-Au Deposit and the Origin of the Chilean Iron Belt, Based on Re-Os Isotopes: Economic Geology, v. 97, p. 59-71.

McDougall, I., and Harrison, T. M., 1988, Geochronology and thermochronology by the $^{40}Ar/^{39}Ar$ method: New York, Axford Uni. Press, 212 p.

Montel, J.M., Foret, S., Veschambre, M., Nicollet, C., and Provost, A., 1996, Electron microprobe dating of monazite: Chemical Geology, v. 131, p. 37-53.

Moore, F., and Modabberi, S., 2003, Origin of Choghart iron oxide deposit, Bafq mining district, Central Iran: new isotopic and geochemical evidence: Journal of Science, Islamic Republic of Iran v. 14(3), p. 259-269.

Morad, S., and Felitsyn, S., 2001, Identification of primary Ce-anomaly signatures in fossil biogenic apatite: implication for the Cambrian oceanic anoxia and phosphogenesis: Sedimentary Geology, v. 143, p. 259-264.

Mücke, A., Younessi, R., 1994, Magnetite-apatite deposits (Kiruna-type) along the Sanandaj-Sirjan zone and in the Bafq area, Iran, associated with ultramafic and calcalkaline rocks and carbonatites: Mineralogy and Petrology, v. 50, p. 219-244.

Naslund, H.R., Aguirre, R., Dobbs, F.M., Henriquez, F.J., and Nyström, J.O., 2000, The origin, emplacement, and eruption of ore magmas: IX Congreso Geologico Chileno, v. 2, p. 135-139.

Naslund, H.R., Henriquez, F.J., Nyström, J.O., Vivallo, W., and Dobbs, F.M., 2002, Magmatic iron ores and associated mineralization: Examples from the Chilean High Andes and Coastal Cordillera, in Porter, T.M. ed., Hydrothermal iron oxide copper-gold & related deposits: A global perspective: PGC Publishing, Adelaide, v. 2, p. 207-226.

Nyström, J.O., and Henriquez, F., 1994, Magmatic features of iron ores of the Kiruna type in Chile and Sweden: ore textures and magnetite geochemistry: Economic Geology, v. 89, p. 820-839.

Ohmoto, H., 2003, Nonredox transformations of magnetite-hematite in hydrothermal systems: Economic Geology, v. 98, p. 157-161.

Oliver, N.H.S., Cleverley, J.S., Mark, G., Pollard, P.J., Fu, B., Marshall, L.J., Rubenach, M.J., Williams, P.J., and Baker, T., 2004, Modeling the role of sodic alteration in the genesis of iron oxide-copper-gold deposits, Eastern Mount Isa Block, Australia: Economic Geology, v. 99, p. 1145-1176.

Oliver, N.H.S., Rawling, T.R., Cartwright, I., and Pearson, P.J., 1994, High temperature fluid-rock interaction and scapolitization in a large extension-related hydrothermal system, Mary Kathleen, Australia: Journal of Petrology, v. 35, p. 1455-1491.

Oreskes, N., and Einaudi, M.T., 1990, Origin of REE-enriched hematite breccias at the Olympic Dam Cu-U-Au-Ag deposit, Roxby Downs, South Australia: Economic Geology, v. 85, p. 1-28.

Pan, Y., Fleet, M.E., and Macrae, N.D., 1993, Oriented monazite inclusions in apatite porphyroblasts from the Hemlo gold deposit, Ontario, Canada: Mineralogical Magazine, v. 57, p. 697-707.

Parak, T., 1975, Kiruna iron ores are not “intrusive-magmatic ores of the Kiruna type”: Economic Geology, v. 70, p. 1242-1258.

Parrish, R.R., 1990, U-Pb dating of monazite and its application to geological problems: Canadian Journal of Earth Sciences, v. 27, p. 1431-1450.

Parsons, I., Rex., D.C., Guise, P., and Halliday, A.N., 1988, Argon-loss by alkali feldspars: Geochimica et Cosmochimica Acta, v. 52, p. 1097-1112.

Partington, G.A., and Williams, P.J., 2000, Proterozoic lode gold and (iron)-copper-gold deposits: A comparison of Australian and global examples: Reviews of Society of Economic Geologists, v. 13, p. 69-101.

Pearce, J.A., Harris, N.B.W., and Tindle, A.G., 1984, Trace element discrimination diagrams for the tectonic interpretation of granitic rocks: Journal of Petrology, v. 25, p. 956-983.

Piccoli, P.M., and Candela, P.A., 2002, Apatite in igneous systems, in Kohn, M.J., Rakovan, J., and Hughes, J.M. eds., Phosphates: geochemical, geobiological, and materials importance: Reviews in Mineralogy and Geochemistry, Mineralogical Society of America, Washington, D.C., v. 48, p. 255-292.

Poitrasson, F., Chenery, S., and Shepherd, T.J., 2000, Electron microprobe and LA-ICP-MS study of monazite hydrothermal alteration: Implications for U-Th-Pb geochronology and nuclear ceramics: Geochimica et Cosmochimica Acta, v. 64, p. 3283-3297.

Pollard, P.J., 2000, Evidence of a magmatic fluid and metal source for Fe-oxide Cu-Au mineralization, in Porter, T.M. ed., Hydrothermal iron oxide copper-gold & related deposits: A global perspective: PGC Publishing, Adelaide, v. 1, p. 27-41.

Pollard, P.J., 2001, Sodic (-calcic) alteration associated with Fe-oxide-Cu-Au deposits: An origin via unmixing of magmatic-derived H_2O-CO_2-salt fluids: Mineralium Deposita, v. 36, p. 93-100.

Pollard, P.J., 2006, An intrusion-related origin for Cu–Au mineralization in iron oxide–copper–gold (IOCG) provinces: Mineralium Deposita, v. 41, p. 179-187.

Porter, T.M. (editor), 2000, Hydrothermal iron oxide copper-gold and related deposits: A global perspective, Volume 1: PGC Publishing, Adelaide, 349 p.

Pyle, J.M., Spear, F.S., and Wark, D.A., 2002, Electron microprobe analysis of REE in apatite, monazite and xenotime: Protocols and pitfalls, in Kohn, M.J., Rakovan, J., and Hughes, J.M. eds., Phosphates: geochemical, geobiological, and materials importance: Reviews in Mineralogy and Geochemistry, Mineralogical Society of America, Washington, D.C., v. 48, p. 337-362.

Pyle, J.M., Spear, F.S., Wark, D.A., Daniel, C.G., and Storm, L.C., 2005, Contributions to precision and accuracy of monazite microprobe ages: American Mineralogist, v. 90, p. 547-577.

Ramezani, J., and Tucker, R.D., 2003, The Saghand region, Central Iran: U-Pb geochronology, petrogenesis and implications for Gondwana tectonics: American Journal of Science, v. 303, p. 622-665.

Ray, G.E., and Dick, L.A., 2002, The Productora prospect in north-central Chile: An example of an intrusion-related, Candelaria type Fe-Cu-Au hydrothermal system, in Porter, T.M., ed., Hydrothermal iron oxide copper-gold and related deposits: A global perspective: PGC Publishing, Adelaide, v. 2, p. 131-151.

Ray, G.E., and Lefebure, D.V., 2000, A synopsis of iron oxide ± Cu ± Au ± P ± REE deposits of the Candelaria-Kiruna-Olympic Dam family: British Columbia Ministry of Energy and Mines, Geological Fieldwork 1999, Paper 2000-1, p. 267-272.

Requia, K., and Fontboté, L., 2000, The Salobo iron-oxide copper-gold deposit, Carajas, Northern Brazil, in Porter, T.M., ed., Hydrothermal iron oxide copper-gold and related deposits: A global perspective: PGC Publishing, Adelaide, v. 1, p. 225-236.

Requia, K., Stein, H., Fontboté, L., and Chiaradia, M., 2003, Re-Os and Pb-Pb geochronology of the Archean Salobo iron oxide copper-gold deposit, Carajas mineral province, northern Brazil: Mineralium Deposita, v. 38, p. 727-738.

Reynolds, L.J., 2000, Geology of the Olympic Dam Cu-U-Au-Ag-REE deposit, in Porter, T.M., ed., Hydrothermal iron oxide copper-gold and related deposits: A global perspective: PGC Publishing, Adelaide, v. 1, p. 93-104.

Roberts, D.E., and Hudson, G.R.T., 1983, The Olympic Dam copper-uranium-gold-silver deposit, Roxby Downs, South Australia: Economic Geology, v. 78, p. 799-822.

Roddick, J.C., 1983, High precision intercalibration of 40Ar/39Ar standards: Geochimica et Cosmochimica Acta, v. 47, p. 887-898.

Roeder, P.L., MacArthur, D., Ma, X.P., Palmer, G.R., and Mariano, A.N., 1987, Cathodoluminescence and microprobe study of rare-earth elements in apatite: American Mineralogist, v. 72, p. 801-811.

Rose, N.M., Bird, D.K., and Liou, J.G., 1992, Experimental investigation of mass transfer-albite, Ca Al silicates and aqueous solutions: American Journal of Science, v. 292, p. 21-57.

Samani, B.A., 1988, Metallogeny of the Precambrian in Iran: Precambrian Research, v. 39, p. 85-106.

Schandl, E.S., and Gorton, M.P., 2004, A textural and geochemical guide to the identification of hydrothermal monazite: Criteria for selection of samples for dating epigenetic hydrothermal ore deposits: Economic Geology, v. 99, p. 1027-1035.

Sillitoe, R.H., 2003, Iron oxide-copper-gold deposits: an Andean view: Mineralium Deposita v. 38, p. 787-812.

Sillitoe, R.H., and Burrows, D.R., 2002, New field evidence bearing on the origin of the El Laco magnetite deposit, Northern Chile: Economic Geology, v. 97, p. 1101-1109.

Skirrow, R.G., Bastrakov, E., Raymond, O.L., Davidson, G., and Heithersay, P., 2002, The geological framework, distribution and controls of Fe-Oxide Cu-Au mineralisation in the Gawler Craton, South Australia, in Porter, T.M., ed., Hydrothermal iron oxide copper-gold and related deposits: A global perspective: PGC Publishing, Adelaide, v. 2, p. 33-47.

Smith, M., and Chengyu, W., 2000, The geology and genesis of the Bayan Obo Fe-REE-Nb deposit: A review, in Porter, T.M., ed., Hydrothermal iron oxide copper-gold and related deposits: A global perspective: PGC Publishing, Adelaide, v. 1, p. 271-281.

Smith, M.P., Henderson, P., and Campbell, L.S., 2000, Fractionation of the REE during hydrothermal processes: Constraints from the Bayan Obo Fe-REE-Nb deposit, Inner Mongolia, China: Geochimica et Cosmochimica Acta, v. 64, p. 3141-3160.

Snee, L. W., Sutter, J. F., and Kelly, W.C., 1988, Termochronology of economic mineral deposits: dating the stages of mineralization at Panasqueira, Portugal, by high-precision ^{40}Ar/^{39}Ar age spectrum techniques on moscuvite: Economic Geology, v. 83, p. 335-354.

Steiger, R. H., and Jäger, E., 1977, Subcommission on geochronology: Convention on the use of decay constants in geo- and cosmochronology: Earth Planet. Sci. Letters, v. 36, p. 359-362.

Stöcklin. J., 1968, Structural history and tectonics of Iran: A review: Bulltein of the American Association of Petroleum Geologists, v. 52, p. 1229-1258.

Stormer, J.C., Jr., Pierson, M.L., and Tacker, R.C., 1993, Variation of F and Cl X-ray intensity due to anisotropic diffusion in apatite during electron microprobe analysis: American Mineralogist, v. 78, p. 641-648.

Stosch, H.G., Romer, R.L., and Daliran, F., 2007, Age of magnetite-apatite deposits and geochemistry of host rocks, Bafq District, Central Iran: Goldschmidt Conference Abstracts, A977.

Suzuki, K., and Adachi, M., 1991, Precambrian provenance and Silurian metamorphism of the Tsubonosawa paragneiss in the South Kitakami terrane, Northeast Japan, revealed by the chemical Th-U-total Pb isochron ages of monazite, zircon and xenotime: Geochemical Journal, v. 25, p. 357-376.

Torab, F.M., and Lehmann, B., 2006, Iron oxide-apatite deposits of the Bafq district, Central Iran: an overview from geology to mining: World of Mining - Surface and Underground, v. 58, p. 355-362.

Torab, F.M., and Lehmann, B., 2007, Magnetite-apatite deposits of the Bafq district, Central Iran: apatite geochemistry and monazite geochronology: Mineralogical Magazine, v. 71, p. 347-363.

Turner, G., 1968, The distribution of potassium and argon in chondrites, in Ahrens., L.H., ed., Origin and distribution of the elements: London, Pergamon Press, p. 387-398.

USGS (U.S. Geological Survey), 2006, Mineral commodity summaries-Iron ore, p. 86-87.

Verdel, C., Wernicke, B.P., Ramezani, J., Hassanzadeh, J., Renne, P.R., and Spell, T.L., 2007, Geology and thermochronology of Tertiary Cordilleran-style metamorphic core complexes in the Saghand region of Central Iran: Bulletin of Geological Society of America, v. 119, p. 961-977.

Vielreicher, N.M., Groves, D.I., and Vielreicher, R.M., 2000, The Phalabowra (Palabora) deposit and its potential connection to iron-oxide copper-gold deposits of Olympic Dam type, in Porter, T.M., ed., Hydrothermal iron oxide copper-gold and related deposits: A global perspective: PGC Publishing, Adelaide, v. 1, p. 321-329.

Williams, M.L., Jercinovic, M.J., Goncalves, P., and Mahan, K., 2006, Format and philosophy for collecting, compiling, and reporting microprobe monazite ages: Chemical Geology, v. 225, p. 1-15.

Williams, P.J., Barton, M.D., Johnson, D.A., Fontbote, L., Haller, A.D., Mark, G., Oliver, N.H.S., and Marschik, R., 2005, Iron oxide copper-gold deposits: geology, space-time distribution, and possible modes of origin: Economic Geology, 100th Anniversary Volume, p. 371-405.

Winchester, J.A., Floyd, P.A., 1977, Geochemical discrimination of different magma series and their differentiation products using immobile elements: Chemical Geology, v. 20, p. 325-343.

Yang, X.M., Le Bas, M.J., 2004, Chemical compositions of carbonate minerals from Bayan Obo, Inner Mongolia, China: implications for petrogenesis: Lithos, v. 72, p. 97-116.

Yang, X.-M., Yang, X.-Y., Zheng, X.-Y., and Le Bas, M.J., 2003, A rare earth element-rich carbonatite dyke at Bayan Obo, Inner Mongolia, North China: Mineralogy and Petrology, v. 78, p. 93-110.

Zharkov, M.A., 1984, Paleozoic Salt bearing formations of the world, Springer-Verlag, Berlin, 427 pp.

Zhu, C., and Sverjensky, D.A., 1991, Partitioning of F-Cl-OH between minerals and hydrothermal fluids: Geochimica et Cosmochimica Acta, v. 55, p. 1837-1858.

Ziemann, M.A., Förster, H.J., Harlov, D.E., and Frei, D., 2005, Origin of fluorapatite-monazite assemblages in a metamorphosed, sillimanite-bearing pegmatoid, Reinbolt Hills, East Antartica: European Journal of Mineralogy, v. 17, p. 567-579.

Appendices

Appendix 1

Appendix 1a: Sample location

Appendix 1b: Analytical techniques

Appendix 1c: Bulk rock analytical data

Appendix 2

Electron microprobe analyses

Appendix 3

Analytical techniques used for Sm-Nd and Ar-Ar isotope analyses

Appendix 1

Appendix 1a: Sample location

Location of outcrop samples

Sample No.	Sample location	Rock type
ES1	Esfordi	Silicified dolomite
ES2	Esfordi	Limestone
ES3	Esfordi	Limestone
ES4	Esfordi	Dolomite
ES5	Esfordi	Metasomatite-albitite
ES6	Esfordi	Silicified dolomite
ES7	Esfordi	Rhyolite
ES8	Esfordi	Silicified dolomite
ES9	Esfordi	Rhyolite
ES10	Esfordi	Doleritic dike
ES11	Esfordi	Spilitic basalt
ES12	Esfordi	Magnetite-apatite ore
ES13	Esfordi	Magnetite-apatite ore
ES14	Esfordi	Iron ore
ES15	Esfordi	Magnetite Apatite Ore
ES16	Esfordi	Spilitic basalt
ES17	Esfordi	Spilitic basalt
ES-WD	Esfordi	Waste dump
ES-LG	Esfordi	Low grade ap. con.
ES-HG	Esfordi	High grade ap. con.
CH1	Choghart	Iron apatite ore
CH2	Choghart	Iron apatite ore
CH3	Choghart	Iron apatite ore
CH4	Choghart	Rhyolite-albitite
CH5	Choghart	Metasomatite-albitite
CH6	Choghart	Iron apatite ore
MA1	Chador-Malu	Rhyolite
MA2	Chador-Malu	Diorite
MA3	Chador-Malu	Poor iron ore
MA4	Chador-Malu	Rich iron ore
MA5	Chador-Malu	Rich iron ore

Location of borehole samples (Esfordi deposit)

Sample No.	Borehole No.	Sampling depth (m)	Rock type
B3 - S1	B3	60-61	Rhyolite
B9 - S1	B9	52-53	Apatite ore
B12 - S1	B12	40-41	Metasomatite
B12 - S2	B12	86-87	Apatite ore
B15 - S1	B15	25-26	Metasomatite
B15 - S2	B15	62-63	Apatite ore
B16 - S1	B16	12-13	Apatite vein
B20 - S1	B20	16-17	Metasomatite
B20 - S2	B20	35-36	Apatite ore
B20 - S3	B20	42-43	Iron ore
B20 - S4	B20	54-55	Apatite ore
B21 - S5	B21	71-72	Agglomerate
B23 - S1	B23	11-12	Metasomatite
B23 - S2	B23	26-27	Apatite ore
B23 - S3	B23	34-35	Iron ore
B23 - S4	B23	44-45	Apatite ore
B26 - S5	B26	54-55	Volcanic tuff
B27 - S1	B27	11-12	Apatite ore
B27 - S2	B27	32-33	Iron ore
B27 - S3	B27	48-49	Iron ore
B30 - S1	B30	9-10	Iron ore
B30 - S2	B30	27-28	Iron ore
B30 - S3	B30	40-41	Apatite vein
B31 - S1	B31	52-53	Metasomatite-albitite
B31 - S2	B31	78-79	Apatite ore
B35 - S1	B35	35-36	Rhyolite
B39 - S1	B39	17-18	Iron ore
B39 - S2	B39	35-36	Apatite vein
B39 - S3	B39	44-45	Iron ore
B40 - S4	B40	52-53	Doleritic dike
B42 - S1	B42	1-2	Apatite ore
B42 - S2	B42	3-4	Iron ore
B42 - S4	B42	17-18	Metasomatite
B43 - S1	B43	7-8	Rhyolite
B43 - S2	B43	38-39	Volcanic tuff
B45 - S1	B45	7-8	Magnetite-apatite ore
B45 - S2	B45	17-18	Apatite vein
B45 - S3	B45	42-43	Iron ore
B46 - S1	B46	3-4	Iron ore
B46 - S2	B46	9-10	Apatite vein
B46 - S3	B46	17-18	Magnetite-apatite ore
B46 - S4	B46	26-27	Apatite ore
B46 - S5	B46	32-33	doleritic dike
B47 - S2	B47	29-30	Apatite vein
B48 - S1	B48	3-4	Apatite vein
B48 - S2	B48	12-13	Metasomatite
B52 - S1	B52	5-6	Metasomatite
B52 - S2	B52	84-85	Apatite vein
B56 - S1	B56	21-22	Diorite
B56 - S3	B56	62-63	Metasomatite
B63 - S1	B63	105-106	Apatite ore
B63 - S2	B63	113-114	Metasomatite
B65 - S2	B65	25-26	Apatite vein
B65 - S3	B65	35-36	Metasomatite
B65 - S4	B65	49-50	Apatite vein
B66 - S2	B66	52-53	Doleritic dike
B67 - S1	B67	7-8	Metasomatite
B67 - S2	B67	16-17	Iron ore

Appendix 1b: Analytical techniques

X-ray fluorescence (XRF)

X-ray fluorescence spectrometry analysis was performed at the Geological Survey of Germany in Hannover. The analytical technique is based upon the excitation of a sample by X-ray and is applicable for major and some trace element analysis. A primary X-ray beam excites secondary X-rays (X-ray fluorescence) which have wavelengths characteristic of the elements present in the sample. The intensity of the secondary X-rays is used to determine the concentrations of the elements comparing to calibration standards. The XRF analysis of rock samples involves the preparation of the rock in two different forms, a pressed powder disc for trace element analysis and a glass bead made from the powdered sample fused with lithium metaborate or tetraborate for major element analysis. In the following Table, analytical errors of this method are presented.

Analytical errors in XRF method

Element	SiO_2	TiO_2	Al_2O_3	Fe_2O_3	MnO	MgO	CaO	Na_2O	K_2O	P_2O_5
Analytical range (%)	40-100	0.1-1.5	0.2-20	0.2-25	0.001-0.15	0.01-3	0.01-5	0.01-5	0.05-5	0.01-0.5
Uncertainty (%)	1	2	2	1	3	2	2	2	1	3
Element	As	Ba	Ce	Co	Cr	Cu	Ga	La	Nb	Ni
Analytical range (ppm)	up to 500	up to 2200	up to 150	up to 20	up to 60	up to 60	up to 30	up to 400	up to 30	up to 30
Uncertainty (%)	15	10	20	20	25	20	10	25	15	30
Element	Pb	Rb	Sc	Sr	Th	U	V	Y	Zn	Zr
Analytical range (ppm)	up to 200	up to 200	up to 20	up to 4000	up to 50	up to 20	up to 200	up to 25	up to 150	up to 200
Uncertainty (%)	15	5	15	5	30	20	15	25	10	10

Instrumental neutron activation analysis (INAA)

Instrumental neutron activation technique was performed at Actlabs in Canada to analyze trace elements especially rare earth elements. In this technique, about 100 mg of powdered sample is placed in a neutron flux in a neutron reactor together with standards. The sample and standards are irradiated for up to 30 hours. Each activated element will emit a fingerprint of gamma radiation, at a specific energy level, which can be measured and quantified. Corrections are made for overlapping lines in the spectrum and concentrations are determined by comparison with the standards analyzed at the same time. In the following

Table, analytical errors of this method are presented. Systematic and random errors are calculated on the basis of internal standards and duplicate samples, respectively.

Analytical errors in INAA method

Element	Au	Zn	As	Ba	Co	Cr	Eu	Fe	Na	Sb	Sc	Th	W	La	Ce	Sm	Tb	Yb	Lu
Systematic error (%)	20.9	14.3	2.6	34.3	2.3	11.9	15.2	1.3	11.5	45.8	1.3	28.2	5.9	1.8	11.1	11.1	18.5	15.1	17.0
Random error (%)	4.3	13.3	0.6	5.5	2.5	5.5	11.1	1.0	0.7	54.9	1.1	26.7	7.4	1.9	10.8	8.8	16.7	1.2	5.2

Inductively coupled plasma emission spectrometry (ICP)

ICP analysis was done at Actlabs in Canada as a complement technique for trace element analysis. The technique is based on digestion of 0.25 g of powdered sample in 10 ml $HClO_4$-HNO_3-HCl-HF at 200°C and dilution to 100 ml with dilute aqua regia (hydrochloric and nitric acids). The sample solution is passed as aerosol from a nebulizer into an argon plasma. The inductively coupled plasma is a stream of argon atoms, heated by the inductive heating of a radio-frequency coil and ignited by a high-frequency Tesla spark, with a flame temperature in the range 6000-10000 °K. The sample dissociates in the argon plasma and a large number of atomic spectral lines are excited. The spectral lines are detected by a range of photomultipliers, they are compared with calibration lines, and their intensities are converted into concentrations. In the following Table, analytical errors of this method are presented. Systematic and random errors are calculated on the basis of internal standards and duplicate samples, respectively.

Analytical errors in ICP method

Element	Ag	Cu	Cd	Mo	Pb	Ni	Zn	S	Al	Be	Bi	Ca	K	Mg	Mn	P	Sr	Ti	V	Y
Systematic error (%)	9.6	4.2	34.0	1.8	4.8	5.6	3.2	4.0	63.5	9.1	6.3	10.5	8.5	8.7	5.9	20.2	9.0	1.6	4.8	28.7
Random error (%)	-	6.3	20.0	-	26.7	7.7	3.2	-	15.1	-	33.3	8.7	1.6	2.1	6.8	15.0	3.6	7.8	9.7	17.5

Appendix 1c: Bulk rock analytical data of magnetite-apatite ores and host rocks of the Bafq deposits

Sample No.	Description	SiO2 (%)	TiO2 (%)	Al2O3 (%)	Fe2O3 (%)	MnO (%)	MgO (%)	CaO (%)	Na2O (%)	K2O (%)	P2O5 (%)	SO3 (%)	Cl (%)	F (%)	LOI (%)	Sum (%)	Be (ppm)	Sc (ppm)
		XRF	*XRF*	*XRF*	*XRF*	*XRF*	*XRF*	*XRF*	*XRF*	*XRF*	*XRF*	*XRF*	*XRF*	*XRF*	*Grav.*	*XRF*	*ICP*	*INAA*
ES1	Silicified dolomite	40.99	1.163	9.3	5.38	0.392	5.91	13.886	2.9	0.876	0.261	0.1	0.007	0.12	18.24	99.52	1	17.2
ES2	Limestone	2.09	0.031	0.64	2.54	0.475	0.61	49.7	0.01	0.102	0.033	0.07	0.004	0.15	42.89	99.34	< 1	0.9
ES3	Limestone	8.75	0.189	1.06	1.11	0.716	0.41	46.641	0.02	0.336	0.09	0.04	0.003	0.09	39.97	99.43	< 1	2.5
ES4	Dolomite	7.76	0.092	1.76	5.49	0.575	16.44	25.294	0.05	0.494	0.052	0.09	0.004	0.11	41.56	99.77	< 1	1.8
ES5	Metasomatite-albitite	66.4	0.17	10.77	3.28	0.049	3.72	4.065	4.08	2.808	0.014	0.03	0.032	<0.05	4.23	99.67	2	1.8
ES6	Silicified dolomite	49.65	0.336	8.02	5.73	0.114	3.88	12.314	0.22	2.125	0.361	0.12	0.027	0.11	16.52	99.54	2	5.5
ES7	Rhyolite	73.08	0.212	11.64	1.75	0.024	0.21	0.478	0.26	8.465	0.022	0.07	0.046	<0.05	3.06	99.35	2	2
ES8	Silicified dolomite	21.31	0.181	3.7	3.27	0.239	12.24	22.705	0.45	0.87	0.186	0.06	0.006	0.06	34.49	99.76	1	3.3
ES9	Rhyolite	72.22	0.35	15.02	1.08	0.007	1.31	0.228	0.22	4.906	0.072	<0.01	0.043	0.1	4.21	99.78	2	4.7
ES10	Doleritic dike	63.81	0.833	12.83	6.57	0.079	2.77	2.166	0.61	3.837	0.151	0.03	0.022	0.08	5.82	99.61	3	10.2
ES11	Spilitic basalt	42.07	1.952	14.03	8.81	0.372	6.44	8.923	2.71	1.429	0.36	0.1	0.01	0.17	12.27	99.64	2	24.7
ES12	Magnetite-apatite ore	12.73	0.716	0.18	37.69	0.045	1.28	22.848	<0.01	0.038	16.008	0.13	0.054	1.3	6.22	99.23	2	1.3
ES13	Magnetite-apatite ore	32.6	0.128	0.34	27.41	0.148	3.06	16.356	0.01	0.082	7.659	0.15	0.058	0.72	10.74	99.45	1	3.5
ES14	Iron ore	7.91	1.066	0.28	76.14	0.027	1.29	4.428	<0.01	0.028	1.296	0.13	0.029	0.11	6.68	99.3	1	0.7
ES15	Magnetite Apatite Ore	24.16	0.523	0.18	43.38	0.013	0.26	14.842	<0.01	0.036	11.142	0.08	0.066	0.82	3.84	99.33	1	1.4
ES16	Spilitic basalt	42.29	1.748	12.66	6.81	0.515	4.49	11.839	2.59	1.873	0.35	0.21	0.008	0.21	13.99	99.58	2	24.4
ES17	Spilitic basalt	43.72	1.942	14.23	6.93	0.403	4.62	9.536	3.4	1.857	0.423	0.23	0.009	0.18	12.07	99.55	2	28.6
ES-WD	Waste dump	18.5	0.853	1.66	44.94	0.046	2.35	12.858	0.64	0.353	7.102	0.75	0.083	0.6	8.52	99.24	2	1.4
ES-LG	Low grade apatite concentrate	5.02	0.141	0.21	5.64	0.02	1.51	47.362	0.12	0.039	33.687	0.26	0.144	2.9	3.38	100.44	2	0.8
ES-HG	High grade apatite concentrate	4.58	0.116	0.15	3.48	0.021	1.86	48.661	0.11	0.035	34.825	0.19	0.158	3.14	3.22	100.55	2	1.2
CH1	Iron apatite ore	2.59	0.179	0.08	35.21	0.022	1.72	30.8	0.01	0.035	22.66	0.13	0.172	1.81	4.22	99.64	1	1
CH2	Iron apatite ore	2.23	0.408	0.17	66.58	0.031	1.7	12.63	<0.01	0.039	8.228	0.1	0.084	0.65	6.7	99.49	1	0.7
CH3	Iron apatite ore	18.6	0.108	0.07	28.06	0.028	0.89	25.896	0.07	0.04	18.986	0.11	0.168	1.34	5	99.37	1	< 0.1
CH4	Rhyolite-albitite	70.81	0.201	11.91	1.74	0.027	1.1	1.924	5.75	1.043	0.161	0.05	0.016	<0.05	4.95	99.72	2	2
CH5	Metasomatite-albitite	64.04	0.146	12.06	4.39	0.052	5.68	2.681	6.88	0.357	0.058	0.1	0.018	0.07	3.2	99.75	2	1.8
CH6	Iron apatite ore	5.45	0.176	0.1	47.34	0.05	2.4	20.45	<0.01	0.036	12.135	0.09	0.047	0.96	10.16	99.37	1	1.5
MA1	Rhyolite	65.94	0.213	10.77	6.1	0.059	0.93	1.834	0.27	8.894	0.056	0.03	0.028	<0.05	4.5	99.66	< 1	1.4
MA2	Diorite	49.66	2.771	13.13	14.63	0.2	3.7	4.546	6.7	0.213	0.972	0.07	0.061	0.12	2.86	99.64	3	23.8
MA3	Poor iron ore	7.28	0.177	0.45	66.53	0.182	0.53	11.654	<0.01	0.027	0.721	0.06	0.008	0.08	11.86	99.46	< 1	1.7
MA4	Rich iron ore	2.37	0.446	0.18	92.05	0.032	0.14	0.462	<0.01	0.047	0.123	0.03	0.007	0.11	3.58	99.44	< 1	1.5
MA5	Rich iron ore	0.61	0.008	<0.05	94.31	0.032	0.06	0.481	<0.01	0.026	0.244	0.04	0.007	0.52	3.38	99.58	< 1	2.2

Appendix 1c: Continued

Sample No.	Description	V (ppm)	Cr (ppm)	Co (ppm)	Ni (ppm)	Cu (ppm)	Zn (ppm)	Ga (ppm)	As (ppm)	Se (ppm)	Br (ppm)	Rb (ppm)	Sr (ppm)	Y (ppm)	Zr (ppm)	Nb (ppm)	Mo (ppm)
		XRF	*XRF*	*XRF*	*XRF*	*ICP*	*XRF*	*XRF*	*INAA*	*INAA*	*INAA*	*XRF*	*XRF*	*XRF*	*XRF*	*XRF*	*INAA*
ES1	Silicified dolomite	190	77	33	42	162	121	10	11.2	< 3	< 0.5	29	74	24	96	3	10
ES2	Limestone	15	<3	45	3	51	14	<3	37	< 3	< 0.5	17	353	5	14	2	< 1
ES3	Limestone	13	<3	<3	<3	14	128	4	1.2	< 3	< 0.5	17	155	7	18	<2	< 1
ES4	Dolomite	44	10	6	<3	16	29	4	16.3	8	2.3	15	42	6	23	<2	7
ES5	Metasomatite-albitite	50	5	<3	8	6	24	12	1.9	< 3	< 0.5	63	135	25	149	2	1
ES6	Silicified dolomite	79	27	16	26	58	52	13	10.2	< 3	< 0.5	61	49	37	124	6	3
ES7	Rhyolite	11	7	<3	6	4	29	18	5.7	< 3	< 0.5	115	146	9	188	4	1
ES8	Silicified dolomite	39	25	10	13	5	46	6	2.5	< 3	< 0.5	34	113	32	55	6	3
ES9	Rhyolite	21	6	<3	<3	7	14	34	18	< 3	4	150	14	<3	227	6	2
ES10	Doleritic dike	90	25	17	8	46	89	21	6	< 3	3.2	157	29	20	203	4	2
ES11	Spilitic basalt	249	106	23	57	8	117	19	2.4	< 3	< 0.5	51	66	20	147	3	< 1
ES12	Magnetite-apatite ore	1179	<3	18	39	43	13	12	46.2	< 3	< 0.5	22	170	885	10	<2	< 1
ES13	Magnetite-apatite ore	577	9	6	86	18	59	8	12.7	< 3	< 0.5	11	162	535	33	<2	2
ES14	Iron ore	2072	<3	18	130	15	25	23	7.6	< 3	< 0.5	27	36	95	8	<2	< 1
ES15	Magnetite Apatite Ore	999	<3	14	23	6	19	10	30	< 3	< 0.5	15	102	746	5	<2	< 1
ES16	Spilitic basalt	217	102	26	56	31	96	15	2.5	< 3	< 0.5	63	89	26	133	3	2
ES17	Spilitic basalt	248	121	27	64	42	104	18	2	< 3	< 0.5	62	86	26	145	6	< 1
ES-WD	Waste dump	1157	16	13	84	29	38	17	11.2	< 3	< 0.5	17	231	576	27	<2	3
ES-LG	Low grade apatite concentrate	148	<3	18	19	11	12	<3	66.9	< 3	< 0.5	11	417	1177	11	<2	< 1
ES-HG	High grade apatite concentrate	110	<3	21	19	22	16	<3	95.6	< 3	< 0.5	7	414	1306	10	2	< 1
CH1	Iron apatite ore	670	<3	10	82	4	22	13	98.7	< 3	< 0.5	12	198	755	<3	3	< 1
CH2	Iron apatite ore	1396	<3	23	168	8	36	12	35.6	< 3	< 0.5	12	187	298	5	2	< 1
CH3	Iron apatite ore	537	<3	41	64	5	31	9	88.3	< 3	< 0.5	8	185	649	4	<2	< 1
CH4	Rhyolite-albitite	<5	<3	<3	<3	2	18	18	2.9	< 3	< 0.5	27	31	30	186	4	2
CH5	Metasomatite-albitite	34	8	6	12	8	43	7	2.8	< 3	< 0.5	12	23	31	215	<2	1
CH6	Iron apatite ore	867	<3	68	99	6	29	11	78.4	< 3	< 0.5	16	242	443	5	<2	< 1
MA1	Rhyolite	42	8	16	3	4	30	8	2.7	< 3	4	82	27	38	159	<2	7
MA2	Diorite	199	<3	31	4	11	90	25	7.1	< 3	8.1	5	70	73	304	8	1
MA3	Poor iron ore	1404	9	16	130	10	13	8	6.2	< 3	< 0.5	19	55	28	5	<2	7
MA4	Rich iron ore	1932	6	<3	162	10	36	17	4.1	< 3	1.5	19	3	4	6	2	< 1
MA5	Rich iron ore	2248	20	33	174	7	17	4	2.8	< 3	< 0.5	10	4	11	<3	<2	< 1

Appendix 1c: Continued

Sample No.	Description	Ag (ppm)	Cd (ppm)	Sn (ppm)	Sb(ppm)	Cs (ppm)	Ba (ppm)	La (ppm)	Ce (ppm)	Pr (ppm)	Nd (ppm)	Sm (ppm)	Eu (ppm)	Tb (ppm)	Yb (ppm)	Lu (ppm)
		ICP	*ICP*	*XRF*	*INAA*	*INAA*	*XRF*	*INAA*	*INAA*	*XRF*	*INAA*	*INAA*	*INAA*	*INAA*	*INAA*	*INAA*
ES1	Silicified dolomite	< 0.3	0.3	<2	0.5	< 1	132	14	27	<50	17	3.8	0.7	0.6	2.5	0.41
ES2	Limestone	< 0.3	< 0.3	<2	0.2	< 1	60	12.2	16	<50	< 5	0.9	0.3	< 0.5	0.4	0.05
ES3	Limestone	< 0.3	< 0.3	<2	< 0.1	< 1	56	4.6	12	<50	< 5	1.5	0.6	< 0.5	1	0.2
ES4	Dolomite	< 0.3	0.3	<2	0.5	< 1	186	12.5	24	<50	6	2	0.5	< 0.5	0.5	0.12
ES5	Metasomatite-albitite	< 0.3	< 0.3	3	< 0.1	2	357	10	28	<50	17	4	0.6	< 0.5	3.7	0.65
ES6	Silicified dolomite	< 0.3	< 0.3	4	1.2	2	1018	44.9	99	<50	40	6.7	1.2	0.9	4.5	0.76
ES7	Rhyolite	< 0.3	< 0.3	<2	0.9	< 1	4289	30.3	57	<50	17	2.5	0.7	< 0.5	2	0.44
ES8	Silicified dolomite	< 0.3	< 0.3	<2	0.3	< 1	145	17.9	40	<50	15	3.6	0.8	0.8	3.5	0.57
ES9	Rhyolite	0.4	< 0.3	<2	3	1	256	1.4	5	<50	< 5	0.4	< 0.2	< 0.5	0.9	0.25
ES10	Doleritic dike	< 0.3	0.4	2	0.7	3	585	20.2	49	<50	18	4	1.5	0.6	3	0.52
ES11	Spilitic basalt	< 0.3	0.4	<2	< 0.1	< 1	73	4.9	12	<50	< 5	2.4	0.9	< 0.5	2.4	0.44
ES12	Magnetite-apatite ore	< 0.3	1.5	9	< 0.1	< 1	23	1230	2390	323	1130	196	16.1	33.6	50.5	7.18
ES13	Magnetite-apatite ore	< 0.3	1.4	27	0.7	< 1	52	447	758	224	269	55.2	5.1	8.6	22.2	3.41
ES14	Iron ore	< 0.3	1.9	12	< 0.1	< 1	13	130	226	<50	68	15.6	1.2	1.8	5.1	0.84
ES15	Magnetite Apatite Ore	< 0.3	1.6	15	< 0.1	< 1	13	717	1410	262	716	134	9.8	26.3	39	5.7
ES16	Spilitic basalt	< 0.3	< 0.3	<2	< 0.1	1	70	9.3	20	<50	12	3.5	1.2	< 0.5	2.8	0.49
ES17	Spilitic basalt	< 0.3	0.4	<2	< 0.1	2	133	8.8	20	<50	15	3.6	1.3	< 0.5	3.2	0.54
ES-WD	Waste dump	< 0.3	1.8	12	< 0.1	< 1	80	382	642	238	204	45.6	3.8	7.5	18.2	2.98
ES-LG	Low grade apatite concentrate	< 0.3	< 0.3	<2	0.4	< 1	60	1300	2440	573	1120	206	18.8	37.4	41.6	5.98
ES-HG	High grade apatite concentrate	< 0.3	< 0.3	<2	0.4	< 1	60	1660	3170	614	1700	256	22.4	41.7	56.4	8.59
CH1	Iron apatite ore	< 0.3	1.7	6	0.5	< 1	7	1310	2220	389	927	135	14.7	23	33.2	4.63
CH2	Iron apatite ore	< 0.3	3.1	15	0.4	< 1	23	664	1120	125	476	67.7	7.3	10.5	14.7	2.33
CH3	Iron apatite ore	< 0.3	1.5	2	< 0.1	< 1	14	1360	2390	418	1040	140	13.9	18.9	28.5	3.76
CH4	Rhyolite-albitite	< 0.3	< 0.3	<2	< 0.1	< 1	82	29.9	67	<50	20	4.8	0.6	< 0.5	2.6	0.44
CH5	Metasomatite-albitite	< 0.3	< 0.3	6	0.2	< 1	44	8.9	23	<50	< 5	3.2	0.5	< 0.5	2.9	0.41
CH6	Iron apatite ore	< 0.3	2.8	23	< 0.1	< 1	44	771	1360	215	579	86.6	8.9	12.6	20.2	2.7
MA1	Rhyolite	< 0.3	0.4	10	0.6	< 1	785	34.2	105	<50	43	12.9	2	1.8	3.2	0.41
MA2	Diorite	< 0.3	0.6	<2	0.6	< 1	70	23.8	47	<50	24	9.4	2.4	1.9	7	1.08
MA3	Poor iron ore	< 0.3	2.7	4	0.5	< 1	206	70.6	174	<50	52	11.4	1.1	< 0.5	2.1	0.28
MA4	Rich iron ore	< 0.3	3.5	28	0.5	< 1	39	18.3	46	<50	15	2.9	0.3	< 0.5	0.7	0.13
MA5	Rich iron ore	< 0.3	3.8	12	0.3	< 1	<5	31.9	64	<50	17	3.5	0.3	< 0.5	0.7	0.07

Appendix 1c: Continued

Sample No.	Description	Hf (ppm)	Ta (ppm)	W (ppm)	Ir (ppb)	Au (ppb)	Hg (ppm)	Pb (ppm)	Bi (ppm)	Th (ppm)	U (ppm)
		INAA	*INAA*	*INAA*	*INAA*	*INAA*	*INAA*	*ICP*	*ICP*	*INAA*	*INAA*
ES1	Silicified dolomite	2	< 0.5	< 1	< 5	< 2	< 1	18	6	1.8	< 0.5
ES2	Limestone	< 1	< 0.5	< 1	< 5	< 2	< 1	< 3	3	0.3	1.4
ES3	Limestone	< 1	< 0.5	< 1	< 5	< 2	< 1	4	4	< 0.2	0.7
ES4	Dolomite	< 1	< 0.5	< 1	< 5	< 2	< 1	26	7	1.4	4.6
ES5	Metasomatite-albitite	3	< 0.5	< 1	< 5	< 2	< 1	< 3	5	11.3	< 0.5
ES6	Silicified dolomite	2	< 0.5	< 1	< 5	< 2	< 1	< 3	10	7.7	4.2
ES7	Rhyolite	5	< 0.5	< 1	< 5	< 2	< 1	< 3	10	19.5	6.8
ES8	Silicified dolomite	< 1	< 0.5	< 1	< 5	< 2	< 1	5	7	2.8	3.8
ES9	Rhyolite	5	< 0.5	< 1	< 5	< 2	< 1	< 3	10	2.5	1.5
ES10	Doleritic dike	4	< 0.5	< 1	< 5	3	< 1	7	4	15.1	3.7
ES11	Spilitic basalt	2	< 0.5	< 1	< 5	< 2	< 1	< 3	< 2	< 0.2	< 0.5
ES12	Magnetite-apatite ore	< 1	< 0.5	< 1	< 5	< 2	< 1	12	< 2	36.9	15.2
ES13	Magnetite-apatite ore	< 1	< 0.5	< 1	< 5	8	< 1	14	< 2	14.1	< 0.5
ES14	Iron ore	< 1	< 0.5	3	< 5	9	< 1	11	< 2	2.6	< 0.5
ES15	Magnetite Apatite Ore	< 1	< 0.5	< 1	< 5	13	< 1	10	5	21.6	17.4
ES16	Spilitic basalt	2	< 0.5	< 1	< 5	< 2	< 1	< 3	3	0.9	< 0.5
ES17	Spilitic basalt	3	< 0.5	< 1	< 5	< 2	< 1	< 3	< 2	1.3	< 0.5
ES-WD	Waste dump	< 1	< 0.5	5	< 5	28	< 1	9	< 2	17.1	4.9
ES-LG	Low grade apatite concentrate	< 1	< 0.5	< 1	< 5	< 2	< 1	11	< 2	42.5	< 0.5
ES-HG	High grade apatite concentrate	< 1	< 0.5	< 1	< 5	40	< 1	10	< 2	55.3	< 0.5
CH1	Iron apatite ore	< 1	< 0.5	< 1	< 5	< 2	< 1	16	< 2	55.6	< 0.5
CH2	Iron apatite ore	< 1	< 0.5	< 1	< 5	< 2	< 1	15	< 2	21.4	< 0.5
CH3	Iron apatite ore	16	< 0.5	< 1	< 5	< 2	< 1	28	< 2	48	< 0.5
CH4	Rhyolite-albitite	3	2.2	< 1	< 5	< 2	< 1	6	3	16.4	2.6
CH5	Metasomatite-albitite	3	1.4	< 1	< 5	< 2	< 1	3	3	3.3	< 0.5
CH6	Iron apatite ore	< 1	< 0.5	< 1	< 5	< 2	< 1	11	< 2	30.3	< 0.5
MA1	Rhyolite	5	0.6	8	< 5	< 2	< 1	11	3	6	1.5
MA2	Diorite	6	< 0.5	< 1	< 5	< 2	< 1	< 3	< 2	1.1	< 0.5
MA3	Poor iron ore	< 1	< 0.5	< 1	< 5	< 2	< 1	51	< 2	5.2	< 0.5
MA4	Rich iron ore	< 1	< 0.5	< 1	< 5	< 2	< 1	15	< 2	5.5	< 0.5
MA5	Rich iron ore	< 1	< 0.5	< 1	< 5	< 2	< 1	17	< 2	9.7	< 0.5

Appendix 1c: Continued

Sample No.	Description	SiO2 (%)	TiO2 (%)	Al2O3 (%)	Fe2O3 (%)	MnO (%)	MgO (%)	CaO (%)	Na2O (%)	K2O (%)	P2O5 (%)	SO3 (%)	Cl (%)	F (%)	LOI (%)	Sum (%)	Be (ppm)	Sc (ppm)
		XRF	*XRF*	*XRF*	*XRF*	*XRF*	*XRF*	*XRF*	*XRF*	*XRF*	*XRF*	*XRF*	*XRF*	*XRF*	*Grav.*	*XRF*	*ICP*	*INAA*
B3 - S1	Rhyolite	61.95	0.103	10.49	3.28	0.023	7.75	3.62	0.27	6.456	0.626	0.21	0.038	0.19	4.38	99.38	1	2.9
B9 - S1	Apatite ore	8.26	0.482	0.24	5.67	0.087	1.91	45.18	0.19	0.013	29.663	0.26	0.211	2.53	4.24	98.93	2	0.3
B12 - S1	Metasomatite	48.11	0.278	6.58	5.7	0.073	6.18	16.299	2.43	1.321	8.071	0.4	0.062	0.63	3.24	99.37	4	2.3
B12 - S2	Apatite ore	9.09	0.811	0.83	27.65	0.052	1.99	32.49	0.17	0.161	21.359	0.18	0.129	1.95	2.18	99.04	<1	2.5
B15 - S1	Metasomatite	48.93	0.147	6.52	5.55	0.083	7.43	16.382	2.65	1.062	6.77	0.18	0.065	0.58	3.01	99.37	4	6.2
B15 - S2	Apatite ore	7.71	0.549	1.11	7.7	0.04	1.62	44.033	0.2	0.199	30.716	0.21	0.154	2.71	2.13	99.07	<1	4.1
B16 - S1	Apatite vein	18	0.254	2.84	10.79	0.05	3.23	33.872	0.39	1.346	22.717	0.2	0.138	1.95	3.34	99.11	1	0.3
B20 - S1	Metasomatite	48.45	0.624	3.13	20.28	0.075	11.59	10.411	1.36	0.608	0.463	0.01	0.013	<0.05	2.55	99.58	4	19.9
B20 - S2	Apatite ore	16.03	0.882	0.33	13.23	0.075	3.85	35.929	0.23	0.046	22.764	0.16	0.157	2.03	3.48	99.2	<1	12.3
B20 - S3	Iron ore	11.73	1.23	0.33	59.52	0.035	0.84	15.072	<0.01	0.028	8.616	0.37	0.08	1.34	0.35	99.55	<1	2.4
B20 - S4	Apatite ore	21.52	0.389	2.08	31.81	0.026	3.72	20.971	0.13	0.147	14.44	0.09	0.094	1.12	2.7	99.23	3	2.3
B21 - S5	Agglomerate	32.4	0.396	6.31	10.94	0.241	4.21	21.024	0.09	1.758	1.471	2.56	0.045	0.28	17.88	99.62	1	9.3
B23 - S1	Metasomatite	50.6	0.609	0.48	10.08	0.11	15.3	13.456	0.33	0.071	4.478	0.12	0.049	0.32	3.48	99.48	4	26.7
B23 - S2	Apatite ore	11.41	0.781	0.39	24.49	0.02	3.75	31.457	0.14	0.035	22.623	0.1	0.123	1.89	1.58	98.79	1	3.0
B23 - S3	Iron ore	2.1	1.811	0.26	87.47	0.016	0.63	3.944	<0.01	0.025	1.07	0.07	0.072	0.63	1.38	99.47	<1	1.0
B23 - S4	Apatite ore	11.3	1.35	1.15	56.38	0.055	2.73	15.372	0.08	0.052	9.111	0.13	0.035	0.87	0.24	98.85	<1	2.2
B26 - S5	Volcanic tuff	43.05	0.267	7.27	8.78	0.185	7.69	13.234	0.15	2.541	1.602	1.03	0.042	0.25	13.6	99.68	3	3.8
B27 - S1	Apatite ore	17.15	0.584	0.28	42.09	0.022	3.76	18.705	0.08	0.042	12.557	0.11	0.091	1.11	2.79	99.37	2	1.1
B27 - S2	Iron ore	13.43	0.933	0.25	73.9	0.014	0.66	5.274	<0.01	0.034	3.132	0.02	0.064	0.22	1.44	99.37	<1	0.9
B27 - S3	Iron ore	8.59	1.308	0.4	77.52	0.03	0.43	5.867	<0.01	0.063	2.385	0.07	0.055	0.27	2.48	99.47	<1	1.4
B30 - S1	Iron ore	10.24	1.05	0.24	62.77	0.014	2.27	12.123	<0.01	0.043	7.877	0.07	0.049	0.6	1.94	99.29	1	1.1
B30 - S2	Iron ore	15.4	0.742	0.24	55.05	0.026	4.39	12.036	0.01	0.044	8.534	0.05	0.056	0.67	2.02	99.27	3	1.4
B30 - S3	Apatite vein	8.29	0.229	0.9	8.07	0.029	1.94	42.732	0.18	0.12	30.926	0.17	0.115	2.6	2.79	99.09	<1	2.2
B31 - S1	Metasomatite-albitite	59.92	0.194	9.75	5.17	0.064	5.41	7.232	4.78	0.961	2.534	0.06	0.035	0.28	3.34	99.74	3	2.4
B31 - S2	Apatite ore	34.19	0.254	5.13	4.11	0.059	7.87	23.682	0.09	1.594	15.629	0.14	0.064	1.31	5.49	99.6	2	4.1
B35 - S1	Rhyolite	63.29	0.145	9.72	3.31	0.017	8.55	3.424	0.44	5.254	1.071	0.05	0.033	0.18	4.19	99.68	3	2.2
B39 - S1	Iron ore	11.35	1.152	0.31	65.01	0.014	0.37	11.351	<0.01	0.048	8.039	0.05	0.034	0.65	0.96	99.34	<1	1.7
B39 - S2	Apatite vein	20.15	0.409	0.5	32.88	0.007	0.15	24.402	0.05	0.06	18.424	0.09	0.07	1.34	0.59	99.12	<1	3.1
B39 - S3	Iron ore	5.2	1.197	0.23	76.66	0.009	0.14	8.498	<0.01	0.069	6.366	0.02	0.029	0.49	0.52	99.43	<1	1.1

Appendix 1c: Continued

Sample No.	Description	V (ppm)	Cr (ppm)	Co (ppm)	Ni (ppm)	Cu (ppm)	Zn (ppm)	Ga (ppm)	As (ppm)	Se (ppm)	Br (ppm)	Rb (ppm)	Sr (ppm)	Y (ppm)	Zr (ppm)	Nb (ppm)	Mo (ppm)
		XRF	*XRF*	*XRF*	*XRF*	*ICP*	*XRF*	*XRF*	*INAA*	*INAA*	*INAA*	*XRF*	*XRF*	*XRF*	*XRF*	*XRF*	*INAA*
B3 - S1	Rhyolite	82	50	10	25	29	65	10	9.8	<3	2.6	139	67	47	181	<2	<1
B9 - S1	Apatite ore	225	18	11	16	16	20	<3	81.6	<3	<4.4	6	384	1197	17	18	<1
B12 - S1	Metasomatite	143	24	21	17	21	19	9	30.5	<5	<1	24	188	445	107	<2	<1
B12 - S2	Apatite ore	775	<3	33	68	<1	18	6	87.3	<3	<0.5	4	266	946	16	8	<1
B15 - S1	Metasomatite	105	17	16	18	9	29	7	21.1	<5	<0.9	22	205	372	99	<2	<1
B15 - S2	Apatite ore	241	<3	18	25	12	18	4	64.4	<13	<2.5	9	378	1248	14	5	<1
B16 - S1	Apatite vein	294	8	29	36	23	45	<3	53.2	<3	<2.1	25	247	989	36	<2	<1
B20 - S1	Metasomatite	523	74	23	72	129	133	9	2.0	<3	1.9	20	87	126	67	3	<1
B20 - S2	Apatite ore	336	11	28	42	21	66	<3	50.6	<12	<2.4	8	242	1004	22	10	<1
B20 - S3	Iron ore	1741	10	59	164	11	41	20	26.5	<5	<0.8	5	89	328	4	5	<1
B20 - S4	Apatite ore	844	23	28	94	65	43	10	60.2	<6	<1.4	5	198	841	34	<2	<1
B21 - S5	Agglomerate	188	44	14	31	7	38	11	13.9	<3	<0.5	47	87	74	84	3	<1
B23 - S1	Metasomatite	221	44	33	41	8	124	4	17.2	<5	<1.1	4	72	304	47	6	<1
B23 - S2	Apatite ore	873	10	31	87	9	2335	7	58.2	<12	<2.5	<2	227	1051	12	<2	<1
B23 - S3	Iron ore	2706	<3	<3	145	22	32	44	5.8	<3	4.4	14	29	113	17	<2	<1
B23 - S4	Apatite ore	1599	4	55	167	6	79	13	35.4	<5	<1.2	<2	91	372	8	2	<1
B26 - S5	Volcanic tuff	117	38	11	35	38	237	13	18.6	<3	2.5	49	89	103	144	3	<1
B27 - S1	Apatite ore	1129	29	45	123	<1	42	9	53.3	<5	<1.1	5	146	932	7	3	<1
B27 - S2	Iron ore	1972	10	<3	82	25	55	20	12.8	<3	<0.5	17	30	272	6	7	<1
B27 - S3	Iron ore	1882	<3	4	67	6	9	22	15.0	<3	3.1	14	52	159	7	<2	10
B30 - S1	Iron ore	1740	<3	41	185	163	30	18	54.4	<5	<1.1	14	107	490	10	<2	<1
B30 - S2	Iron ore	1468	14	44	154	117	40	19	55.7	<5	<1.1	22	113	635	9	<2	<1
B30 - S3	Apatite vein	290	3	28	213	5	78	13	115.2	<19	<3.2	16	383	1381	16	<2	<1
B31 - S1	Metasomatite-albitite	98	29	15	18	14	88	10	9.8	<3	<0.5	17	156	159	177	<2	<1
B31 - S2	Apatite ore	115	18	15	20	<1	43	12	169.6	<8	<1.3	67	227	634	93	<2	7
B35 - S1	Rhyolite	103	36	<3	46	18	35	18	9.8	<3	2.5	153	30	124	195	2	5
B39 - S1	Iron ore	1842	11	18	66	20	14	20	16.2	<4	4.6	18	91	387	15	6	<1
B39 - S2	Apatite vein	641	23	7	17	18	43	4	32.9	<9	<1.6	7	224	1163	15	<2	<1
B39 - S3	Iron ore	1439	20	11	101	5	25	24	12.6	<3	<0.6	19	86	301	12	<2	3

Appendix 1c: Continued

Sample No.	Description	Ag (ppm)	Cd (ppm)	Sn (ppm)	Sb(ppm)	Cs (ppm)	Ba (ppm)	La (ppm)	Ce (ppm)	Pr (ppm)	Nd (ppm)	Sm (ppm)	Eu (ppm)	Tb (ppm)	Yb (ppm)	Lu (ppm)
		ICP	*ICP*	*XRF*	*INAA*	*INAA*	*XRF*	*INAA*	*INAA*	*XRF*	*INAA*	*INAA*	*INAA*	*INAA*	*INAA*	*INAA*
B3 - S1	Rhyolite	<0.3	<0.3	<2	0.7	3	2546	129	221	<50	106	16.1	2.1	2.3	5.8	0.86
B9 - S1	Apatite ore	<0.3	0.3	6	<0.9	<1	29	3090	4040	771	95	11.9	1.8	20.7	59.4	8.78
B12 - S1	Metasomatite	<0.3	<0.3	9	<0.2	<1	296	955	1432	223	483	81.6	7.7	13.0	29.5	4.03
B12 - S2	Apatite ore	<0.3	0.9	6	1.8	<2	54	2010	3730	652	1590	236.0	22.1	31.0	46.4	7.40
B15 - S1	Metasomatite	<0.3	<0.3	6	<0.1	<1	428	716	1090	183	354	60.8	6.5	10.0	27.0	3.69
B15 - S2	Apatite ore	<0.3	0.4	<2	<0.5	<3	169	2560	3460	733	1860	216.8	29.5	30.0	55.1	7.81
B16 - S1	Apatite vein	<0.3	0.6	3	<0.4	<1	193	1820	2490	570	165	22.0	2.9	13.1	41.8	5.21
B20 - S1	Metasomatite	<0.3	<0.3	9	<0.1	<1	118	46	114	<50	57	16.6	2.4	3.3	15.8	2.15
B20 - S2	Apatite ore	<0.3	0.6	4	<0.4	<3	39	2200	3130	608	1960	213.6	28.0	29.5	53.3	8.03
B20 - S3	Iron ore	<0.3	2.1	14	<0.1	<1	58	574	936	172	368	65.8	7.2	11.0	19.7	2.42
B20 - S4	Apatite ore	<0.3	0.8	11	<0.3	<1	81	1030	1672	353	1180	148.8	15.2	24.0	48.1	5.89
B21 - S5	Agglomerate	<0.3	0.6	2	1.6	<1	976	154	322	70	121	21.4	4.3	3.2	5.8	0.78
B23 - S1	Metasomatite	<0.3	<0.3	6	0.6	<1	150	710	1270	152	572	72.2	9.3	11.2	21.9	2.99
B23 - S2	Apatite ore	<0.3	1.0	13	<0.4	<2	46	2040	3830	584	2000	220.0	24.2	35.0	43.8	5.86
B23 - S3	Iron ore	<0.3	0.9	32	0.3	<1	67	113	244	<50	79	18.5	2.8	3.6	6.6	0.82
B23 - S4	Apatite ore	<0.3	1.3	7	<0.2	<1	50	786	1530	246	653	84.0	10.5	13.5	23.2	2.93
B26 - S5	Volcanic tuff	<0.3	2.3	6	0.6	2	403	203	440	75	168	25.8	3.3	3.6	7.4	0.98
B27 - S1	Apatite ore	<0.3	1.0	10	1.0	<1	29	849	1730	339	881	132.8	11.7	26.0	46.1	5.99
B27 - S2	Iron ore	<0.3	2.2	17	0.5	<1	37	218	440	88	142	28.0	2.6	6.9	13.0	1.74
B27 - S3	Iron ore	<0.3	1.8	18	1.1	<1	69	193	386	<50	117	23.0	2.7	4.6	9.0	1.17
B30 - S1	Iron ore	<0.3	1.5	12	<0.2	<1	42	628	1250	151	571	84.8	8.8	16.0	24.4	3.36
B30 - S2	Iron ore	<0.3	1.1	6	1.5	<1	29	771	1530	164	705	105.6	10.0	19.5	32.7	4.38
B30 - S3	Apatite vein	<0.3	0.5	5	<0.9	22	17	2700	4940	689	1760	307.0	36.6	38.0	54.7	8.08
B31 - S1	Metasomatite-albitite	<0.3	0.5	5	1.2	<1	116	288	508	59	205	38.8	4.3	5.3	11.6	1.65
B31 - S2	Apatite ore	<0.3	<0.3	6	2.0	<1	159	1060	1940	290	796	139.0	16.6	16.5	26.2	4.34
B35 - S1	Rhyolite	<0.3	<0.3	9	0.5	3	359	147	324	57	108	20.9	3.1	2.8	7.7	1.16
B39 - S1	Iron ore	<0.3	1.5	20	<0.2	<1	47	546	1060	175	399	82.4	6.9	9.6	16.2	2.36
B39 - S2	Apatite vein	<0.3	2.2	20	<0.3	<2	31	1600	3050	491	1300	238.0	18.1	28.5	49.3	7.34
B39 - S3	Iron ore	<0.3	1.8	13	1.7	<1	56	426	796	146	289	57.2	5.2	6.9	12.8	1.91

Appendix 1c: Continued

Sample No.	Description	Hf (ppm)	Ta (ppm)	W (ppm)	Ir (ppb)	Au (ppb)	Hg (ppm)	Pb (ppm)	Bi (ppm)	Th (ppm)	U (ppm)
		INAA	*INAA*	*INAA*	*INAA*	*INAA*	*INAA*	*ICP*	*ICP*	*INAA*	*INAA*
B3 - S1	Rhyolite	6	<0.5	<1	<5	<2	<1	<3	<2	14.9	1.2
B9 - S1	Apatite ore	<1	<3.5	<6	<5	<2	<1	13	<2	51.3	<3
B12 - S1	Metasomatite	4	<1.35	<2	<11	<2	<2	14	<2	32.1	<1.05
B12 - S2	Apatite ore	<1	<1.95	<1	<5	<12	<1	7	<2	57.5	<1.65
B15 - S1	Metasomatite	<1	3.3	<1	<11	<2	<2	7	<2	49.4	3.6
B15 - S2	Apatite ore	<2	10.3	<3	180	46	<5	14	<2	96.3	11.3
B16 - S1	Apatite vein	<1	9.0	<3	<5	<2	<1	13	<2	36.9	2.2
B20 - S1	Metasomatite	2	<0.5	<1	<5	<2	<1	<3	<2	16.5	1.3
B20 - S2	Apatite ore	6	<3.5	<3	<24	<13.6	<5	10	<2	71.1	<2.95
B20 - S3	Iron ore	<1	<0.9	<1	<5	<2	<1	<3	3	20.5	<0.85
B20 - S4	Apatite ore	12	<1.85	<3	<13	14	<3	3	<2	45.4	<1.5
B21 - S5	Agglomerate	3	0.9	3	<5	<2	<1	5	<2	11.3	4.1
B23 - S1	Metasomatite	<1	<1.3	<2	<5	<2	<2	0	<2	35.2	3.5
B23 - S2	Apatite ore	<2	<3.45	<4	<23	<13.6	<5	9	<2	70.7	11.6
B23 - S3	Iron ore	<1	0.9	<1	<5	<2	<1	<3	2	10.3	21.9
B23 - S4	Apatite ore	<1	4.4	<2	<5	<2	<2	<3	<2	30.3	<1.15
B26 - S5	Volcanic tuff	4	<0.5	3	<5	7	<1	6	<2	14.5	10.8
B27 - S1	Apatite ore	<1	<1.4	<2	<10	<2	<2	6	<2	30.5	<1.2
B27 - S2	Iron ore	<1	<0.5	<1	<5	<2	<1	<3	<2	7.7	14.0
B27 - S3	Iron ore	<1	<0.5	8	<5	<2	<1	<3	3	13.6	33.3
B30 - S1	Iron ore	5	<1.2	<2	<5	<2	<2	<3	<2	23.9	10.7
B30 - S2	Iron ore	8	<1.3	<2	36	<2	<2	<3	<2	28.5	9.8
B30 - S3	Apatite vein	<2	<5.85	<5	<41	<17.6	<9	10	<2	88.5	<5.2
B31 - S1	Metasomatite-albitite	7	<0.9	<1	<5	<2	<1	<3	<2	20.8	4.0
B31 - S2	Apatite ore	<1	<2.1	<2	24	<2	<3	6	<2	46.7	160.5
B35 - S1	Rhyolite	4	<0.5	<1	<5	<2	<1	<3	<2	14.9	1.9
B39 - S1	Iron ore	<1	<1	<1	<5	4	<2	<3	<2	29.8	14.0
B39 - S2	Apatite vein	<1	<2.5	<2	<17	18	<4	8	<2	56.5	20.1
B39 - S3	Iron ore	<1	<0.8	<1	32	<2	<1	<3	2	34.1	31.5

Appendix 1c: Continued

Sample No.	Description	SiO2 (%)	TiO2 (%)	Al2O3 (%)	Fe2O3 (%)	MnO (%)	MgO (%)	CaO (%)	Na2O (%)	K2O (%)	P2O5 (%)	SO3 (%)	Cl (%)	F (%)	LOI (%)	Sum (%)	Be (ppm)	Sc (ppm)
		XRF	*XRF*	*XRF*	*XRF*	*XRF*	*XRF*	*XRF*	*XRF*	*XRF*	*XRF*	*XRF*	*XRF*	*XRF*	*Grav.*	*XRF*	*ICP*	*INAA*
B40 - S4	Doleritic dike	51.52	0.248	8.72	25.31	0.013	3.76	2.509	0.18	2.99	1.531	0.02	0.026	0.26	2.57	99.66	4	2.3
B42 - S1	Apatite ore	4.6	0.436	0.32	20.91	0.015	0.23	39.346	0.12	0.068	29.581	0.16	0.1	2.53	0.7	99.12	<1	1.5
B42 - S2	Iron ore	13.85	1.565	1.43	69	0.02	1.08	6.143	0.01	0.29	3.484	0.02	0.029	0.31	2.17	99.41	<1	2.2
B42 - S4	Metasomatite	46.32	0.124	5.97	8.61	0.097	8.19	15.808	1.84	1.372	6.24	0.07	0.038	0.47	4.43	99.58	4	5.4
B43 - S1	Rhyolite	62.82	0.205	10.43	5.41	0.041	5.05	3.886	0.34	6.059	0.487	0.06	0.031	0.1	4.75	99.68	2	3.9
B43 - S2	Volcanic tuff	49	0.688	14.48	10.33	0.085	6.04	4.292	1.99	3.776	0.818	0.75	0.012	0.14	6.41	98.82	2	30.5
B45 - S1	Magnetite-apatite ore	28.25	0.609	1.94	31.13	0.017	0.62	19.418	0.14	0.111	13.918	0.07	0.064	1.18	2.07	99.55	2	6.6
B45 - S2	Apatite vein	38.54	0.24	5.7	13.8	0.02	6.25	16.681	0.09	0.354	11.463	0.13	0.034	1.04	5.21	99.55	4	3.5
B45 - S3	Iron ore	5.79	0.65	0.65	79.75	0.047	1.45	6.565	<0.01	0.064	3.835	0.11	0.032	0.36	0.14	99.44	<1	4.3
B46 - S1	Iron ore	6.46	2.036	0.27	72.97	0.029	0.71	8.748	<0.01	0.029	5.656	0.07	0.034	0.52	1.94	99.47	<1	2.4
B46 - S2	Apatite vein	13.57	0.518	0.49	28.25	0.012	0.22	30.297	0.08	0.051	22.883	0.1	0.121	1.84	0.8	99.23	<1	2.0
B46 - S3	Magnetite-apatite ore	7.56	1.178	0.38	39.06	0.022	0.41	27.098	<0.01	0.048	20.166	0.08	0.102	1.49	1.58	99.18	<1	1.5
B46 - S4	Apatite ore	11.23	0.526	0.25	20.46	0.009	0.21	36.17	0.04	0.063	27.369	0.08	0.078	2.1	0.73	99.32	<1	3.9
B46 - S5	doleritic dike	21.16	0.148	2.51	60.69	0.009	0.64	6.804	0.07	0.392	4.366	0.02	0.046	0.38	1.91	99.14	3	8.6
B47 - S2	Apatite vein	35.35	0.214	5.35	16.38	0.019	1.63	20.339	0.13	0.243	14.777	0.07	0.086	1.26	3.69	99.54	4	3.5
B48 - S1	Apatite vein	15.5	0.49	2.26	23.74	0.032	1.45	29.245	0.19	1.297	18.831	0.11	0.095	1.61	4.56	99.41	<1	1.6
B48 - S2	Metasomatite	53.68	0.139	9.01	7.2	0.05	7.26	8.721	3.4	2.016	1.575	0.05	0.054	0.22	6.34	99.72	3	2.3
B52 - S1	Metasomatite	57.86	1.132	3.36	7.57	0.088	7.41	12.598	1.51	0.512	2.816	0.14	0.042	0.31	4.19	99.54	7	22.2
B52 - S2	Apatite vein	4.16	0.39	0.4	12.55	0.033	0.42	44.376	0.1	0.032	30.14	0.25	0.155	2.68	3.51	99.21	<1	3.4
B56 - S1	Diorite	44.72	2.599	13.2	11.63	0.156	6.34	7.158	3.74	2.474	0.989	0.2	0.048	0.14	6.13	99.53	3	15.7
B56 - S3	Metasomatite	44.27	0.736	7.55	6.98	0.164	6.84	13.942	1.61	2.229	0.524	0.07	0.029	0.11	14.54	99.58	3	19.0
B63 - S1	Apatite ore	11.12	0.372	1.34	17.62	0.085	1.1	36.577	0.17	0.333	20.872	0.51	0.112	1.72	7.4	99.33	<1	1.5
B63 - S2	Metasomatite	56.74	0.196	8.96	6.7	0.071	7.1	8.197	0.79	3.8	1.279	0.04	0.047	0.08	5.63	99.63	3	4.4
B65 - S2	Apatite vein	14.58	0.052	0.4	1.92	0.033	1.87	43.532	0.24	0.061	31.222	0.34	0.165	2.61	1.79	98.82	3	2.7
B65 - S3	Metasomatite	36.18	0.902	11.72	18.31	0.032	7.17	9.657	2.92	1.876	5.977	0.13	0.041	0.66	4.06	99.62	1	28.8
B65 - S4	Apatite vein	14.71	0.392	2.13	8.07	0.074	2.33	38.118	0.32	0.897	23.262	0.19	0.135	1.96	6.63	99.23	1	3.3
B66 - S2	Doleritic dike	40.52	1.23	9.66	13.08	0.057	9.86	9.111	0.44	2.83	3.512	0.36	0.054	0.38	8.48	99.58	4	9.1
B67 - S1	Metasomatite	49.76	0.339	9.92	6.72	0.013	1.29	13.358	0.14	5.032	9.495	0.05	0.064	0.77	2.34	99.3	1	4.2
B67 - S2	Iron ore	7.39	1.034	1.18	74.2	0.053	1.72	7.688	0.04	0.183	3.079	0.13	0.029	0.28	2.49	99.5	<1	3.2

Appendix 1c: Continued

Sample No.	Description	V (ppm)	Cr (ppm)	Co (ppm)	Ni (ppm)	Cu (ppm)	Zn (ppm)	Ga (ppm)	As (ppm)	Se (ppm)	Br (ppm)	Rb (ppm)	Sr (ppm)	Y (ppm)	Zr (ppm)	Nb (ppm)	Mo (ppm)
		XRF	*XRF*	*XRF*	*XRF*	*ICP*	*XRF*	*XRF*	*INAA*	*INAA*	*INAA*	*XRF*	*XRF*	*XRF*	*XRF*	*XRF*	*INAA*
B40 - S4	Doleritic dike	421	23	4	28	6	24	5	7.8	<3	<0.5	95	36	96	124	<2	4
B42 - S1	Apatite ore	692	<3	11	28	34	18	7	77.0	<22	<3.2	7	392	1286	16	<2	<1
B42 - S2	Iron ore	1878	22	4	57	11	27	16	16.8	<3	<0.6	21	47	179	19	<2	<1
B42 - S4	Metasomatite	129	21	17	24	26	80	10	65.3	<4	3.9	39	213	376	87	<2	<1
B43 - S1	Rhyolite	86	32	11	23	21	47	13	5.2	<3	3.6	135	45	54	175	<2	6
B43 - S2	Volcanic tuff	262	79	18	24	3	85	15	3.2	<3	<0.5	138	365	44	128	6	<1
B45 - S1	Magnetite-apatite ore	506	25	<3	22	6	17	8	24.3	<3	6.8	7	165	633	43	<2	<1
B45 - S2	Apatite vein	224	34	19	33	11	42	10	30.7	<5	<1.1	16	192	683	79	<2	<1
B45 - S3	Iron ore	995	<3	58	193	12	66	10	38.0	<3	<0.7	7	76	128	21	<2	<1
B46 - S1	Iron ore	1755	10	<3	68	7	22	18	10.8	<3	<0.7	17	79	255	14	<2	<1
B46 - S2	Apatite vein	620	17	21	33	15	122	7	34.2	<9	<1.7	8	262	1117	19	<2	<1
B46 - S3	Magnetite-apatite ore	739	6	31	26	<1	10	9	27.0	<8	<1.5	13	242	903	17	<2	<1
B46 - S4	Apatite ore	324	<3	18	9	5	7	<3	40.8	<18	<2.5	10	291	1077	10	<2	<1
B46 - S5	doleritic dike	800	16	10	12	515	14	4	10.2	<15	<1.4	27	68	273	40	3	5
B47 - S2	Apatite vein	214	8	32	84	112	35	7	28.3	<7	<1.3	13	198	603	81	2	<1
B48 - S1	Apatite vein	650	10	10	38	<1	20	5	68.6	<8	<1.9	25	216	800	38	<2	<1
B48 - S2	Metasomatite	146	17	16	23	26	64	14	7.1	<3	<0.5	42	132	151	135	<2	<1
B52 - S1	Metasomatite	169	39	12	25	15	51	6	14.1	<3	<0.5	11	131	333	77	15	<1
B52 - S2	Apatite vein	367	<3	19	30	119	31	4	97.6	<18	<2.4	9	305	1178	13	2	<1
B56 - S1	Diorite	137	181	44	122	35	187	24	7.1	<3	<0.5	59	450	33	520	78	4
B56 - S3	Metasomatite	141	55	9	24	71	821	9	8.7	<3	3.0	45	78	111	127	7	<1
B63 - S1	Apatite ore	397	<3	51	29	61	34	7	59.7	<9	<2	20	326	952	38	3	9
B63 - S2	Metasomatite	115	29	18	22	25	80	14	11.8	<3	<0.5	59	171	184	131	<2	<1
B65 - S2	Apatite vein	64	<3	11	4	106	114	<3	63.1	<15	<3	5	510	1306	10	<2	<1
B65 - S3	Metasomatite	411	177	21	64	28	138	12	27.0	<5	<0.9	37	161	226	99	3	<1
B65 - S4	Apatite vein	185	<3	15	13	5	161	<3	71.9	48	<2.3	25	233	1036	40	3	<1
B66 - S2	Doleritic dike	212	116	28	112	13	147	19	14.1	<3	<0.6	58	116	189	226	20	<1
B67 - S1	Metasomatite	99	38	<3	16	11	196	8	57.0	<7	<1	101	153	471	221	6	7
B67 - S2	Iron ore	1198	<3	58	190	47	141	22	21.2	<3	<0.6	16	86	130	24	2	<1

Appendix 1c: Continued

Sample No.	Description	Ag (ppm)	Cd (ppm)	Sn (ppm)	Sb(ppm)	Cs (ppm)	Ba (ppm)	La (ppm)	Ce (ppm)	Pr (ppm)	Nd (ppm)	Sm (ppm)	Eu (ppm)	Tb (ppm)	Yb (ppm)	Lu (ppm)
		ICP	*ICP*	*XRF*	*INAA*	*INAA*	*XRF*	*INAA*	*INAA*	*XRF*	*INAA*	*INAA*	*INAA*	*INAA*	*INAA*	*INAA*
B40 - S4	Doleritic dike	<0.3	0.8	22	1.1	3	147	207	402	94	163	29.4	2.8	3.0	6.1	0.94
B42 - S1	Apatite ore	<0.3	1.0	9	<0.8	19	203	2550	4460	703	1670	290.0	31.6	35.5	47.2	7.41
B42 - S2	Iron ore	<0.3	1.3	14	2.2	<1	89	388	713	<50	246	49.9	4.7	6.2	11.6	1.53
B42 - S4	Metasomatite	<0.3	<0.3	5	0.8	<1	210	562	1130	147	424	91.4	9.1	10.4	20.9	3.34
B43 - S1	Rhyolite	<0.3	<0.3	4	1.2	2	847	71	138	<50	60	11.3	1.4	1.7	6.1	0.91
B43 - S2	Volcanic tuff	<0.3	0.4	<2	1.3	11	7597	89	163	<50	70	13.0	1.6	1.7	3.6	0.54
B45 - S1	Magnetite-apatite ore	<0.3	1.1	22	<0.2	<1	43	949	1328	284	691	124.0	10.6	16.0	30.4	4.71
B45 - S2	Apatite vein	<0.3	0.3	8	<0.2	<1	87	957	1456	210	705	146.0	14.3	15.5	41.5	6.61
B45 - S3	Iron ore	<0.3	2.7	15	<0.1	<1	528	409	562	87	228	34.9	2.9	3.5	6.9	0.97
B46 - S1	Iron ore	<0.3	1.6	26	3.0	<1	89	431	635	64	299	56.7	5.4	6.8	15.7	2.45
B46 - S2	Apatite vein	<0.3	1.9	17	<0.4	<2	39	1640	2310	502	1230	213.0	18.8	25.0	47.9	7.28
B46 - S3	Magnetite-apatite ore	<0.3	0.9	15	2.3	<1	44	1450	1900	477	1040	180.0	15.0	19.0	35.1	5.69
B46 - S4	Apatite ore	<0.3	0.9	4	2.8	<3	27	2020	3360	546	1370	233.0	20.9	29.0	47.7	7.02
B46 - S5	doleritic dike	<0.3	1.6	304	35.7	<3	20	1010	1780	364	669	116.0	11.3	11.6	14.9	2.64
B47 - S2	Apatite vein	<0.3	0.8	6	<0.3	<1	22	1080	1580	282	782	135.0	11.5	16.0	30.1	4.51
B48 - S1	Apatite vein	<0.3	1.0	5	<0.3	<2	176	1460	2220	396	1320	203.0	16.6	26.5	42.5	6.73
B48 - S2	Metasomatite	<0.3	<0.3	3	0.9	<1	232	123	228	<50	92	25.6	2.3	4.5	15.0	2.26
B52 - S1	Metasomatite	<0.3	<0.3	6	0.7	<1	857	320	498	135	205	63.2	6.0	10.5	29.0	4.12
B52 - S2	Apatite vein	<0.3	0.8	<2	<0.6	<3	21	2570	3540	689	1850	284.0	25.4	35.0	54.4	8.53
B56 - S1	Diorite	0.3	<0.3	4	0.3	4	633	87	132	<50	51	12.7	3.1	1.6	3.2	0.49
B56 - S3	Metasomatite	<0.3	6.2	8	3.5	3	333	77	168	56	89	21.7	2.5	3.6	13.1	1.95
B63 - S1	Apatite ore	<0.3	1.2	12	<0.3	<2	323	1590	2310	404	1370	212.0	17.7	30.5	43.2	6.36
B63 - S2	Metasomatite	<0.3	<0.3	8	1.4	2	400	128	249	<50	123	28.1	2.9	5.3	16.2	2.42
B65 - S2	Apatite vein	<0.3	<0.3	<2	<0.7	<4	2070	3040	4140	766	2220	322.0	29.4	47.5	59.1	9.16
B65 - S3	Metasomatite	<0.3	2.7	7	<0.2	<1	172	582	872	137	350	81.1	7.3	8.8	18.6	2.58
B65 - S4	Apatite vein	<0.3	1.3	5	<0.6	<3	185	2430	3260	539	1580	252.0	22.7	32.0	60.3	8.85
B66 - S2	Doleritic dike	<0.3	<0.3	10	1.0	6	339	421	833	138	330	49.4	6.6	7.0	14.7	1.92
B67 - S1	Metasomatite	<0.3	1.2	7	<0.2	6	889	1040	2310	266	721	105.6	16.0	15.0	29.1	4.49
B67 - S2	Iron ore	<0.3	3.8	26	0.4	<1	84	294	558	96	215	29.1	3.5	4.3	7.6	1.14

Appendix 1c: Continued

Sample No.	Description	Hf (ppm)	Ta (ppm)	W (ppm)	Ir (ppb)	Au (ppb)	Hg (ppm)	Pb (ppm)	Bi (ppm)	Th (ppm)	U (ppm)
		INAA	*INAA*	*INAA*	*INAA*	*INAA*	*INAA*	*ICP*	*ICP*	*INAA*	*INAA*
B40 - S4	Doleritic dike	3	<0.5	<1	<5	<2	<1	<3	<2	15.9	3.7
B42 - S1	Apatite ore	<2	<5.35	66	<41	<16.8	<9	6	<2	97.1	<4.9
B42 - S2	Iron ore	<1	<0.75	13	36	<2	<1	4	<2	26.6	4.4
B42 - S4	Metasomatite	<1	<1.2	13	<5	<2	<2	5	<2	67.0	<0.95
B43 - S1	Rhyolite	5	<0.5	2	<5	<2	<1	3	<2	18.8	4.7
B43 - S2	Volcanic tuff	4	0.9	2	<5	<2	<1	<3	<2	15.2	4.0
B45 - S1	Magnetite-apatite ore	<1	<1.2	<2	<5	<2	<1	8	<2	39.6	16.6
B45 - S2	Apatite vein	7	<1.5	<2	<5	4	<2	9	<2	54.9	3.8
B45 - S3	Iron ore	<1	<0.8	<1	41	<2	<1	4	3	18.2	2.9
B46 - S1	Iron ore	<1	<0.8	14	<5	<2	<1	<3	<2	21.6	10.0
B46 - S2	Apatite vein	<1	<2.5	<2	<17	<8.8	<4	10	<2	54.4	13.7
B46 - S3	Magnetite-apatite ore	<1	6.3	<2	<15	26	<3	7	<2	55.5	8.3
B46 - S4	Apatite ore	<2	<4.15	<4	<33	67	<7	12	<2	90.4	<3.95
B46 - S5	doleritic dike	<2	<2.9	58	45	16	<6	<3	<2	67.3	25.8
B47 - S2	Apatite vein	<1	<1.9	10	<13	44	<3	8	<2	46.1	15.6
B48 - S1	Apatite vein	<1	<2.55	<2	<18	16	<3	6	<2	62.2	9.2
B48 - S2	Metasomatite	2	<0.5	<1	<5	<2	<1	6	<2	31.8	3.0
B52 - S1	Metasomatite	2	<0.75	<1	<5	10	<1	<3	<2	31.1	3.8
B52 - S2	Apatite vein	<2	<4.35	<5	<39	<18.4	<7	13	<2	90.8	20.6
B56 - S1	Diorite	9	6.4	<1	<5	<2	<1	6	<2	10.2	2.6
B56 - S3	Metasomatite	3	<0.5	<1	<5	6	<1	8	<2	35.2	3.5
B63 - S1	Apatite ore	<1	<2.6	<3	<18	42	<3	9	<2	54.2	33.1
B63 - S2	Metasomatite	3	1.3	<1	<5	<2	<1	3	<2	23.1	4.3
B65 - S2	Apatite vein	<2	<5.2	<6	<46	26	<8	15	<2	102.0	<4.55
B65 - S3	Metasomatite	3	<1.35	<2	<10	<2	<2	4	<2	20.0	<1.05
B65 - S4	Apatite vein	<2	<4	<5	<37	<16.8	<7	12	<2	80.1	14.0
B66 - S2	Doleritic dike	4	<0.85	15	<5	2	<1	7	2	25.1	54.5
B67 - S1	Metasomatite	8	<1.55	14	<13	4	<2	8	<2	49.6	4.6
B67 - S2	Iron ore	<1	<0.6	<1	<5	<2	<1	<3	4	13.7	8.0

Appendix 2

Electron microprobe analyses

A summary of electron microprobe analyses, performed on different samples with different mineral compositions, have been reported in this appendix. Electron microprobe analyses were done with a CAMECA-SX100 at the Institute of Mineralogy and Mineral Resources of Technical University of Clausthal. The analyses were performed under the following operating conditions:

Apatite and monazite analysis

An acceleration voltage of 15 kV and a beam current of 20 nA have been used for major elements in apatite (Ca, P, F, Cl, as well as Na, Si, K, Mg), and in monazite (P, Ca and Si). Trace elements (Sr, Nb, Y, Mn, and REE) were measured at 20 kV and 40-60 nA. To minimize errors by volatilization of light anions during apatite analysis, F and Cl were counted first. However, the diffusion and the anisotropy in F and Cl X-ray intensities, mentioned by Stormer et al. (1993), have not been observed.

For the geochronological study of monazite, we used an acceleration voltage of 20 kV, a beam current of 120 nA, and a beam diameter of 1 µm. Wavelength-dispersive spectral scans on the samples were used to determine the peak and background positions of each element and to identify overlapping peaks. Counting times (peak + background) were 200 s for Pb and U, and 40 s for all other elements, with the M lines used for Th, U, and Pb (Th $M\alpha_1$, U $M\beta_1$, Pb $M\alpha_1$). Minerals and synthetic glasses were used as standards and the PAP correction program was used to correct matrix effects. The detection limits for Th, U, and Pb were 275, 180, and 240 ppm, respectively. Interference correction was performed for each analysis using calibration factors according to Pyle et al. (2002) and the analytical error was calculated on the basis of Cocherie et al. (2005).

Magnetite analysis

An acceleration voltage of 15 kV and a beam current of 140 nA have been used for analysis of trace elements in magnetite (or hematite). Due to presence of big crystals, beam diameter was selected large enough (10 µm). The Kα lines were used for all trace elements. The elements were measured in different counting times up to 150 s for Ti. In these conditions the detection limits were satisfactorily Mg=120 ppm, Si=110 ppm, Ca=60 ppm, Ti=120 ppm, V=210 ppm, Cr=50 ppm, Mn=80 ppm, Ni=120 ppm, Al=100 ppm, and Fe=500 ppm.

Institut fuer Mineralogie und Mineralische Rohstoffe
Technische Universitaet Clausthal
Cameca SX100 Quantitative Analysis Report

Label: Apatite-Bright phase

Elements	#1	#2	#3	#4	#5	#6	#7	#8	#9	#10
Ca	39.144	39.183	39.345	39.623	39.024	39.508	39.289	38.760	38.836	38.915
K	0.001	0.001	0.001	0.007	0.000	0.000	0.003	0.019	0.009	0.017
Cl	0.693	0.654	0.680	0.661	0.715	0.641	0.664	0.716	0.669	0.688
P	18.210	18.171	18.028	18.187	17.917	18.147	18.053	18.098	18.282	17.998
F	2.328	2.419	2.317	2.981	2.663	2.538	2.749	2.633	2.321	2.132
Na	0.225	0.245	0.227	0.210	0.239	0.209	0.251	0.258	0.251	0.300
Mg	0.049	0.044	0.042	0.020	0.063	0.011	0.026	0.029	0.018	0.039
Si	0.124	0.121	0.116	0.101	0.127	0.105	0.169	0.129	0.107	0.101
Sr	0.038	0.045	0.072	0.042	0.034	0.039	0.019	0.029	0.033	0.014
Nb	0.000	0.003	0.005	0.023	0.018	0.022	0.000	0.017	0.014	0.049
Y	0.185	0.164	0.162	0.157	0.146	0.174	0.191	0.149	0.142	0.104
La	0.322	0.312	0.315	0.257	0.318	0.279	0.306	0.344	0.322	0.428
Mn	0.014	0.016	0.012	0.011	0.010	0.011	0.005	0.014	0.007	0.007
Ce	0.761	0.760	0.745	0.722	0.751	0.672	0.723	0.865	0.760	0.898
O	38.506	38.435	38.341	38.330	37.939	38.419	38.222	38.095	38.443	38.248
total	100.599	100.570	100.407	101.331	99.962	100.774	100.669	100.153	100.214	99.939

Elements	#11	#12	#13	#14	#15	#16	#17	#18	#19	#20
Ca	39.331	39.162	39.157	39.170	39.270	38.880	38.109	37.752	38.670	38.220
K	0.008	0.006	0.000	0.008	0.000	0.000	0.019	0.000	0.015	0.002
Cl	0.681	0.619	0.631	0.739	0.628	0.674	0.787	0.787	0.770	0.743
P	18.210	18.090	18.046	17.974	17.956	18.165	17.780	17.619	18.177	17.873
F	2.533	2.389	2.592	2.409	2.849	2.441	2.753	2.312	2.604	2.616
Na	0.267	0.258	0.272	0.235	0.256	0.257	0.490	0.517	0.324	0.366
Mg	0.025	0.038	0.051	0.046	0.024	0.034	0.035	0.031	0.050	0.042
Si	0.120	0.105	0.106	0.131	0.142	0.128	0.116	0.116	0.106	0.125
Sr	0.029	0.049	0.023	0.021	0.011	0.019	0.024	0.051	0.026	0.021
Nb	0.002	0.039	0.000	0.018	0.009	0.040	0.017	0.028	0.045	0.037
Y	0.149	0.154	0.128	0.176	0.155	0.184	0.214	0.208	0.188	0.192
La	0.386	0.357	0.341	0.321	0.329	0.348	0.591	0.587	0.442	0.481
Mn	0.013	0.006	0.008	0.008	0.008	0.014	0.005	0.014	0.013	0.004
Ce	0.849	0.812	0.800	0.856	0.827	0.867	1.212	1.259	0.933	1.051
O	38.507	38.348	38.188	38.190	38.037	38.333	37.545	37.399	38.217	37.697
total	101.110	100.432	100.341	100.302	100.500	100.383	99.695	98.679	100.580	99.469

Institut fuer Mineralogie und Mineralische Rohstoffe
Technische Universitaet Clausthal
Cameca SX100 Quantitative Analysis Report

Label: Apatite-Bright phase

Elements	#21	#22	#23	#24	#25	#26	#27
Ca	38.029	38.694	38.621	38.412	38.812	39.199	38.087
K	0.000	0.010	0.005	0.000	0.022	0.003	0.012
Cl	0.715	0.741	0.810	0.850	0.774	0.790	0.705
P	18.202	17.974	17.991	17.836	18.039	17.743	17.816
F	2.425	2.555	2.481	2.408	2.288	2.448	2.541
Na	0.409	0.330	0.339	0.410	0.273	0.309	0.437
Mg	0.031	0.040	0.040	0.040	0.058	0.052	0.040
Si	0.118	0.130	0.127	0.117	0.136	0.113	0.134
Sr	0.036	0.030	0.043	0.024	0.047	0.021	0.016
Nb	0.020	0.038	0.022	0.000	0.000	0.004	0.000
Y	0.172	0.186	0.184	0.213	0.182	0.153	0.182
La	0.517	0.495	0.509	0.479	0.361	0.342	0.511
Mn	0.011	0.010	0.009	0.015	0.009	0.019	0.012
Ce	1.141	0.932	1.012	1.083	0.789	0.881	1.181
O	38.149	38.020	38.040	37.797	38.202	37.884	37.662
total	99.975	100.184	100.230	99.683	99.993	99.959	99.336

Institut fuer Mineralogie und Mineralische Rohstoffe
Technische Universitaet Clausthal
Cameca SX100 Quantitative Analysis Report

Label: Apatite-Dark phase

Elements	#1	#2	#3	#4	#5	#6	#7	#8	#9	#10
Ca	40.469	40.749	40.432	40.145	41.042	41.111	40.810	40.364	40.247	40.335
K	0.000	0.000	0.000	0.000	0.000	0.000	0.007	0.000	0.009	0.000
Cl	0.237	0.158	0.109	0.094	0.157	0.112	0.135	0.432	0.488	0.374
P	18.278	18.671	18.582	18.679	18.724	18.618	18.948	18.152	18.498	18.407
F	2.838	2.937	2.815	2.753	3.084	2.654	3.098	2.443	2.823	2.660
Na	0.099	0.020	0.004	0.011	0.035	0.018	0.025	0.063	0.056	0.078
Mg	0.007	0.005	0.000	0.000	0.000	0.000	0.002	0.009	0.000	0.007
Si	0.056	0.000	0.023	0.010	0.000	0.009	0.016	0.077	0.084	0.085
Sr	0.000	0.006	0.040	0.015	0.014	0.036	0.011	0.017	0.000	0.031
Nb	0.047	0.001	0.022	0.006	0.034	0.036	0.019	0.030	0.039	0.025
Y	0.063	0.033	0.075	0.045	0.068	0.025	0.064	0.131	0.138	0.084
La	0.038	0.014	0.000	0.002	0.000	0.008	0.000	0.049	0.045	0.063
Mn	0.008	0.011	0.004	0.001	0.001	0.003	0.008	0.010	0.010	0.003
Ce	0.091	0.011	0.044	0.000	0.015	0.023	0.000	0.160	0.130	0.196
O	38.667	39.134	38.998	38.999	39.275	39.358	39.483	38.629	38.853	38.876
total	100.896	101.749	101.148	100.760	102.449	102.011	102.626	100.566	101.418	101.221

Elements	#11	#12	#13	#14	#15	#16	#17
Ca	40.360	40.229	39.975	40.148	40.564	40.122	40.000
K	0.000	0.048	0.010	0.000	0.008	0.000	0.009
Cl	0.502	0.514	0.503	0.409	0.417	0.436	0.609
P	18.349	18.428	18.460	18.203	18.406	18.510	18.466
F	2.570	2.723	2.520	2.299	2.472	3.022	2.686
Na	0.050	0.117	0.109	0.058	0.058	0.064	0.066
Mg	0.000	0.000	0.014	0.000	0.000	0.004	0.009
Si	0.082	0.111	0.078	0.101	0.083	0.079	0.100
Sr	0.023	0.033	0.041	0.030	0.037	0.019	0.042
Nb	0.023	0.069	0.007	0.015	0.025	0.031	0.000
Y	0.140	0.167	0.243	0.197	0.140	0.172	0.160
La	0.026	0.073	0.053	0.040	0.047	0.041	0.091
Mn	0.010	0.008	0.013	0.007	0.010	0.013	0.009
Ce	0.155	0.251	0.172	0.182	0.145	0.170	0.245
O	38.805	38.898	38.878	38.712	39.031	38.762	38.802
total	101.094	101.668	101.073	100.401	101.442	101.444	101.292

Institut fuer Mineralogie und Mineralische Rohstoffe
Technische Universitaet Clausthal
Cameca SX100 Quantitative Analysis Report

Label: Monazite

	#1	#2	#3	#4	#5	#6	#7	#8	#9	#10
P_2O_5	27.66	28.78	28.84	28.88	28.69	28.87	26.68	28.72	27.03	28.39
SiO_2	0.77	0.32	0.30	0.30	0.34	0.45	0.60	0.37	1.07	0.41
ThO_2	0.11	0.43	< 0.03	< 0.03	< 0.03	0.36	< 0.03	0.07	0.07	0.42
Y_2O_3	0.66	0.80	0.66	0.71	0.72	0.59	0.37	0.65	0.69	0.56
La_2O_3	16.67	11.69	14.37	14.31	14.46	17.11	18.47	16.70	17.16	16.62
Ce_2O_3	32.90	28.71	33.23	33.74	34.20	33.60	34.14	33.73	34.43	35.06
Pr_2O_3	8.26	7.31	7.90	7.95	7.92	8.15	8.17	8.52	8.18	7.85
Nd_2O_3	7.73	14.20	9.18	9.48	9.47	7.93	6.00	8.84	7.81	8.21
Sm_2O_3	1.24	2.89	1.39	1.43	1.43	1.34	0.89	1.42	1.31	1.10
Gd_2O_3	0.54	1.53	0.65	0.62	0.64	0.59	0.35	0.69	0.65	0.52
CaO	1.57	0.55	1.01	0.89	0.91	1.09	1.75	1.19	1.99	0.23
Sum	98.11	97.21	97.53	98.31	98.78	100.08	97.42	100.90	100.39	99.37

	#11	#12	#13	#14	#15	#16	#17	#18	#19	#20
P_2O_5	28.31	27.18	27.84	27.83	28.64	29.20	28.84	28.60	28.17	28.18
SiO_2	0.38	0.47	0.42	0.42	0.36	0.44	0.30	0.30	0.27	0.39
ThO_2	0.44	0.29	0.40	0.18	0.53	0.37	-	-	-	-
Y_2O_3	0.25	0.55	0.48	0.34	0.26	0.42	0.71	0.69	0.90	0.55
La_2O_3	18.35	17.68	16.33	17.98	17.48	19.00	15.68	16.28	14.77	17.32
Ce_2O_3	35.54	34.68	34.94	35.52	35.31	36.01	34.50	34.58	33.91	34.46
Pr_2O_3	8.09	7.15	7.42	7.66	8.22	8.17	8.22	8.12	7.78	8.45
Nd_2O_3	6.99	6.47	8.54	6.67	7.65	6.46	8.10	7.94	8.92	7.51
Sm_2O_3	0.91	0.97	1.24	0.91	1.02	0.84	1.29	1.25	1.41	1.16
Gd_2O_3	0.30	0.40	0.54	0.37	0.37	0.34	0.62	0.59	0.58	0.53
CaO	0.16	1.67	0.18	1.20	0.17	0.25	1.30	1.70	1.65	1.72
Sum	99.72	97.51	98.33	99.08	100.01	101.50	99.56	100.05	98.36	100.27

Institut fuer Mineralogie und Mineralische Rohstoffe
Technische Universitaet Clausthal
Cameca SX100 Quantitative Analysis Report

Label: Magnetite-Hematite
(Choghart Deposit)

Comment	Mg	Si	Ca	Ti	V	Cr	Mn	Ni	Al	Fe
CH2	0.174	0.296	0.044	0.092	0.276	0.005	0.008	0.033	0.021	70.324
CH2	0.09	0.211	0.018	0.089	0.266	0.005	0.009	0.028	0.019	67.484
CH2	0.036	0.219	0.015	0.023	0.274	0.005	0.008	0.028	0.036	68.303
CH2	0.044	0.098	0.029	0.035	0.274	0.005	0.012	0.024	0.012	69.825
CH2	0.041	0.137	0.011	0.07	0.269	0.005	0.009	0.031	0.023	68.738
CH2	0.027	0.039	0.006	0.098	0.285	0.005	0.009	0.035	0.011	70.317
CH2	0.012	0.016	0.006	0.083	0.286	0.005	0.008	0.031	0.007	70.063
CH2	0.191	0.285	0.018	0.079	0.261	0.005	0.016	0.024	0.016	70.352
CH2	0.077	0.143	0.022	0.053	0.27	0.005	0.008	0.03	0.01	69.909
CH2	0.016	0.068	0.012	0.058	0.281	0.005	0.01	0.032	0.022	68.924
CH2	0.079	0.163	0.023	0.119	0.274	0.005	0.013	0.033	0.02	69.764
CH2	0.022	0.114	0.009	0.098	0.27	0.005	0.012	0.03	0.019	69.163
CH2	0.126	0.234	0.019	0.072	0.275	0.005	0.009	0.027	0.018	68.668
CH2	0.068	0.127	0.016	0.072	0.276	0.005	0.008	0.026	0.018	71.291
CH2	0.083	0.15	0.037	0.074	0.27	0.005	0.008	0.027	0.034	69.121
CH2	0.015	0.03	0.006	0.06	0.285	0.005	0.008	0.031	0.018	71.444
CH2	0.086	0.114	0.006	0.093	0.269	0.005	0.014	0.026	0.041	70.243
CH2	0.046	0.147	0.006	0.16	0.282	0.005	0.008	0.032	0.012	67.902
CH2	0.103	0.244	0.009	0.113	0.275	0.005	0.01	0.033	0.05	67.226
CH2	0.219	0.331	0.07	0.342	0.261	0.005	0.009	0.024	0.073	69.444

Institut fuer Mineralogie und Mineralische Rohstoffe
Technische Universitaet Clausthal
Cameca SX100 Quantitative Analysis Report

Label: Magnetite-Hematite
(Esfordi Deposit)

Comment	Mg	Si	Ca	Ti	V	Cr	Mn	Ni	Al	Fe
B39-S1	0.012	0.01	0.006	0.126	0.437	0.005	0.008	0.012	0.01	68.775
B39-S1	0.012	0.01	0.006	0.04	0.334	0.005	0.008	0.012	0.01	69.117
B39-S1	0.012	0.013	0.006	0.195	0.151	0.005	0.008	0.012	0.01	69.482
B39-S1	0.012	0.01	0.006	0.062	0.027	0.005	0.008	0.012	0.014	69.701
B39-S1	0.012	0.015	0.036	0.036	0.104	0.005	0.008	0.012	0.01	69.543
B39-S1	0.012	0.013	0.006	0.055	0.288	0.005	0.008	0.012	0.01	69.753
B39-S1	0.012	0.01	0.006	0.058	0.03	0.005	0.008	0.012	0.012	69.595
B39-S1	0.012	0.01	0.006	0.062	0.028	0.005	0.008	0.012	0.013	69.692
B39-S1	0.012	0.014	0.006	0.062	0.241	0.005	0.008	0.012	0.01	69.448
B39-S1	0.012	0.01	0.006	0.092	0.331	0.005	0.008	0.012	0.01	70.006
B39-S1	0.012	0.01	0.015	0.047	0.328	0.005	0.008	0.012	0.01	69.585
B39-S1	0.012	0.01	0.006	0.077	0.357	0.005	0.008	0.012	0.01	69.037
B39-S1	0.012	0.01	0.006	0.054	0.035	0.005	0.008	0.012	0.013	69.648
B39-S1	0.012	0.012	0.006	0.13	0.282	0.005	0.008	0.012	0.01	69.093
B39-S1	0.012	0.01	0.006	0.127	0.274	0.005	0.008	0.012	0.01	69.306
B39-S1	0.012	0.011	0.006	0.012	0.313	0.006	0.008	0.012	0.01	68.83
B39-S1	0.012	0.01	0.006	0.06	0.344	0.005	0.008	0.012	0.01	68.958
B39-S1	0.012	0.01	0.006	0.045	0.406	0.005	0.008	0.012	0.01	68.216

Institut fuer Mineralogie und Mineralische Rohstoffe
Technische Universitaet Clausthal
Cameca SX100 Quantitative Analysis Report

Label: Magnetite-Hematite
(Chador-Malu Deposit)

Comment	Mg	Si	Ca	Ti	V	Cr	Mn	Ni	Al	Fe
MA-5	0.02	0.164	0.045	0.012	0.304	0.005	0.008	0.023	0.01	72.062
MA-5	0.044	0.241	0.062	0.012	0.286	0.005	0.008	0.025	0.011	71.378
MA-5	0.104	0.446	0.145	0.012	0.294	0.005	0.008	0.026	0.015	71.139
MA-5	0.026	0.219	0.063	0.012	0.305	0.005	0.008	0.02	0.01	71.773
MA-5	0.045	0.24	0.072	0.012	0.305	0.005	0.008	0.015	0.012	71.533
MA-5	0.056	0.334	0.092	0.012	0.289	0.005	0.008	0.025	0.014	71.65
MA-5	0.012	0.01	0.006	0.012	0.176	0.005	0.008	0.012	0.01	69.909
MA-5	0.012	0.017	0.006	0.012	0.306	0.005	0.008	0.025	0.01	69.539
MA-5	0.012	0.01	0.006	0.012	0.278	0.005	0.008	0.02	0.01	70.131
MA-5	0.012	0.048	0.006	0.012	0.331	0.005	0.008	0.012	0.01	70.262
MA-5	0.072	0.305	0.093	0.012	0.314	0.005	0.008	0.028	0.017	71.494
MA-5	0.032	0.171	0.049	0.012	0.297	0.005	0.008	0.013	0.01	71.89
MA-5	0.023	0.136	0.037	0.012	0.299	0.005	0.008	0.02	0.01	72.258
MA-5	0.119	0.609	0.167	0.012	0.302	0.005	0.008	0.019	0.017	70.529
MA-5	0.132	0.548	0.165	0.012	0.308	0.005	0.008	0.023	0.016	71.262
MA-5	0.094	0.428	0.135	0.012	0.287	0.005	0.008	0.013	0.017	71.097
MA-5	0.062	0.28	0.085	0.012	0.289	0.005	0.008	0.02	0.013	71.828
MA-5	0.072	0.354	0.118	0.012	0.289	0.005	0.008	0.022	0.01	71.284
MA-5	0.184	0.815	0.243	0.012	0.281	0.005	0.008	0.016	0.019	70.154
MA-5	0.112	0.571	0.16	0.012	0.291	0.005	0.008	0.013	0.015	70.853
MA-5	0.037	0.222	0.07	0.012	0.298	0.005	0.008	0.019	0.011	71.521
MA-5	0.021	0.136	0.032	0.012	0.287	0.005	0.008	0.024	0.012	71.954
MA-5	0.1	0.474	0.138	0.012	0.295	0.005	0.008	0.015	0.026	71.149
MA-5	0.062	0.279	0.083	0.012	0.299	0.005	0.008	0.013	0.011	71.173
MA-5	0.043	0.249	0.068	0.012	0.321	0.005	0.008	0.017	0.01	71.615

Appendix 3

Analytical techniques used for Sm-Nd and Ar-Ar isotope analyses

Sm-Nd isotope analysis technique

Sm-Nd isotope analyses were performed at the Laboratory of Isotopic Geochronology and Geochemistry of the Institute of Precambrian Geology and Geochronology of the Russian Academy of Sciences, St Petersburg, Russia (analyst: Boris Belyatsky). All isotope measurements were completed on multicollector mass-spectrometer Tritone TI (Thermo) under static mode. In-run corrections for mass-bias were done on mass-ratio ^{146}Nd/^{144}Nd=0.7219. Total blank level during analytical processing was not exceeded 0.01 ng for Nd and 0.005 ng for Sm. The international neodimium isotope standard JNdi-1 during analytical period was ^{143}Nd/^{144}Nd= 0.512108±4.

Ar-Ar isotope analysis technique

The Ar-Ar isotope analyses using ^{40}Ar/^{39}Ar thermal release method were performed in the Department of Earth, Atmospheric & Environmental Sciences, University of Manchester (analyst: Ray Burgess). The pulverized bulk sample were cleaned in acetone followed by deionised water in an ultrasonic bath and then dried using an infra-red heating lamp. Samples were weighed, wrapped in Al foil and sealed in quartz ampoules together with the flux monitor Hb3gr (t = 1073.6 ± 5.3Ma, Jourdan *et al*. 2006). Nuclear irradiation was carried out in position B2W of the SAFARI-1 reactor at Pelindaba, South Africa, in July 2006. Error-weighted average irradiation parameters were determined from Hb3gr and are defined and listed in Table 6-4. Argon was extracted from the samples using a Ta resistance furnace over the temperature interval 400-1400°C using heating steps of 30 minutes duration. The Ar was purified using a SEAES NP10 getter at 250°C and transferred to the MS1 mass spectrometer for isotopic analysis. The MS1 is a 90° sector noble gas mass spectrometer with a Baur-Signer source and Faraday detector. Blank levels determined at three temperatures during the course of the experiments, in units of 10^{-15} moles ^{40}Ar, these were: 22 ± 4 (600°C); 40 ± 9 (1000°C) and 97 ± 19 (1400°C). All blanks had an approximately atmospheric Ar isotope composition. Raw data were corrected for mass discrimination (calibrated using atmospheric argon), radioactive decay and neutron interference corrections. The latter were determined from pure CaF_2 and K_2SO_4 salts included in the ampoule with the following values: (^{40}Ar/^{39}Ar)K = 0.044 ±0.023; (^{38}Ar/^{39}Ar)K = 0.01243 ±0.00002; (^{39}Ar/^{37}Ar)Ca = 0.000745 ±0.000003; and ^{36}Ar/^{37}Ar)Ca = 0.000269 ±0.000007. Irradiation parameters and Ar-Ar stepped heating data are given in Table 6-4. All ages in Table 6-4 are reported at the 2б level of uncertainty.

Curriculum Vitae

Personal Details:

Full name: **Farhad Mohammad Torab**
Date and place of birth: 27 Dec. 1970, Tehran-Iran
Position: University lecturer (Yazd University, Iran)
Marital status: Married-one child
Present address: Institute of Mineralogy and Mineral Resources, Technical University of Clausthal, Clausthal-Zellerfeld, Germany
Tel: 0049-5323-722878 , Fax: 0049-5323-722511
Email: farhad.torab@tu-clausthal.de
Permanent address: Mining Engineering Department, Yazd University, Yazd, Iran
Email: fmtorab@yazduni.ac.ir

University Education:

1994: B.Sc. (as top student) in Mining Engineering (Mineral Exploration), Amirkabir University of Technology, Tehran, Iran
1997: M.Sc. (as top student) in Mining Engineering (Mineral Exploration), Amirkabir University of Technology, Tehran, Iran
2004-present: PhD student, Technical University of Clausthal, Germany (title of PhD thesis: Geochemistry and metallogeny of magnetite-apatite deposits of the Bafq mining district, Central Iran)

Experiences:

1995-1997: Consultant of mining geology and exploration department, Kavoshgaran Consulting Engineers Co., Tehran, Iran
1997-2004: University lecturer, Mining Engineering Department, Yazd University, Yazd, Iran (courses taught: exploration geochemistry, ore reserve estimation, mineral analysis methods)

Publications and research:

1-Torab, F.M., and Lehmann, B., 2007, Magnetite-apatite deposits of the Bafq district, Central Iran: apatite geochemistry and monazite geochronology: Mineralogical Magazine, v. 71, p. 347-363.
2-Torab, F.M., and Lehmann, B., 2007, Magnetite-apatite deposits of the Bafq district, Central Iran: monazite geochronology and ore formation: Digging Deeper, Proceedings of the Ninth Biennial SGA Meeting, Dublin, v. 1, p. 439-442.
3-Torab, F.M., and Lehmann, B., 2006, Iron oxide-apatite deposits of the Bafq district, Central Iran: an overview from geology to mining: World of Mining - Surface and Underground, v. 58, p. 355-362.
4-Torab, F.M., and Kohsari, A.H., 2003, Mineralogical studies of bentonite reserves in Yazd province; implication for activation using chemical methods: Iranian Journal of Crystallography and Mineralogy, v.11, no.1, p. 3-14 (in Persian with English abstract).
5-Torab, F.M., and others, 2002, Designing and manufacturing of an earth resistivity meter for geoelectrical surveys (Research project in Yazd University, Iran).

6-Torab, F.M., and others, 1999, Prefeasibility study for production of active bentonite from bentonite reserves in Yazd Province, Central Iran (Research project in Yazd University, Iran).

7-Torab, F.M., 1997, Detailed geochemical exploration and exploration model for the Mouteh Gold Mine, Iran (M.Sc. thesis in Persian with English abstract, Amirkabir University of Technology, Tehran, Iran).

8-Torab, F.M., 1994, Reserve estimation of the Mehdi-Abad lead & zinc ore deposit, Central Iran (B.Sc. thesis in Persian, Amirkabir University of Technology, Tehran, Iran).

Membership:
2005-present: member of SGA (Society for Geology Applied to Mineral Deposits)

Awards:
PhD scholarship grant by the Ministry of Science, Research and Technology of Iran